UTILIZING HIGH-THROUGHPUT IN VIVO NANOPARTICLE SCREENS TO IMPROVE DRUG DELIVERY

A Dissertation Presented to
The Academic Faculty

By

Melissa Prasangi Lokugamage

In Partial Fulfillment
of the Requirements for the Degree
Doctor of Philosophy in Biomedical Engineering in the
Wallace H. Coulter Department of Biomedical Engineering

Georgia Institute of Technology and Emory University

May 2021

Copyright © 2021 by Melissa Prasangi Lokugamage

UTILIZING HIGH-THROUGHPUT IN VIVO NANOPARTICLE SCREENS TO IMPROVE DRUG DELIVERY

Approved By:

James E. Dahlman, Ph.D., Advisor
Wallace H. Coulter Department of Biomedical Engineering*, Georgia Institute of Technology and Emory University*

Philip J. Santangelo, Ph.D.
Wallace H. Coulter Department of Biomedical Engineering*, Georgia Institute of Technology and Emory University*

Edward A. Botchwey, Ph.D.
Wallace H. Coulter Department of Biomedical Engineering*, Georgia Institute of Technology and Emory University*

Wilbur Lam, M.D., Ph.D.
Wallace H. Coulter Department of Biomedical Engineering*, Georgia Institute of Technology,* Division of Hematology/Oncology, Department of Pediatrics, *Emory University School of Medicine*

Eric Sorscher, M.D.
Department of Pediatrics*, Emory University School of Medicine*

Date Approved: March 25, 2021

This thesis is dedicated to my mother, Sumithra Lokugamage,

without whom none of this would be possible.

ACKNOWLEDGEMENTS

I have had the privilege of working with some of the greatest scientific minds at Georgia Tech and in the Dahlman lab. I would first like to thank my committee members for their mentorship during my PhD. I have had opportunity to be trained by an incredible mentor, James Dahlman. He has supported me without fail, cultivated my scientific curiosity, and motivated me when I was unsure of myself. I am forever grateful that he took a chance on me. In addition, I wanted to thank my mentors, Cory Sago and Kalina Paunovska, for helping me develop the technology in this thesis and providing their friendship through my degree. I have also had the pleasure and honor of working closely with the best people. My teammates and co-authors are a key part of my success and happiness.

I am grateful for the amazing people in my life who have supported my dreams. Kala Chinnaswamy and Madeleine Haddix, my oldest and dearest friends, thank you for your love and devotion. Stephanie Allred, thank you for all your words of comfort and wisdom. Ivana Vasic, thank you for always taking an adventure with me. Sami Villarreal, Andrea McGovern, and Sabby King, thank you for the endless laughs, constant support, and encouraging pep talks. Last, but certainly not least, Christopher Towne, thank you for being the most supportive partner a human could ask for through this process.

Finally, I owe a great deal to my family. I was raised by truly admirable people. My father, Prasad Lokugamage, taught me to be bold and ambitious from an early age. I attribute my drive and motivation to him. My brother, Ryan Lokugamage, has always been a source of comfort and love. He is my greatest cheerleader and best friend. I hope one day to be as kind and compassionate as he. My mother, Sumithra Lokugamage, taught me to build my character, be intentional with my actions, and stick to my principles. She showed me how to be fearless in the face of uncertainty. Everything I do is in her honor.

TABLE OF CONTENTS

LIST OF FIGURES

LIST OF SYMBOLS AND ABBREVIATIONS

AAV	Adeno-associated virus
ASGPR	Asialoglycoprotein receptor
BSA	Bovine serum albumin
CAV1	Caveolin 1
CTLA-4	Cytotoxic T-lymphocyte-associated protein 4
CRISPR	Clustered Regularly Interspaced Short Palindromic Repeats
DC	Dendritic cell
ddPCR	Digital droplet PCR
DLS	Dynamic light scattering
DNA	Deoxyribonucleic acid
DOPE	1,2-dioleoyl-sn-glycero-3-phosphoethanoloamine
EC	Endothelial cell
ECGS	Endothelial cell growth supplement
EGFR	Epidermal growth factor
FACS	Fluorescence activated cell sorting
FBS	Fetal bovine serum
FIND	Fast identification of nanoparticle delivery
GalNAc	N-acetylgalactosamine conjugates
GeCKO	Genome-scale CRISPR-Cas9 knockout screening
gDNA	Genomic DNA
GFP	Green fluorescent protein
HDL	High density lipoprotein

IACUC	Institutional Animal Care and Use Committee
ICAM2	Intracellular adhesion molecule 2
IDT	Integrated DNA technologies
iMAEC	Immortalized mouse aortic endothelial cells Indel Insertion/deletion
IVT	*In vitro* transcribed
JORDAN	Joint rapid DNA analysis of nanoparticles
LDL	Low density lipoprotein
LDLR	Low density lipoprotein receptor
LNP	Lipid nanoparticle
LPS	Lipopolysaccharide
LSL	Lox-stop-lox
MFI	Mean fluorescent intensity
miRNA	Micro RNA
mRNA	Messenger RNA
NGS	Next generation sequencing
NHP	Non-human primate
PBS	Phosphate Buffered Saline
PCR	Polymerase chain reaction
PD-1	Programmed cell death protein 1
PEG	Poly(ethylene glycol)
PKR	Protein kinase R
QUANT	Quantitative analysis of nucleic acid therapeutics
RNA	Ribonucleic acid
RNAi	RNA interference

sgRNA	Single guide RNA
siGFP	Small interfering RNA targeting GFP
SARS-CoV-2	Severe acute respiratory syndrome coronavirus 2
siICAM-2	Small interfering RNA targeting ICAM-2
siRNA	Small interfering RNA
TALEN	Transcription factor-like effectors
TLC	Thin layer chromatography
TLR3	Toll-like receptor 3
TLR4	Toll-like receptor 4
TLR9	Toll-like receptor 9
VLDL	Very low-density lipoprotein
VLDLR	Very low-density lipoprotein receptor
WT	Wildtype
ZFN	Zinc fingers

SUMMARY

Nanoparticles improve drug efficacy by delivering drugs to sites of disease. To effectively deliver a drug *in vivo*, a nanoparticle must overcome physical and physiological hurdles that are not present in cell culture, yet *in vitro* screens are used to predict nanoparticle delivery *in vivo*. An ideal nanoparticle discovery pipeline would enable scientists to study thousands of nanoparticles *in vivo*. Here, we discuss technologies, such as DNA barcoding, to enable the efficient delivery of nucleic acid therapies and study the delivery of lipid-based nanoparticles.

This work will specifically describe the improvement and development of nucleic acid delivery vehicles. In Chapter 2, we report new DNA barcodes designed with minimal secondary structure, dispersed semi-randomized sequences, and a ddPCR site can be quantified at low doses *in vitro*. We demonstrate that *in vivo* nanoparticle biodistribution measured with fluorescence underestimates the number of targeted cell types *in vivo* compared to ddPCR DNA barcodes. These study shows that rationally designed DNA barcodes can quantify delivery with higher sensitivity than traditional fluorescence-based assays.

In Chapter 3, we quantified how over 100 nanoparticles delivered siRNA to 9 cell types in vivo using a novel siGFP-based barcoding system and bioinformatics. We found nanomaterials containing conformationally constrained lipids formed stable LNPs, herein named constrained lipid nanoparticles (cLNPs). cLNPs delivered siRNA and sgRNA to T cells at doses as low as 0.5 mg / kg, and unlike previously reported LNPs, did not preferentially target hepatocytes. The data suggest natural lipid trafficking pathways can promote T cell delivery, offering an alternative to active targeting approaches.

In Chapter 4, we explored the relationship between inflammation and drug delivery. Specifically, we found that TLR4 activation could override LNP-mediated mRNA delivery. We determined that TLR4 activation blocked mRNA translation in several cell types, without significantly reducing LNP uptake Notably, the data suggest that the mechanism could be driven,

in part, by TLR4-mediated reductions in endosomal escape and was likely driven by a TLR4-mediated reduction in mRNA translation. More generally, this suggests a LNP which delivers mRNA to one inflammatory disease may not deliver mRNA to another.

In Chapter 5, we identify design rules for nebulized LNP delivery of mRNA using an *in vivo*, iterative, cluster-based experiments. We found that PEG-lipids are crucial for LNP formulation, low PEG molar percentages improve LNPs with neutral helper lipids, and high PEG molar percentages improve LNPs with cationic helper lipids. We also identified an LNP that delivers mRNA to the lungs at low doses and used this LNP to protect adult mice from a lethal H1N1 flu challenge.

In Chapter 6, we studied whether a single LNP trait can reduce liver delivery and increase non-liver delivery. Using DNA barcoding, we identified three novel LNPs with distinct *in vivo* mRNA delivery profiles at clinically relevant doses, enabling us to edit genes in the lung by co-delivering Cas9 mRNA and sgRNA.

Finally, in Chapter 7, we proposed new ideas within the field of nucleic acid drug delivery. We discuss ways to continue improving nucleic acid drug delivery. Specifically, we emphasize the need for new screening approaches, ways to understand the genes involved in drug delivery, and the importance of studying drug delivery across larger animal models.

CHAPTER 1. INTRODUCTION

The work presented here is a modified excerpt from Lokugamage MP, Sago CD, Dahlman JE. "Testing thousands of nanoparticles *in vivo* using DNA barcodes" Current Opinion in Biomedical Engineering, 2018.

1.1 Nucleic acid-based therapies

1.1.1 RNA therapies are limited by inefficient delivery to target tissues

Advances in genomics have armed scientists with lists of genes that cause diseases. This has brought about a significant change in the way drugs are designed and discovered. Researchers were previously limited to targeting broad cellular phenotypes; for example, cisplatin intercalates into double-stranded DNA, causing toxicity in any cell undergoing cell division. Although many of these drugs successfully treated disease, they also caused severe side effects driven by drug activity in "off-target" cells. Researchers now often use small molecules that target specific mutations. However, only 15% of the protein coding genome—and a much smaller percentage of the non-coding genome—is "druggable" using small molecules[1]. This has led scientists to develop technologies to target all genes.

RNA therapies have emerged as a promising solution to the problem of "undruggable" targets[2]. RNAs can specifically turn any gene in the genome on or off, regardless of its eventual protein structure. Gene silencing can be mediated by RNA interference (RNAi), a well-characterized mechanism where base pairing between small interfering RNA (siRNA) and target mRNA catalyzes RISC-mediated mRNA degradation. Gene silencing can also be mediated by DNA nucleases, including those derived from zinc fingers (ZFNs)[3], transcription factor-like effectors (TALENs)[4], or clustered regularly interspaced short palindromic repeats and their associated proteins (CRISPR-Cas) systems[5,6]. Similarly, mRNA-based therapies can transiently upregulate genes[7]. To date, siRNA therapies have shown the most promise in patients. In one

example, a degenerative disease that was uniformly fatal has been halted (and in some cases, reversed) in Phase III clinical trials[8,9]. More generally, over 1,200 patients have been treated with siRNA, some for as long as 36 months. With a few exceptions, primarily limited to antisense nucleotides (which are distinct from siRNA)[10], siRNA therapies have been well tolerated and efficacious. Advances in siRNA biochemistry[11] and improved delivery vehicles[12] raise the exciting prospect that once-yearly injections to treat genetic disease are within reach.

Although siRNA is currently the most clinically advanced RNA therapy, DNA nucleases and mRNA therapies are up and coming. They have shown efficacy in mice[13,14] and non-human primates[15], and are poised to treat disease in humans[16-18]. The results described above have one limitation: most clinical trials have involved RNAs locally injected into muscle (e.g., vaccines), eye, or lymph nodes, administered to cells *ex vivo*, or systemically delivered to hepatocytes. Systemically delivering therapeutic RNA outside the liver remains a substantial unsolved problem[19] that limits the development of gene therapies targeting other organs. RNA therapies will require delivery because naked RNAs are quickly degraded by nucleases, and their large molecular weight and highly negative phosphodiester backbone prevent them from crossing the anionic cell membrane[20].

1.1.2 RNA therapies are clinically relevant

RNA therapies have tremendous clinical potential but will require on-target drug delivery to reach the clinic. siRNA drugs in the liver are a great example; several patient populations are already benefiting from treatments that silence genes in hepatocytes. However, without new delivery vehicles, the clinical impact will be limited to local injection and to the liver[19]. To target new cell types, it is important to test as many nanoparticles as possible. Traditional screening methods test delivery vehicles *in vitro*; however, *in vitro* particle screens may inaccurately predict delivery *in vivo*. In conjunction with rapid nanoparticle synthesis, high-throughput *in vivo* nanoparticle screening methods will allow scientists to track more particles simultaneously than

ever before. Over time, this may allow scientists to better understand how nanoparticles behave in the body. We envision a time when enough nanoparticles have been tested *in vivo* that nanoparticles which target a given cell type can be rationally designed. We find it likely these high-throughput approaches will help accelerate the development of new genetic therapies.

1.2 DNA barcodes allow for the testing of thousands of particles simultaneously *in vivo*

1.2.1 Nanoparticles screened in vitro *may not predict in vivo delivery*

RNA delivery vehicles are designed to protect the nucleic acid and transport it to the target cell. Although many drug delivery vehicles have been used to deliver RNA, we will focus on nanoparticles, which have generated promising clinical data[8]. Here we define a nanoparticle as a structure with all three dimensions less than 1,000 nm. Scientists have made steady advances in nanoparticle design. Nanoparticles can be made with variable size[21], ionizability[22], hydrophilicity[23], shape[24], and varying degrees of active targeting ligands[25]. Large, chemically diverse libraries have been synthesized using simple synthetic routes including, but not limited to, Michael addition[26], epoxides[27], peptide[28], and thiol chemistry[29]. Importantly, advances in nanoparticle formulation—defined here as the process of "loading" the nucleic acid into the nanoparticle—have also been reported. High-throughput microfluidics has been shown to reliably make small, consistent batches of nanoparticles that are stable for weeks[30,31]. It is still difficult to cover the entire nanoparticle chemical space; formulating nanoparticles using available chemistries, it is feasible to formulate between 100 million and 200 billion chemically distinct nanoparticles (**Fig. 1.1**).

After nanoparticles are formulated, they are screened *in vitro*. More specifically, scientists (a) synthesize thousands of different nanoparticles before (b) evaluating whether they deliver RNA in easily expandable cell lines (e.g., HeLa). Scientists have also used primary cells in place of immortalized cells[32]. Based on *in vitro* results, a very small number of nanoparticles are (c) tested *in vivo*. This process is only an efficient use of time and resources if *in vitro* nanoparticle delivery predicts *in vivo* delivery. To test this, we compared how the same 300 nanoparticles delivered

nucleic acids *in vitro* and *in vivo* in multiple cell types; we found no correlation[33] (**Fig 1.2A**). The discrepancy between *in vitro* and *in vivo* delivery is not necessarily surprising. If a nanoparticle is systemically administered, it must travel through the blood stream and enter the target tissue. Several physical factors dictate where the nanoparticles go. For example, it is difficult for nanoparticles to access the brain, which is physically cordoned off by the blood–brain barrier. Nanoparticles can also be physically disassembled by the glomerular membrane in the kidney[34]. As a counterexample, nanoparticles often target hepatocytes since nanoparticles can exit the blood via nanoscale pores in sinusoidal blood vessels and basement membrane[35]. Physiological factors also influence nanoparticle delivery. For example, serum proteins can bind to nanoparticles in the blood[36,37], changing nanoparticle interactions with the immune system and target cells[38]. Interestingly, systemic nanoparticle delivery can also change with local disease states; in one example, scientists found that delivery to systemic organs was affected by the presence of a primary tumor[39]. Even if the nanoparticle reaches its target cell, it must enter the cytoplasm, often by escaping an endosome. Endosomal escape is inefficient; an LNP that delivers siRNA to hepatocytes very efficiently (50% target gene silencing after a 0.01 mg/kg injection) still had >95% of its siRNA sequestered within endosomes[40]. The nanoparticle must also evade liver, kidney, and splenic clearance, as well as avoid initiating an immune response. The majority of these obstacles are not recapitulated *in vitro*. Some processes are required for *in vitro* delivery and *in vivo* delivery (e.g., endocytosis and endosomal escape). However, these processes are carefully regulated[41] by gene expression that is likely to change with microenvironmental cues. Increasing evidence suggests that gene expression in cultured cells may not reliably predict gene expression in primary cells or *in vivo*[42].

1.2.2 Barcoding enables simultaneous analysis of >100 nanoparticles in vivo

The lines of evidence described above suggest that screening nanoparticles directly *in vivo* would be useful. However, the expensive nature of *in vivo* experiments has limited the field to

testing a few *in vivo*. This is a universal problem in nanomedicine, and it has driven groups to design systems that facilitate high-throughput *in vivo* nanoparticle screens. In all cases, these systems utilize "multiplexed" signals, which are signals that can be quantified without interfering with one another. In the simplest case, nanoparticle 1, with chemical structure 1, is "barcoded" (i.e., "tagged") with signal 1; nanoparticle N, with chemical structure N, is barcoded with signal N. The nanoparticles are co-administered, and later, signals 1 and N are quantified simultaneously. In one example, scientists isotopically barcoded silver nanoparticles with different functional peptides to evaluate potential targeting ligands[43]. Another group used quantum dots to barcode polymeric nanoparticles; *in vivo* screens were performed to understand how nanoparticle surface modifications altered delivery through the blood–brain barrier[44].

One multiplexed signal that has been used by groups (including ours) is DNA[33,45,46]. DNA is an excellent molecule for multiplexing. The number of different barcodes scales exponentially faster than any other signaling molecule; 4N different barcodes can be generated with a DNA sequence N nucleotide long. An 8-nucleotide barcode can create 65,536 different sequences. Additionally, DNA sequence readouts are easy to analyze. The cost of DNA sequencing has decreased more rapidly than Moore's Law; it is now possible to generate 400 million DNA reads for $2,000 using a machine that fits on a desktop. Because DNA sequencing has become an increasingly more common tool in several fields[47], easy-to-use software packages are readily available to help analyze and interpret the data.

Two distinct nanoparticle DNA barcoding systems have been reported to date[33,45,47]. In one example, DNA was formulated into liposomes alongside different chemotherapies[46] (**Fig. 1.2B**). By varying the primers or altering the barcode length, different sequences were detected using gel electrophoresis or real-time PCR. The authors tested several drugs at once *in vivo* and concluded that the DNA barcodes found in dead cells corresponded to nanoparticles containing effective chemotherapies. This method may be used in the future to test hundreds of different cancer drugs *in vivo*. We developed a separate DNA barcoding system that utilizes next-generation sequencing.

Our barcodes contain (i) universal primer sites, (ii) a 7 nucleotide region with fully randomized sequences (to monitor for biased PCR amplification), and (iii) an 8 nucleotide barcode region in the center[45] (**Fig 1.3A**). Initially, we demonstrated that this system predicted siRNA delivery *in vivo* and generated DNA sequencing outputs that were linear with respect to the administered DNA[45]. Later, we demonstrated that this system, which we named Joint Rapid DNA Analysis of Nanoparticles (JORDAN), could simultaneously analyze over 150 nanoparticles simultaneously *in vivo*[33] (**Fig 1.3B**).

Although there are different ways to design DNA barcodes, specific traits help increase the robustness of the data. Most importantly, universal primer sites—which are primer sites that do not change—confer an important advantage, maximizing the chance all barcodes are amplified in an unbiased way. This seems counterintuitive, but the vast majority of a DNA barcode should be identical; the barcode region of the DNA should be small. Adding chemical modifications including phosphorothioates to the 5' and 3' termini increase barcode stability. The barcode regions should also be designed to work together on solid-phase next-generation sequencing (NGS) platforms like Illumina. Since solid-phase NGS relies on fluorophores (**Fig. 1.3C**), each individual barcode must have a "base distance" of at least 3; in other words, each barcode must be different from all other barcodes at three of the eight positions (**Fig. 1.3D**). We have designed >200 barcodes with base distances of 3 or more[33]. It is also critical to sequence the DNA "input" administered to the animals. This allows us to normalize the data and compare different cell types to each other within an experiment. Finally, like all big data systems, nanoparticle DNA barcoding experiments should include proper controls in each experiment. Two examples include a liposome loaded with caffeine (instead of a chemotherapeutic)[46] and a naked barcode[33]; in both cases, the negative controls performed poorly relative to the experimental conditions, as expected.

DNA barcodes enable nanotechnologists to track how hundreds of distinct nanoparticles deliver drugs *in vivo* for the first time; this enables nanoparticle studies that were not feasible using traditional methods. As an example, we compared how dozens of different nanoparticles delivered

DNA to eight different cell subtypes in the spleen. Using unbiased Euclidean clustering—a common bioinformatics technique that analyzes large datasets—we found that specific types of immune cells tended to be targeted by the same nanoparticles[33]. DNA barcodes have enabled large-scale experiments in fields as varied as oncology, developmental biology, and viral delivery. As an example, by using the single-guide RNA (sgRNA) sequence as a "barcode" to denote a gene that was knocked out, scientists performed whole genome screens to identify genes and non-coding regions that regulate cellular response to cancer and immunotherapies[48-51]. More specifically, a system named Genome-Scale CRISPR-Cas9 Knockout Screening (GeCKO) helped determine which genes promote resistance to anti-cancer drugs[50]. GeCKO was used to target 18,080 in the same experiment; multiple sgRNAs were designed per gene. The pool of sgRNAs was administered to human cancer cell lines that also expressed Cas9; as a result, each cell—on average—had no gene knocked out, or 1 gene knocked out. After adding an anti-cancer drug, cells were allowed to grow; enriched sgRNA sequences in live cells corresponded to genes that increased drug resistance (**Fig 1.4A**). The same approach has been used to study metastasis *in vivo*. In this case, a pool of tumor cells was edited using GeCKO and administered in the hind limb of a mouse. After waiting a period of time, the authors isolated metastatic tumor cells from different organs, and thereby identified genes that promoted metastasis[52]. Similar approaches have been used to identify genes that suppress primary tumor growth in the liver and brain (**Fig. 1.4B**)[53,54]. Scientists also designed a combinatorial DNA barcode system named PolyLox that identified stem and progenitor cells that led to the development of the immune system[55]. Finally, there are reports of "capsid shuffling" and other combinatorial cloning strategies; these use sequences that code for amino acids as barcodes that denote which amino acids successfully enabled AAV vectors that facilitate cellular entry and DNA delivery[56-58]. Given that DNA is a highly efficient method to store and access information, it is likely that many other biology and engineering fields will use DNA barcodes in the future.

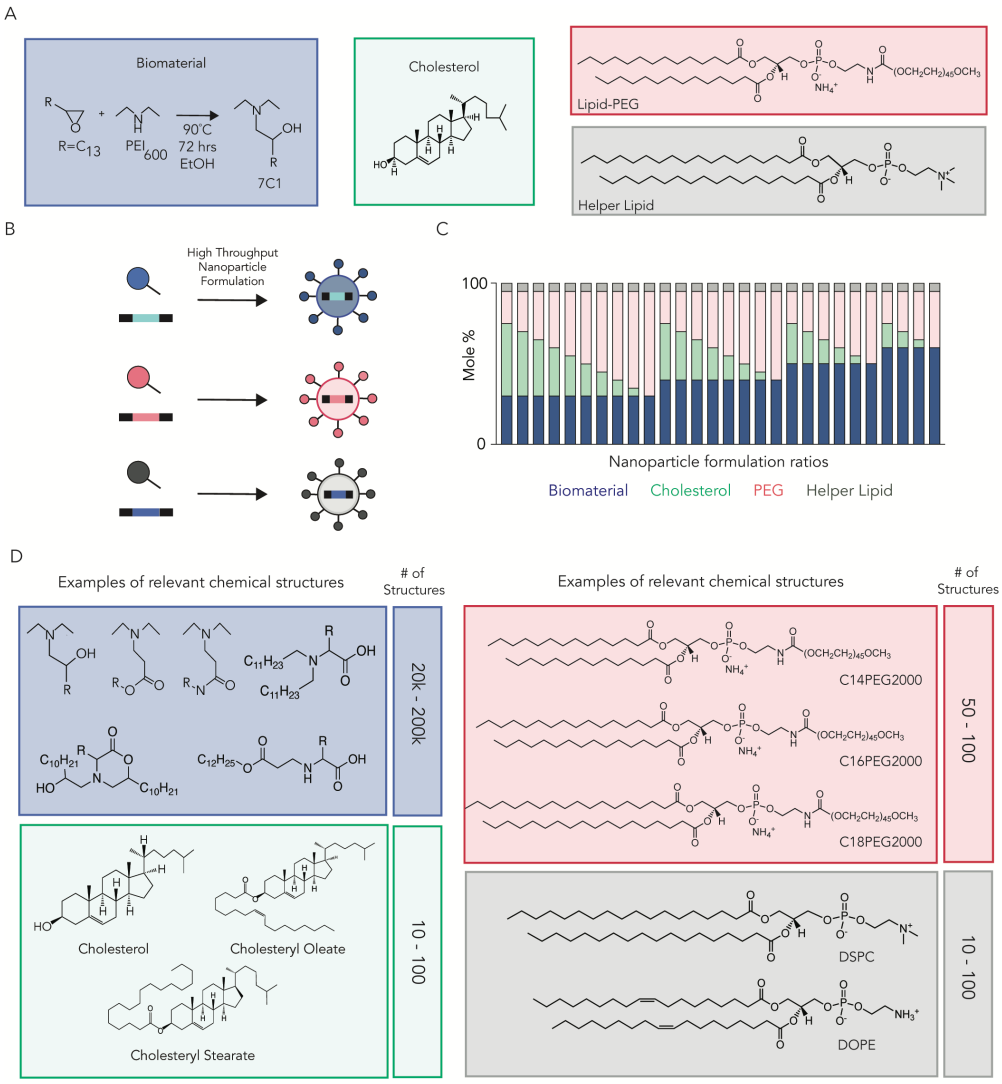

Figure 1.1 (A) Lipid nanoparticle libraries can be generated with a variety of chemical compounds. LNPs are formulated by combining different biomaterials with cholesterols, lipid-PEG compounds, and helper lipids. **(B)** High-throughput nanoparticle formulation allows for the rapid production of large, diverse libraries. **(C)** Nanoparticle libraries can be generated by varying the molar ratio of biomaterials, cholesterols, PEG, and helper lipids. **(D)** Between 1 x 10^8 and 2 × 10^{11} chemically distinct nanoparticles can be made by combining these compounds. Notably, these numbers do not include variations in the molar ratio of the compounds (e.g., Figure 1.1C).

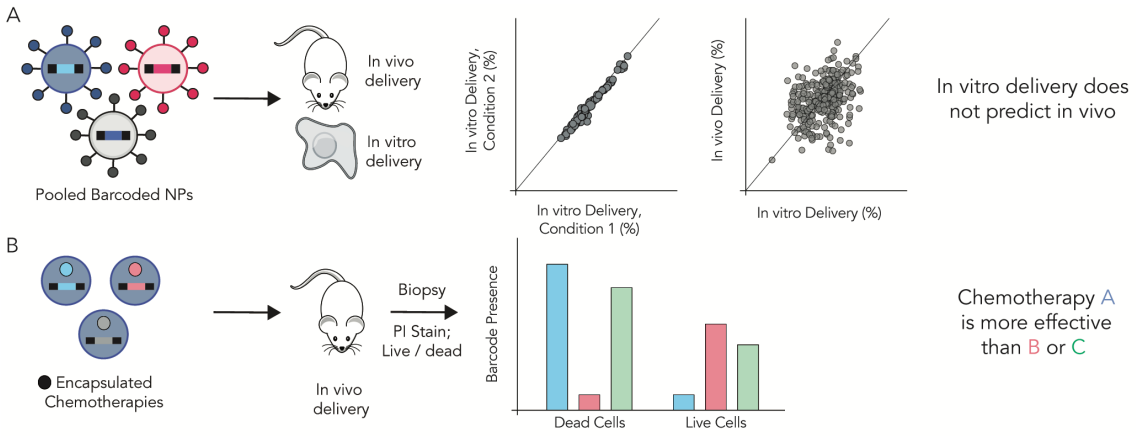

Figure 1.2 (A) Chemically diverse LNPs are tagged with unique DNA barcodes. LNPs were pooled together and administered both *in vitro* and *in vivo*. For in vitro studies, delivery at condition 1 often correlates with delivery at condition 2. However, in vitro delivery does not correlate to *in vivo* delivery. These results were consistent across many cell types, and across different experiments, for >300 different LNPs. **(B)** Liposomes carrying different chemotherapies were formulated with unique barcodes. After administering the liposomes *in vivo*, tissues were removed and cells were stained with propidium iodine (PI), which distinguishes dead cells from live cells. Barcodes enriched in dead cells corresponded to successful chemotherapy agents.

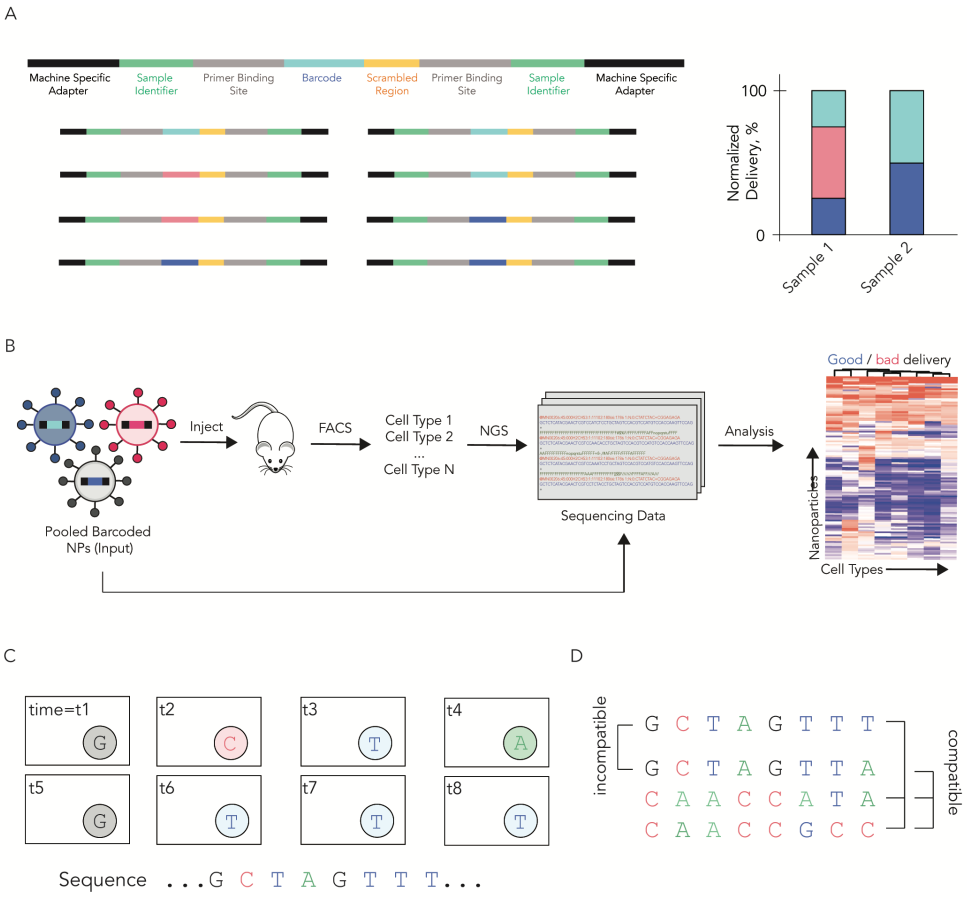

Figure 1.3 (A) JORDAN barcodes contain universal primer sites, a 7 nucleotide randomized region, and an 8 nucleotide barcode region. This barcode design allows us to multiplex hundreds of different barcodes. The normalized delivery for every barcoded LNP is determined; this is analogous to 'counts per million' in RNAseq studies. **(B)** JORDAN uses DNA barcodes and NGS to analyze the biodistribution of thousands of particles *in vivo*. Next generation sequencing is an effective way to read DNA barcodes. **(C)** Solid phase NGS reads each nucleotide of the sequencing using fluorescent nucleotides. Understanding how NGS generates data is important to understanding barcode design; NGS is reviewed extensively in reference 47. **(D)** For example, each barcode must differ from all other barcodes at 3 of the 8 positions. If any reading errors during sequencing occur, this difference will still allow each barcode to be distinguishable from other barcodes.

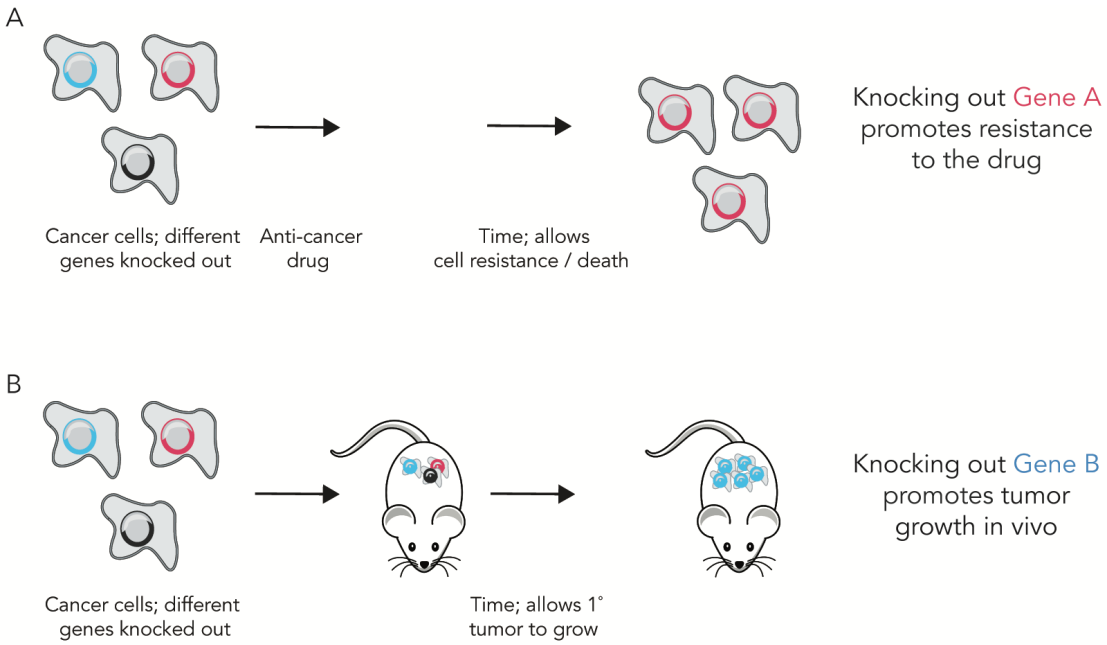

Figure 1.4 (A) In cancer cells, each gene in the genome of Cas9 expressing cells was knocked out individually using sgRNAs. The sgRNA served as the barcode that denoted which gene was silenced. After knocking every protein coding gene, an anti-cancer drug is added to the cells and time is allotted to facilitate drug resistance. Enriched sgRNA sequences in the live cells correspond to genes that affect cancer drug resistance. In this example, knocking down Gene A promotes drug resistance. **(B)** The same whole genome studies have identified genes that – when knocked down – promote primary tumor growth.

CHAPTER 2. MODIFYING A COMMONLY EXPRESSED ENDOCYTIC RECEPTOR RETARGETS NANOPARTICLES IN VIVO

The work presented here is an excerpt from Sago CD*, Lokugamage MP*, Lando GN, Djeddar N, Shah NN, Syed C, Bryksin AV, Dahlman JE. "Modifying a Commonly Expressed Endocytic Receptor Retargets Nanoparticles *in vivo.*" Nano Letters, 2018.

2.1 Introduction.

siRNAs delivered to hepatocytes have treated disease in patients[8,59,60], but delivery to other cell types remains challenging[61]. The liver exhibits physiological advantages that promote nanoparticle accumulation[62,63], and as a result, rational approaches will be required to minimize unwanted liver delivery. An ideal approach would involve (i) synthesizing hundreds of nanoparticles with diverse chemical structures, and (ii) analyzing them *in vivo* using an animal model that (iii) tests a specific biological hypothesis (e.g., gene X alters delivery) *in vivo*. However, the current gold standard is to study nanoparticles *in vitro.* Thousands of nanoparticles can be synthesized for nucleic acid delivery, but they are screened *in vitro*[27,28,64-67], which can be a poor predictor of *in vivo* delivery[68]. Genes that alter nanoparticle delivery *in vitro* have been identified[69-72]; genes that affect systemic nanoparticle delivery *in vivo* remain much more difficult to study. Exceptions to this[73-76] have provided valuable insights, but have focused on soluble factors in serum[73,74] or receptors on hepatocytes[74-76]. Whether a commonly expressed gene can exert cell type-specific effects on nanoparticle delivery *in vivo* remains unexplored.

Nanomedicines are often delivered using ligands that bind receptors expressed on target cells[77]. For example, the ASGPR is expressed on hepatocytes; GalNAc has targeted ASGPR[78], leading to delivery in animals and patients. Other receptors include EGFR[79], folate receptor[80], transferrin receptor[81], VCAM-1[51], and ICAM-1[82]. Given that few receptors are (i) highly expressed

on one cell type and (ii) induce nanomedicine endocytosis upon binding, we envisioned an alternative approach: manipulating an endocytosis receptor expressed on many cells. An ideal receptor would inhibit delivery to cell type A more than cell type B, promoting delivery to cell type B. This approach is timely. Our understanding of cell heterogeneity is progressing; RNA-seq[83] has revealed that gene expression varies with disease state[84] and within cell populations previously believed to be homogeneous[85,86]. Large scale approaches like the Human Cell Atlas[87] are likely to uncover endocytic genes whose importance varies with cell type. Since hundreds of genes are in involved in endocytosis[88], and many genes are regulated by disease- and microenvironment-derived cues[41,89], it is foreseeable that manipulating 1 gene could alter delivery in a tissue- or disease-specific manner. To test the hypothesis that manipulating a commonly expressed receptor can affect nanoparticle delivery in cell type-dependent manner, we focused on Cav1, a gene involved in caveolin-mediated endocytosis[90]. Caveolin can endocytose nanoparticles *in vitro*[91] and *in vivo*[92]. Its expression changes with fibrosis[93-96], lung disease[97], cancer[98-101], neurological disease[102,103], and other pathologies[104-106], demonstrating that its expression is regulated by microenvironmental signals and disease.

2.2 Results.

2.2.1 QUANT barcodes are designed to provide highly sensitive readouts.

Given that *in vitro* nanoparticle delivery can be a poor predictor of *in vivo* delivery[68] and that gene expression can change when cells are cultured *in vitro*[42], we tested our hypothesis *in vivo,* eventually testing 226 chemically distinct LNPs. This approach is distinct from previous studies for 2 reasons. First, LNP studies typically evaluate many nanoparticles *in vitro* before selecting a small number to test *in vivo*[27,28,64-67]. Second, most LNP studies focus on hepatocytes, not macrophages[27,28,65-67].

We used microfluidics[107] to formulate a validated ionizable LNP that has delivered siRNAs *in vivo*[64,108-112]. The LNP carried a single stranded DNA (ssDNA) (**Fig. 2.1A**) that was chemically modified with phosphorothioates to reduce exonuclease degradation, and fluorescently tagged with Alexa-647. We chose Alexa-647 since it was significantly brighter than Alexa488 (**Fig. 2.1B**). One hour after intravenously injecting WT or Cav1 deficient ($Cav1^{-/-}$) mice with the clinically relevant[113] dose of 0.5 mg / kg DNA, we quantified Alexa-647 MFI in 13 cell types (**Fig. 2.1C**) using flow cytometry (**Fig. 2.1D,E**). In WT mice, >75% of the MFI signal was found in Kupffer cells or hepatic endothelial cells; we could not reliably quantify delivery in other cell types. The same was true for $Cav1^{-/-}$ mice, suggesting Cav1 did not change LNP biodistribution (**Fig. 2.1F**).

Given the role of Cav1 in nanoparticle endocytosis[114], the fact caveolin inhibitors affect this LNP *in vitro*[64], and the fact this LNP delivers siRNA and sgRNA to pulmonary and cardiovascular endothelial cells *in vivo*[64,108-112], we hypothesized that our Alexa-647 biodistribution data were inaccurate. Our hypothesis was recently strengthened by demonstrations that the fluorescent biodistribution of small molecules delivered by nanoparticles can change in ways that do not reflect delivery[115]. Since nucleic acids are degraded by nucleases that cleave phosphodiester bonds[116] - and fluorophores are not – we reasoned the fluorescent signal may not track with the nucleic acid. To test this, we engineered a novel biodistribution assay named QUANT; QUANT utilizes ddPCR – a technique used to quantify rare genomic events[117] – to quantify the biodistribution of the nucleic acid itself with high sensitivity, allowing us to directly compare it to the biodistribution of the fluorescent readout. This is important since fluorescent biodistribution studies are ubiquitously used throughout to measure nucleic acid biodistribution.

Since ddPCR requires efficient DNA amplification, we rationally designed QUANT DNA barcodes to increase DNA polymerase access (**Fig. 2.2A,B, Fig. 2.1A**). We minimized DNA 2˚ structure on the forward and reverse primer sites and minimized G-quadruplex formation by separating our randomized 7 nucleotide region[68,118] into semi-randomized NWNH and NWH sites.

We flanked the primer sites with 3 additional phosphorothioate-modified nucleotides to reduce exonuclease degradation of the primer site. Finally, we identified universal primer binding sites that would not amplify mouse or human gDNA. Specifically, we designed primers with similar melting temperatures (within 1˚C) and added them to human and mouse gDNA without barcode template (**Fig. 2.3A**). We identified primers that did not amplify gDNA after 40 cycles (**Fig. 2.3B**), but amplified barcode templates with 20 cycles. Based on these results, we added the 'no gDNA background' primer sites to our barcodes. We then optimized the ddPCR protocol (**Fig. 2.3C-G**) by varying annealing temperatures, primer concentrations, and probe concentrations. We increased the signal: noise ratio 14-fold compared to current standard protocols[117]. As a control, we scrambled the ddPCR probe site; no signal was generated, demonstrating that the signal required specific barcode-probe interactions (**Fig. 2.3H**).

Standard curve experiments revealed QUANT was highly sensitive. QUANT ddPCR signal was linear (with respect to the DNA added) when barcodes were diluted in Tris-EDTA buffer to a concentration between 750 aM and 12 fM (R^2 = 1.00) and was detected at 300 aM (**Fig. 2.2C,D**). As a control, we reduced the concentration to 30 aM, and did not observe readouts above an untreated baseline. QUANT was also highly sensitive *in vitro*. We fluorescently tagged QUANT barcodes and administered them to iMAECs[119] in 96 well plates with L2K at doses between 1 pg and 400 ng / well. Twenty-four hours later, we quantified biodistribution using flow cytometry, and observed measurable (but non-linear) increases in MFI above 10 pg / well (**Fig. 2.4A**). Separately, we administered QUANT barcodes without a fluorophore at doses between 60 and 16,000 zeptogram (zg) / well. ddPCR readouts were linear (R^2 = 0.91) between 120 and 8000 zg / well (**Fig. 2.2E**), 10^8x lower than the minimum dose required for a fluorescent signal. We then formulated QUANT barcodes into validated LNPs[64] using microfluidics[107]; LNPs carrying barcodes formed nanoparticles with an average hydrodynamic diameter of 53 nm. We intravenously administered them at 0.5 mg / kg, isolated lung endothelial cells using FACS 24 hours later, and quantified barcode delivery using ddPCR. We compared samples immediately after

completing the experiment to samples analyzed after storage at -20˚C for 20 or 31 days. Readouts were consistent when performed by different individuals using different reagent stocks (**Fig.2.2F**).

2.2.2 QUANT biodistribution is more sensitive than fluorescence in vivo.

We hypothesized that fluorescent biodistribution would yield different results than QUANT. We formulated the same LNP[64] with QUANT barcodes that were, or were not, fluorescently tagged with Alexa-647. One hour after intravenously administering 0.5 mg / kg, we isolated the same 13 cell types (**Fig. 2.1C**) using FACS and quantified LNP delivery using Alexa-647 MFI or QUANT (**Fig. 2.5A**). 87% of the Alexa-647 signal was found in liver cells; the remaining 10 cell types only generated 13% of the total fluorescent signal (**Fig. 2.5B-D**). QUANT biodistribution was different; only 56% of the ddPCR signal derived from the liver (**Fig. 2.5B-D**). We compared delivery in all 13 cell types and found statistically significant differences in 7 of them (**Fig. 2.5E**). In Figure 2E, we normalized delivery to Kupffer cells, which readily clear nanoparticles[62,63]. Notably, in all cases, fluorescence overestimated liver biodistribution. To exclude the possibility these results were due to a specific timepoint, we performed a pharmacokinetics experiment in 5 cell types: liver endothelial cells, Kupffer cells, hepatocytes, lung endothelial cells, and lung macrophages. We intravenously injected mice with 0.5 mg / kg QUANT barcodes, and sacrificed mice 0.4, 0.75, 1.25, 12, 24, and 36 hours later (**Fig. 2.6A**). At the 0.4-, 0,75-, and 1.25-hour timepoints, fluorescent biodistribution was localized to liver cells; only 1 of 6 non-liver signals (2 cell types, 3 timepoints) were statistically significant compared to untreated mice. At later timepoints, fluorescent biodistribution was not significantly above PBS-treated mice in any cell type. Out 30 potential data points (5 cell types, 6 time points), only 6 generated a fluorescent signal that was statistically significant compared to untreated mice (**Fig. 2.6B**). By contrast, QUANT-based biodistribution was observed in all 30 data points (**Fig. 2.6B**). We calculated under the curve (**Fig. 2.6C**) and the maximum DNA delivery (**Fig. 2.6D**); once again, the results suggested Alexa-647 fluorescence overestimated delivery to the liver. Finally, we

investigated how robust QUANT readouts were across experiments. We compared the absolute ddPCR values from all 5 cell types in the first QUANT biodistribution experiment (**Fig. 2.5**) and the pharmacokinetic experiment (**Fig. 2.6**) at similar timepoints (1 and 1.25 hours, respectively). ddPCR readouts were reproducible (R^2=0.98) between experiments (**Fig. 2.6E**). Figures 1-3 demonstrate that QUANT is a sensitive and repeatable method of quantifying nanoparticle biodistribution.

2.2.3 Distribution profiles of over one hundred can be analyzed with QUANT.

QUANT enabled us to measure LNP delivery with increased sensitivity; we took advantage of this to test the hypothesis Cav1 affects LNP delivery in a cell type-specific manner *in vivo*. To ensure our results were not specific to 1 LNP chemical structure, we exploited a second advantage of QUANT: it can be multiplexed so the distribution of >100 LNPs is analyzed at once. Multiplexed analysis of nanoparticle delivery has been reported by our group[68,118] and others[120], but critically, these barcoding systems can only quantify delivery of LNP-1 relative to LNP-2 within the same sample; it cannot quantify absolute delivery. Without the ability to quantify absolute delivery, it is difficult to directly compare readouts (i) between different tissues, (ii) between different mouse models (e.g., WT and Cav1$^{-/-}$), or (iii) between ddPCR and fluorescence.

We performed 2 high-throughput *in vivo* LNP screens. We formulated LNP-1, with chemical structure 1, so it carried QUANT barcode 1; we formulated LNP-N, with chemical structure N, to carry QUANT barcode N (**Fig. 2.7A-C**). The 8-nucleotide barcode region on the QUANT DNA sequence - located in the center - can generate 65,536 unique barcodes; we designed 156 that were compatible with one another on Illumina sequencing machines. Each barcode has a base distance of 3 or more, which means every 8-nucleotide barcode sequence is different from all other 8 nucleotide barcode at 3 of the 8 positions (or more). We used microfluidics[107] to formulate LNPs with QUANT barcodes[68,118]. We analyzed the hydrodynamic diameter of each LNP individually using dynamic light scattering and pooled LNPs together if they met 2 inclusion

criteria: (i) hydrodynamic diameters between 20 and 200 nm, and (ii) an autocorrelation curve with 1 inflection point (**Fig. 2.7D, Fig. 2.8A**); We also included a naked DNA barcode, which served as a negative control. We selected these LNP criteria, and the control based on experience with a different barcoding system[68]. We studied 2 LNP libraries; as expected, the normalized delivery of the naked DNA barcode was lower than the normalized delivery for barcodes carried by LNPs in library 1 (**Fig. 2.7E,F**) and library 2 (**Fig. 2.8B,C**). Normalized delivery quantifies how well an LNP performs, relative to all other LNPs in a given sample (**Fig. 2.7A, Fig. 2.8D**). It is analogous to counts per million in RNA-seq[83], and can describe nanoparticle biodistribution[68,118].

2.2.4 Cav1 influenced nanoparticle delivery in a tissue- and cell-type dependent way

We intravenously administered the LNPs to WT and Cav1$^{-/-}$ mice at a total DNA dose of 0.5 mg / kg and used FACS to isolate 10 cell types 24 hours after administering the LNPs (**Fig. 2.8E**). We focused on endothelial cells and macrophages since they exist in every tissue; this allowed us to study cell- and tissue-level effects. In LNP library 1, we formulated 128 LNPs; 111 met our 2 inclusion criteria and were pooled together (**Fig. 2.7C,D, Fig. 2.8F,G**). Multiple lines of evidence suggested Cav1 influenced nanoparticle delivery in a tissue- and cell-type dependent way. First, the 'total experimental' biodistribution – defined as the total ddPCR counts in the 10 tested cell types – was reduced in Cav1$^{-/-}$ mice, relative to WT mice (**Fig. 2.9A**). In these pie charts, the area corresponds to total ddPCR counts. It is important to note this pie chart is not equal to the total clearance for the organ, since we did not measure the clearance in every cell type, and the values are not weighted by the percentage of a given cell type within the organ. We chose not to weight the values since the percentage of each cell type within an organ, for all tested organs, was not available.

The decrease in ddPCR counts was not constant across different tissues; Cav1 exerted tissue-specific changes on LNP delivery. For example, the biodistribution to the liver was predominant in WT mice but was much less so in Cav1$^{-/-}$ mice (**Fig. 2.9A**). The decrease in liver

delivery was substantial; the total number of ddPCR counts in the liver of (**Fig. 2.9B**) $Cav1^{-/-}$ mice decreased by 93%. The $Cav1^{-/-}$ counts in lung and kidney were reduced by 43% and 27%, respectively, relative to WT mice (**Fig. 2.9C,D**). We then analyzed this effect at the cellular level in all 3 organs. In the liver, most of the decrease in $Cav1^{-/-}$ barcode readouts were due to decreased Kupffer cell delivery (**Fig. 2.9E**). Delivery to hepatic endothelial cells also decreased, but delivery to hepatocytes was not impacted significantly (**Fig. 2.9B,E**).

The data above describe the average change in barcode counts for all LNPs. We then quantified how all 111 individual LNPs were affected by Cav1 expression. We multiplied the ddPCR readouts by the normalized delivery, to calculate absolute delivery for each LNP. We then plotted absolute delivery for each LNP in WT and $Cav1^{-/-}$ mice for 3 cell types in the liver (**Fig. 2.9F**). Delivery to Kupffer cells in $Cav1^{-/-}$ mice was visibly lower than delivery to Kupffer cells in WT mice, even when plotted on a Log_{10} scale (**Fig. 2.9F**). Delivery to Kupffer cells was affected more than endothelial cells and hepatocytes. Notably, the high throughput analysis of absolute delivery has not been reported before; it is not possible to generate these plots using previous LNP DNA barcoding technologies.

We repeated this experiment using a second LNP library. We rationally designed LNP library 2 to be similar to LNP library 1, with an important distinction: In library 1, LNPs contained the 7C1 lipid, cholesterol, PEG, and the helper lipid 1,2-distearoyl-sn-glycero-3-phosphocholine (DSPC); in library 2, LNPs contained the 7C1 lipid, cholesterol, and PEG. We omitted DSPC to exclude the possibility that the effects we observed in macrophages were due to changes in CD36 expression. CD36 is expressed by macrophages; it acts as a receptor for phosphocholine, which is present in DSPC[121]. Critically, CD36 expression can be modulated by Cav1[122]. We formulated 120 LNPs, of which 115 were stable, pooled, and injected (**Fig. 2.8H-J**). Most of the observations we made with LNP library 1 were consistent in LNP library 2. The 'total experimental' biodistribution was – once again - reduced in $Cav1^{-/-}$ mice, relative to WT mice (**Fig. 2.10A**). There was a pronounced change in delivery to the liver (72% reduction) (**Fig. 2.10B**), and very little change in

the kidney (**Fig. 2.10C**). Unlike library 1, in library 2, delivery to the lung was also reduced (**Fig. 2.10D**). When we measured the cell type-specific changes in the liver, we found that Kupffer cell delivery was reduced again, strongly suggesting any effects we observed did not require the phosphocholine group in the LNPs (**Fig. 2.10B,E**). Delivery to hepatic endothelial cells and hepatocytes were decreased significantly (**Fig. 2.10E**). Finally, we calculated the delivery for all 115 individual LNPs, and were able to visually observe the differences in Kupffer cells more so than hepatic endothelial cells and hepatocytes (**Fig. 2.10F**).

2.2.5 Cav1 influences distribution of LNPs to Kupffer cells.

Given the consistent results in Kupffer cells, we investigated whether Cav1 similarly affected pulmonary and renal macrophages (**Fig. 2.11A**). The total ddPCR counts in pulmonary macrophages did not change with Cav1 expression; renal macrophage delivery decreased, but not significantly. When assessing absolute delivery in WT Kupffer cells as well as pulmonary and renal macrophages, we observed that average nanoparticle delivery was ~10-fold higher in Kupffer cells than in lung and renal macrophages (**Fig. 2.11B**). To exclude the possibility the Kupffer cell reduction was due to (i) fewer Kupffer cells or (ii) differences in Kupffer cell phenotype in $Cav1^{-/-}$ mice, we measured the (i) number of Kupffer cells / total liver immune cells, and (ii) the expression of CD86 and CD206, 2 markers for Kupffer cell activation in livers of WT and $Cav1^{-/-}$ mice after they were injected with a 1 mg / kg dose of the same previously validated 7C1 LNP we used in our QUANT studies (**Fig. 2.5, Fig. 2.6**). In all previous experiments, we injected 0.5 mg / kg; in this experiment, we injected a 1 mg / kg dose to increase the chance we would observe immune activation. We reasoned this was the most clinically relevant experiment, since all 226 LNPs included the 7C1 compound. The LNPs contained a siRNA that did not target any murine gene (siLuciferase) to minimize the chance gene silencing affected Kupffer cell behavior. We found no differences between number and phenotype of Kupffer cells in WT and $Cav1^{-/-}$ mice (**Fig. 2.11C-**

E). Taken together, these results suggest that caveolin-mediated endocytosis of nanomedicines by macrophages varies with tissue type.

We also observed that Cav1 exerted cell type-specific effects on endothelial cell delivery. We first quantified the ddPCR counts in different endothelial cell beds in WT mice, and found LNPs were delivered to liver, lung, heart, and kidney endothelial cells with differential efficiency (**Fig. 2.12A**). We then calculated the barcode delivery in $Cav1^{-/-}$ mice and normalized to delivery in WT mice (**Fig. 2.12B**). $Cav1^{-/-}$ had a statistically significant impact on barcode delivery in liver, lung, and heart endothelial cells. Interestingly, delivery to kidney endothelial cells was impacted less. We next measured the individual biodistribution of all 226 LNPs tested in both WT and $Cav1^{-/-}$ and found that barcode delivery to endothelial cells was consistently impaired in $Cav1^{-/-}$ mice (**Fig. 2.12C-E**).

2.3 Discussion.

Here we show that Cav1 affects LNP delivery in a cell type-specific manner *in vivo*. Delivery to Kupffer cells was significantly altered, leading to changes in nanoparticle biodistribution. Interestingly, Kupffer cell delivery was affected more than delivery to lung or kidney macrophages. These results suggest that Caveolin plays a more prominent role in LNP clearance in Kupffer cells, relative to other macrophage populations. These results are important for drug delivery systems, given that macrophages clear administered LNPs. Given that LNPs are lipid-like nanomaterials with compositions that can be similar to HDL, LDL, and VLDL, it will be interesting to evaluate whether the observations we made here extend to these 'natural' nanoscale carriers[76,123]. If so, these results could elucidate how cholesterol is trafficked to different tissues. Our results suggest macrophage uptake changes with tissue type. If future studies elucidate the cell signaling pathways that govern these differences, this cell signaling pathways could be manipulated to alter nanoparticle targeting.

Independent of the Cav1 results, we believe the discovery of QUANT is an important advance. More specifically, we found that a rationally designed ddPCR-based barcode system can quantify delivery with very high sensitivity. Previous DNA barcode technologies designed to track nanoparticle biodistribution could only compare relative biodistribution within the same cell type, but could not be used to compare biodistribution between different cell types[124]. We anticipate future studies further improving the design of QUANT barcodes by incorporating different patterns of chemical modification. Moreover, given that QUANT was able to read out delivery to all tested cell types here, we anticipate it will help scientists identify nanoparticles that target stem cells, immune cells, neurons, and other hard-to-target cell types.

We found that fluorescent biodistribution overestimated delivery to the liver, compared to readouts of the nucleic acid itself. Our results were consistent over several experiments, and echo results generated by scientists studying small molecule delivery[115]. Given that the known mechanisms of nucleic acid degradation[116] are different than the mechanisms that degrade fluorophores, we hypothesize the degradation of the nucleic acid is different from the degradation of the fluorophore. Further studies will be required to confirm or disprove this hypothesis. If confirmed, our results will be important, since most LNPs are thought to preferentially target the liver – often based on fluorescent biodistribution assays. These results could have important implications for nanoparticle discovery pipelines.

It is important note the limitations of our work. First, we only used 1 nucleic acid size; changing the size of QUANT barcodes may better model different classes of nucleic acid drugs. Second, toxic or unstable LNPs will not work with QUANT. Nonetheless, QUANT enables new types of nanoparticle studies that will help elucidate the biological factors that affect LNP targeting and provides proof of principle data that manipulating one gene can be used to retarget nanomedicines.

2.4 Materials and Methods

Nanoparticle Formulation. Nanoparticles were formulated using a microfluidic device as previously described[26]. Briefly, nucleic acids (DNA barcodes) were diluted in 10mM citrate buffer (Teknova) while lipid-amine compounds, alkyl tailed PEG, cholesterol, and helper lipids were diluted in ethanol. All PEGs, cholesterol, and helper lipids were purchased from Avanti Lipids. Citrate and ethanol phases were combined in a microfluidic device by syringes (Hamilton Company) at a flow rate of 600 μL/min and 200 μL/min, respectively.

DNA Barcoding. Each chemically distinct LNP was formulated to carry its own unique DNA barcode. For example, LNP1 carried DNA barcode 1, while the chemically distinct LNP2 carried DNA barcode 2. 91 nucleotide long single stranded DNA sequences were purchased as ultramers from IDT. Three nucleotides on the 5' and 3' ends were modified with phosphorothioates to reduce exonuclease degradation and improve DNA barcode stability. To ensure equal amplification of each sequence, the we included universal forward and reverse primer regions on all barcodes. Each barcode was distinguished using a unique 8nt sequence. An 8nt sequence can generate over 4^8 (65,536) distinct barcodes. We used 156 distinct 8nt sequences designed by to prevent sequence bleaching on the Illumina MiniSeq™ sequencing machine. A 26nt probe was purchased from IDT with 5' FAM as the fluorophore, while internal Zen and 3' Iowa Black FQ were used as quenchers. Fluorescent barcode was purchased from IDT with AlexaFluor647 or AlexaFluor488 conjugated to the 5' end.

In Vitro L2K. IMAECS were seeded at 10,000 cells per well in a 96-well plate. 24 hours after seeding, QUANT barcodes or Alexa-647-barcodes were transfected using Lipofectamine 2000. 24 hours after transfection, DNA was isolated from cells treated with QUANT barcodes and fluorescent barcodes were measured using a DN Accuri C6 flow cytometer.

Nanoparticle Characterization. LNP hydrodynamic diameter was measured using high throughput DLS (DynaPro Plate Reader II, Wyatt). LNPs were diluted in sterile 1X PBS to a concentration of ~0.06 μg/mL, and analyzed. To avoid using unstable LNPs, and to enable sterile purification using a 0.22 μm filter, LNPs were included only if they met the criteria of monodisperse population with diameter between 20 and 200nm. Particles that met these criteria were dialyzed with 1X phosphate buffered saline (PBS, Invitrogen), and were sterile filtered with a 0.22 μm filter.

Animal Experiments. All animal experiments were performed in accordance with the Georgia Institute of Technology IACUC. C57BL/6J (#000664) and Caveolin1$^{-/-}$ (#007083) mice were purchased from The Jackson Laboratory and used between 5-8 weeks of age. In all *in vitro* and *in* vivo experiments, we used N=3-5 group. Mice were injected intravenously via the lateral tail vein. The nanoparticle concentration was determined using NanoDrop (Thermo Scientific). For *in vivo* nanoparticle screens, mice were administered at a dose of 0.5 mg/kg.

Cell Isolation & Staining. Cells were isolated 24 (for screens) or 96 (for *in vivo* gene editing) hours after injection with LNPs unless otherwise noted. Mice were perfused with 20 mL of 1X PBS through the right atrium. Tissues were finely cut, and then placed in a digestive enzyme solution with Collagenase Type I (Sigma Aldrich), Collagenase XI (Sigma Aldrich) and Hyaluronidase (Sigma Aldrich) at 37 ºC at 550 rpm for 45 minutes. The digestive enzyme for heart and spleen included Collagenase IV[64,108,110]. Cell suspension was filtered through 70μm mesh and red blood cells were lysed. Cells were stained to identify specific cell populations and sorted using the BD FacsFusion and BD Facs Aria IIIu cell sorters in the Georgia Institute of Technology Cellular Analysis Core. For *in vitro* flow cytometry experiments, a BD Accuri C6 was used in the Georgia Institute of Technology Cellular Analysis Core. The antibody clones used were: anti-CD31 (390,

BioLegend), anti-CD45.2 (104, BioLegend), anti-CD68 (FA-11, Biolegend), and anti-CD11b (M1/70, Biolegend). Representative flow gates are located in Supplementary Figure 2.1.

Digital Droplet PCR. The QX200™ Droplet Digital™ PCR System (Bio-Rad) was used to prep and analyze all ddPCR results. All PCR samples were prepared with 10μL ddPCR with ddPCR™ Supermix for Probes (Bio-Rad), 1μL of primer and probe mix (solution of 10μM of target probe and 20μM of Reverse/Forward Primers), 1μL of template/TE buffer, and 8μL water. 20μL of each reaction and 70μL of Droplet Generation Oil for Probes (Bio-Rad) were loaded into DG8™ Cartridges and covered with DG8™ Gaskets. Cartridges were placed in the QX200™ Droplet Generator to create water-oil emulsion droplets. Cycle conditions for PCR were as follows: 1 cycle of 95º for 10 minutes, followed by 40 cycles of 94ºC for 30 seconds, 60ºC for 1 minute, and 1 cycle of 95ºC for 10 minutes. Plates were stored at 4ºC until ran on the QX200™ Droplet Digital™ PCR System. For each biological rep, 3 technical repetitions were completed. In all cases, technical reps were averaged. Technical reps were only excluded if they saturated the detection or showed inconsistent positive event amplitudes.

PCR Amplification for Illumina Sequencing. All samples were amplified and prepared for sequencing using a two-step, nested PCR protocol **(Fig. 2.3C)**. More specifically, 2 μL of primers (10 uM for Base Reverse/Forward) were added to 5 μL of Kapa HiFi 2X master mix, and 3 μL template DNA/water. This first PCR reaction was ran for 20-30 cycles. The second PCR, to add Nextera XT chemistry, indices, and i5/i7 adapter regions was ran for 5-10 cycles and used the product from 'PCR 1' as template. Dual-indexed samples were ran on a 2% agarose gel to ensure that PCR reaction occurred before being pooled and purified using BluePippin (Sage Science).

Deep Sequencing. Illumina sequencing was conducted in Georgia Institute of Technology's Molecular Evolution core. Runs were performed on an Illumina Miniseq. Primers were designed based on Nextera XT adapter sequences.

Barcode Sequencing Normalization. Counts for each particle, per cell type, were normalized to the barcoded LNP mixture applied to cells or injected into the mouse.

Data Analysis & Statistics. Sequencing results were processed using a custom R script to extract raw barcode counts for each tissue. These raw counts were then normalized with an R script prior for further analysis. Statistical analysis was done using GraphPad Prism 7; more specifically, 1-tail T-test, Paired 2-tail T-test, or One-way ANOVAs were used where appropriate. Data is plotted as mean ± standard error mean unless otherwise stated.

a

G*A*T*GCTCTCATACGAACTCGTCCNHNWCCTGCTAGTCCACGTCCATGTCCACCNWNHTGATATTGNWHGTGGTTAGTCGAGCAGAGAC*T*A*G

Red = phosphorothioate linkages (*) act to increase resistance to exonucleases.
Green = Universal primer binding sites allow for amplification from cells/tissues and linkage to next generation sequence adapters
Blue= Probe binding site. This functionality is used in ddPCR
Orange = 8nt Barcode. This 8nt sequence is referenced to identify nanoparticle composition and track nanoparticle distribution.
Light Blue= 4nt placer used to prevent steric blocking of universal forward primer and probe in ddPCR.
Black = Random nucleotide region used to minimize PCR bias.
N= A, T, G, or C; W= A or T; H= A, T, or C.

b

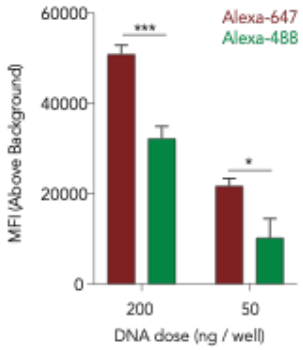

c

Cell Type	FACS Markers	Tissue
B cells	CD3- CD19+	*S*
T cells	CD19- CD3+	*S*
Macrophages	CD31- CD45+ CD11b+	*L,K*
Kupffer Cells	CD31- CD45+ CD68+	*v*
Endothelial cells	CD31+ CD45-	*v,H,L,K*
Immune	CD31- CD45+ CD11b-	*v,L,K*
Hepatocytes	CD31- CD45-	*v*

Liver, ***H***eart, ***L***ung, ***S***pleen, ***K***idney

d

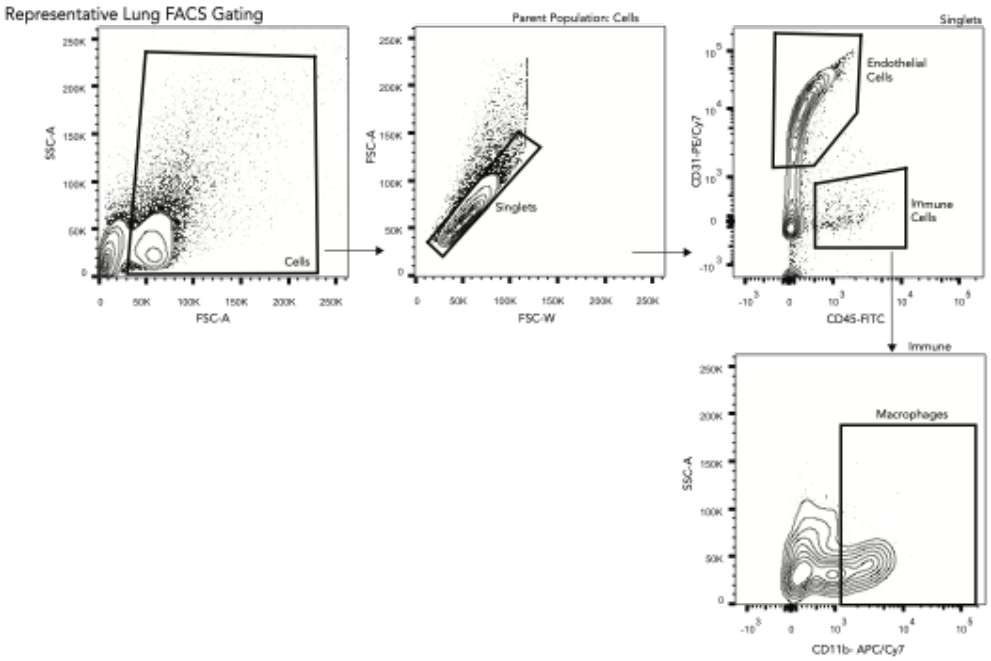

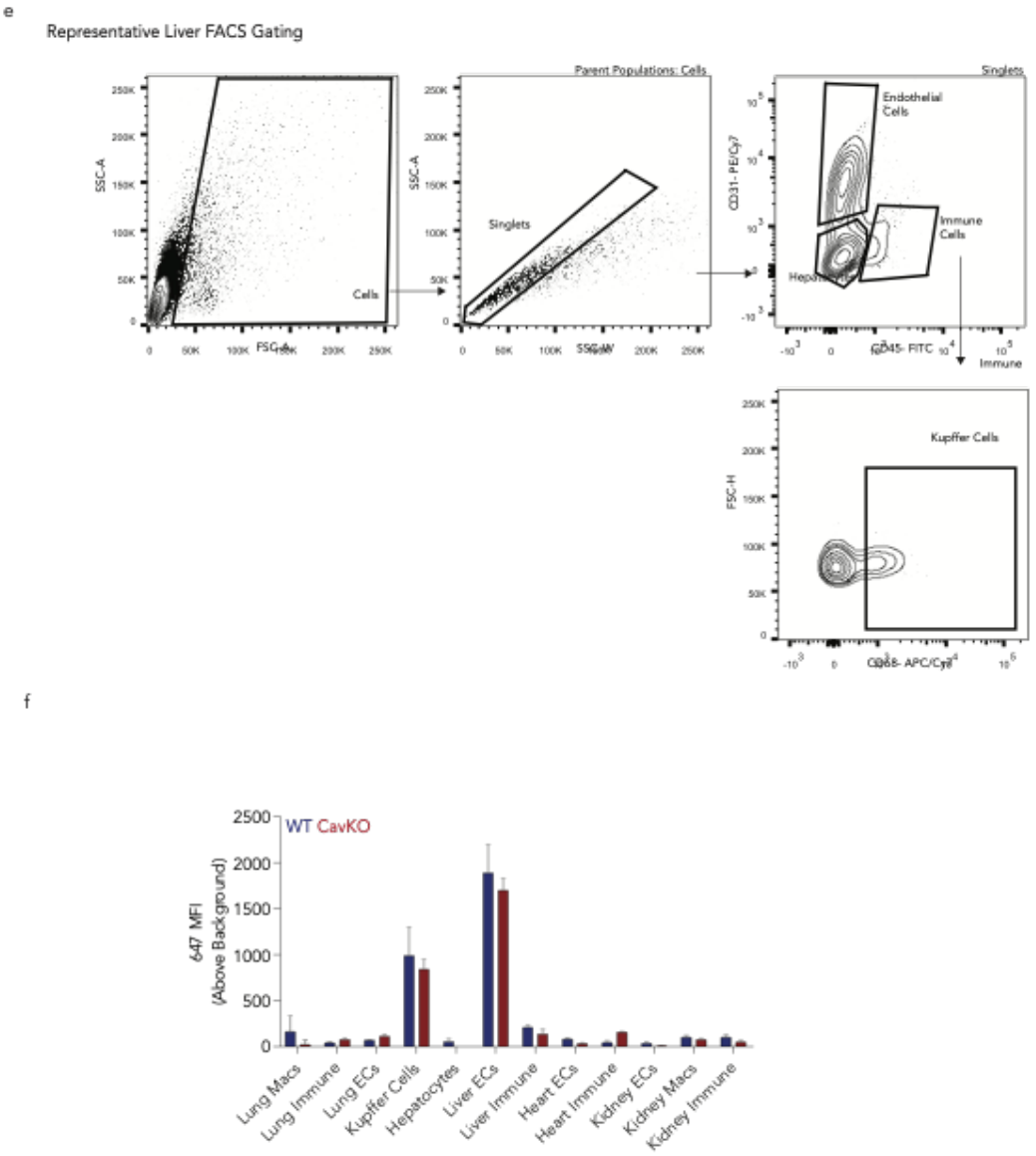

Figure 2.1 (A) QUANT Barcode Design. **(B)** Comparison of Mean Fluorescent Intensity of barcodes conjugated with Alexa-488 and Alexa-647 at 200ng and 50ng per well. *p<0.05,***p<0.001, 2 tailed t-test. **(C)** Cell types in the liver, heart, lung, spleen, and kidney were sorted based on the following FACS Markers. **(D)** Representative FACS gating for lung. We isolated endothelial cell (CD31+CD45-) and macrophages (CD31-CD45+CD11b+). **(E)** Representative FACS gating for liver. We isolated endothelial cells (CD31+CD45-), Kupffer cells (CD31-CD45+CD68+), and Hepatocytes (CD31-CD45-CD68-). **(f)** MFI of barcodes conjugated with Alexa-647 in WT and Cav1 -/- mice.

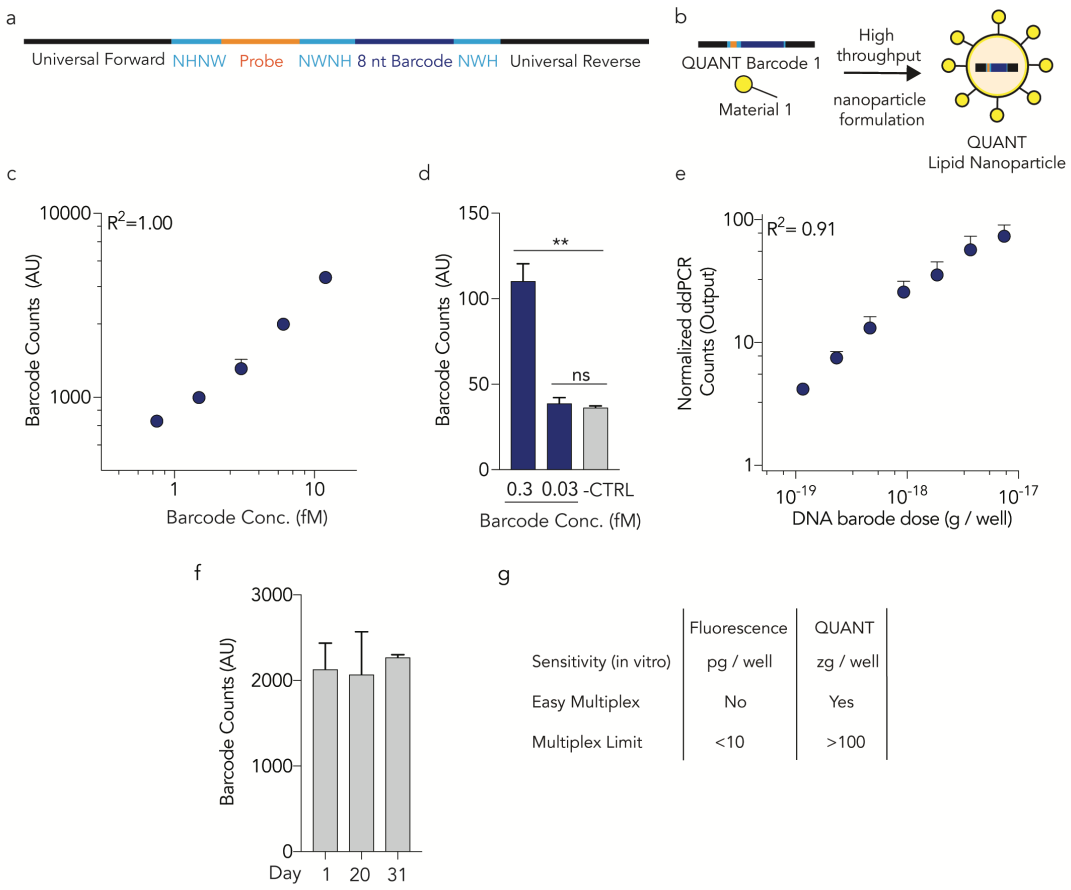

Figure 2.2 (A) QUANT barcodes are rationally designed to provide highly sensitive readouts of nanoparticle delivery. QUANT barcodes contain universal primer sites, an 8 nucleotide barcode region, a probe binding site, and splitsemi-randomized regions. These designs reduce DNA secondary structure and increase DNA polymerase access. **(B)** Barcodes can be formulated into chemically distinct lipid nanoparticles using high throughput microfluidics. **(C)** Standard curve of QUANT barcodes diluted in TE buffer; **(D)** barcodes can be identified above background at 300aM concentrations. **p<0.01, 2 tailed t-test. **(E)** An in vitro standard curve; barcodes were quantified 24 hours afterbeing delivered to cell using Lipofectamine 2000. **(F)** QUANT barcode readouts immediately after DNA was isolatedfrom cells following in vivo nanoparticle delivery, or after the samples were stored at -20˚C for 20 or 31 days. Eachexperiment was performed using different stock reagents, demonstrating the repeatability of the assay. **(G)** Comparison of fluorescence and QUANT-based methods of analyzing nanoparticle biodistribution.

a

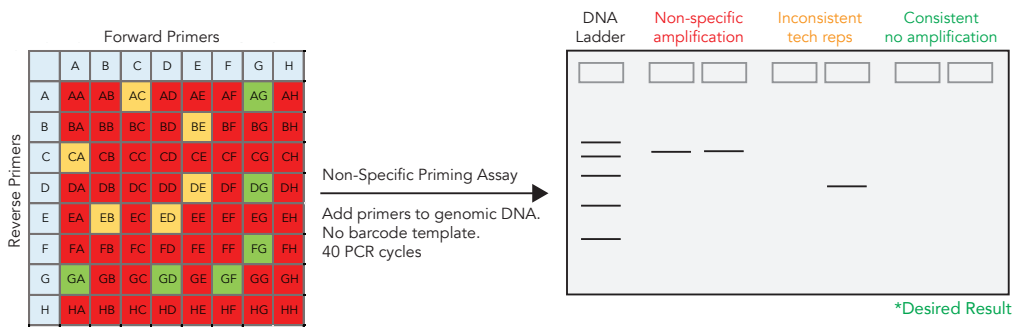

b

A	GCACGCCTTACGACTCATCT	
B	GCTCAATACTGTTCCACCGC	
C	ACTCACTTCGCATTAGCCGC	
D	GCTCTCATACGAACTCGTCC	Forward Primer
E	GCACACCGCTCTTCGAATCT	
F	ATCTCTCGCACTCTCAACGG	
G	GTCTCTGCTCGACTAACCAC	Reverse Primer
H	ATCACTCCGCACCGCTTATG	

c

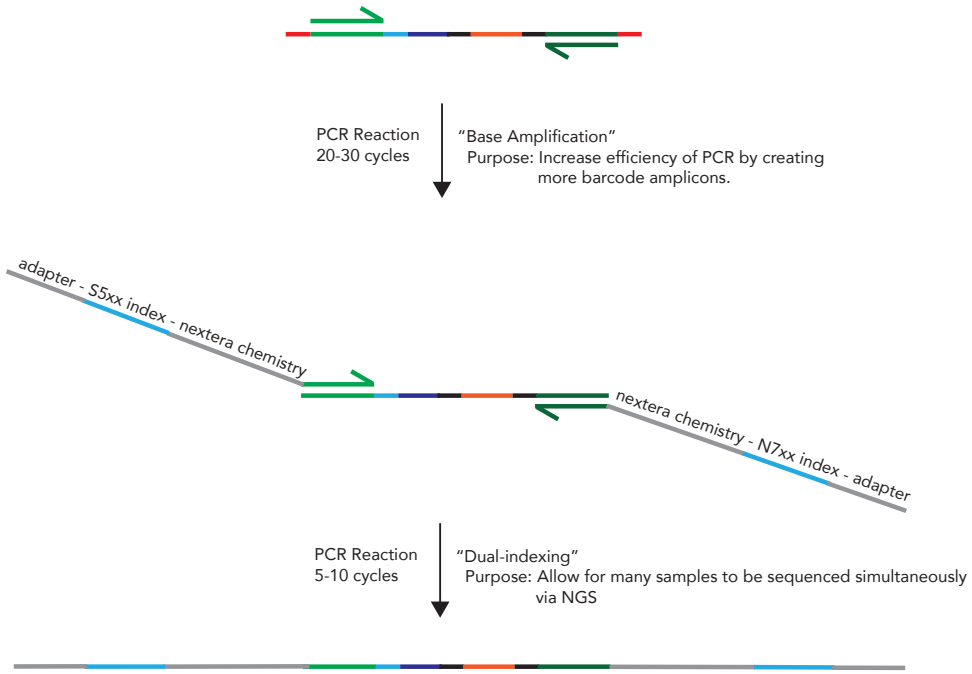

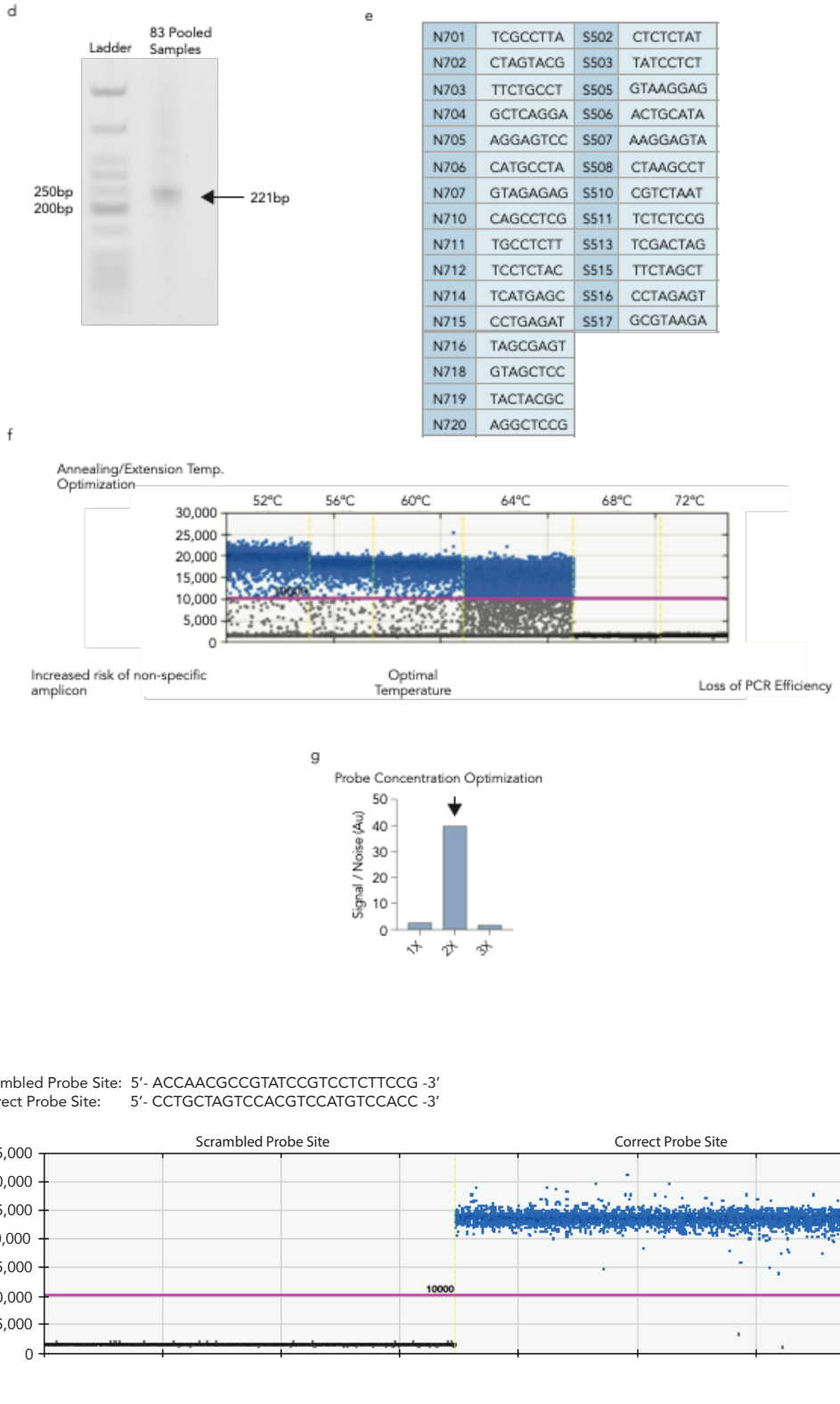

Figure 2.3. (A) A multi-step approach to optimizing the signal generated by ddPCR QUANT barcodes. Primer combinations were tested to avoid non-specific amplification by genomic DNA

(gDNA). Different primer pairs were added to mouse and human gDNA without any barcode template. **(B)** Primers that didnot amplify gDNA were selected. **(C)** A two-step PCR adds Illumina nextera chemistry regions, indices,and Illumina adapters for Illumina sequencing and **(D)** produces a clear product. **€** Dual indices allow formultiplexed Illumina sequencing. **(F)** ddPCR was optimized using an annealing temperature of 60°C and **(G)** probe concentration 2x more than the ddPCR standard protocol concentration. **(H)** A scrabbled probesite was tested to verify the specificity of the probe-based signal.

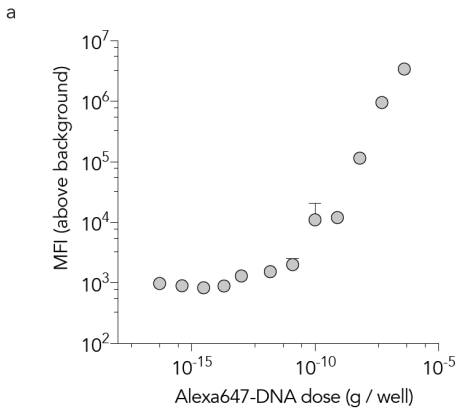

Figure 2.4. (A) Alexa-647 fluorescence 24 hours after fluorescently labeled QUANT barcodes were administered in vitro to iMAECs with Lipofectamine 2000 and analyzed with flow cytometry.

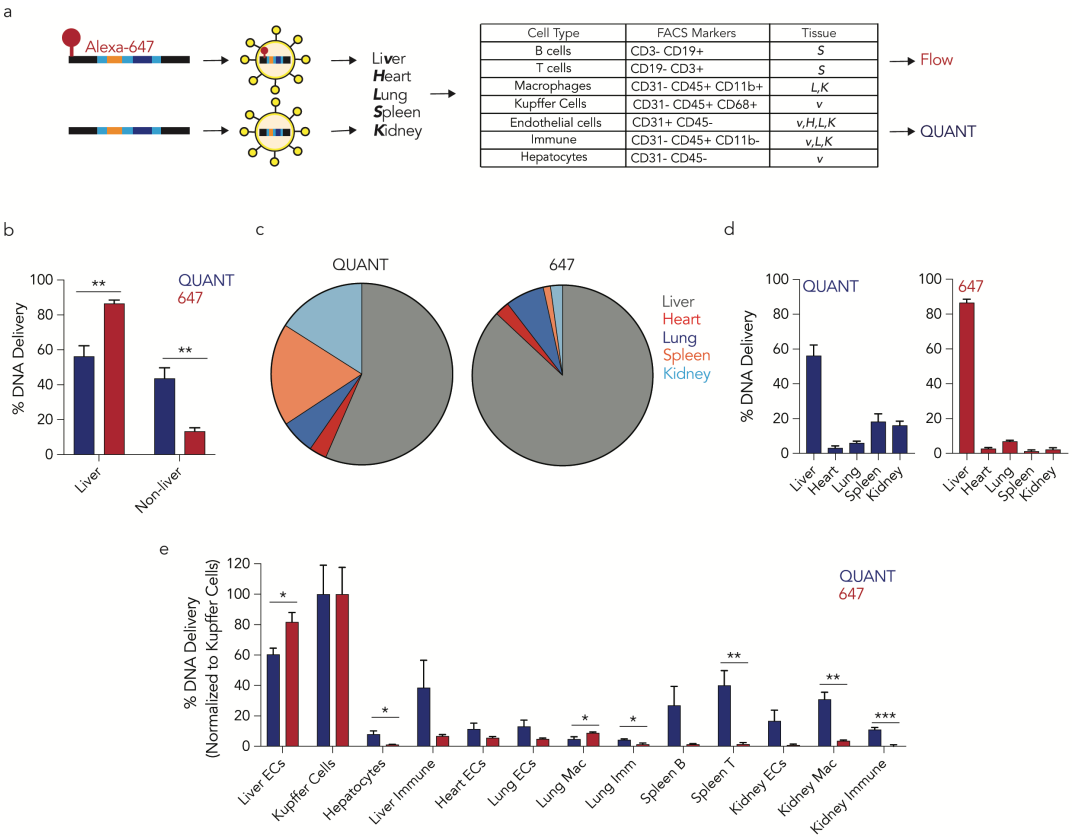

Figure 2.5. (A) A direct comparison of fluorescent- and ddPCR-based biodistribution in vivo reveals differences. QUANT barcodes with (or without) a fluorophore was formulated into a LNP and injected intravenously. Five tissues were isolated and barcode delivery to 13 cell types isolated by FACS was measured by QUANT or fluorescence. **(B)** Cumulative biodistribution measured by QUANT or fluorescence in liver and non-liver cell types. **p<0.01, 2 tailed t-test. **(C,D)** Cumulative biodistribution within the 5 tissues examined by QUANT and fluorescence. Fluorescence readouts overestimate liver delivery. **(E)** Comparison of biodistribution in the 13 cell types examined by QUANT and fluorescence. *p<0.05, **p<0.01, ***p<0.001, 2 tailed t-test.

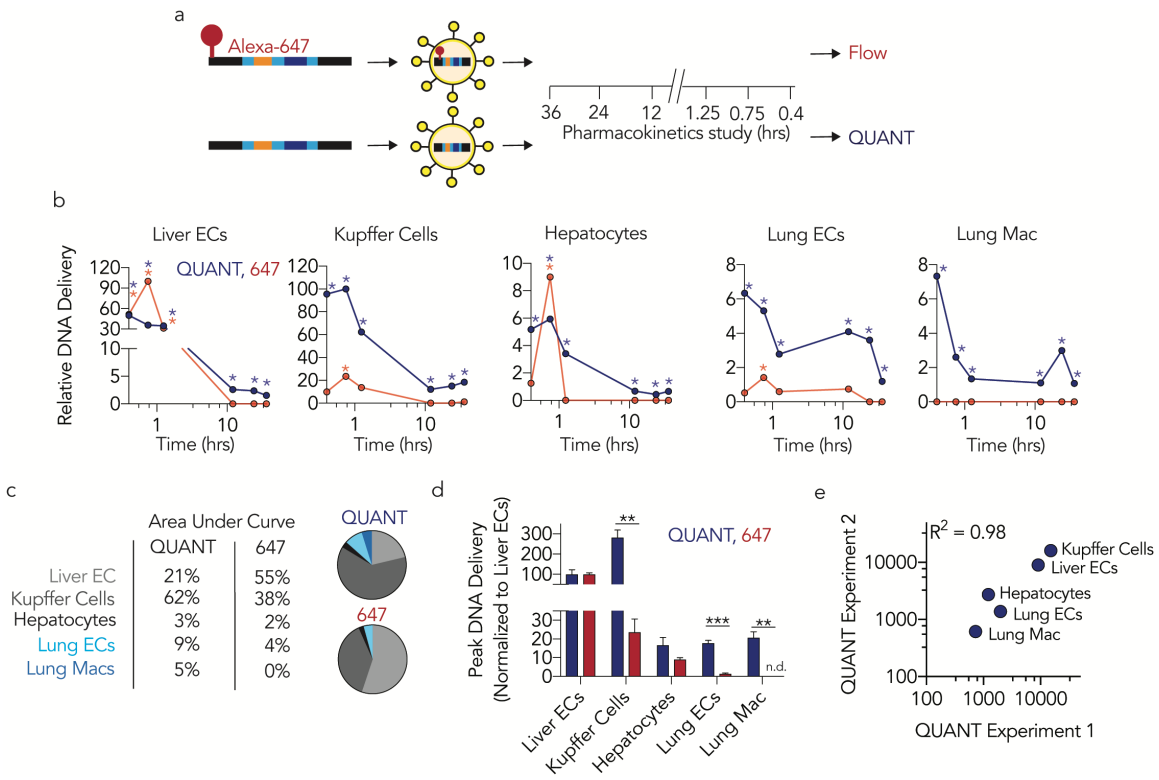

Figure 2.6. (A) QUANT barcodes with (or without) a fluorophore were formulated into LNPs, injected intravenously, and isolated at different timepoints. Nanoparticle distribution was measured using QUANT or fluorescence. **(B)** Relative nanoparticle biodistribution (normalized to maximal signal in any cell type) 0.4, 0.75, 1.25, 12, 24, and 36 hours after administration of a LNP carrying 647-QUANT barcode or QUANT barcodes at a dose of 0.5 mg / kg. Asterisk denotes a signal that was significantly different than PBS-treated mice. **(C)** Comparisons of area under the curve as measured by QUANT or fluorescence. Delivery to the lungs was underestimated by >3 fold by fluorescence. **(D)**Peak DNA delivery (normalized to liver ECs) as measured by QUANT and fluorescence. No fluorescent signal was detected in lung macrophages. **p<0.01, ***p<0.001 2 tailed t-test. **(E)** R2 analysis of QUANT absolutely counts from the 1 hour timepoint (Figure 2.5) and the 1.25 hour timepoint (Figure 2.6) across two experiments performed on separate days.

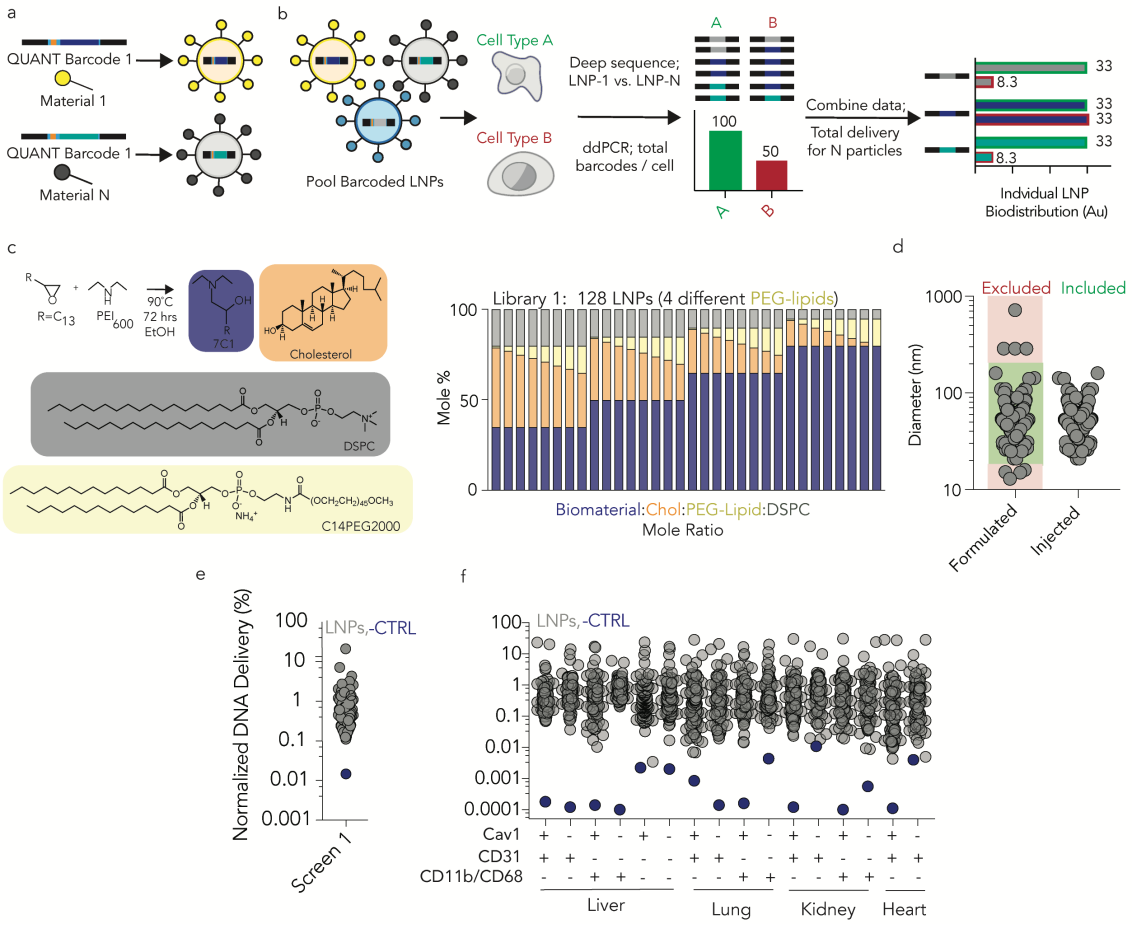

Figure 2.7. (A) QUANT was applied to screen over 100 nanoparticles in WT and Cav1-/- mice. Unique QUANT barcodes can be formulated into chemically distinct nanoparticles. **(B)** QUANT ddPCR readouts can be coupled with deep sequencing to measure absolute delivery mediated by >100 LNPs at once in vivo. **(C)** LNPs libraries can be synthesized with the LNP 7C1, Cholesterol, DSPC, and PEG compounds at variable molar ratios;128 different LNPs were formulated for screen 1. **(D)** The diameter of each LNP in screen 1 was measured individually; stable LNPs, with diameters between 20 and 200 nm, were included. **(E)** The average normalized delivery from all LNPs and the naked barcode (negative control) from screen 1. **(F)** As expected, the naked barcode–the negative control–was delivered less efficiently than barcodes carried by LNPs in every cell type.

a

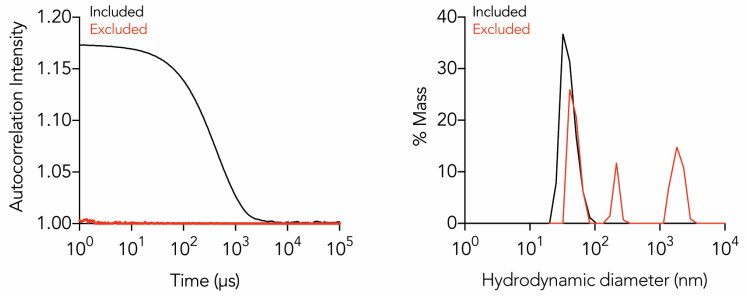

b

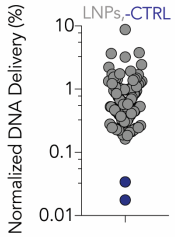

c

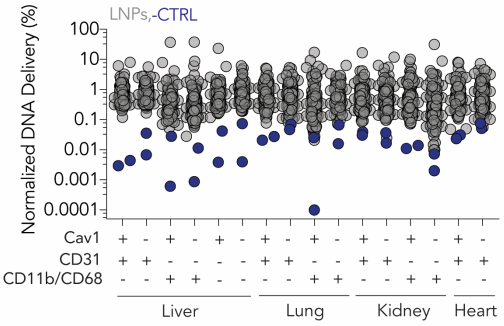

d

		Raw Counts Lung Endothelial Cells			Raw Counts Kidney Endothelial Cells			
LNP	Barcode	Mouse 1	Mouse 2	Mouse 3	Mouse 1	Mouse 2	Mouse 3	Input
1	GACACAGT	100	80	200	300	200	250	100
2	GCATAACG	50	45	110	100	60	70	120
3	ACAGAGGT	120	105	250	150	90	110	110
Total Counts		270	230	560	550	350	430	330

		Normalized Counts Lung ECs (%)			Normalized Counts Kidney ECs (%)			
LNP	Barcode	Mouse 1	Mouse 2	Mouse 3	Mouse 1	Mouse 2	Mouse 3	Input
1	GACACAGT	37	35	36	55	57	58	30
2	GCATAACG	19	20	20	18	17	16	36
3	ACAGAGGT	44	46	45	27	26	26	33
Total (%)		100	100	100	100	100	100	100

		Normalized to input Counts Lung ECs (%)			Normalized to input Counts Kidney ECs (%)			
LNP	Barcode	Mouse 1	Mouse 2	Mouse 3	Mouse 1	Mouse 2	Mouse 3	
1	GACACAGT	40	38	39	58	60	61	
2	GCATAACG	17	18	18	16	15	14	
3	ACAGAGGT	44	45	44	26	25	24	
Total (%)		100	100	100	100	100	100	

e

Cell Type	FACS Markers	Tissue
Endothelial cells	CD31+ CD45-	*v, H, L, K*
Macrophages	CD31-CD45+CD11b+	*L,K*
Kupffer Cells	CD31- CD45+ CD68+	*v*
Immune Cells	CD31- CD45+ CD11b-	*L,K*
Hepatocytes	CD31- CD45- CD68-	*v*

Li***v***er, ***H***eart, ***L***ung, ***K***idney

f

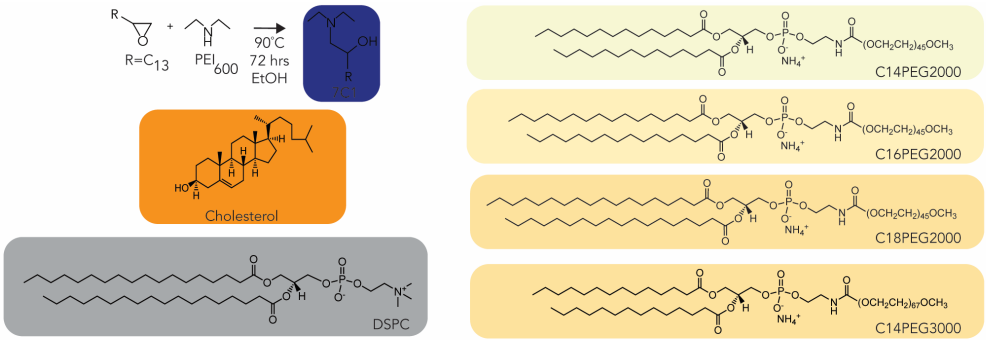

g

Library 1: 128 LNPs (4 PEG-lipids)

Number	Lipomer Type	Chol Type	PEG Tail	PEG MW	HL Type	Lipomer %	Chol %	PEG %	HL %	Diameter (nm)
1	7C1	Chol	C14PEG	2000	DSPC	35	44	1	20	110
2	7C1	Chol	C14PEG	2000	DSPC	35	42	3	20	21
3	7C1	Chol	C14PEG	2000	DSPC	35	40	5	20	41
4	7C1	Chol	C14PEG	2000	DSPC	35	38	7	20	46
5	7C1	Chol	C14PEG	2000	DSPC	35	36	9	20	26
6	7C1	Chol	C14PEG	2000	DSPC	35	34	11	20	16
7	7C1	Chol	C14PEG	2000	DSPC	35	32	13	20	25
8	7C1	Chol	C14PEG	2000	DSPC	35	30	15	20	15.2
9	7C1	Chol	C14PEG	2000	DSPC	50	34	1	15	110
10	7C1	Chol	C14PEG	2000	DSPC	50	32	3	15	143
11	7C1	Chol	C14PEG	2000	DSPC	50	30	5	15	60
12	7C1	Chol	C14PEG	2000	DSPC	50	28	7	15	62
13	7C1	Chol	C14PEG	2000	DSPC	50	26	9	15	37
14	7C1	Chol	C14PEG	2000	DSPC	50	24	11	15	50
15	7C1	Chol	C14PEG	2000	DSPC	50	22	13	15	48
16	7C1	Chol	C14PEG	2000	DSPC	50	20	15	15	59
17	7C1	Chol	C14PEG	2000	DSPC	35	44	1	20	68
18	7C1	Chol	C16PEG	2000	DSPC	35	42	3	20	48
19	7C1	Chol	C16PEG	2000	DSPC	35	40	5	20	31
20	7C1	Chol	C16PEG	2000	DSPC	35	38	7	20	47
21	7C1	Chol	C16PEG	2000	DSPC	35	36	9	20	36
22	7C1	Chol	C16PEG	2000	DSPC	35	34	11	20	54
23	7C1	Chol	C16PEG	2000	DSPC	35	32	13	20	34
24	7C1	Chol	C16PEG	2000	DSPC	35	30	15	20	39
25	7C1	Chol	C16PEG	2000	DSPC	50	34	1	15	59
26	7C1	Chol	C16PEG	2000	DSPC	50	32	3	15	88
27	7C1	Chol	C16PEG	2000	DSPC	50	30	5	15	55
28	7C1	Chol	C16PEG	2000	DSPC	50	28	7	15	61
29	7C1	Chol	C16PEG	2000	DSPC	50	26	9	15	27
30	7C1	Chol	C16PEG	2000	DSPC	50	24	11	15	36
31	7C1	Chol	C16PEG	2000	DSPC	50	22	13	15	49
32	7C1	Chol	C16PEG	2000	DSPC	50	20	15	15	47
33	7C1	Chol	C18PEG	2000	DSPC	35	44	1	20	92
34	7C1	Chol	C18PEG	2000	DSPC	35	42	3	20	29
35	7C1	Chol	C18PEG	2000	DSPC	35	40	5	20	55.5
36	7C1	Chol	C18PEG	2000	DSPC	35	38	7	20	140
37	7C1	Chol	C18PEG	2000	DSPC	35	36	9	20	32
38	7C1	Chol	C18PEG	2000	DSPC	35	34	11	20	35
39	7C1	Chol	C18PEG	2000	DSPC	35	32	13	20	46
40	7C1	Chol	C18PEG	2000	DSPC	35	30	15	20	83
41	7C1	Chol	C18PEG	2000	DSPC	50	34	1	15	39
42	7C1	Chol	C18PEG	2000	DSPC	50	32	3	15	110
43	7C1	Chol	C18PEG	2000	DSPC	50	30	5	15	60
44	7C1	Chol	C18PEG	2000	DSPC	50	28	7	15	53
45	7C1	Chol	C18PEG	2000	DSPC	50	26	9	15	53
46	7C1	Chol	C18PEG	2000	DSPC	50	24	11	15	56
47	7C1	Chol	C18PEG	2000	DSPC	50	22	13	15	46
48	7C1	Chol	C18PEG	2000	DSPC	50	20	15	15	43
49	7C1	Chol	C14PEG	3000	DSPC	35	44	1	20	51
50	7C1	Chol	C14PEG	3000	DSPC	35	42	3	20	47
51	7C1	Chol	C14PEG	3000	DSPC	35	40	5	20	39
52	7C1	Chol	C14PEG	3000	DSPC	35	38	7	20	78
53	7C1	Chol	C14PEG	3000	DSPC	35	36	9	20	288
54	7C1	Chol	C14PEG	3000	DSPC	35	34	11	20	15
55	7C1	Chol	C14PEG	3000	DSPC	35	32	13	20	31
56	7C1	Chol	C14PEG	3000	DSPC	35	30	15	20	76
57	7C1	Chol	C14PEG	3000	DSPC	50	34	1	15	55
58	7C1	Chol	C14PEG	3000	DSPC	50	32	3	15	21
59	7C1	Chol	C14PEG	3000	DSPC	50	30	5	15	46
60	7C1	Chol	C14PEG	3000	DSPC	50	28	7	15	29
61	7C1	Chol	C14PEG	3000	DSPC	50	26	9	15	101
62	7C1	Chol	C14PEG	3000	DSPC	50	24	11	15	108
63	7C1	Chol	C14PEG	3000	DSPC	50	22	13	15	66
64	7C1	Chol	C14PEG	3000	DSPC	50	20	15	15	66

Number	Lipomer Type	Chol Type	PEG Tail	PEG MW	HL Type	Lipomer %	Chol %	PEG %	HL %	Diameter (nm)
65	7C1	Chol	C14PEG	2000	DSPC	65	24	1	10	13
66	7C1	Chol	C14PEG	2000	DSPC	65	22	3	10	55
67	7C1	Chol	C14PEG	2000	DSPC	65	20	5	10	720
68	7C1	Chol	C14PEG	2000	DSPC	65	18	7	10	287
69	7C1	Chol	C14PEG	2000	DSPC	65	16	9	10	67
70	7C1	Chol	C14PEG	2000	DSPC	65	14	11	10	77
71	7C1	Chol	C14PEG	2000	DSPC	65	12	13	10	160
72	7C1	Chol	C14PEG	2000	DSPC	65	10	15	10	35
73	7C1	Chol	C14PEG	2000	DSPC	80	14	1	5	100
74	7C1	Chol	C14PEG	2000	DSPC	80	12	3	5	69
75	7C1	Chol	C14PEG	2000	DSPC	80	10	5	5	57
76	7C1	Chol	C14PEG	2000	DSPC	80	8	7	5	16
77	7C1	Chol	C14PEG	2000	DSPC	80	6	9	5	66
78	7C1	Chol	C14PEG	2000	DSPC	80	4	11	5	33
79	7C1	Chol	C14PEG	2000	DSPC	80	2	13	5	60
80	7C1	Chol	C14PEG	2000	DSPC	80	0	15	5	60
81	7C1	Chol	C16PEG	2000	DSPC	65	24	1	10	25
82	7C1	Chol	C16PEG	2000	DSPC	65	22	3	10	287
83	7C1	Chol	C16PEG	2000	DSPC	65	20	5	10	51
84	7C1	Chol	C16PEG	2000	DSPC	65	18	7	10	36
85	7C1	Chol	C16PEG	2000	DSPC	65	16	9	10	66
86	7C1	Chol	C16PEG	2000	DSPC	65	14	11	10	41
87	7C1	Chol	C16PEG	2000	DSPC	65	12	13	10	73
88	7C1	Chol	C16PEG	2000	DSPC	65	10	15	10	44
89	7C1	Chol	C16PEG	2000	DSPC	80	14	1	5	66
90	7C1	Chol	C16PEG	2000	DSPC	80	12	3	5	49
91	7C1	Chol	C16PEG	2000	DSPC	80	10	5	5	66
92	7C1	Chol	C16PEG	2000	DSPC	80	8	7	5	40
93	7C1	Chol	C16PEG	2000	DSPC	80	6	9	5	67
94	7C1	Chol	C16PEG	2000	DSPC	80	4	11	5	47
95	7C1	Chol	C16PEG	2000	DSPC	80	2	13	5	59
96	7C1	Chol	C16PEG	2000	DSPC	80	0	15	5	51
97	7C1	Chol	C18PEG	2000	DSPC	65	24	1	10	30
98	7C1	Chol	C18PEG	2000	DSPC	65	22	3	10	38
99	7C1	Chol	C18PEG	2000	DSPC	65	20	5	10	41
100	7C1	Chol	C18PEG	2000	DSPC	65	18	7	10	85
101	7C1	Chol	C18PEG	2000	DSPC	65	16	9	10	83
102	7C1	Chol	C18PEG	2000	DSPC	65	14	11	10	83
103	7C1	Chol	C18PEG	2000	DSPC	65	12	13	10	65
104	7C1	Chol	C18PEG	2000	DSPC	65	10	15	10	55
105	7C1	Chol	C18PEG	2000	DSPC	80	14	1	5	47
106	7C1	Chol	C18PEG	2000	DSPC	80	12	3	5	53
107	7C1	Chol	C18PEG	2000	DSPC	80	10	5	5	36
108	7C1	Chol	C18PEG	2000	DSPC	80	8	7	5	52
109	7C1	Chol	C18PEG	2000	DSPC	80	6	9	5	50
110	7C1	Chol	C18PEG	2000	DSPC	80	4	11	5	26
111	7C1	Chol	C18PEG	2000	DSPC	80	2	13	5	34
112	7C1	Chol	C18PEG	2000	DSPC	80	0	15	5	25
113	7C1	Chol	C14PEG	3000	DSPC	65	24	1	10	58
114	7C1	Chol	C14PEG	3000	DSPC	65	22	3	10	46
115	7C1	Chol	C14PEG	3000	DSPC	65	20	5	10	70
116	7C1	Chol	C14PEG	3000	DSPC	65	18	7	10	68
117	7C1	Chol	C14PEG	3000	DSPC	65	16	9	10	90
118	7C1	Chol	C14PEG	3000	DSPC	65	14	11	10	61
119	7C1	Chol	C14PEG	3000	DSPC	65	12	13	10	34
120	7C1	Chol	C14PEG	3000	DSPC	65	10	15	10	52
121	7C1	Chol	C14PEG	3000	DSPC	80	14	1	5	57
122	7C1	Chol	C14PEG	3000	DSPC	80	12	3	5	67
123	7C1	Chol	C14PEG	3000	DSPC	80	10	5	5	46
124	7C1	Chol	C14PEG	3000	DSPC	80	8	7	5	47
125	7C1	Chol	C14PEG	3000	DSPC	80	6	9	5	44
126	7C1	Chol	C14PEG	3000	DSPC	80	4	11	5	48
127	7C1	Chol	C14PEG	3000	DSPC	80	2	13	5	43
128	7C1	Chol	C14PEG	3000	DSPC	80	0	15	5	36

h

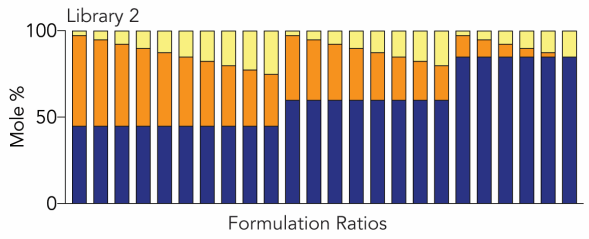

i

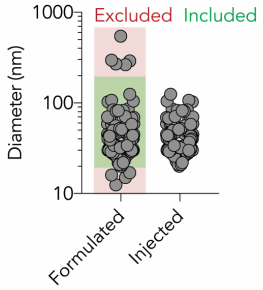

j

LNP #	Lipomer Type	Chol Type	PEG Alkyl	PEG MW	Lipomer Mole %	Chol Mole %	PEG Mole %	Diameter (nm)	LNP #	Lipomer Type	Chol Type	PEG Alkyl	PEG MW	Lipomer Mole %	Chol Mole %	PEG Mole %	Diameter (nm)
1	7C1	CHOL	C14	2000	60	37.5	2.5	50	61	7C1	CHOL	C18	2000	45	42.5	12.5	30
2	7C1	CHOL	C14	2000	60	35	5	55	62	7C1	CHOL	C18	2000	45	40	15	29
3	7C1	CHOL	C14	2000	60	32.5	7.5	290	63	7C1	CHOL	C18	2000	45	37.5	17.5	40
4	7C1	CHOL	C14	2000	60	30	10	27	64	7C1	CHOL	C18	2000	45	35	20	84
5	7C1	CHOL	C14	2000	60	27.5	12.5	47	65	7C1	CHOL	C18	2000	45	32.5	22.5	32
6	7C1	CHOL	C14	2000	60	25	15	31	66	7C1	CHOL	C18	2000	45	30	25	68
7	7C1	CHOL	C14	2000	60	22.5	17.5	103	67	7C1	CHOL	C18	2000	85	12.5	2.5	69
8	7C1	CHOL	C14	2000	60	20	20	58	68	7C1	CHOL	C18	2000	85	10	5	17
9	7C1	CHOL	C14	2000	45	52.5	2.5	40	69	7C1	CHOL	C18	2000	85	7.5	7.5	21
10	7C1	CHOL	C14	2000	45	50	5	59	70	7C1	CHOL	C18	2000	85	5	10	20
11	7C1	CHOL	C14	2000	45	47.5	7.5	12.5	71	7C1	CHOL	C18	2000	85	2.5	12.5	83
12	7C1	CHOL	C14	2000	45	45	10	107	72	7C1	CHOL	C18	2000	85	0	15	33
13	7C1	CHOL	C14	2000	45	42.5	12.5	27	73	7C1	CHOL	C14	3000	60	37.5	2.5	30
14	7C1	CHOL	C14	2000	45	40	15	45	74	7C1	CHOL	C14	3000	60	35	5	21
15	7C1	CHOL	C14	2000	45	37.5	17.5	28	75	7C1	CHOL	C14	3000	60	32.5	7.5	42
16	7C1	CHOL	C14	2000	45	35	20	56	76	7C1	CHOL	C14	3000	60	30	10	35
17	7C1	CHOL	C14	2000	45	32.5	22.5	26	77	7C1	CHOL	C14	3000	60	27.5	12.5	26
18	7C1	CHOL	C14	2000	45	30	25	31	78	7C1	CHOL	C14	3000	60	25	15	56
19	7C1	CHOL	C14	2000	85	12.5	2.5	42	79	7C1	CHOL	C14	3000	60	22.5	17.5	70
20	7C1	CHOL	C14	2000	85	10	5	45	80	7C1	CHOL	C14	3000	60	20	20	30
21	7C1	CHOL	C14	2000	85	7.5	7.5	43	81	7C1	CHOL	C14	3000	45	52.5	2.5	50
22	7C1	CHOL	C14	2000	85	5	10	57	82	7C1	CHOL	C14	3000	45	50	5	68
23	7C1	CHOL	C14	2000	85	2.5	12.5	15	83	7C1	CHOL	C14	3000	45	47.5	7.5	50
24	7C1	CHOL	C14	2000	85	0	15	22	84	7C1	CHOL	C14	3000	45	45	10	30
25	7C1	CHOL	C16	2000	60	37.5	2.5	41	85	7C1	CHOL	C14	3000	45	42.5	12.5	30
26	7C1	CHOL	C16	2000	60	35	5	34	86	7C1	CHOL	C14	3000	45	40	15	31
27	7C1	CHOL	C16	2000	60	32.5	7.5	50	87	7C1	CHOL	C14	3000	45	37.5	17.5	37
28	7C1	CHOL	C16	2000	60	30	10	27	88	7C1	CHOL	C14	3000	45	35	20	34
29	7C1	CHOL	C16	2000	60	27.5	12.5	264	89	7C1	CHOL	C14	3000	45	32.5	22.5	71
30	7C1	CHOL	C16	2000	60	25	15	47	90	7C1	CHOL	C14	3000	45	30	25	32
31	7C1	CHOL	C16	2000	60	22.5	17.5	25	91	7C1	CHOL	C14	3000	85	12.5	2.5	33
32	7C1	CHOL	C16	2000	60	20	20	28	92	7C1	CHOL	C14	3000	85	10	5	297
33	7C1	CHOL	C16	2000	45	52.5	2.5	59	93	7C1	CHOL	C14	3000	85	7.5	7.5	28
34	7C1	CHOL	C16	2000	45	50	5	58	94	7C1	CHOL	C14	3000	85	5	10	30
35	7C1	CHOL	C16	2000	45	47.5	7.5	57	95	7C1	CHOL	C14	3000	85	2.5	12.5	35
36	7C1	CHOL	C16	2000	45	45	10	30	96	7C1	CHOL	C14	3000	85	0	15	29
37	7C1	CHOL	C16	2000	45	42.5	12.5	270	97	7C1	CHOL	C18	3000	60	37.5	2.5	33
38	7C1	CHOL	C16	2000	45	40	15	41	98	7C1	CHOL	C18	3000	60	35	5	43
39	7C1	CHOL	C16	2000	45	37.5	17.5	86	99	7C1	CHOL	C18	3000	60	32.5	7.5	52
40	7C1	CHOL	C16	2000	45	35	20	33	100	7C1	CHOL	C18	3000	60	30	10	40
41	7C1	CHOL	C16	2000	45	32.5	22.5	38	101	7C1	CHOL	C18	3000	60	27.5	12.5	34
42	7C1	CHOL	C16	2000	45	30	25	n	102	7C1	CHOL	C18	3000	60	25	15	39
43	7C1	CHOL	C16	2000	85	12.5	2.5	30	103	7C1	CHOL	C18	3000	60	22.5	17.5	545
44	7C1	CHOL	C16	2000	85	10	5	50	104	7C1	CHOL	C18	3000	60	20	20	40
45	7C1	CHOL	C16	2000	85	7.5	7.5	28	105	7C1	CHOL	C18	3000	45	52.5	2.5	33
46	7C1	CHOL	C16	2000	85	5	10	25	106	7C1	CHOL	C18	3000	45	50	5	43
47	7C1	CHOL	C16	2000	85	2.5	12.5	54	107	7C1	CHOL	C18	3000	45	47.5	7.5	51
48	7C1	CHOL	C16	2000	85	0	15	66	108	7C1	CHOL	C18	3000	45	45	10	30
49	7C1	CHOL	C18	2000	60	37.5	2.5	33	109	7C1	CHOL	C18	3000	45	42.5	12.5	21
50	7C1	CHOL	C18	2000	60	35	5	16	110	7C1	CHOL	C18	3000	45	40	15	37
51	7C1	CHOL	C18	2000	60	32.5	7.5	37	111	7C1	CHOL	C18	3000	45	37.5	17.5	32
52	7C1	CHOL	C18	2000	60	30	10	46	112	7C1	CHOL	C18	3000	45	35	20	22
53	7C1	CHOL	C18	2000	60	27.5	12.5	23	113	7C1	CHOL	C18	3000	45	32.5	22.5	29
54	7C1	CHOL	C18	2000	60	25	15	43	114	7C1	CHOL	C18	3000	45	30	25	30
55	7C1	CHOL	C18	2000	60	22.5	17.5	63	115	7C1	CHOL	C18	3000	85	12.5	2.5	81
56	7C1	CHOL	C18	2000	60	20	20	47	116	7C1	CHOL	C18	3000	85	10	5	125
57	7C1	CHOL	C18	2000	45	52.5	2.5	105	117	7C1	CHOL	C18	3000	85	7.5	7.5	82
58	7C1	CHOL	C18	2000	45	50	5	33	118	7C1	CHOL	C18	3000	85	5	10	34
59	7C1	CHOL	C18	2000	45	47.5	7.5	54	119	7C1	CHOL	C18	3000	85	2.5	12.5	58
60	7C1	CHOL	C18	2000	45	45	10	49	120	7C1	CHOL	C18	3000	85	0	15	44

Figure 2.8. (a) Using DLS, LNPs were includedif they met the following inclusion criteria: autocorrelation curves with 1 inflection point and hydrodynamicdiameters between 20 nm and 200 nm. **(B)** Average normalized delivery of each LNP from library 2. **(C)** In all samples of library 2, naked barcode – the negative control – was delivered less efficiently thanbarcodes carried by LNPs, as expected. **(D)** The following example illustrates how our deep sequencingdata was normalized. **(E)** Cells were sorted on the indicated FACS markers. **(F)** LNPs libraries for screens1 and 2 were synthesized with the LNP 7C1, Cholesterol, DSPC, and variable PEG compounds atvariable molar

ratios. **(G)** The formulation ratios and diameter of each LNP for screen 1. **(H)** Nanoparticleformulation ratios for screen 2; in this screen, we formulated 120 different LNPs. **(I)** Stable LNPs withdiameters between 20 and 200 nm were included. **(J)** The formulation ratios and diameter of each LNPfor screen 2.

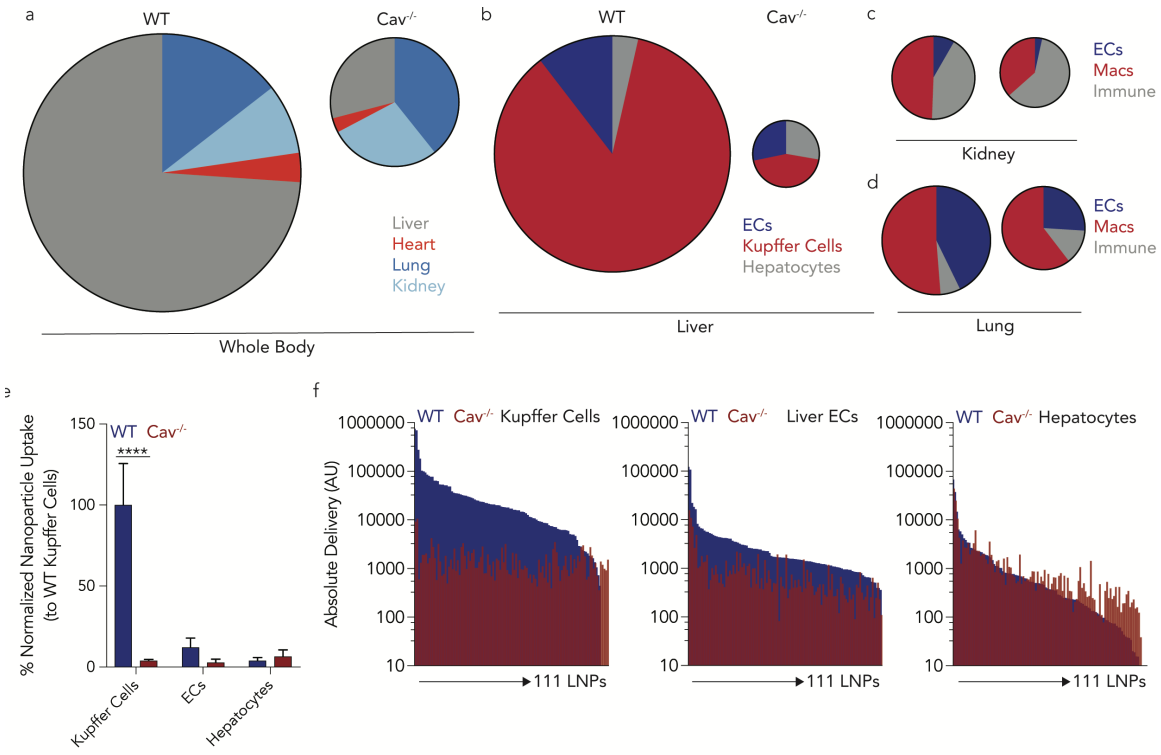

Figure 2.9. High throughput QUANT studies reveal Caveolin1 affects delivery in atissue- and cell-type dependent manner in vivo. **(A)** The total ddPCR counts in alltested cell types – which are equal to the area of the circle - were used to determinethe 'total experimental' biodistribution in WT and Cav1-/- mice. **(B)** The total ddPCRcounts were determined in different cell-types from the liver, **(C)** lung and **(D)** kidney.Compared to cells isolated from WT mice, ddPCR counts from Cav1-/- decreased, with the most dramatic effect in the liver. **(E)** Within the liver cell-types,normalized library 1 nanoparticle biodistribution demonstrates that Kupffer cells inCav1-/- uptake less nucleic acids when compared to Kupffer cells from WT mice.****$p<0.0001$ 2-way ANOVA. **(F)** Combined sequencing data and ddPCR resultsshows the absolute delivery of 111 nanoparticles for each LNP in the liver in WT(blue) and Cav1-/- (red) mice, from library 1, in Kupffer cells, liver endothelial cells,and hepatocytes.

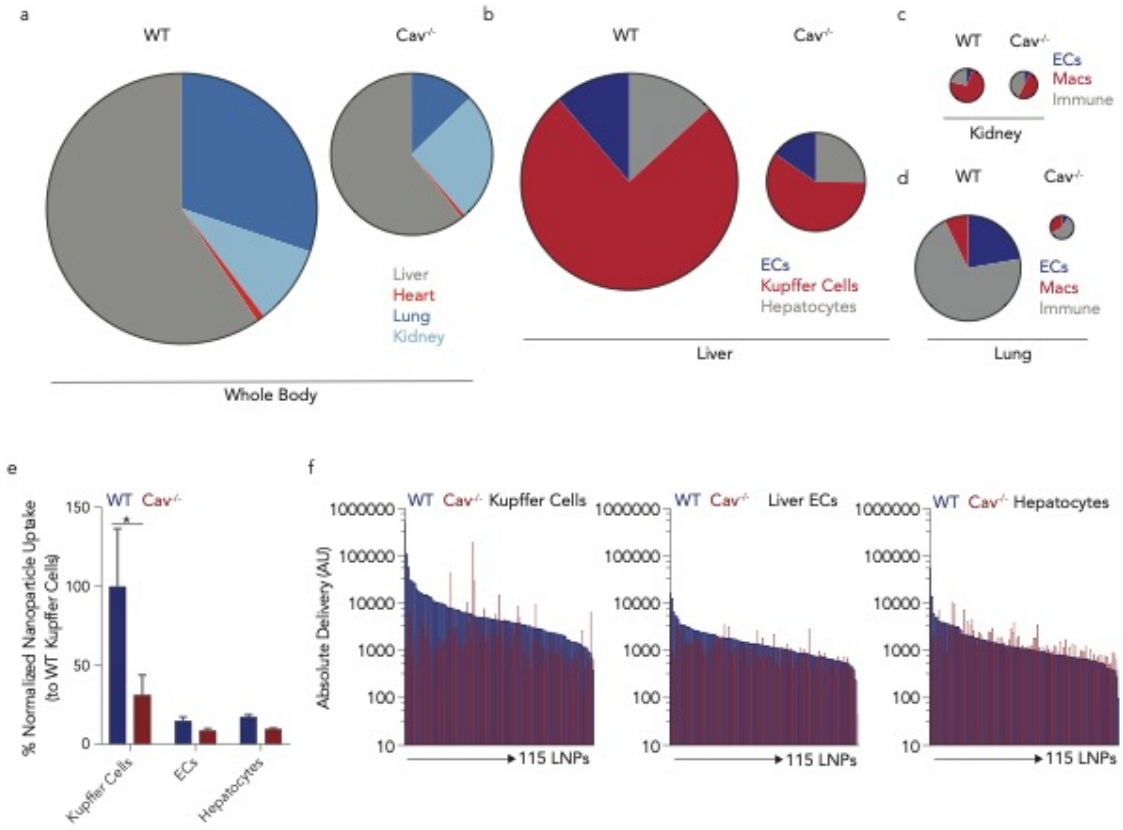

Figure 2.10. (A) Total ddPCR barcode counts for library 2 – equal to the area of the circle - were used to determine the overall biodistribution from the LNP screens previously described across multiple organs from WT and Cav1-/- mice. **(B)** The total ddPCR counts were determined in different cell-types from the liver, **(C)** lung and **(D)** kidney. **(E)** Within the liver cell-types, normalized nanoparticle biodistribution demonstrates that Kupffer cells in Cav1-/- uptake less nucleic acids when compared to Kupffer cells from WT mice. *p<0.05 2-way ANOVA. **(F)** Combined sequencing data and ddPCR results shows the absolute delivery of 115 nanoparticles for each LNP in the liver in WT (blue) and Cav1-/- (red) mice, from library 1, in Kupffer cells, liver endothelial cells, and hepatocytes.

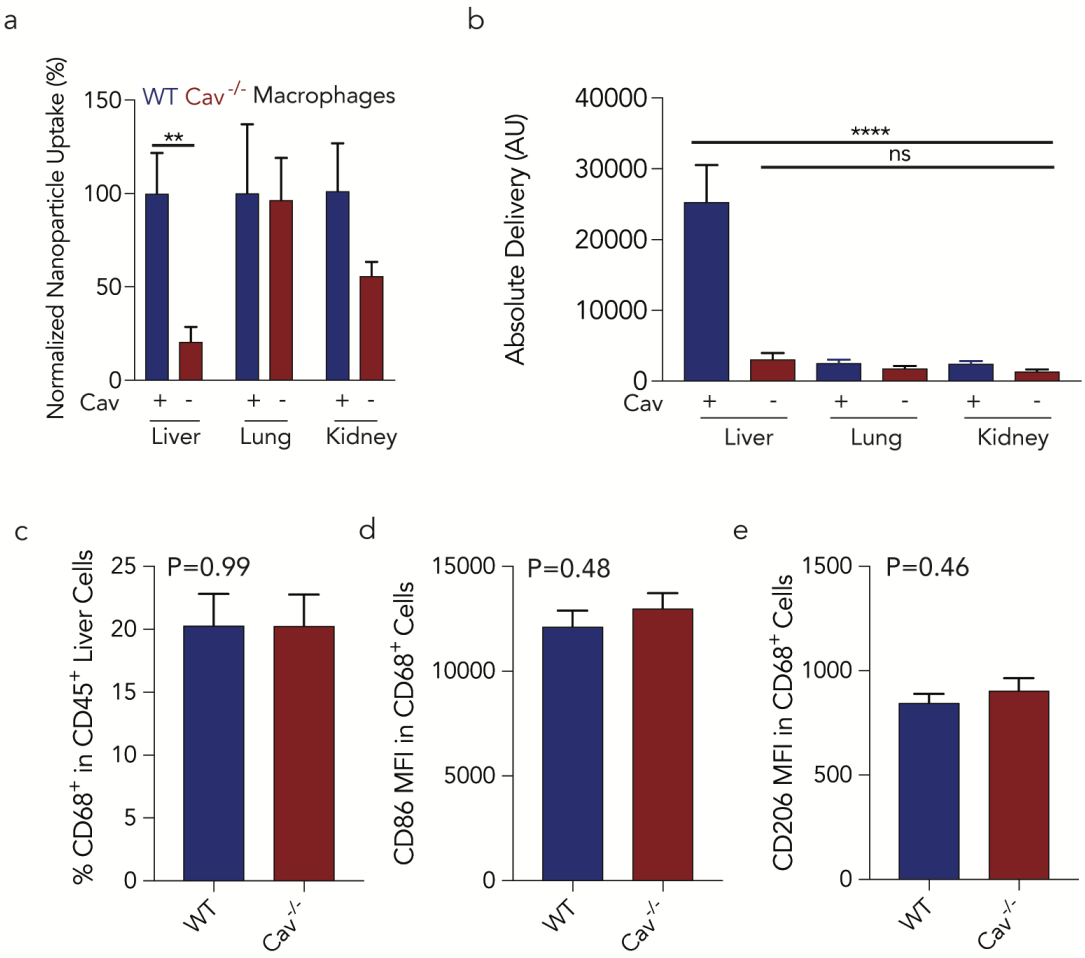

Figure 2.11. QUANT studies show Caveolin1 significantly affects delivery in Kupffer cells in vivo. **(A)** Nanoparticlebiodistribution in macrophages were isolated from multiple tissues from WT and Cav1-/- mice. Lungand kidney macrophages were less impacted by the loss of caveolin. **p<0.01 1-tailed t-test. **(B)** Absolutenanoparticle delivery to WT and Cav1-/- macrophages in the liver, lung, and kidney. Kupffer cells werestatistically significant compared to other macrophage beds. ****p<0.0001 One-way ANOVA. **(C)** The percentageof Kupffer cells (CD68+ CD45+) within the immune cell population (CD45+) in WT and Cav1-/-mice were similar. Phenotype variations in WT and Cav1-/- Kupffer (CD68+ CD45+) cells populationswere determined by MFI of **(D)** CD86 and **(E)** CD206.

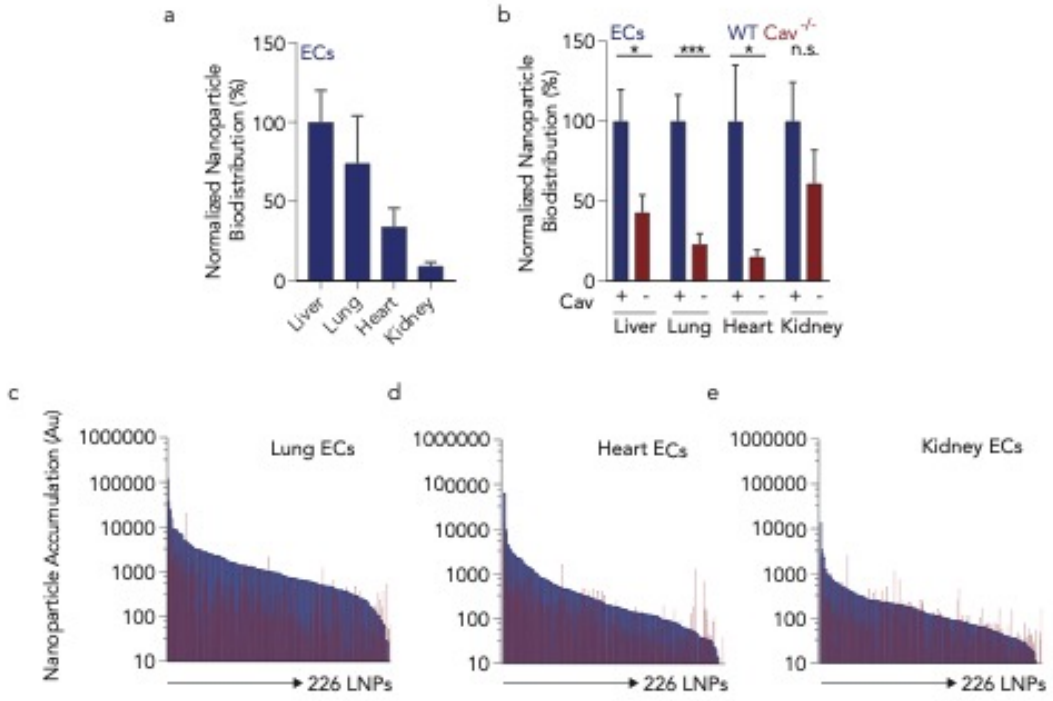

Figure 2.12. (A) Normalized nanoparticle biodistribution across two screens (226 LNPs) in liver, lung, heart, and kidney endothelial cells. **(B)** QUANT demonstrates that endothelial cells in Cav1-/- uptake less QUANT barcodes than endothelial cells in WT mice. *p<0.05, ***p<0.001 1 tailed t-test. **(C)** Combined sequencing data and ddPCR results for each LNP in lung endothelial cells in WT (blue) and Cav1-/- (red) mice from screen 1 and screen 2 in lung, **(D)** heart, and **(E)** kidney endothelial cells.

CHAPTER 3. CONSTRAINED NANOPARTICLES DELIVER SIRNA AND SGRNA TO T-CELLS IN VIVO WITHOUT TARGETING LIGANDS

The work presented here is an excerpt from Lokugamage MP*, Sago CD*, Islam FZ, Gan Z, Krupzak BR, Dahlman JE, "Constrained nanoparticles deliver siRNA and sgRNA to T cells in vivo without targeting ligands." *Advanced Materials*, 2019.

3.1 Introduction

T lymphocytes help regulate immune responses, which makes them important drug targets. For example, antibodies that block T cell CTLA-4 or PD-1 signaling can drive anti-tumor responses[125]. However, antibodies target druggable proteins, which constitute approximately 15% of total proteins. By contrast, siRNA can inhibit the translation of any gene; many 'undruggable' proteins were recently implicated in T cell-mediated immunity[126].

Clinically relevant RNA delivery to cells other than hepatocytes[9] remains challenging[19]. However, there have been advances in T cell siRNA delivery. For example, siRNA was delivered to T cells using a single chain antibody linked to a cationic peptide; this led to gene silencing at 5 mg / kg[127]. In a second example, nanoparticles were coated with anti-CD4 antibodies, leading to 20% target gene silencing at 1 mg / kg doses[128]. More recently, LNPs that target hepatocytes were re-targeted to T cells by coating them with CD4 antibodies, leading to 50% in vivo T cell gene silencing at 6 mg / kg doses[25]. These papers (and others)[129] achieve T cell delivery using peptide-, protein-, or aptamer-based targeting ligands, and more generally, ligand-based targeting is used throughout nanomedicine. However, ligands can make reproducible manufacturing at human scales more challenging[130].

One alternative to active targeting is to exploit endogenous lipid trafficking; notably, the only FDA approved RNA nanoparticle therapy[9] utilizes LNPs without ligands that are trafficked to hepatocytes via endogenous cholesterol transport[36]. Natural trafficking has not been exploited to

promote nanoparticle delivery to T cells, yet these cells can interact with viruses and lipoprotein particles, which can have diameters similar to LNPs[76,131]. We therefore hypothesized that LNPs could interact with T cells without targeting ligands. To test this hypothesis, we quantified how well 168 LNPs delivered siRNA to 9 cell types in vivo. Using traditional 1-by-1 in vivo approaches, this would require FACS analysis of hundreds of mice. Thus, to generate large scale in vivo data, we developed a siGFP / DNA barcode-based screening system. This system quantifies how over 100 nanoparticles deliver siGFP to any desired combination of on- and off-target cell types in vivo. This in vivo approach contrasts with previous LNP research, which utilizes in vitro screening to select a small number of nanoparticles for in vivo evaluation[132]. The approach is supported by evidence that in vitro nanoparticle delivery can be a poor predictor of in vivo nanoparticle delivery[33]. By combining high throughput in vivo analyses and bioinformatics, we found that a new class of materials, named conformationally constrained lipids, can form stable LNPs. We also found these 'constrained LNPs' (cLNPs) can deliver siRNA to T cells in vivo. These data demonstrate that the conformational state of lipids can alter LNP tropism and provide intriguing preliminary evidence that natural trafficking can promote T cell delivery, offering a potential alternative to active targeting.

3.2 Results

3.2.1 Lipid nanoparticles containing a constrained lipid can form stable LNPs

We synthesized 13 chemically diverse lipids containing amines or boronic acid. The library was constructed to investigate whether the structure of the (i) head groups and (ii) lipid tail affected delivery. We purified a 'scaffold' containing the unsaturated lipid linoleate and two ester bonds (**Fig. 3.1A, Fig. 3.2A**). This scaffold did not have any ionizable components; we attached head group variants to the reactive sites, in order to create chemical diversity. At reactive site 1, we added 11 head groups (labeled 1-11) via esterification, resulting in head groups linked by ester or carbonate linkages, respectively (**Fig. 3.1B**). At reactive site 2, we added 3 lipid tails (labeled A-

C) with diverse structures (**Fig. 3.1C**) via esterification. Tail A contained adamantane, a constrained lipid with a defined 'armchair' structure. Tail B contained 2 lipid tails, bringing the total number of tails to 3. The control tail, C, was linoleate; this created a construct with two identical lipid tails. After synthesis, we confirmed the chemical structure of all 13 lipids using high resolution mass spectroscopy or 1H-NMR (**Fig. 3.2B-D**). We named each lipid with the nomenclature 'head group number – tail letter' (e.g. 11-A).

We then investigated whether the 13 ionizable lipids formed stable LNPs. We measured the hydrodynamic diameter of LNPs carrying a siRNA targeting GFP[76] (siGFP) as well as a DNA barcode[133]; the LNPs were formulated using microfluidics[107]. The siGFP was chemically modified to reduce immunostimulation and enhance on-target silencing via preferential antisense RISC loading (**Fig. 3.3A**). To minimize the chance our results were affected by other constituents added to the LNP, we added previously validated constituents: C14PEG2000, unmodified cholesterol, and either DSPC or DOPE (**Fig. 3.1D**). As a control to ensure our results were not affected by the molar ratio of the 4 components, we formulated each of the 13 lipids with 2 phospholipids and 4 molar ratios, producing a total of 104 chemically distinct LNPs (**Fig. 3.1D**). Encouragingly, 100 of the 104 LNPs formed small, monodisperse populations, as evidenced by hydrodynamic diameter and polydispersity index; these 100 LNPs were pooled together. The diameter for individual LNPs varied between 30 and 170 nm. As a control, we also measured the diameter and polydispersity of the pooled LNPs. We found them to be 76 nm (**Fig. 3.1E**) and 0.23 (**Fig. 3.1F**), respectively, which was within the range of the individuals comprising the pool. We then analyzed the hydrodynamic diameter as a function of ionizable lipid (**Fig. 3.3B**), molar ratio of the four constituents (**Fig. 3.3C**), and the type of phospholipid (DSPC / DOPE) added to the formulation (**Fig. 3.3D**). In all cases, the average diameter varied between 50 and 100 nm. These data led us to conclude these lipids could form LNPs with hydrodynamic diameters similar to lipoproteins and viruses.

3.2.2 A high-throughput siRNA screen reveals LNPs with constrained lipids have biological activity in T cells

We evaluated how each LNP delivered siRNA to target cells (in this case, T lymphocytes) as well as 8 off-target cell types in vivo (**Fig. 3.4**). Our approach utilizes DNA barcodes and siGFP, to evaluate how many distinct LNPs functionally delivered siGFP, in any combination of target cells, in a single mouse. We formulated LNP-1, with chemical structure 1, to carry siGFP and DNA barcode 1; we separately formulated LNP-N, with chemical structure N, to carry siGFP and DNA barcode N (**Fig. 3.5A**). We included naked barcodes as a negative control[133], since DNA does not readily enter cells. We pooled the LNPs together, and intravenously injected them into mice that constitutively express GFP under a CAG promoter (**Fig. 3.5B**). The GFP acted as the functional delivery readout; LNPs which functionally delivered siGFP into the cytoplasm would have lower GFP protein expression. Thus, 3 days after injecting mice, we isolated GFPLow cells using FACS, and deep sequenced the DNA barcodes in GFPLow cells. In this way, we isolated barcodes co-localized with cells in which GFP protein silencing occurred. After sequencing the barcodes, we calculated normalized delivery, i.e., the number of barcodes for each individual barcode, divided by the total number of barcodes within that sample. Normalized delivery is analogous to counts per million in RNAseq experiments[124]. Since GFP is expressed in all cell types, this assay allows us to (i) compare GFP knockdown in any combination of on- / off-target cells and (ii) identify LNPs that co-localized in GFPLow cells.

Three days after injecting a total dose of 1.5 mg / kg into mice (100 distinct LNPs, 0.015 mg / kg / particle on average), we quantified GFP silencing in 9 cell types. Compared to PBS treated mice, there was an increased number of GFPLow splenic B cells and splenic T cells (**Fig. 3.5C**). The average GFP protein silencing, quantified by mean fluorescent intensity, was greatest in splenic T cells, followed by liver immune cells, splenic B cells, and lung endothelial cells (**Fig. 3.5D**). Surprisingly, we found no evidence of silencing in hepatocytes (**Fig. 3.5C,D**), which are preferentially targeted by many LNPs[127]. We then monitored the controls included in our data; we

sequenced the GFPLow splenic T cells as well as lung endothelial cells, splenic B cells, and liver immune cells. In all 4 cell types, the normalized delivery of both negative controls (naked barcodes) was lower than barcodes delivered by LNPs, as expected (**Fig. 3.5E**).

We then performed a large in vivo structure-function analysis, using the DNA sequencing data to evaluate whether any nanoparticle material properties promoted delivery to splenic T cells. First, we calculated the enrichment for different nanoparticle properties (**Fig. 3.6**). Briefly, we calculated the odds a nanoparticle with a particular property would show up by chance in particles that (i) performed in the top 10%, and separately, (ii) particles that performed in the bottom 10%. Nanoparticles formulated with DSPC were enriched in effective particles (i.e., particles with high normalized delivery), whereas nanoparticles formulated with DOPE were enriched in particles that performed poorly (**Fig. 3.5F**). To validate these results, we then compared the normalized delivery for all LNPs formulated with DSPC and DOPE, respectively, and found that DSPC-containing LNPs outperformed DOPE-containing LNPs (**Fig. 3.7A**). As an additional validation, we calculated the normalized delivery of 'paired' LNPs, i.e., LNPs that had the same molar ratios and ionizable lipids (but different phospholipids). We found that DSPC LNPs outperformed their paired DOPE containing LNP (**Fig. 3.7B**). Based on these data, we concluded that the phospholipid contained within the LNP affected splenic T cell delivery. We therefore limited future chemical analysis to DSPC containing formulations.

We then analyzed enrichment for the 13 ionizable lipids, in order to evaluate the effect of the lipid tail and head group and found 3 ionizable lipids were enriched (**Fig. 3.5G**). As a control, we plotted enrichment of each headgroup versus headgroup molecular weight, hydrophobicity (LogP), and polar surface area (**Fig. 3.8A-D**); we did not observe correlations between these traits and enrichment. The lipid that was most enriched, 11-A, contained a conformationally constrained adamantane tail. Notably, the enrichment (**Fig. 3.5G**) and normalized DNA delivery (**Fig. 3.5H**) of 11-A was higher than 11-B and 11-C, the two compounds with identical head groups, but unconstrained lipid tails. We then performed a paired analysis using compounds with the same

molar ratio and found that adamantane containing tails outperformed other tail structures (**Fig. 3.8E**). Finally, as a control, we analyzed how LNP size affected delivery. We plotted normalized T cell delivery against LNP size and found no relationship (**Fig. 3.8F**). Taken together, these data provided initial evidence that adamantane-containing LNPs could deliver nucleic acids to T cells in vivo, without the use of a targeting ligand.

3.2.3 A second high-throughput siRNA screen suggests that adamantanes can deliver siRNA to T cells

To further investigate the relationship between adamantane and siRNA delivery, we performed a second in vivo screen with adamantane-containing LNPs. The second library was designed based on the results of the first screen. To do this, we first synthesized new ionizable lipids, using the most enriched components from the first screen, head group 1 (**Fig. 3.1B**) and adamantane tail (tail A, **Fig. 3.1C**). More specifically, at reactive site 3, we added 15 lipids tails (labeled D-S) with diverse structures (**Fig. 3.9A,B**) via esterification. We also included the top-ranked LNP from our first screen (**Fig. 3.9C**). Thus, we synthesized 16 ionizable lipids in total. We named each lipid in the following manner: 'head group number (R1) – tail letter (R2) – tail letter (R3)' (e.g. 11-A-M). We formulated each LNP with C14PEG2000, cholesterol, and DSPC. Once again, to control against effects driven by the molar ratio of the components, we formulated all 16 ionizable lipids at 4 molar ratios, for a total of 64 LNPs (**Fig. 3.9D**). Each LNP carried siGFP and a unique barcode. 55 of the LNPs formed small, monodisperse populations, based on the hydrodynamic diameter and polydispersity index, and were therefore pooled together. The diameter for individual LNPs varied between 20 and 200 nm, with an average of 92 nm (**Fig. 3.9E**) and an average PDI of 0.20 (**Fig. 3.9F**). We plotted hydrodynamic diameter for each ionizable lipid (**Fig. 3.11A**) and each molar ratio (**Fig. 3.11B**), and found that all the compositions formed LNPs within the 20-200 nm range.

We then administered all 55 LNPs intravenously to mice at a total dose of 1.5 mg / kg. Three days later, we quantified GFP silencing in 9 cell types. Once again, we (i) found GFPLow splenic T cells (**Fig. 3.9G**), (ii) measured GFP protein silencing in splenic T cells (Figure 3H), (iii) found no evidence of silencing in hepatocytes (**Fig. 3.9G,H**), and (iv) found no relationship between nanoparticle size and delivery (**Fig. 3.11C**). As a control, we quantified the normalized delivery of both negative controls (naked barcodes), and found they were lower than barcodes delivered by LNPs (**Fig. 3.9I**). We then evaluated whether the molecule added to reactive site 3 (**Fig. 3.9B**) altered delivery when adamantane was present. Using enrichment (**Fig. 3.10J**), we found reactive group D, I, and M were enriched. We were unable to identify why these variants performed well. However, compared to the top performing cLNP from screen 1, we found delivery was not greatly improved with any alteration to the reactive site 3 molecule (**Fig. 3.9K**). It is interesting to note that the top performing cLNP from screen 1 (11-A-M) was enriched more than any other cLNP (**Fig. 3.9J**). These data provided additional evidence to support the hypothesis that LNPs can deliver siRNA to T cells without targeting ligands.

3.2.4 cLNPs deliver small RNAs that change gene expression in CD8+ T cells

Like all high throughput screening systems, the value of this siGFP / DNA barcode assay is related to its ability to make predictions. We therefore evaluated whether the top-ranked LNPs from our first (11-A-M) and second (1-A-N) screens delivered siRNA in vivo (**Fig. 3.10A**). We formulated each LNP with siGFP and analyzed physical traits; each LNP had similar hydrodynamic diameter, polydispersity and pKa (**Fig. 3.10B**). We then intravenously injected mice with 1.5 mg / kg; 3 days later, we isolated cells and measured GFP protein expression. When compared to mice treated with a non-targeting, chemically modified siRNA (siLuc), we found 11-A-M silenced GFP more than 1-A-N (**Fig. 3.10C**). To validate the activity of 1-A-N, we formulated it with siCD45, and quantified CD45 silencing three days after injecting mice with 1.5 mg / kg; we found statistically significant silencing in T cells (**Fig. 3.11D,E**). Based on these head-to-head data, we

focused on compound 11-A-M. We performed a siRNA gene silencing dose response in vivo, and found that 11-A-M silenced GFP as doses as low as 0.5 mg / kg (**Fig. 3.10D**). We quantified silencing in subsets of T cells, focusing on CD4+ and CD8+ cells, respectively, and observed more potent protein silencing in CD8+ T cells (**Fig. 3.10E**). During this experiment, we also evaluated whether 11-A-M delivered siGFP to other common 'off-target' cell types by quantifying GFP silencing. Recapitulating observations made in both screens, we observed no significant silencing at doses as high as 1.5 mg / kg in other cell types, including hepatic T cells, bone marrow T cells, and splenic macrophages (**Fig. 3.12**). We then quantified on- and off-target biodistribution using QUANT, a highly sensitive ddPCR-based method we recently reported[133]. We formulated 11-A-M to carry the chemically modified QUANT barcode and injected 1.0 mg / kg intravenously. 24 hours later, we isolated cell types using FACS, and measured biodistribution in 8 cell types. We found that 11-A-M distribution was highest in splenic CD8+ T cells, CD4+ T cells, and B cells. Distribution was lower in splenic macrophages as well as endothelial cells, Kupffer cells, hepatocytes, and T cells isolated from the liver (**Fig. 3.13A,B**). We also quantified biodistribution mediated by 1-A-N in all 8 cell types, and found that splenic macrophages acted as the primary 'sink' for this LNP (**Fig. 3.13C,D**). These data suggest that the 11-A-M cLNP may preferentially silence genes in splenic CD8+ T cells.

Finally, we utilized 11-A-M to facilitate in vivo gene editing in T cells. We formulated it to carry a chemically modified sgRNA targeting GFP (**Fig. 3.14**) into mice[112] constitutively expressing Cas9 and GFP. Five days after administration, we quantified GFP expression in CD3+ T cells as well as in CD4+ and CD8+ T Cells. We observed a similar tropism; GFP protein was silenced more robustly in CD8+ than in CD4+ T cells (**Fig. 310F**). We did not observe changes in GFP expression when a control sgRNA targeting the gene ICAM-2 was administered to the mice (**Fig. 310F**). Notably, cLNPs did not lead to weight loss 24 hours after administration in any experiment (**Fig. 3.15A**). Taken together, these data led us to conclude that cLNPs without targeting ligands can deliver siRNA and sgRNA to splenic T cells. Finally, we analyzed additional traits of

11-A-M cLNPs formulated with siGFP using transmission electron microscopy. We found that the cLNPs formed small, monodisperse spherical structures (**Fig. 310G**).

3.3 Discussion

Nanoparticles that deliver RNA systemically to non-hepatocytes are difficult to design[19], in large part because (i) there is no high throughput method to study nanoparticle siRNA delivery in vivo and (ii) natural trafficking mechanisms to non-liver cells remain elusive. This universal problem in nanomedicine slows the development of all RNA therapies; currently, scientists perform high throughput nanoparticle assays in vitro, even though cell culture does not[33] recapitulate all the factors that affect delivery in vivo. Notably, the results from our first siGFP screen predicted that preferential T cell delivery would occur; these data were confirmed by the second siGFP screen, and by several in vivo experiments with cLNPs selected from the library. These data suggest that high throughput in vivo siRNA screens can identify nanoparticles with novel tropism. The screening data (**Fig. 3.5C,D, Fig. 3.9G,H**) suggested that other immune cell subsets may be targeted with LNPs. Although our current data do not allow us to predict how endosomal escape varies between T cells and other immune cells, we believe future studies utilizing traditional cell signaling techniques may elucidate genes and pathways that govern (and differentiate) endosomal escape in subsets of immune cells. Notably, evidence suggests a given immune cell 'type' actually encompasses a spectrum of transcriptionally and phenotypically distinct cells[134]. We therefore hypothesize that the relationship between uptake and cytoplasmic delivery will vary along this spectrum.

It is important to acknowledge the limitations of our work. First, the siGFP system will not work with unstable nanoparticles. It is critical to (i) analyze the size and polydispersity of each individual nanoparticle before pooling, (ii) include the naked DNA barcode control, (iii) use untreated GFP mice to gate during FACS, and (iv) individually confirm any lead candidates identified by the screen. Second, although we observed protein silencing in T cells at 0.5 mg / kg

doses, we will need to reduce this dose more than 30-fold before it matches the potency of a FDA-approved siRNA delivery vehicle in mice[22]. We anticipate iterative in vivo approaches we recently reported[135] may further improve T cell LNP potency. Lastly, we did not identify the natural trafficking pathways that promoted delivery to T cells. However, we believe that identifying the genes or pathways that promote LNP delivery to T cells without ligands constitutes an exciting scientific opportunity. In this way, we hope future work on cLNPs will lead to more effective, scalable RNA immunotherapies[136], as well as fundamental advances in our understanding of T cell lipid trafficking. More generally, these data may inspire other efforts to identify natural mechanisms to target cells which – to date – have only been targeted with active ligands.

3.4 Materials and Methods

Nanoparticle Formulation. Nanoparticles were formulated using a microfluidic device[30] as previously described. Briefly, nucleic acids (siRNA, sgRNA and DNA barcodes) were diluted in citrate buffer while lipid-amine compounds, alkyl tailed PEG, cholesterol, and DSPC were diluted in 100% ethanol. PEG, cholesterol, and DSPC was purchased from Avanti Lipids. Citrate and ethanol phases were combined in a microfluidic device by syringe pumps at a relative flow rate of 3:1.

DNA Barcoding. Each chemically distinct LNP was formulated to carry its own unique DNA barcode and siRNA. For example, LNP1 carried DNA barcode 1 and siGFP, while the chemically distinct LNP2 carried DNA barcode 2 and siGFP. Single stranded DNA sequences were purchased from IDT. To ensure equal amplification of each sequence, we included universal forward and reverse primer regions. Each barcode was distinguished using a unique 8 nucleotide sequence. We used 156 distinct sequences designed to prevent sequence 'bleaching' on the Illumina MiniSeq sequencing machine.

Nanoparticle Characterization. LNP hydrodynamic diameter was measured using a plate reader formatted dynamic light scattering machine (Wyatt). LNPs were diluted in sterile 1X PBS to a concentration of ~0.06 μg/mL and analyzed. LNPs were only included if they formed monodisperse populations with diameter between 20 and 200nm. Particles that met these criteria were dialyzed with 1X phosphate buffered saline (PBS, Invitrogen), and were sterile filtered with a 0.22 μm filter.

Animal Experiments. All animal experiments were performed in accordance with the Georgia Institute of Technology's IACUC. C57BL/6J (#000664), GFP (#003291), and constitutive SpCas9 (#026179) mice were purchased from The Jackson Laboratory and used between 5-12 weeks of age. In all experiments, we used N=3-5 mice/group. Mice were injected intravenously via the lateral tail vein. The nanoparticle concentration was determined using NanoDrop (Thermo Scientific).

Cell Isolation & Staining. Cells were isolated 72 hours (for screens and siRNA silencing) or 120 hours (for *in vivo* Cas9 gene editing) hours after LNP injection unless otherwise noted. Mice were perfused with 20 mL of 1X PBS through the right atrium. As we previously described[64,68], tissues were cut and placed in a digestive enzyme solution with Collagenase Type I (Sigma Aldrich), Collagenase XI (Sigma Aldrich) and Hyaluronidase (Sigma Aldrich) at 37 ºC for 45 minutes. Cell suspension was filtered through 70μm mesh and red blood cells were lysed. Cells were stained to identify populations and sorted using the BD FacsFusion in the Georgia Institute of Technology Cellular Analysis Core for *in vivo* experiments. The antibody clones used were: anti-CD31 (390, BioLegend), anti-CD45.2 (104, BioLegend), anti-CD68 (FA-11, BioLegend), anti-CD19 (6D5, Biolegend), anti-CD3 (17A2, Biolegend), anti-CD8a (53-6.7, Biolegend), and anti-CD4 (GK1.5, Biolegend). Representative FACS plots are found in Supporting Information **Figure 3.4**.

PCR Amplification for Illumina Sequencing. All samples were amplified and prepared for sequencing using nested PCR. 2 µL of primers were added to 5 µL of Kapa HiFi 2X master mix, and 3 µL template DNA/water. The second PCR added Nextera XT chemistry, indices, and i5/i7 adapter regions. Dual-indexed samples were run on a 2% agarose gel to ensure that PCR reaction occurred before being pooled and gel purified.

Deep Sequencing. Illumina sequencing was conducted in Georgia Institute of Technology's Molecular Evolution core. Runs were performed on an Illumina Miniseq. Primers were designed based on Nextera XT adapter sequences.

Barcode Sequencing Normalization. Counts for each particle, per cell type, were normalized to the barcoded LNP mixture applied to cells or injected into the mouse.

TNS Assay. The pKa of 11-A-M and 1-A-N was measured as previously described[64]. Briefly, a stock solution of 10mM HEPES (Sigma), 10mM MES (Sigma), 10mM sodium acetate (Sigma), and 140nM sodium chloride (Sigma) was prepared and pH adjusted with hydrogen chloride and sodium hydroxide to a range of pH between 4 and 10. Using 4 replicates for each nanoparticle at each pH, 140 µL pH-adjusted buffer was added to a 96-well plate, followed by the addition 5 µL of 2-(p-toluidino)-6-napthalene sulfonic acid (60 µg / mL). 5uL of each nanoparticle was added to each well. After 5 minutes of incubation under gentle shaking, fluorescence absorbance was measured using excitation wavelengths of 325 nm and emission wavelength of 435nm.

RNA interference. siRNAs were chemically modified at the 2' position to increase stability and negate immunostimulation. Seventy-two hours after injection, tissues were isolated and protein expression was determined via flow cytometry. GFP mean fluorescent intensity in PBS-treated mice was made 100%, and GFP expression in treated mice was normalized to that value.

In vivo Cas9 Editing. Mice constitutively expressing SpCas9 were injected with cLNP carrying 2 mg / kg of sgGFP. 5 days after injection, cells were isolated via FACS.

Data Analysis & Statistics. Sequencing results were processed using a custom R script to extract raw barcode counts for each tissue. These raw counts were then normalized with an R script prior for further analysis. Statistical analysis was done using GraphPad Prism 7; more specifically Paired 2-tail T-test or One-way ANOVAs were used where appropriate. Data is plotted as mean ± standard error mean unless otherwise stated.

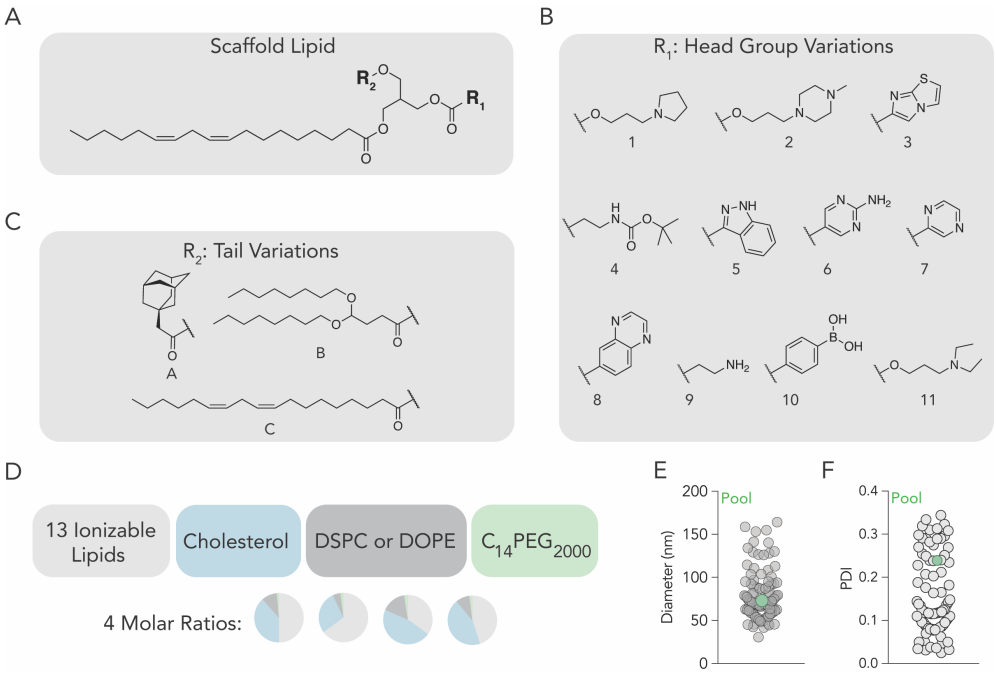

Figure 3.1. (A) Ionizable lipid scaffold to which **(B)** tail variants and **(C)** head group variants were added. **(D)** Using 4 molar rations, each of the 13 ionizable lipids were formulated with cholesterol, lipid-PEG, and either DSPC or DOPE, to create 104 distinct LNPs. **(E)** Hydrodynamic diameter and **(F)** polydispersity index of all formulated LNPs, measured individually.

A

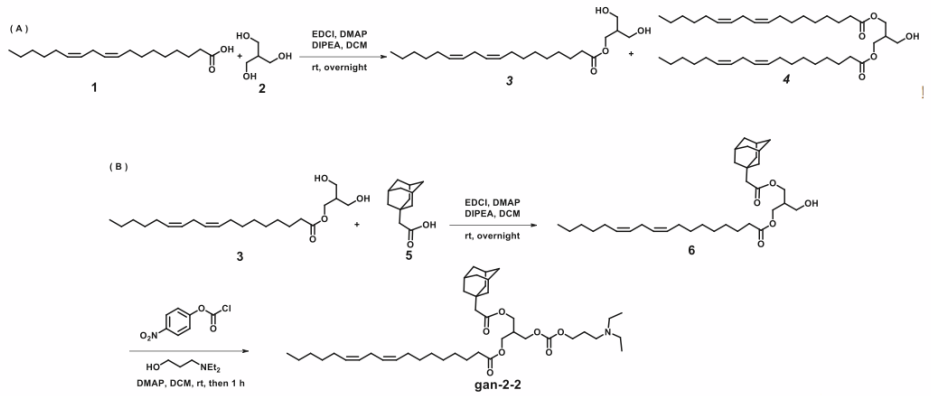

11A: To a solution of linoleic acid 1 (4.0 g, 14.2 mmol), 4-dimethylaminopyridine (DMAP) (0.4 g, 2.9 mmol), N, N-diisopropylethylamine (DIPEA) (3.7 mL, 20.5 mmol) and 2-(hydroxymethyl) propane-1,3-diol (1.5 g, 14.2 mmol) in anhyd. CH_2Cl_2 (40 mL) under nitrogen atmosphere was added N-(3-dimethylaminopropyl)-N'-ethylcarbodiimide hydrochloride (EDCI) (4.1 g, 20.5 mmol) at 25 °C. The reaction mixture was stirred at room temperature for overnight and linoleic acid 1 was consumed completely monitored by TLC, then the reaction mixture was directly concentrated under reduced pressure. Purification of the crude residue via silica gel flash column chromatography (gradient eluent: 1-30% of EtOAc/hexane) afforded compound 3 (2.3 g, 44% yield) and compound 4 (1.7 g, 30% yield) as colourless oil.
To a solution of compound 3 (150 mg, 0.41 mmol), DMAP (10 mg, 0. 1 mmol), DIPEA (0.1 mL, 0.6 mmol) and adamantane (79 mg, 0.41 mmol) in anhyd. CH_2Cl_2 (2 mL) under nitrogen atmosphere was added EDCI (114 mg, 0.6 mmol). The reaction mixture was stirred at room temperature for overnight. and compound 3 was consumed completely monitored by TLC, then the reaction mixture was directly concentrated under r educed pressure. Purification of the crude residue via silica gel flash column chromatography (gradient eluent: 0-20% of EtOAc/hexane) afforded compound 6 (103 mg, 53% yield) as colourless oil.
To a solution of compound 6 (76 mg, 0. 16 mmol) and DMAP (45 mg, 0. 37 mmol) in anhyd. CH_2Cl_2 (2 mL) under nitrogen atmosphere was added 4-nitrophenylchloroformate (65 mg, 0. 32 mmol). After stirring at room temperature for 1 hour, 3-diethylamino-1-propanol (0.44 mL, 0.96 mmol) was added into the reaction mixture and then stirred at room temperature for 1 hour. The reaction mixture was directly concentrated under reduced pressure. Purification of the crude residue via silica gel flash column chromatography (gradient eluent: 0-4% of MeOH /DCM) afforded compound 11A (32 mg, 29% yield) as colorless oil.

B

Lipid-1C: HRMS (ESI, m/z) calculated for $C_{48}H_{84}NO_7$ $[M + H]^+$: 786.6242, found 786.6227.

Lipid-2C: HRMS (ESI, m/z) calculated for $C_{49}H_{87}N_2O_7$ $[M + H]^+$: 815.6508, found 815.6494.

Lipid-3C: HRMS (ESI, m/z) calculated for $C_{46}H_{73}N_2O_6S$ $[M + H]^+$: 781.5187, found 781.5187.

Lipid-4C: HRMS (ESI, m/z) calculated for $C_{48}H_{84}NO_8$ $[M + H]^+$: 802.6191, found 802.6194.

Lipid-5C: HRMS (ESI, m/z) calculated for $C_{48}H_{75}N_2O_6$ $[M + H]^+$: 775.5620, found 775.5645.

Lipid-6C: HRMS (ESI, m/z) calculated for $C_{45}H_{74}N_3O_6$ $[M + H]^+$: 752.5572, found 752.5586.

Lipid-7C: HRMS (ESI, m/z) calculated for $C_{45}H_{73}N_2O_6$ $[M + H]^+$: 737.5463, found 737.5476.

Lipid-8C: HRMS (ESI, m/z) calculated for $C_{49}H_{75}N_2O_6$ $[M + H]^+$: 787.5620, found 787.5628.

Lipid-9C: HRMS (ESI, m/z) calculated for $C_{43}H_{76}NO_6$ $[M + H]^+$: 702.5667, found 702.5686.

Lipid-10C: HRMS (ESI, m/z) calculated for $C_{47}H_{76}BO_8$ $[M + H]^+$: 779.5628, found 779.5628.

Lipid-11C: HRMS (ESI, m/z) calculated for $C_{48}H_{86}NO_7$ $[M + H]^+$: 788.6399, found 788.6412.

Lipid-11B: HRMS (ESI, m/z) calculated for $C_{50}H_{94}NO_9$ $[M + H]^+$: 852.6923, found 852.6903.

Lipid-11A. HRMS (ESI, m/z) calculated for $C_{42}H_{72}NO_7$ $[M + H]^+$: 702.5303, found 702.5277.

^{1}H NMR (500 MHz, $CDCl_3$) δ 0.89 (t, J = 7.0 Hz, 3 H), 1.24-1.36 (m, 22 H), 1.57-1.62 (m, 10 H), 1.64 (s, 2 H), 1.69 (s, 2 H), 1.72 (s, 1 H), 1.97 (s, 2 H), 2.01-2.09 (m, 8 H), 2.31 (t, J = 7.5 Hz, 2 H), 2.43 (m, 1 H), 2.77 (t, J = 6.5, 2 H), 2.89 (m, 4 H), 4.15 (dd, J_1 = 6.0 Hz, J_2 = 13.5 Hz, 4 H), 4.21 (m, 4 H), 5.36 (m, 4 H); ^{13}C NMR (125 MHz, $CDCl_3$) δ 14.0, 14.2, 22.5, 24.8, 25.6, 27.2, 29.1, 29.3,29.6, 29.7, 31.5, 31.9, 32.8, 34.1, 36.6, 37.4, 42.4, 46.7, 48.7, 49.1, 61.0, 61.1, 61.3, 61.4, 64.2, 65.1, 65.3, 65.8, 127.9, 128.0, 130.0, 130.2, 154.7, 171.4, 173.5;

!

C

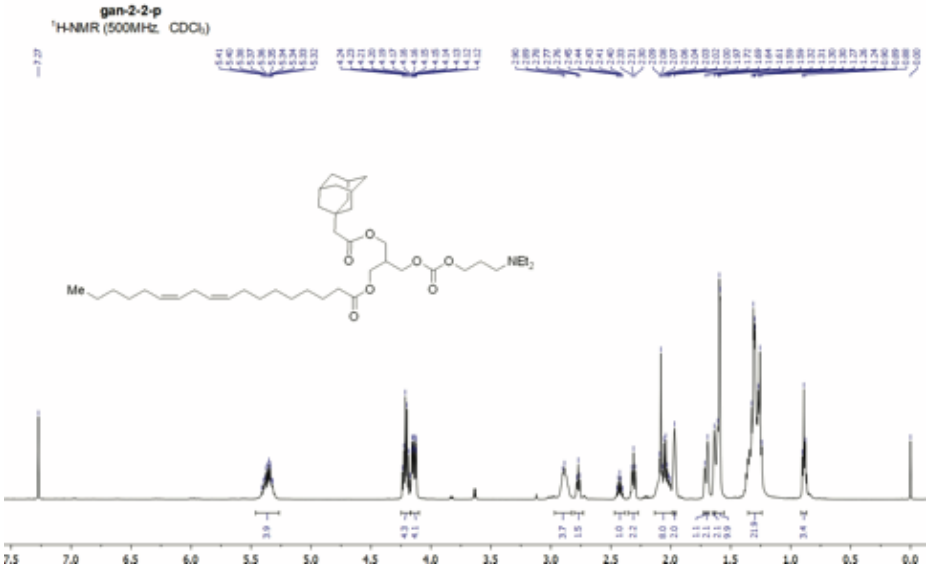

D

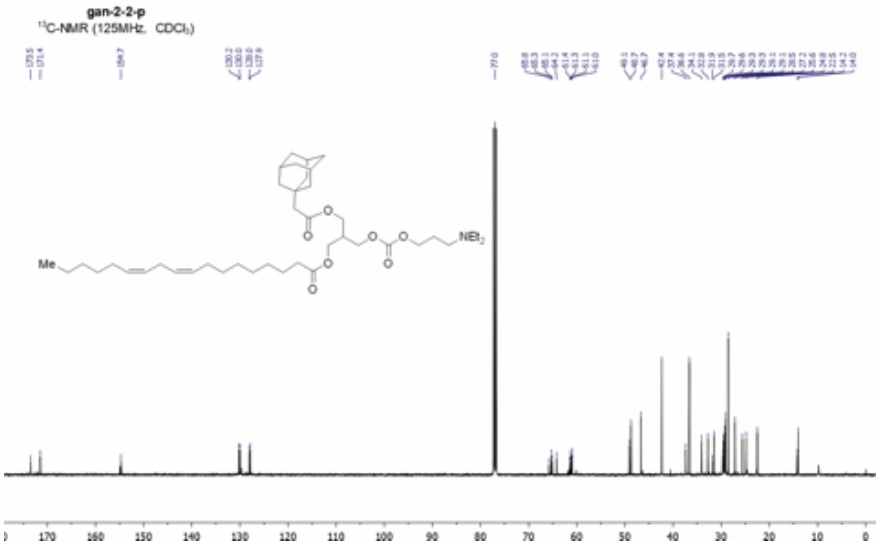

Fig. 3.2. (A) General synthesis for lipid 11A. **(B)** Mass and NMR data for key ionizable lipids. **(C)** 1H NMR spectra for Lipid 11A. **(D)** 13C NMR spectra for Lipid 11A.

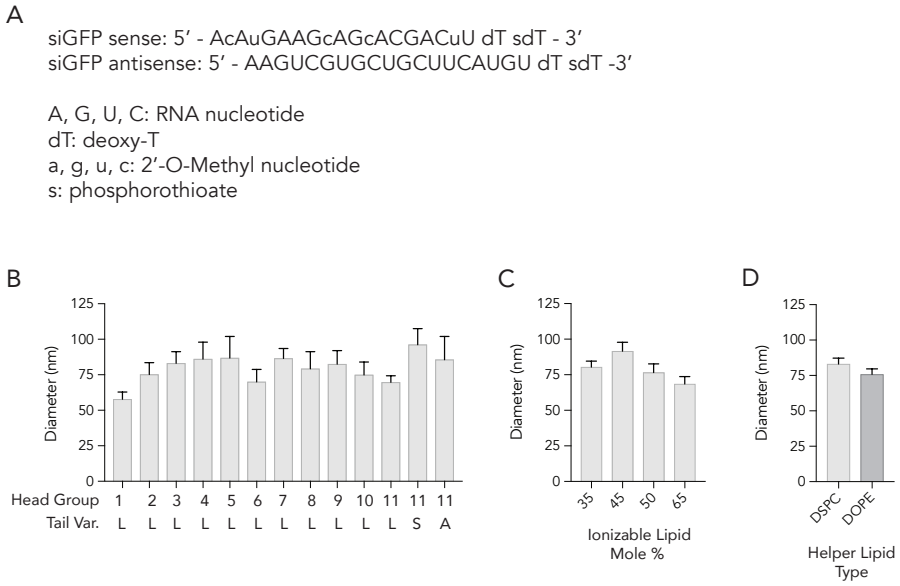

Fig. 3.3. (A) Sequence and chemical modifications of siGFP. Hydrodynamic diameter of LNPs plotted as a function of **(B)** ionizable lipid type, **(C)** molar percent of ionizable lipid, and **(D)** phospholipid type.

A

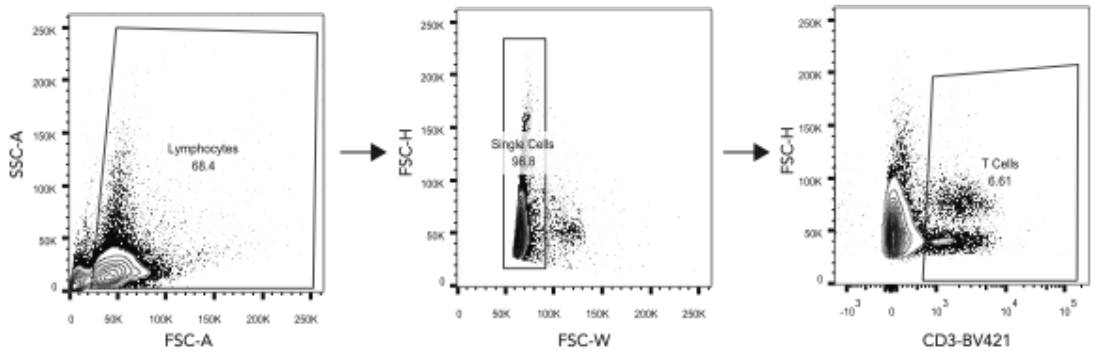

B

Cell Type	FACS Markers	Tissue
Endothelial cells	CD31+ CD45-	*L*, *M*, *v*
Immune Cells	CD31- CD45+ CD11b-	*L*, *M*, *v*
T Cells	CD3+ CD19-	*S*
B Cells	CD3- CD19+	*S*
Hepatocytes	CD31- CD45- CD68-	*v*
Kupffer Cells	CD31- CD45+ CD68+	*v*

Lung, ***M***arrow, ***S***pleen, Li***v***er

Figure 3.4. (A) Representative FACs plots showing gating strategy for splenic CD3+ T cells. (**B)** Cell-type specific markers.

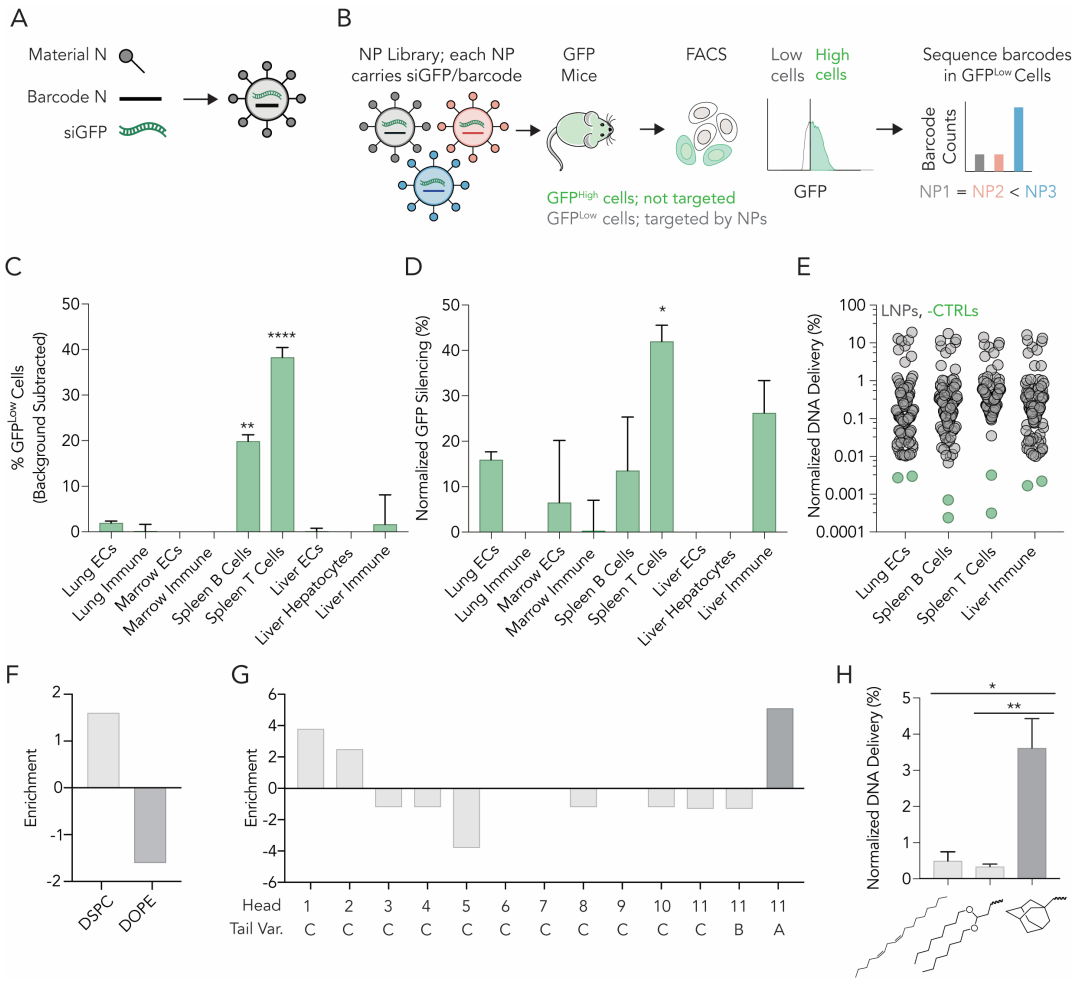

Figure 3.5. (A) Nanoparticles were formulated to carry a distinct DNA barcode and siGFP. **(B)** Of the 104 LNPs formulated, we pooled 100 stable LNPs together, and administered them to mice expressing GFP. After 3 days, we isolated GFPLow cells and sequenced the DNA barcodes within that population. **(C)** Percent GFPLow cells in 9 cell types. Two-way ANOVA, **P<0.01, ****P<0.0001. **(D)** Normalized decrease in GFP MFI in 9 cell types. Two-way ANOVA, *P<0.05. **(E)** Normalized DNA delivery in lung endothelial cells, splenic B and T cells, as well as liver immune cells. **(F)** Enrichment of DSPC-containing LNPs in splenic T cells. **(G)** Enrichment for each of the 13 ionizable lipids. **(H)** Normalized DNA delivery of LNPs formulated with head group 11 and tail L, S, or A. One-way ANOVA, *P<0.05, **P<0.01.

A

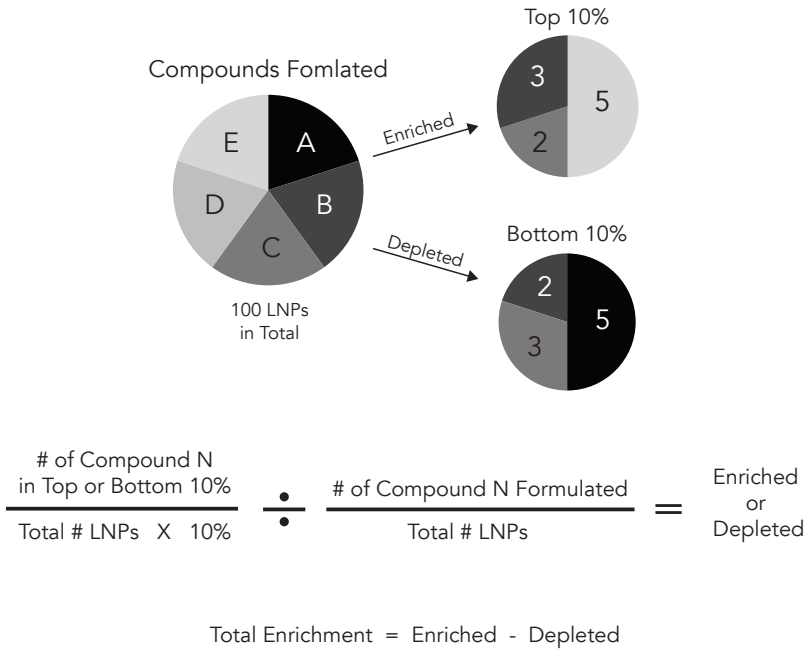

Figure 3.6. (A) An example showing how enrichment is calculated.

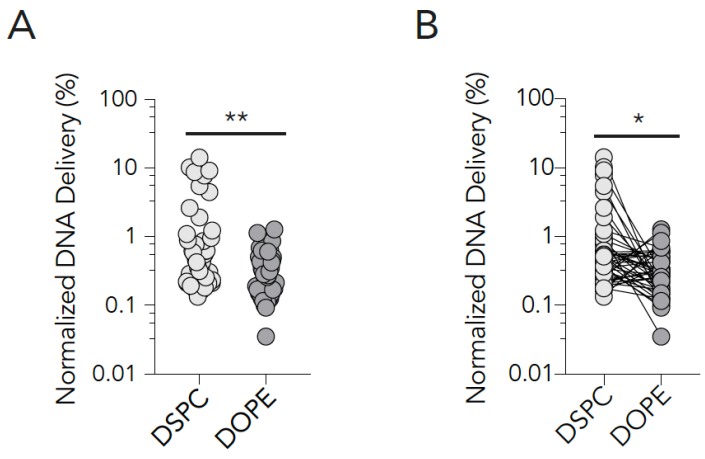

Figure 3.7. (A) Normalized DNA delivery of LNPs plotted as a function of phospholipid. 2-way T test, **P<0.01. **(B)** Paired analysis of normalized DNA delivery of LNPs containing DSPC or DOPE. Paired 2-way T test, *P<0.05.

A

Lipomer	Molecular Weight of Head Group	LogP of Head Group	Total Polar Surface Area of Head Group	Enrichment in T Cells
Gan-1-105	158	0.62	29.5	-1.3
Gan-1-106	156	0.26	29.5	3.9
Gan-1-107	185	-0.3	32.8	2.6
Gan-1-33	158	0.62	29.5	-1.3
Gan-2-10	72	-1.36	43	0
Gan-2-13	149	0.95	57.5	-1.3
Gan-2-2	158	0.62	29.5	5.2
Gan-2-3	151	0.31	32.7	-1.3
Gan-2-5	202	0.44	64.6	-1.3
Gan-2-6	145	0.81	41.4	-3.9
Gan-2-7	122	0.45	67.8	0
Gan-2-8	107	-0.47	41.4	0
Gan-2-9	157	0.95	41.8	-1.3

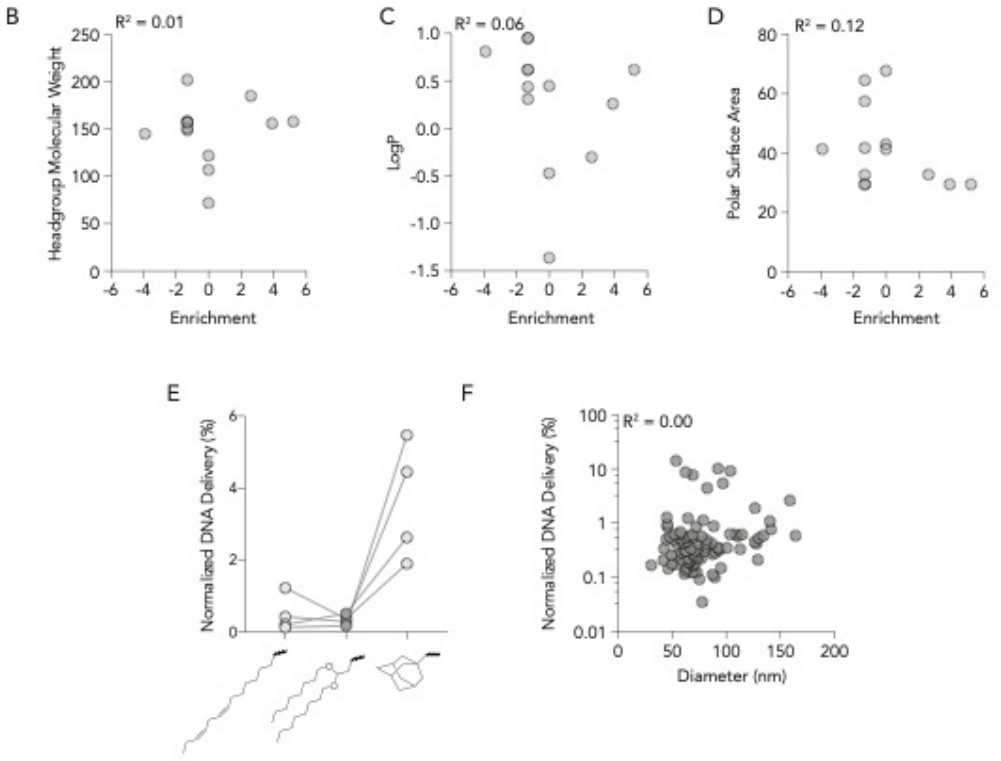

Figure 3.8. (A) Physical and chemical analysis of headgroups. **(B)** Correlation of headgroup molecular weight and enrichment. **(C)** Correlation of headgroup LogP and enrichment. **(D)** Correlation of headgroup polar surface area and enrichment. **(E)** Normalized delivery of LNPs formulated with different ionizable lipids sharing headgroup 11, but with different tail structures. (**F)** Correlation of LNP diameter and normalized DNA delivery.

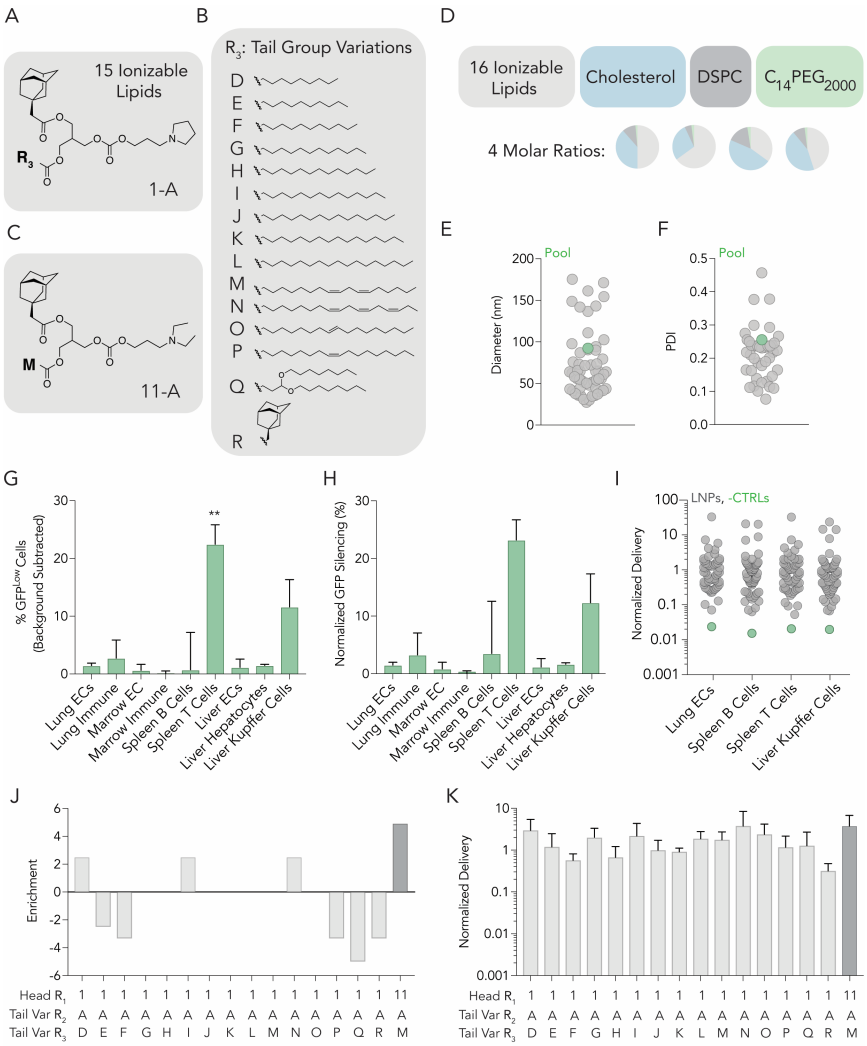

Figure 3.9. (A) 15 cLNPs can be formed with the top performing head group and **(B)** 15 tail variations. **(C)** The top performing constrained lipid from screen 1 was included. **(D)** Using 4 molar rations, each of the 16 ionizable lipids were formulated with cholesterol, lipid-PEG, and DSPC to create 64 distinct LNPs. **(E)** Hydrodynamic diameter and **(F)** polydispersity index of all formulated LNPs, measured individually. **(G)** Percent GFPLow cells in 9 cell types. Two-way ANOVA, *P<0.05. **(I)** Normalized decrease in GFP MFI in 9 cell types. **(J)** Normalized DNA delivery in lung endothelial cells, splenic B and T cells, as well as liver Kupffer cells. (J) Enrichment for each of the 16 ionizable lipids. **(K)** Normalized DNA delivery of each LNP formulated.

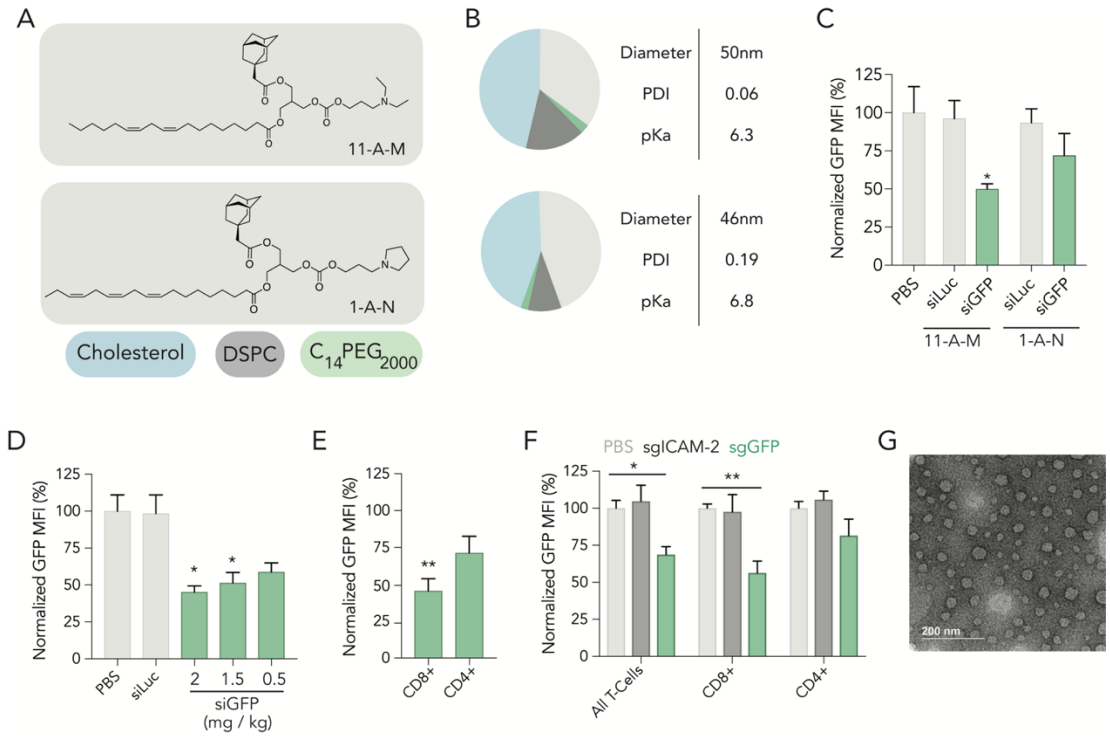

Figure 3.10. (A) Structure of ionizable lipid 11-A-M, top performing cLNP from screen 1 and structure of ionizable lipid 1-A-N, top performing cLNP from screen 2. **(B)** Molar composition and characteristics of 11-A-M and 1-A-N. **(C)** Normalized GFP expression in splenic CD3+ T cells 72 hours after treatment of 2 cLNP carrying siLuc at a dose of 1.5 mg / kg or siGFP at doses of 1.5 mg / kg. **(D)** Normalized GFP MFI in splenic CD3+ T cells 72 hours after treatment of cLNP carrying either siLuc or siGFP at various doses. One-way ANOVA, *P<0.05. **(E)** Normalized GFP MFI in splenic CD8+ and CD4+ T cells 72 hours after treatment of cLNP carrying siGFP at a dose of 2.0 mg / kg. unpaired 2-tail t-test, **P<0.01. **(F)** Normalized GFP MFI in splenic CD3+ T cells as well as CD8+ and CD4+ T cells after treatment of cLNPs carrying sgRNA at a dose of 2.0 mg / kg. Two-way ANOVA, *P<0.05, **P<0.01. **(G)** Transmission electron microscopy image of 11-A-M formulated to carry siGFP.

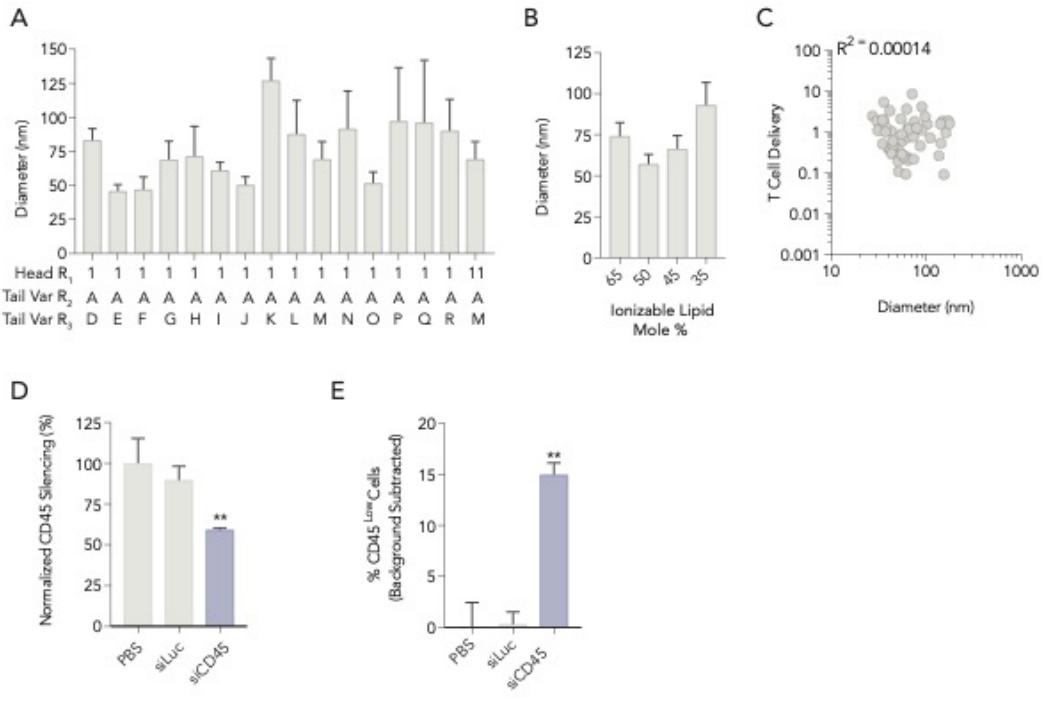

Figure 3.11. (A) Hydrodynamic diameter of LNPs plotted as a function of ionizable lipid type, and **(B)** molar percent of ionizable lipid. **(C)** Normalized delivery of in T Cells plotted against delivery show no correlations between size and delivery.

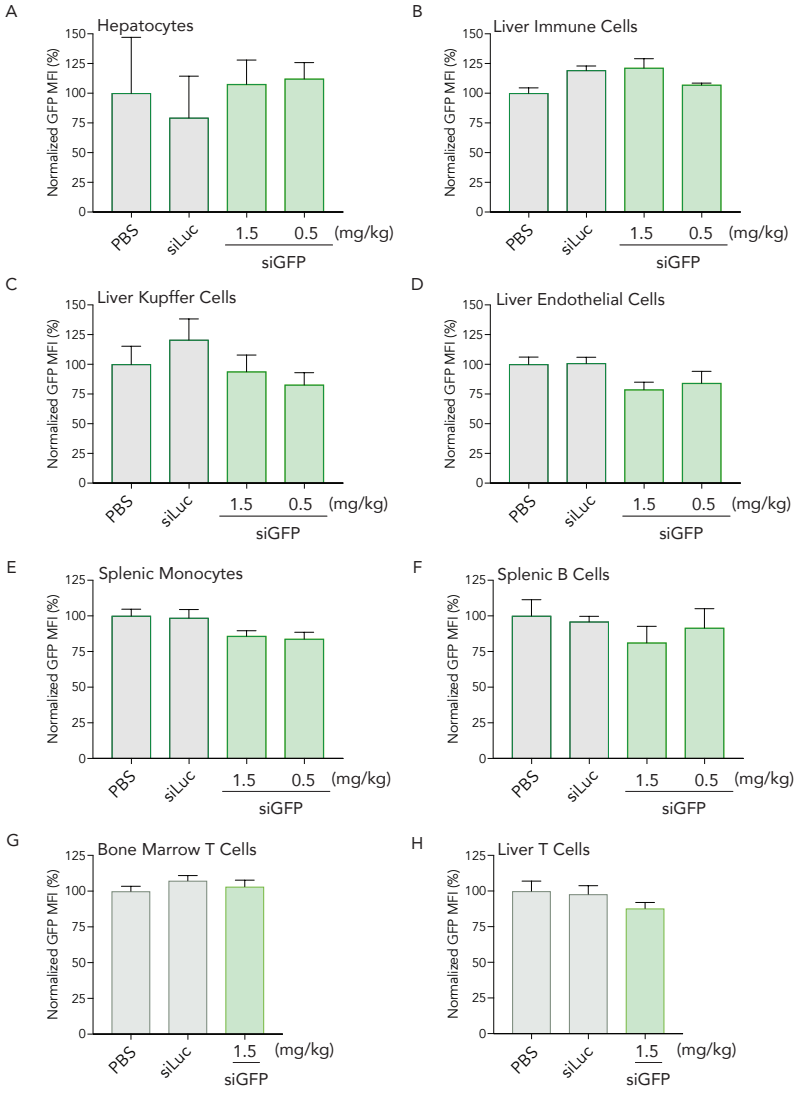

I

Marrow T Cells	7.1%
Liver T Cells	6.9%

Figure 3.12. Normalized GFP MFI of mice treated with either PBS, cLNP carrying 1.5 mg / kg siLuc, or cLNP carrying siGFP at a dose of 0.5 or 1.5 mg / kg in **(A)** hepatocytes, **(B)** liver immune cells, **(C)** liver kupffer cells, **(D)** liver endothelial cells, **(E)** splenic monocytes, **(F)** splenic B cells and **(G)** bone marrow T cells, and **(H)** liver T cells. **(I)** Percent of T cells found in the bone marrow and liver.

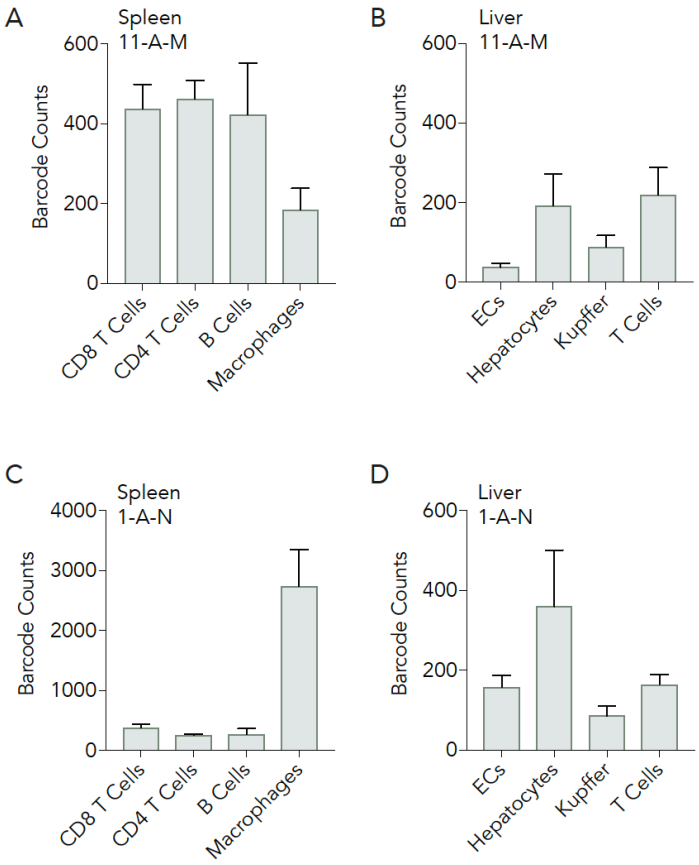

Figure 3.13. (A) Biodistribution of 11-A-M across 4 different cells types in the spleen and B) liver using ddPCR barcodes. C) Biodistribution of 1-A-N across 4 different cells types in the spleen and D) liver using ddPCR barcodes.

sg-EGFP: 5′ - gsgsgsCGAsGsGfsAfsGfsCfUGfUfUCAfCfCGgUUUUA
GagcuagaaauagcaaGUUaAaAuAaggcuaGUccGUUAu
cAAcsususgsasasasasasgugGscascscsgsasgsuscgsg susgscsusususususu - 3′

A, G, U, C: RNA nucleotide
Nf: 2′-Fluoro nucleotide
a, g, u, c: 2′-O-Methyl nucleotide s: phosphorothioate

Figure 3.14. (A) Sequence and chemical modification for sgGFP.

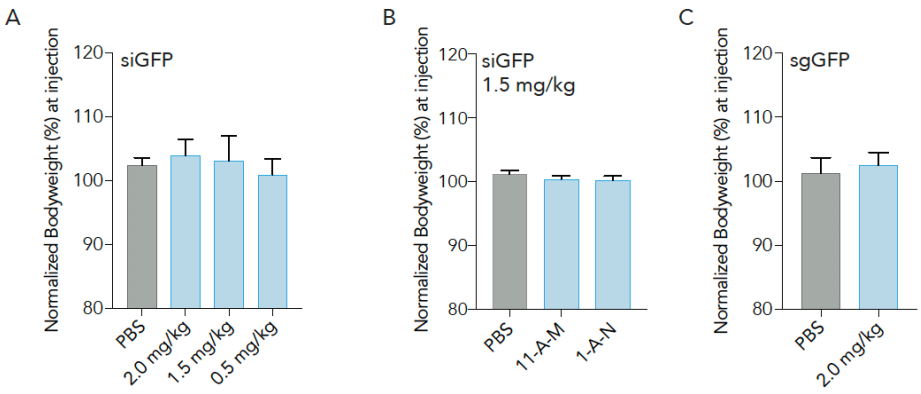

Figure 3.15 (A) Mouse weights 24hrs after administration of PBS or cLNP at various doses of siRNA. **(B)** Mouse weights 24hrs after administration of PBS or cLNP carrying siGFP. **(C)** Mouse weights 24hrs after administration of PBS or cLNP carrying sgGFP.

CHAPTER 4. MILD INNATE IMMUNE ACTIVATION OVERRIDES EFFICIENT NANOPARTICLE-MEDIATED RNA DELIVERY

The work presented here is an excerpt from Lokugamage MP, Gan Z, Zurla, C, Levin J, Islam FZ, Kalathoor S, Sato M, Sago CD, Santangelo PJ, Dahlman JE, "Mild innate immune activation overrides efficient nanoparticle-mediated RNA delivery." *Advanced Materials*, 2019.

4.1 Introduction

Nanoparticles interact with biomolecules that alter nanoparticle efficacy and safety[137]. Insights into biological pathways that affect how nanoparticles (i) interact with the surface of target cells and (ii) are endocytosed are valuable. In an example of (i), the ApoE-mediated mechanism by which LNPs can be delivered to hepatocytes helped lead to a FDA approved siRNA drug[60]. Interactions between LNPs and serum ApoE was necessary for LNPs to bind hepatocytes, and LDLR, a cell surface receptor for ApoE, increased nanoparticle uptake[36]. Reports have also shown that the nanoparticle corona affects delivery[76] by changing how nanoparticles interact with on- and off-target cells. In representative examples of (ii), authors used small molecules, RNAi, CRISPR, and knockout mice to reveal how nanoparticle uptake changes after endocytic genes are inhibited[70,133]. These studies and others[138] identified that clathrin, caveolin, and another now-canonical pathways impact nanoparticle uptake.

We reasoned that another step in the drug delivery process seemed understudied. Specifically, we hypothesized that (iii) inflammation could alter the efficacy of a mRNA drug after the nanoparticle reaches the target cell by changing how the drug was translated. We tested this hypothesis by focusing on the gene toll-like receptor 4 (TLR4). We chose TLR4 for two reasons. First, understanding how TLR4 alters drug delivery is relevant to near-future mRNA therapies. LNP-mediated mRNA delivery[139] is proposed for myocardial infarction[140], colitis[141], and Fabry disease[142], as well as vaccines targeting influenza[16], Zika[143], and others[144]. TLR4 signaling plays a

role in these diseases[145]. In addition, adjuvants have been used in concert with mRNA vaccines, in order to improve their immunogenicity[146]; many adjuvants activate TLRs[147]. For example, authors found that delivering a TLR4 agonist in concert with mRNA encoding a vaccine did not improve vaccine efficacy in non-human primates, relative to the mRNA only[148]; we hypothesized this result could be explained by TLR4-driven reduction in mRNA delivery. The second reason we focused on TLR4 is its critical role dictating how pathogens are endocytosed and processed. This has been reviewed[149]; here we highlight three examples. In one example, scientists found cells exposed to lipopolysaccharide (LPS), which is an agonist for TLR4, led to TLR4 colocalization on endosomes. Imaging and biochemical assays led the authors to conclude that inflammation and endosomal trafficking were linked via TLR4. In another example, by labeling TLR4, authors found it was present at the plasma membrane as well as intracellular vesicles that contained the endosome marker Rab5; the authors concluded TLR4 played a central role in endocytosis[150]. In a third example, scientists found that pathogens evolved to evade recognition by the human immune system by preventing TLR4 recognition[151]. This suggested reducing TLR4 activation could improve the survival of a foreign material in a human system.

To test the hypothesis that TLR4 activation could override LNP-mediated mRNA delivery, we quantified functional mRNA delivery (more specifically, gene editing mediated by a protein encoded by mRNA) in hepatocytes, liver endothelial cells, and Kupffer cells in the presence of LPS, which activated TLR4. TLR4 is expressed on hepatocytes, Kupffer cells and dendritic cells[152]. In our follow-up mechanistic studies, we focused on Kupffer cells, which we selected for two reasons. First, upon TLR4 activation, macrophage gene expression changes[153]. For example, TLR4 activation induces phosphorylation of PKR[154], which reduces mRNA translation[155]. We therefore reasoned TLR4 could reduce mRNA translation, even after mRNA was delivered into the cytoplasm. Second, Kupffer cells play a central role in nanoparticle clearance by removing nanoparticles from circulation[156].

4.2 Results

4.2.1 LPS impacts cKK-E12-mediated delivery of mRNA

Initially, we performed experiments with LNPs formulated with the peptide-lipid cKK-E12. cKK-E12 LNPs have delivered RNA[28,157] to hepatocytes at clinical doses in mice and non-human primates[28]; they are being considered for clinical development. After synthesizing cKK-E12[28], it was mixed with a PEG-lipid, cholesterol, and DOPE (**Fig. 4.1A**) with chemically modified mRNA encoding GFP in a microfluidic device[30], in order to formulate LNPs. The LNPs were small, had a low polydispersity, and a pKa of 6.2 (**Fig. 4.1B**). We investigated whether GFP mRNA delivery changed when cells were exposed to LPS. First, we added LPS or PBS to murine macrophages (RAWS) in a 24 well plate. Six hours later, we added LNPs carrying GFP mRNA at a dose of 1 μg. Twelve hours later, we quantified GFP MFI using flow cytometry. Compared to cells pre-treated with PBS, LPS pre-treated cells exhibited a robust reduction in MFI. Notably, 1 ng of LPS was sufficient to reduce GFP expression by over 75% (**Fig. 4.1C**). We reasoned reduced GFP MFI could be driven by overt cell death. We therefore determined the percent of live / dead cells in our flow cytometry analyses by assessing the size and granularity of the cell populations. We observed no significant decrease in populations after exposure to LPS, suggesting the effect was not caused by overt cell death (**Fig. 4.2A**).

We analyzed the effect of LPS on mRNA delivery in vivo. We formulated cKK-E12 LNPs to carry Cre mRNA, and intravenously injected them into Ai14 mice at the clinical[60] dose of 0.3 mg / kg mRNA. Ai14 mice have a Lox-Stop-Lox-tdTomato construct driven by a CAG promoter. If Cre mRNA is delivered into the cytoplasm and translated into functional Cre protein, the stop site is edited out of the genome, leading to tdTomato+ cells (**Fig. 4.1D**). The percentage of tdTomato+ cells is a validated way to quantify mRNA delivery in vivo[158-160]. Six hours before injecting LNPs, we administered 0.1 mg / kg LPS via an intraperitoneal injection; this dose is considered low[161]. Three days after injecting the LNPs, we quantified the percentage of Kupffer cells (CD68+CD45+CD31-), liver endothelial cells (CD45-CD31+) and hepatocytes (CD31-CD45-

) that were tdTomato+ using flow cytometry. Compared to mice that were not treated with LPS, the percentage of tdTomato+ cells isolated from mice treated with LPS decreased to nearly 0% (**Fig. 4.1E**). We reasoned the effects could be driven by overt cell death. However, four lines of evidence suggested otherwise. First, a 0.1 mg / kg LPS dose is considered low[161]. Second, control- and LPS-treated mice experienced no significant weight loss during the experiment (**Fig. 4.3A**). Third, the data we plotted were the percentage of live hepatocyte, endothelial, or Kupffer cells that were also tdTomato+. Fourth, the size and granularity in cell populations cells isolated from the liver remained unchanged in LPS and control mice (**Fig. 4.3B**).

To ensure the data were not specific to one LNP, we repeated the in vivo experiment using a second clinically relevant LNP named MC3. MC3 has delivered RNA in mice, non-human primates, and led to an FDA-approved siRNA drug[60]. The MC3 results recapitulated the cKK-E12 experiments. Specifically, (i) the percentage of tdTomato+ hepatocytes, endothelial cells, and Kupffer cells decreased in mice treated with LPS compared to mice treated with PBS (**Fig. 4.3C**), and (ii) we did not observe any signs of cell death isolated from mice (**Fig. 4.3D,E**).

4.2.2 In vivo barcoding identifies an LNP that preferentially delivers mRNA to Kupffer cells in vivo.

We then investigated whether a novel LNP selected for Kupffer cell targeting could overcome the LPS-mediated reduction in mRNA delivery. To identify a novel LNP that preferentially delivers RNA to Kupffer cells (instead of hepatocytes) at a clinical dose, we performed a high throughput functional in vivo DNA barcoding screen (**Fig. 4.4A,B**). Briefly, we formulated LNP-1, with chemical structure 1, to carry Cre mRNA and DNA barcode 1, and LNP-96, with chemical structure 96, carried Cre mRNA and DNA barcode 96. The formulation details for all 96 LNPs are detailed (**Fig. 4.4C**). We evaluated the diameter and polydispersity index of each individual LNP, and pooled together LNPs that were stable, monodisperse, and had a diameter less than 200 nm[33]. Of the 96 LNPs, 82 met these quality control criteria (**Fig. 4.5A**). These 82 LNPs were injected a total mRNA dose of 1.0 mg / kg (0.012 mg / kg / particle, on average). Three

days after administering the LNPs to Ai14 mice, we isolated twelve tdTomato+ cell types in order to evaluate the on-target delivery (Kupffer cells) as well as off-target delivery (eleven cell types, **Fig. 4.5B, Fig. 4.4D**). We sequenced the tdTomato+ cells, thereby identifying barcodes colocalized with cells that were functionally transfected by Cre mRNA. We did not observe changes in mouse weight (**Fig. 4.4E**). We then analyzed previously described[76,160] controls. We characterized the size and polydispersity of the 82 pooled LNPs, and found the pool was similar to the LNPs making up the pool (**Fig. 4.5C,D**). Second, we included a 'naked' DNA barcode as a negative control. Since DNA does not readily enter cells on its own, this DNA barcode was delivered into cells less efficiently than barcodes delivered by LNPs (**Fig. 4.5E**). Third, we found the nanoparticle sequencing data was consistent across mouse replicates (**Fig. 4.4F**).

These controls led us to believe that it was appropriate to analyze the in vivo screening results. We quantified the percentage of live cells that were tdTomato+, using 12 cell types. We found that the LNP pool preferentially delivered Cre mRNA to Kupffer cells (~80% tdTomato+), followed by liver endothelial cells (~30% tdTomato+) and hepatocytes (~15% tdTomato+). We then sequenced all 82 barcodes and evaluated whether LNP size or chemical composition affected in vivo delivery. LNP delivery varied with the chemical composition more than the physical structure of the LNP. Specifically, LNPs formulated with epoxide-terminated fully saturated lipid tails consisting of 15 carbons were enriched in tdTomato+ cells, relative to LNPs made with other lipid tails (**Fig. 4.5F**). Enrichment analysis is detailed (**Fig. 4.4G**). LNP diameter did not affect delivery within the tested range of 20 – 200 nm (**Fig. 4.4H-J**), nor did lipid molar ratios (**Fig. 4.4K**).

An important control for any high throughput screen is whether individual compounds perform as predicted. We quantified Cre mRNA delivery mediated by the best LNP from the screen, which we named LNP3 for simplicity (**Fig. 4.5G,H**). Three days after mice were systemically injected with 0.3, 0.1, or 0.03 mg / kg Cre mRNA formulated into LNP3, we observed mRNA delivery quantified by tdTomato+ cell percentage. LNP3 recapitulated the screening results: As the screen predicted, Kupffer cells were preferentially targeted, followed by liver endothelial cells and

hepatocytes (**Fig. 4.5I**). We did not observe delivery after a 0.03 mg / kg dose. Having identified a novel LNP that preferentially targeted Kupffer cells, we tested our hypothesis that LNP3 would overcome the LPS-dependent reduction in mRNA delivery. The data did not support this hypothesis; pre-treating mice with 0.1 mg / kg LPS reduced mRNA delivery in all 3 cell types (**Fig. 4.5J**). To confirm the effect was consistent across LPS batches, we purchased two additional batches from the same company and tested them. Mice were pretreated with LPS six hours prior to LNP administration; three days later, we quantified by tdTomato+ cell percentage. There was a statistically significant reduction of mRNA delivery in all cell types in the liver (**Fig. 4.4L**).

4.2.3 LPS-mediated innate immune activation did not significantly decrease LNP uptake.

Having observed that mRNA delivery mediated by cKK-E12, MC3, and LNP3 was reduced by mild doses of LPS, we studied the biological mechanism, in vitro and in vivo. In order to deliver a mRNA drug that is translated inside the cell, an LNP must (i) reach the target cell and (ii) help the mRNA enter the cytoplasm. Then, the mRNA must be (iii) translated into protein (**Fig. 4.6A**). Based on our data, we first hypothesized that (i) LPS reduced LNP uptake. We analyzed the biodistribution of LNP3 with QUANT, a sensitive system utilizing ddPCR to quantify LNP biodistribution[133]. We formulated LNP3 to carry a DNA barcode and injected mice at a dose of 0.3 mg / kg DNA. Six hours before injecting LNPs, we administered 0.1 mg / kg LPS; control mice were pre-treated with PBS. Twenty-four hours after injecting the LNPs, we isolated Kupffer cells, liver endothelial cells, and hepatocytes using FACS. When compared to mice pre-treated with PBS, we observed increased Kupffer cell uptake in mice pre-treated with LPS. We did not see significant changes in the other two cells types (**Fig. 4.6B**). These data did not support the hypothesis that LPS reduced LNP uptake.

4.2.4 LPS-mediated innate immune activation did not significantly decrease endosomal escape.

We then tested whether (ii) LPS reduced endosome escape. We formulated LNP3 with a fluorescently tagged and chemically modified mRNA encoding Cre. We administered these LNPs to RAWS in a 24 well plate at a dose of 1 μg mRNA / well; six hours beforehand, we treated RAWS with 500 ng of LPS (or did not). Three, six or twenty-four hours after administering the LNPs, we fixed cells for imaging. Cells were stained for the endosomal markers CD63, EEA1, and Rab11, which co-localize with late, early, and recycled endosomes, respectively (**Fig. 4.6C,D, Fig. 4.7A**). We quantified the percentage of mRNA trapped in endosomal compartments using Mander's overlap coefficient in >30 cells per condition as we previously described[162] (**Fig. 4.6E-G**). At three and twenty-four hours, the Mander's overlap coefficient was similar in PBS- and LPS-treated cells. At six hours, the Mander's overlap coefficient was statistically lower in LPS-treated cells, but the difference was not sufficient to explain the complete reduction in protein production. Based on these data, we concluded that LPS-mediated decrease in protein expression was not driven predominantly by reduced endosomal escape.

4.2.5 mRNA translation is altered by LPS through TLR4-mediated PKR activation

We reasoned that LPS caused a difference in cell signaling that affected (iii) mRNA translation after the LNP reached the target cell; we therefore studied the cell signaling that drove this effect. We treated RAW cells with 100 ng of LPS six hours before administering LNPs carrying fluorescently tagged mRNA. Cell were fixed for imaging at one and three hours after LNPs were administered and stained for TLR4 as well as the endosomal markers CD63, EEA1, and Rab11. We observed vesicular localization of TLR4, and colocalization of TLR4 and LNP delivered mRNA. (**Fig. 4.8A**). We reasoned that TLR4 inhibition could rescue mRNA delivery. We pre-treated RAWS in a 24 well plate with 100 nM of TAK-242, a TLR4 inhibitor. One hour later, we administered 100 ng of LPS to cells; six hours later, we delivered 1 μg GFP mRNA using LNP3. Twenty-four hours after GFP mRNA was delivered, we quantified GFP MFI, and found that

delivery was rescued with TAK-242 (**Fig. 4.9A**). TLR4 can activate the downstream effector PKR, which can reduce protein translation[154]. We therefore treated cells with varying doses of C16 (**Fig. 4.9B**), 2AP (**Fig. 4.9C**), and ISRIB (**Fig. 4.9D**), three PKR inhibitors. C16 and 2AP PKR inhibitors improved GFP delivery, while the results from ISRIB were inconclusive. Finally, we evaluated whether it was possible to overcome TLR4-mediated inhibition of mRNA delivery by increasing the LNP dose. We injected LPS pre-treated mice with 0.3 or 2.0 mg / kg Cre mRNA. Increasing the dose led to a non-significant increase in tdTomato+ cells (**Fig. 4.9E**). These data led us to conclude that TLR4 was an especially potent inhibitor of mRNA delivery (**Fig. 4.9F**).

We then evaluated whether other inflammatory signaling affected delivery in a similarly potent way. We treated RAWS in a 24 well plate with 0.1, 1, or 5 μg of CpG or poly(I:C). CpG and poly(I:C) activate TLR3 and TLR9, respectively. Six hours later, we delivered 1 μg GFP mRNA using LNP3. Twenty-four hours later, we quantified GFP MFI. CpG and poly(I:C) activation reduced mRNA delivery, but neither reduced delivery as potently as 1 ng of LPS (**Fig. 4.9G,H**). Finally, to evaluate whether low-grade chronic inflammation reduced mRNA delivery, we injected mice subcutaneously with B16-F10 murine melanoma cells; this model is often used to evaluate immunotherapies[163]. Ten days later, we intravenously injected LNP3 carrying Cre mRNA at a dose of 0.3 mg / kg; as a control, we injected LNP3 into mice without tumors. Three days later, we digested the liver and quantified the percentage of tdTomato+ Kupffer cells, liver endothelial cells, and hepatocytes. When compared to mice that did not have tumors, there was no significant decrease in percentage of tdTomato+ cells (**Fig. 4.9I**). These data suggest that tumor-driven inflammation was not sufficient to reduce delivery to other organs in vivo. These data led us to conclude that although yet-to-be discovered inflammation pathways may also reduce mRNA delivery, TLR4 signaling is particularly potent. At the same time, TLR4 is expressed on the cell membrane while TLR3 and TLR9 are primarily expressed intracellularly; thus, we cannot exclude the possibility that the relative potency of TLR4 signaling was driven by the physical availability of the receptor.

4.3 Discussion

The summation of these data led us to conclude that mild doses of the TLR4 agonist LPS reduce mRNA delivery in vitro and in vivo. Notably, reduced delivery was not caused by reduced cell uptake. Instead, the data suggest that the mechanism could be driven - in part - by TLR4-mediated reductions in endosomal escape and was likely driven by a TLR4-mediated reduction in mRNA translation. Independent of the relative importance of endosomal escape and mRNA translation, the data support the hypothesis that TLR4 activation can block effective mRNA delivery after the LNP reaches the target cell. We believe these results have important implications for mRNA drugs delivered by LNPs. Specifically, they suggest that if an LNP delivers therapeutic mRNA to a given cell type in one disease state, it is not guaranteed to deliver mRNA to the same cell type in another disease. Thus, the on- and off-target delivery profiles of a given LNP could vary with disease state, not just with the LNP. These data demonstrate the need to understand how cell state impacts the safety and efficacy of a given nanoparticle. Historically, cell state has been difficult to study; however, recent advances in single cell RNA-sequencing[87] make near-future experiments relating cell state to delivery feasible. We believe our data provide an impetus for these studies. We also found that a lead compound, LNP3, identified by a high throughput in vivo DNA barcoding screen performed as the screen predicted. Specifically, we generated and analyzed nearly 4,000 in vivo data points. We analyzed these in vivo data points to study the relationship between LNP chemical structure and in vivo delivery. Interesting, LNP3 efficiently delivered mRNA in vivo at clinically relevant doses. This LNP was small, uniform, and potent, and unlike most previously reported LNPs, did not preferentially target hepatocytes in vivo. If these results are recapitulated by others, we believe this will be important for the nanomedicine field, given that historically, in vivo nanoparticle behavior has been difficult to predict using in vitro assays[33].

It is important to acknowledge the limitations of this work. First, our studies were limited to mice. It is possible that the results are not replicated in non-human primates. Second, it is likely that other genes could work in concert with TLR4 to mediate this effect. There are several proteins

involved in LPS-mediated signaling; we hope to detail the genetic networks driving this phenotype in future work using technologies such as RNA-seq to understand global gene expression. Third, our studies were limited to lipid-based nanoparticles. It is possible the results are not recapitulated in other mRNA carriers. Fourth, the high throughput in vivo barcoding system will not work for all nanoparticles; it is critical to include the controls described herein when performing the barcoding studies. Despite these limitations, we believe these data provide compelling evidence that inflammatory signaling can alter LNP delivery, and that high throughput in vivo barcoding can identify nanoparticles that deliver drugs in vivo.

4.4 Materials and Methods

Preparation of LNP3. TLC was performed on precoated silica Gel GF plates and visualized using KMnO4 stains. Column chromatography was performed using silica gel (300-400 mesh) eluting with DCM/MeOH. 1H-NMR spectra were recorded at 400 MHz or 500 MHz (Varian) using CDCl3 with TMS or residual solvent as standard. High-resolution mass spectra (HRMS) were recorded on LC/MS (Agilent Technologies 1260 Infinity II/6120 Quadrupole) or a time-of-flight mass spectrometer by ESI or matrix assisted laser desorption/ionization (MALDI). All other chemicals were obtained from commercial sources and were used as received.

The compound 1 and LNP3 were prepared by reported procedure. Compound 1 (20 g, 41.9 mmol) was charged in a 100 ml flask and trifluoroacetic acid (42 mL) was added slowly at 0 ºC and then stirred at room temperature for 30 min. The solvent was evaporated under reduced pressure and then the crude product dissolved in DMF (5 mL) was added dropwise to pyridine (300 mL) at 0 ºC. The reaction mixture was stirred at room temperature overnight. The solvents were evaporated under reduced pressure to afford a white solid and washed with ethyl acetate to give pure compound 2 (8.4 g, 13.04 mmol, 31% yield).

To a solution of compound 2 in acetic acid/CH2Cl2 (150/150 mL) was added Pd/C (10 wt. %, 3.0 g). The black suspension was degassed for 5 min with hydrogen and stirred at room temperature under hydrogen atmosphere overnight. The reaction mixture was filtered by celite and washed with MeOH. The combined filtrates were concentrated to obtain a crude yellow viscous oil. The oil was solidified by adding ethyl acetate and washed with ethyl acetate to yield compound 3 (4.8 g, 12.76 mmol, 98% yield). 1H NMR (400 MHz, D2O) δ 1.42-1.57 (m, 4H, CH2), 1.70-1.77 (m, 4H, CH2), 1.87-1.92 (m, 4H, CH2), 3.03 (t, J = 7.6 Hz, 4H, NCH2), 4.14 (t, J = 5.2 Hz, 2H, COCH); 13C NMR (100 MHz, D2O) δ 21.0, 26.3, , 32.8, 39.0, 54.1, 170.1; HRMS (ESI, m/z) calcd for C12H25N4O2 [M + H]+: 257.1972, found 257.1968.

To a solution of compound 3 (84 mg, 0.22 mmol) and tridecyloxirane (302 mg, 1.34 mmol) in EtOH (2 mL) was added triethylamine (0.12 mL, 0.88 mmol). The reaction mixture was then irradiated in the microwave reactor at 150 ºC for 5 h. Purification of the crude residue via flash column chromatography (gradient eluent: 1-2.0 % of MeOH /DCM then 2.0-4.0 % MeOH /DCM containing 0.5 % NH4OH) afforded LNP3 (200 mg, 78%) as a light yellow oil. 1H NMR (500 MHz, CDCl3) δ 0.87 (t, J = 6.5 Hz, 12 H, CH3), 1.22-1.32 (m, 88 H, CH2), 1.36-1.56 (m, 16 H, CH2), 1.73-1.99 (m, 4 H, CH2), 2.17-2.68 (br, 12 H, NCH2), 3.62 (m, 4 H, CHOH), 3.98 (m, 2 H, COCH).; HRMS (ESI, m/z) calcd for C72H145N4O6 [M + H]+: 1162.1159, found 1162.1153 (**Fig. 4.10**).

Nanoparticle Formulation. Nanoparticles were formulated with a microfluidic device as previously described26. Briefly, nucleic acids (DNA barcodes, mRNA, and sgRNA) were diluted in 10mM citrate buffer (Teknova). Lipid-amine compounds, alkyl-tailed PEG, cholesterol, and helper lipids were diluted in 100% ethanol. For nanoparticle screens, Cre mRNA and DNA barcodes were mixed at a 10:1 mass ratio. Citrate and ethanol phases were combined in a microfluidic device by syringes

(Hamilton Company) at a flow rate of 3:1. All PEGs, cholesterol, and helper lipids were purchased from Avanti Lipids.

Cell Culture. In vitro experiments were performed using murine macrophages (RAW 264.7, ATCC) and iMAECs, provided by Hanjoong Jo at Emory). RAW cells were maintained with the following culture conditions: 1% penicillin-streptomycin (500 U/mL penicillin G, 0.5 mg/mL streptomycin) (PenStrep, VWR) and 10% (v/v) FBS (VWR) in DMEM F-12 50/50 (Corning). iMAEC cells were maintained with the following culture conditions: 1% penicillin-streptomycin (500 U/mL penicillin G, 0.5 mg/mL streptomycin) (PenStrep, VWR), 10% (v/v) FBS (VWR), 1% (v/v) MEM non-essential amino acid solution (MEMNEAA, Sigma Aldrich), 25 μg/mL ECGS (Emd Millipore) in DMEM with 1 g/L glucose, L-glutamine, and sodium pyruvate (Corning). Unless specified otherwise, cells were seeded in a 24-well plate at a density of 40k cells/well. In each case, LNPs were added 24 hours later. 12 hours after transfection, protein expression was analyzed with flow cytometry (BD Accuri C6 and BD FacsFusion). In all experiments, we used N=3-4 wells/group.

Lipopolysaccharides from Escherichia coli O55:B5 was purchased from Sigma Aldrich and solubilized in 1X PBS. Poly(I:C) was purchased from InvivoGen and solubilized in 1X PBS. CpG (T*C*C*A*T*G*A*C*G*T*T*C*C*T*G*A*C*G*T*T) was purchased from IDT and solubilized in water. TLR4 Inhibitor, TAK-242, was purchased from Sigma Aldrich and solubilized in DMSO.

DNA Barcoding. Each LNP was formulated to carry its own unique DNA barcode. LNP1 carried DNA barcode 1, while the chemically distinct LNP2 carried DNA barcode 2. DNA barcodes were designed rationally with several characteristics, as we previously described. Ninety-one nt long single stranded DNA sequences were purchased from IDT. Additional nucleotides on the 5’ and 3’

ends of the of the ssDNA were modified with phosphorothioates to reduce exonuclease degradation. Universal forward and reverse primer regions were included on all barcodes to ensure equal amplification of each sequence. To monitor for PCR bias, each barcode was also designed with 7 random nucleotides. Each barcode was distinguished using a unique 8 nucleotide sequence. An 8-nucleotide sequence can generate over 48 (65,536) distinct barcodes. We used distinct 8 nucleotide sequences designed by to prevent sequence bleaching and reading errors on the Illumina MiniSeqTM sequencing machine.

Nanoparticle Characterization. LNP hydrodynamic diameter was measured using high throughput DLS (DynaPro Plate Reader II, Wyatt). LNPs were diluted in sterile 1X PBS and analyzed. To avoid using unstable LNPs, and to enable sterile purification using a 0.22 μm filter, LNPs were included only if they met 3 criteria: diameter >20 nm, diameter <200 nm, and correlation function with 1 inflection point. Particles that met these criteria were dialyzed with 1X PBS.

TNS Assay. The pKa of the cKK-E12 LNP and LNP3 were measured as previously described. A stock solution of 10 mM HEPES (Sigma Aldrich), 10 mM MES (Sigma Aldrich), 10 mM sodium acetate (Sigma), and 140 nM sodium chloride (Sigma Aldrich) was prepared and pH adjusted with hydrogen chloride and sodium hydroxide to a range of pH between 4 and 10. Using 4 replicates for each pH, 140 μL pH-adjusted buffer was added to a 96-well plate, followed by the addition 5 μL of 2-(p-toluidino)-6-napthalene sulfonic acid (60 μg/ mL). 5uL of either cKK-E12 or LNP3 were added to each well. After 5 min of incubation under gentle shaking, fluorescence absorbance was measured using excitation wavelengths of 325 nm and emission wavelength of 435 nm using a plate reader (BioTek Synergy H4 Hybrid).

Animal Experiments. All animal experiments were performed in accordance with the Georgia Institute of Technology's IACUC. All animals were bread in the Georgia Institute of Technology Animal Facility. C57BL/6J (#000664) were purchased from The Jackson Laboratory. LSL-

Tomato/Ai14 (#007914) were purchased from The Jackson Laboratory for breeding proposes. In all experiments, we used N=6-10 mice/group. Mice were injected intravenously via the lateral tail vein or intraperitoneal into the abdomen. The nanoparticle concentration was determined using NanoDrop (Thermo Scientific).

Tumor Studies. Tumor experiments were performed using murine melanoma cell line (B16-F10, CRL-6475) purchased from ATCC. B16-F10 cells were maintained with the following culture conditions: 1% penicillin-streptomycin (500 U/mL penicillin G, 0.5 mg/mL streptomycin) (PenStrep, VWR) and 10% (v/v) FBS (VWR) in DMEM F-12 50/50 (Corning). Prior to injections, B16-F10 cells were resuspended in DMEM media without phenol red. C57BL/6J mice, under isoflurane anesthesia, were injected with 2.5 x 105 cells per hind leg.

Cell Isolation & Staining. Cells were isolated 24 or 72 hours after injection with LNPs unless otherwise noted. Mice were perfused with 20 mL of 1X PBS through the right atrium. Tissues were finely cut, and then placed in a digestive enzyme solution with Collagenase Type I (Sigma Aldrich), Collagenase XI (Sigma Aldrich) and Hyaluronidase (Sigma Aldrich) at 37 ºC at 550 rpm for 45 minutes. The digestive enzyme for heart and spleen included Collagenase IV [3, 4]. Cell suspension was filtered through 70□m mesh and red blood cells were lysed. Cells were stained to identify specific cell populations and sorted using the BD FacsFusion and BD Facs Aria IIIu cell sorters in the Georgia Institute of Technology Cellular Analysis Core. The antibody clones used were: anti-CD31 (390, BioLegend), anti-CD45.2 (104, BioLegend), anti-CD68 (FA11, Biolengend), and PE anti-mCD47 (miap301, BioLegend). Representative flow gates are located in **Fig. 4.11**. PBS-injected Ai14 mice were used to gate tdTomato populations for intravenous administration.

ddPCR. The QX200 Droplet Digital PCR System (Bio- Rad) was used to analyze all ddPCR results. ddPCR samples were prepared with 10 μL of ddPCR with ddPCR Supermix for Probes (Bio-Rad),

1 μL of primer and probe mix (solution of 10 μM target probe and 20 μM reverse/forward primers), 1 μL of template/TE buffer, and 8 μL of water. Once prepared, 20 μL of each reaction and 70 μL of Droplet Generation Oil for Probes (Bio-Rad) were loaded into DG8 Cartridges and covered with DG8 Gaskets. Using the QX200 Droplet Generator, water−oil emulsion droplets were created. Cycle conditions for PCR were as follows: 1 cycle of 95 °C for 10 min followed by 40 cycles of 94 °C for 30 s, 60 °C for 1 min, and 1 cycle of 95 °C for 10 min. For each biological rep, three technical repetitions were completed. Unless stated otherwise, technical reps were averaged. Technical reps were only excluded if saturated was detected or there were inconsistent positive event amplitudes.

PCR Amplification. All samples were amplified and prepared for sequencing using a one-step PCR protocol as previously described[2]. More specifically, 1 μL of primers (5 uM for Final Reverse/Forward, 0.5 uM for Base Forward) were added to 5 μL of Kapa HiFi 2X master mix, and 4 μL template DNA/water. When the PCR reaction did not produce clear bands, the primer concentrations, DNA template input, PCR temperature, and number of cycles were optimized for individual samples.

Deep Sequencing. Illumina deep sequencing was conducted in Georgia Tech's Molecular Evolution core. Runs were performed on an Illumina MiniseqTM. Primers were designed based on Nextera XT adapter sequences.

Data Normalization. Counts for each particle, per tissue, were normalized to the barcoded LNP mixture we injected into the mouse. This 'input' DNA provided the DNA counts, and was used to normalize DNA counts from the cells and tissues.

Data Analysis & Statistics. Sequencing results were processed using a custom python-based tool to extract raw barcode counts for each tissue. These raw counts were then normalized with an R script prior for further analysis. Statistical analysis was done using GraphPad Prism 8. Data is plotted as mean +/- standard error mean unless otherwise stated.

Microscopy. mRNA was fluorescently labeled four 2'O-methyl RNA-DNA chimeric oligonucleotides, complementary to 4 adjacent sequences across the 3' UTR region, with the following sequences: MT1: T(C6-Amino)-TTTTT-T(C6-Amino)-MeOG-MeOC-MeOA-MeOA-MeOG-MeOC-MeOC-MeOC-MeOC-MeOG-MeOC-MeOA-MeOG-MeOA-MeOA-MeOG-MeOG-T(C6-Amino). MT2: T(C6-Amino)-TTATT-T(C6-Amino)-MeOA-MeOG-MeOA-MeOG-MeOA-MeOA-MeOG-MeOA-MeOA-MeOG-MeOG-MeOG-MeOC-MeOA-T(C6-Amino)-MeOG-MeOG. MT3: T(C6-Amino)-TTTT-T(C6-Amino)-A-MeOC-MeOC-MeOA-MeOA-MeOG-MeOA-MeOG-MeOG-T(C6-Amino)-MeOA-MeOC-MeOA-MeOG-MeOG-T(C6-Amino)-MeOG-MeOC. MT4: T(C6-Amino)-TTTTTT-MeOC-T(C6-Amino)-MeOA-MeOC-MeOU-MeOC-MeOA-MeOG-MeOG-MeOC-T(C6-Amino)-MeOU-MeOU-MeOA-MeOU-T(C6-Amino)-MeOC (Biosearch Technologies). The oligos were fluorescently labeled by conjugating Cy3B NHS ester (GE Healthcare) to the amino-modified thymidines following manufacturer's instructions, followed by purification with 10kDa filters (Amicon, Fisher Scientific) to remove unbound dyes. IVT mRNA was buffer exchanged into 1X PBS and combined with linear oligos in a 1:0.7 molar ratio. mRNA labeling with fluorescently labeled probes was performed in a thermal cycler by heating the sample at 70ºC and gradually decreasing the temperature at RT in 1ºC/min steps. Labeled mRNA was formulated into LNPs (as previously described) and delivered to RAW 264.7 cells as described.

Cells were seeded in glass-bottom 24-well plates at a density of 50k cells / well. 24 hours later, LNPs were administered. Cells were fixed with 4% paraformaldehyde (Electron Microscopy

Sciences) for 10 min at room temperature. Then, cells were permeabilized with 0.2% Triton X-100 (Sigma-Aldrich) for 5 min at room temperature and blocked with 5% BSA. Cells were stained with CD63 (rabbit polyclonal sc-153633 Santa Cruz Biotechnology), EEA1 (rabbit polyclonal, PA5-29013, Invitrogen) and Rab11 (rabbit polyclonal sc-9020 Santa Cruz Biotechnology), and donkey anti-rabbit secondary antibody, (pre-conjugated to Alexa Fluor 488) (Life Technologies). The samples used for the 1h and 3h time-points were additionally stained with an APC labeled anti-mouse TLR4 antibody (Biolegend SA15-21). All antibodies were used at a 1:250 dilution in 1X PBS. Nuclei were stained with 4',6-diamidino-2-phenylindole (DAPI) (Life Technologies).

Images were aquired with a Hamamatsu Flash 4.0 v2 sCMOS camera on a PerkinElmer UltraView spinning disk confocal microscope mounted to a Zeiss Axiovert 200M body with a 63x NA 1.4 plan-apochromat objective. Images were acquired with Volocity (PerkinElmer) with Z-stacks taken in 0.2 μm increments. Image acquisition and analysis was performed using the Volocity software (PerkinElmer). Thirty or more cells were analyzed per experimental condition; assays were repeated twice and normalized.

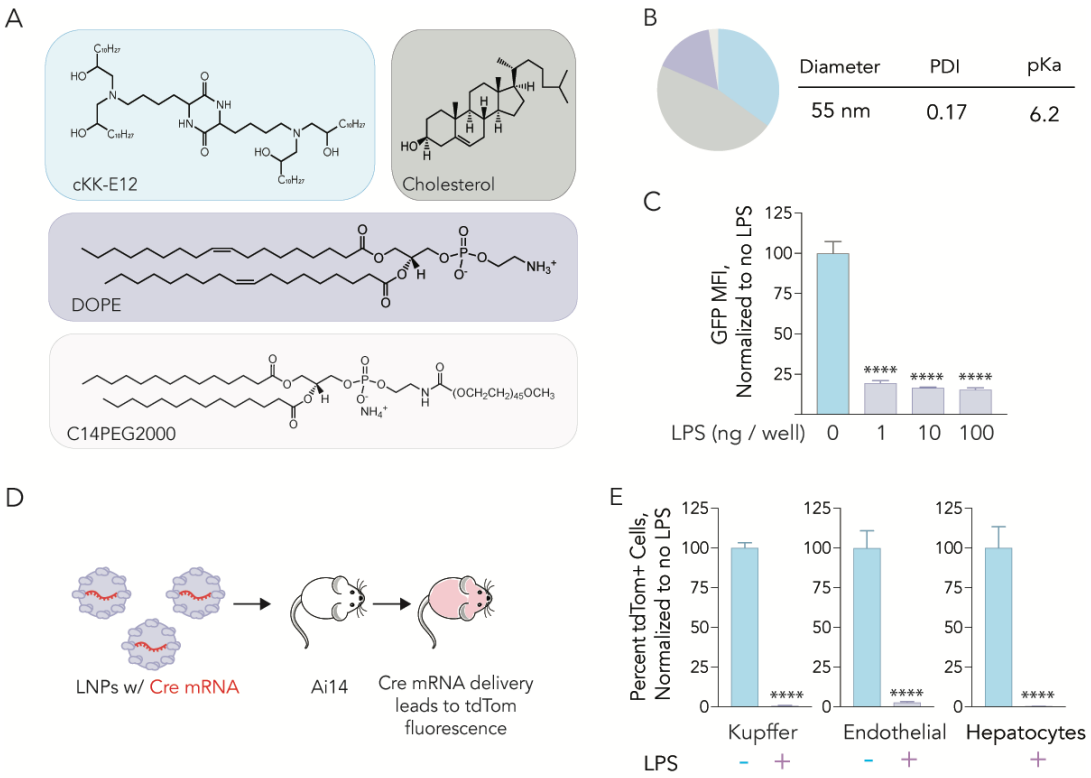

Figure 4.1 (A) cKK-E12 was formulated by combining the ionizable material cKK-E12, C14PEG2000, unmodified cholesterol, and DOPE. **(B)** Characteristics of cKK-E12. **(C)** GFP mean fluorescent intensity twelve hours after cKK-E12 LNPs carrying GFP mRNA were administered. Data are normalized to GFP MFI of control cells that were not treated with LPS. ****$p < 0.0001$, One-way ANOVA. **(D)** To quantify mRNA delivery in vivo, we formulated cKK-E12 LNPs with Cre mRNA and injected them into Ai14 mice. If Cre mRNA is functionally translated into Cre protein, cells become tdTomato+. **(E)** The percentage of tdTomato+ cells in mice pre-treated with PBS or 0.1 mg / kg LPS, then injected with 0.3 mg / kg Cre mRNA. Data are normalized to mice pre-treated with PBS ****$p < 0.0001$, two-way ANOVA.

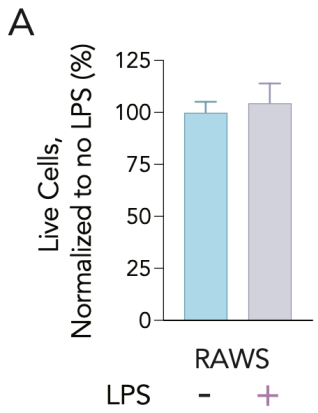

Figure 4.2. (A) Percent of live RAW cells with and without LPS.

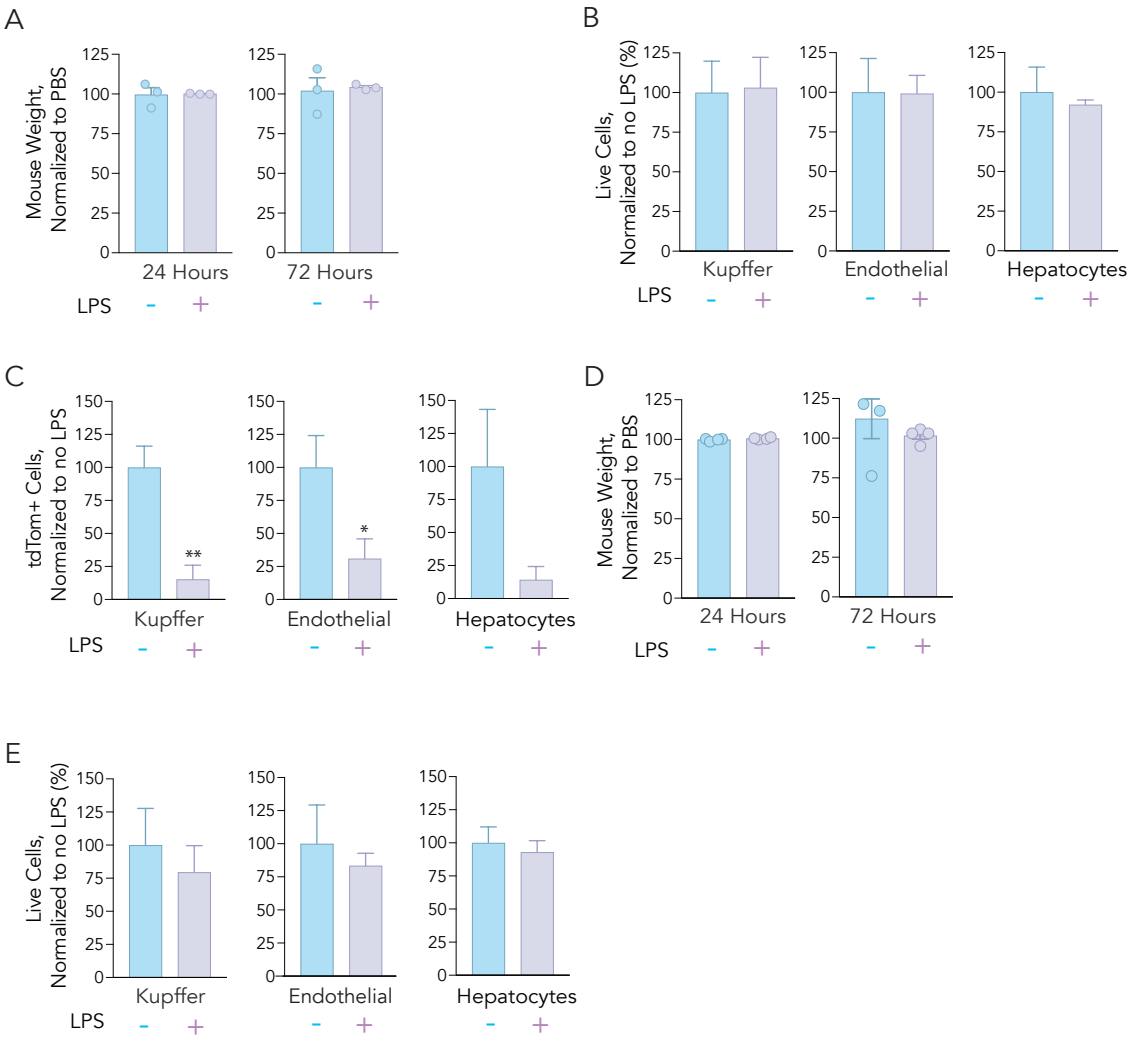

Figure 4.3. (A) Mouse weights, with and without LPS, 24 and 72 hours after injection of cKK-E12. **(B)** Percent of live Kupffer cells, Endothelial cells, and hepatocytes with and without LPS. **(C)** Ai14 mice were injected with 0.1 mg / kg of LPS. Six hours later, MC3 carrying Cre mRNA was administered intravenously at 0.3 mg / kg. Functional Cre mRNA delivery was quantified as %tdTomato+ cells, in three cell types from the liver with and without LPS. **P < 0.006, *P < 0.05, one-tail t test. **(D)** Mouse weights, with and without LPS, 24 and 72 hours after injection of MC3. **(E)** Percent of live Kupffer cells, Endothelial cells, and hepatocytes with and without LPS.

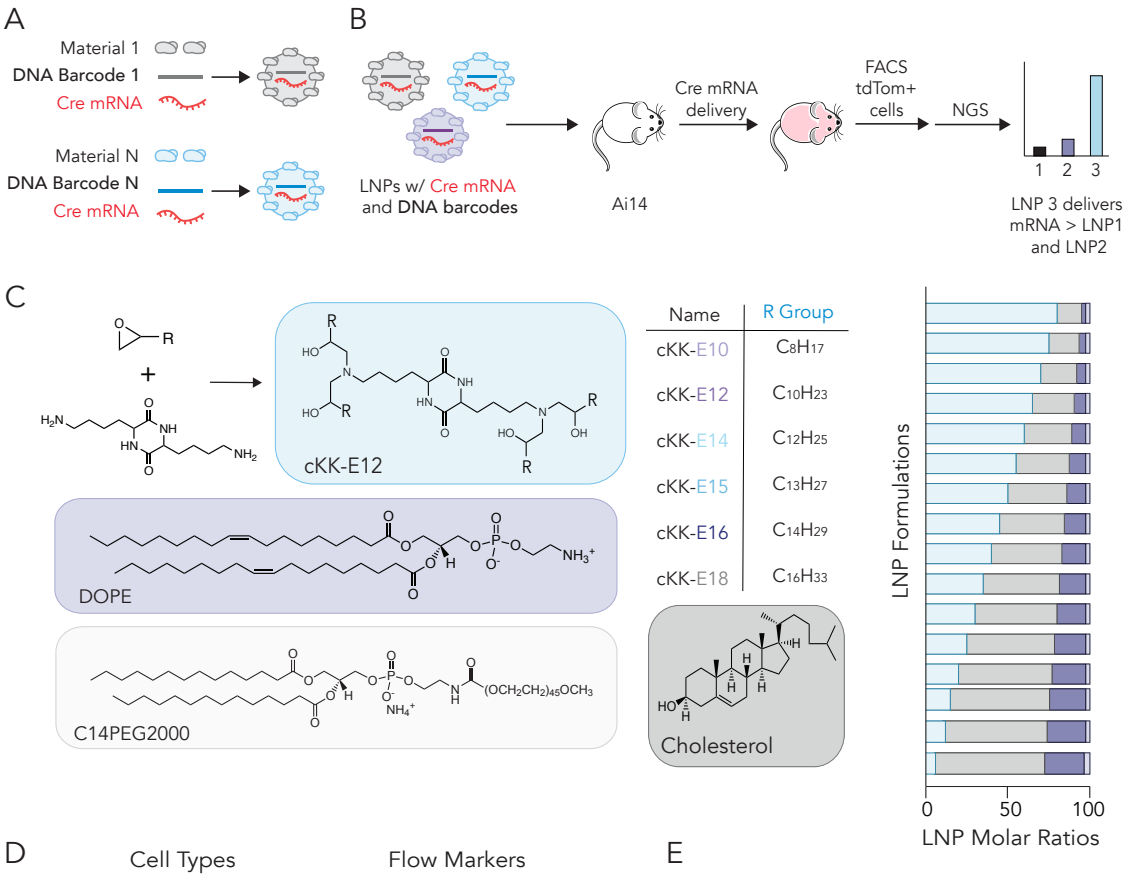

D

Cell Types	Flow Markers
Liver Hepatocytes	CD31- CD45- CD68-
Liver Endothelial Cells	CD31+ CD45- CD68-
Liver Kupffer Cells	CD31- CD45+ CD68+
Lung Endothelial Cells	CD31+ CD45-
Lung Immune Cells	CD31- CD45+
Heart Endothelial Cells	CD31+ CD45-
Heart Immune Cells	CD31- CD45+
Pancreas Endothelial Cells	CD31+ CD45-
Pancrease Immune Cells	CD31- CD45+
Node Endothelial Cells	CD31+ CD45-
Node Immune Cells	CD31- CD45+
Marrow Endothelial Cells	CD31+ CD45-

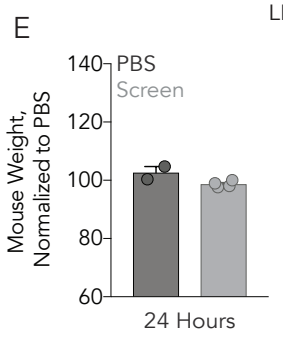

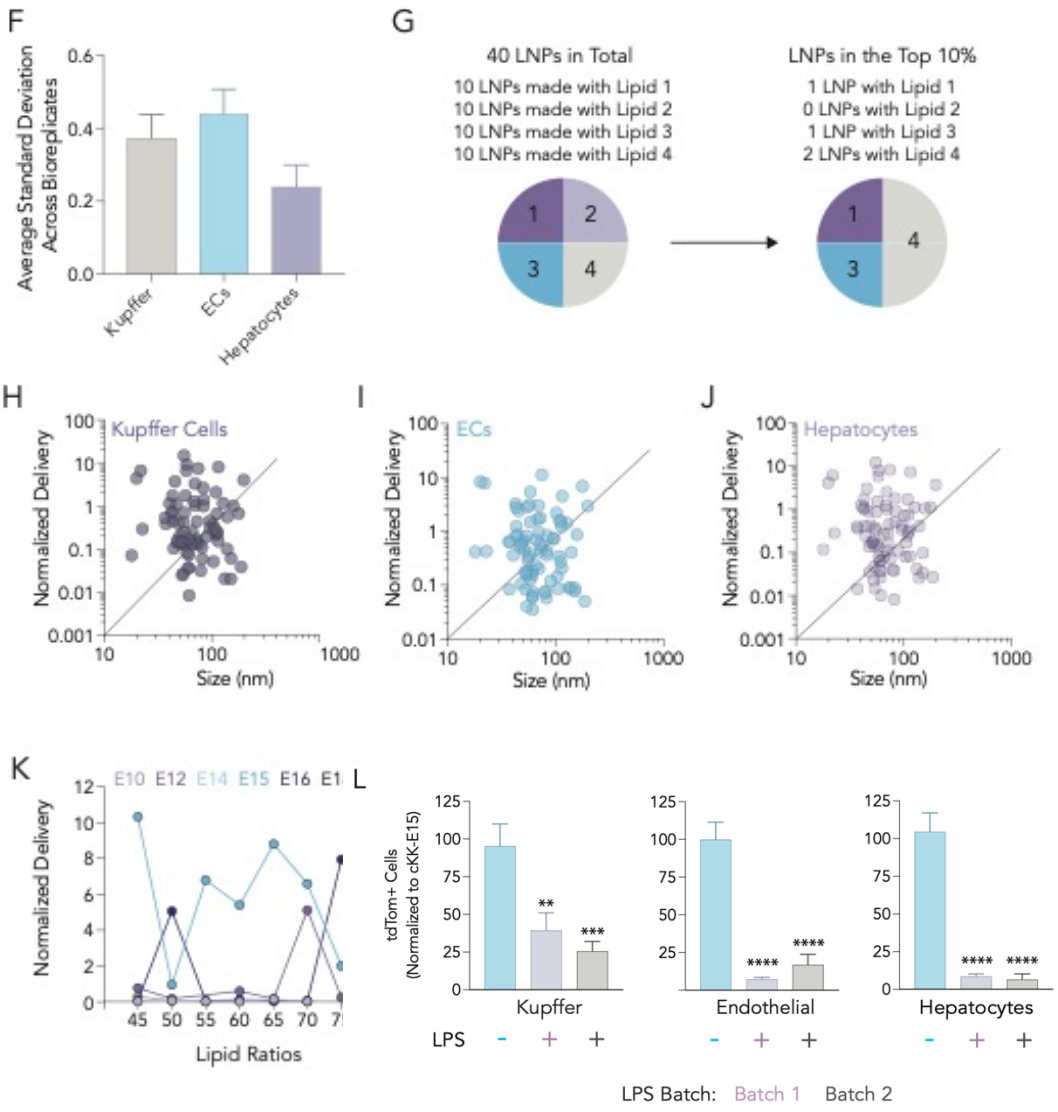

Figure 4.4. (A) Barcoded nanoparticles are formulated with various chemical components, single stranded DNA barcodes, and Cre mRNA. Material 1 is formulated with DNA barcode 1 and cre mRNA; Material N is formulated with DNA barcode N and cre mRNA. **(B)** All stable LNPs are pooled and intravenously administered to Ai14 mice. If Cre mRNA is functionally delivered to the cytoplasm, it is translated into Cre protein, which edits the genome by excising the stop. As a result, the cells become tdTomato+ and are isolated using FACS. Barcodes are sequenced to identify which LNPs deliver mRNA in vivo. **(C)** Six cKK-E12 based lipids can be formed by varying the tail length with six groups. 96 LNPs were formulated with 16 different molar ratios of lipids,

C14PEG2000, cholesterol and DOPE. **(D)** Twelve cell types were isolated from 6 different tissues with FACS. E) Average mouse weights 24 hours after injection with LNP pool. **(F)** Average standard deviation across all mouse replicates from the screen were analyzed to quantify consistency between replicates. **(G)** Example enrichment analysis. **(H)** No correlation between size and delivery was found in Kupffer cells, **(I)** endothelial cells, or **(J)** hepatocytes. **(K)** We found no relationship between delivery and lipid molar ratio. **(L)** Two new batches of LPS (indicated in purple and grey) were used to pretreat mice at 0.1 mg / kg six hours prior to treatment with LNP. tdTomato+ cell percentages were quantified with flow cytometry. **P < 0.002, ***P < 0.0002, ****P < 0.0001, two-way ANOVA.

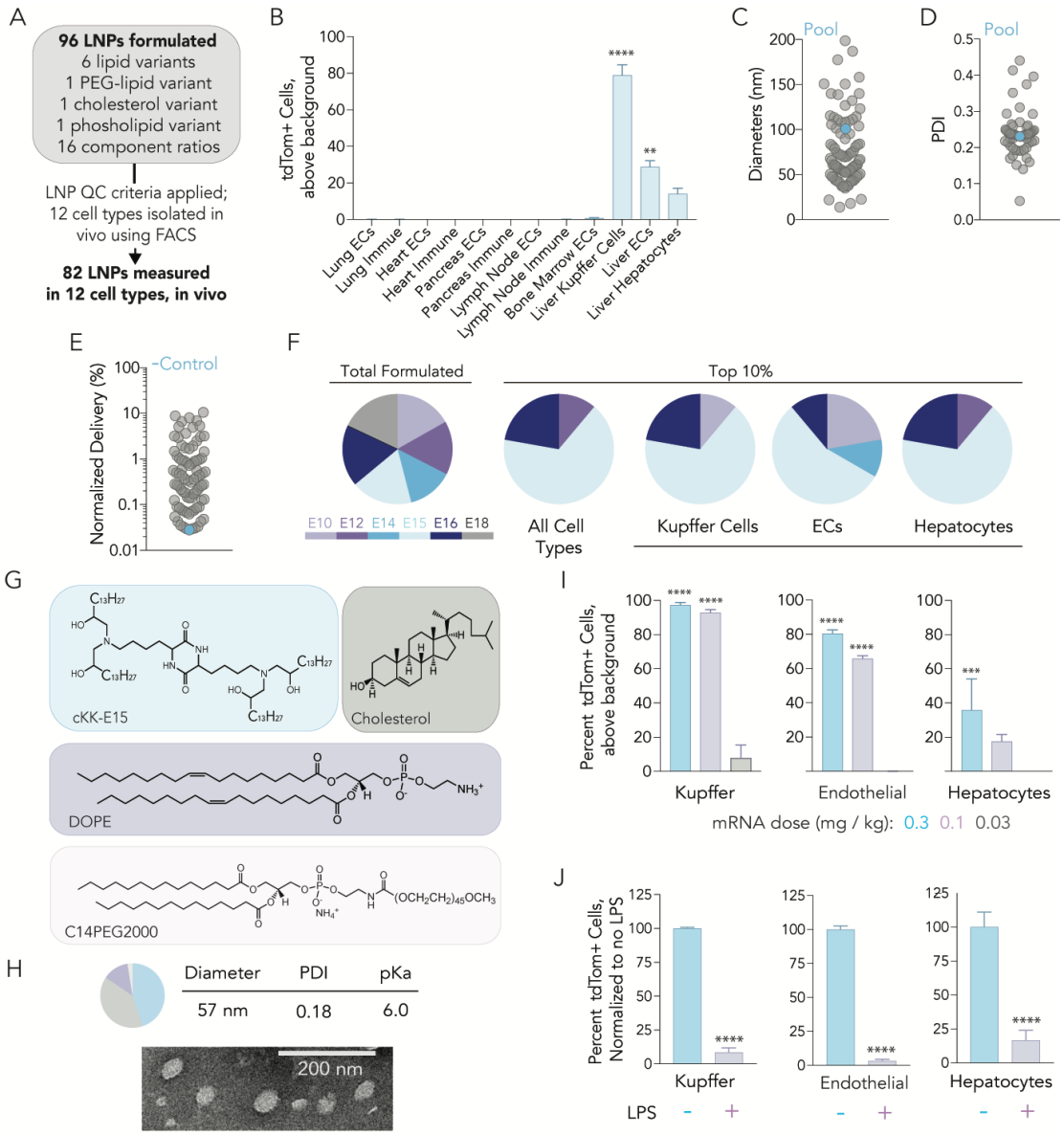

Figure 4.5. (A) Ninety-six chemically distinct LNPs were formulated with Cre mRNA and DNA barcodes. After quality control, 82 LNPs were injected into Ai14 mice. FACS was used to measure mRNA delivery and isolate tdTomato+ cells. **(B)** Twelve different cell types were isolated; the pool preferentially delivered to Kupffer cells. ****$p < 0.0001$, **$p < 0.01$, two-way ANOVA. **(C)** Hydrodynamic diameter and **(D)** polydispersity index of all administered LNPs. **(E)** Normalized delivery of all LNPs across all cell types. The naked barcode control performed poorly as expected.

(F) Enrichment of lipid variants in the top 10% compared to total formulated. cKK-E15 was the most enriched in Kupffer cells, Endothelial cells, and hepatocytes. **(G)** LNP3 was formulated with ionizable material cKK-E15, C14PEG2000, unmodified cholesterol, and DOPE. **(H)** Molar ratio, characteristics, and transmission electron microscopy image of cKK-E15. **(I)** The percentage of cells that are tdTomato+ after injections of 0.03, 0.1, or 0.3 mg / kg Cre mRNA. ****p< 0.0005, ***p< 0.001, two-way ANOVA. J) LNP3 delivery of Cre mRNA at 0.3 mg / kg in mice pre-treated with PBS or LPS. tdTomato+ cells decreased significantly. ****p < 0.0001, two-tailed t test.

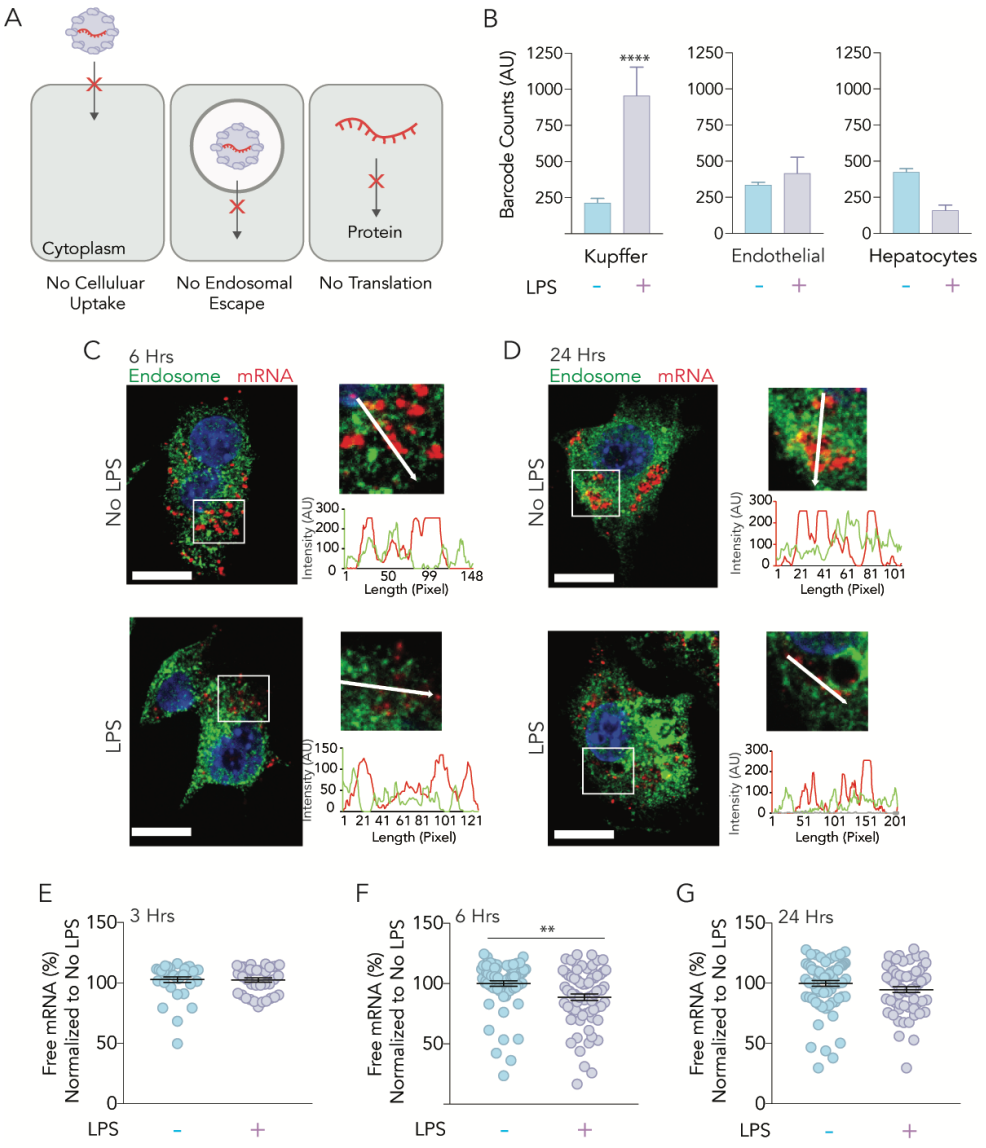

Figure 4.6. (A) To functionally deliver a mRNA drug, a LNP must be taken up by a cell, enter the cytoplasm, and be translated into protein. **(B)** To compare cellular uptake of LNP3 with and without LPS, LNP3 was formulated with QUANT DNA barcodes at 0.3 mg / kg and intravenously injected into mice. Twenty-four hours later, biodistribution was assessed. Biodistribution, shown as barcode counts (AU), for LNP3 with and without LPS. Nucleic acid uptake increased significantly in Kupffer cells when treated with LPS. ****P < 0.0001, two-way ANOVA. **(C)** Colocalization of fluorescently tagged mRNA formulated with LNP3 and endosomal markers in RAWS after

treatment of LPS. Cy3B labeled IVT mRNA (red) formulated with LNP3 was delivered to RAWS untreated or treated with LPS. Six and **(D)** 24 hours later, cells were stained for CD64, EEA1 and Rab11 (green) for early, intermediate and late endosomes, respectively. Scale bar represents 10 μm. Cropped regions are magnifications of white boxes in whole cell images with intensity profiles along the direction of the white arrow. **(E)** Percent of free mRNA was determined at 3, **(F)** 6 and G) 24 hours. $n \geq 30$ cells per group. $^{**}P < 0.005$, two-tailed t-test.

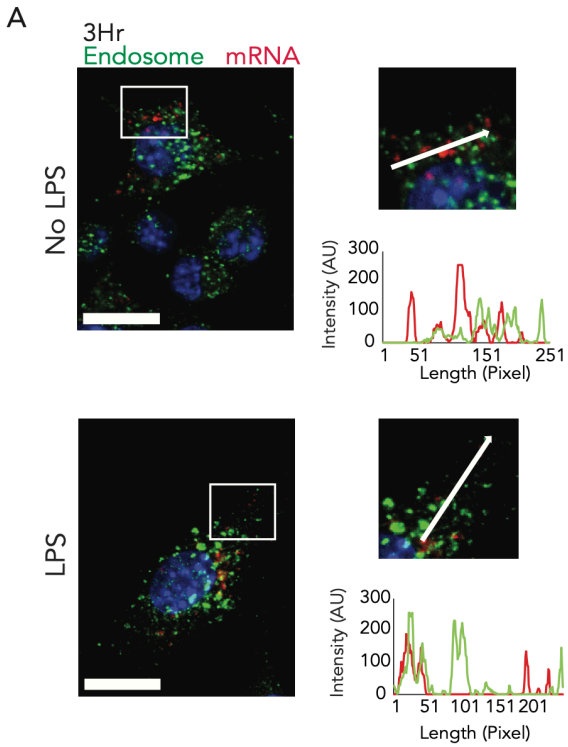

Figure 4.7. (A) Colocalization of IVT mRNA formulated with LNP3 and endosomal markers in RAWS after treatment of LPS. Cy3B labeled IVT mRNA (red) formulated with LNP3 was delivered to RAWS untreated or treated with LPS. 3 hours later, cells were stained for CD64, EEA1 and Rab11 (green) for early, intermediate and late endosomes, respectively. Scale bar represents 10 μm. Cropped regions are magnifications of white boxes in whole cell images with intensity profiles along the direction of the white arrow.

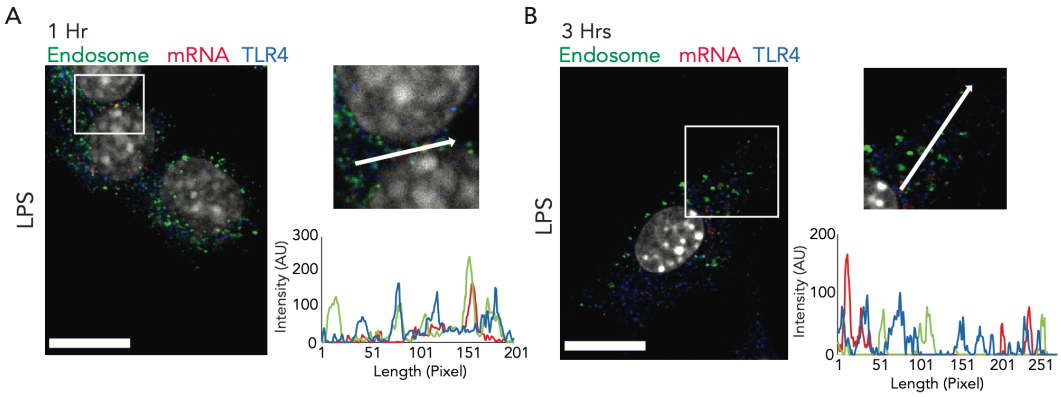

Figure 4.8. (A) Colocalization of IVT mRNA formulated with LNP3, endosomal markers, and TLR4 in RAWS after treatment of LPS. Cy3B labeled IVT mRNA (red) formulated with LNP3 was delivered to RAWS untreated or treated with LPS. 1 and **(B)** 3 hours later, cells were stained for CD64, EEA1 and Rab11 (green) for early, intermediate and late endosomes, respectively, and TLR4 (blue). Scale bar represents 10 μm. Cropped regions are magnifications of white boxes in whole cell images with intensity profiles along the direction of the white arrow.

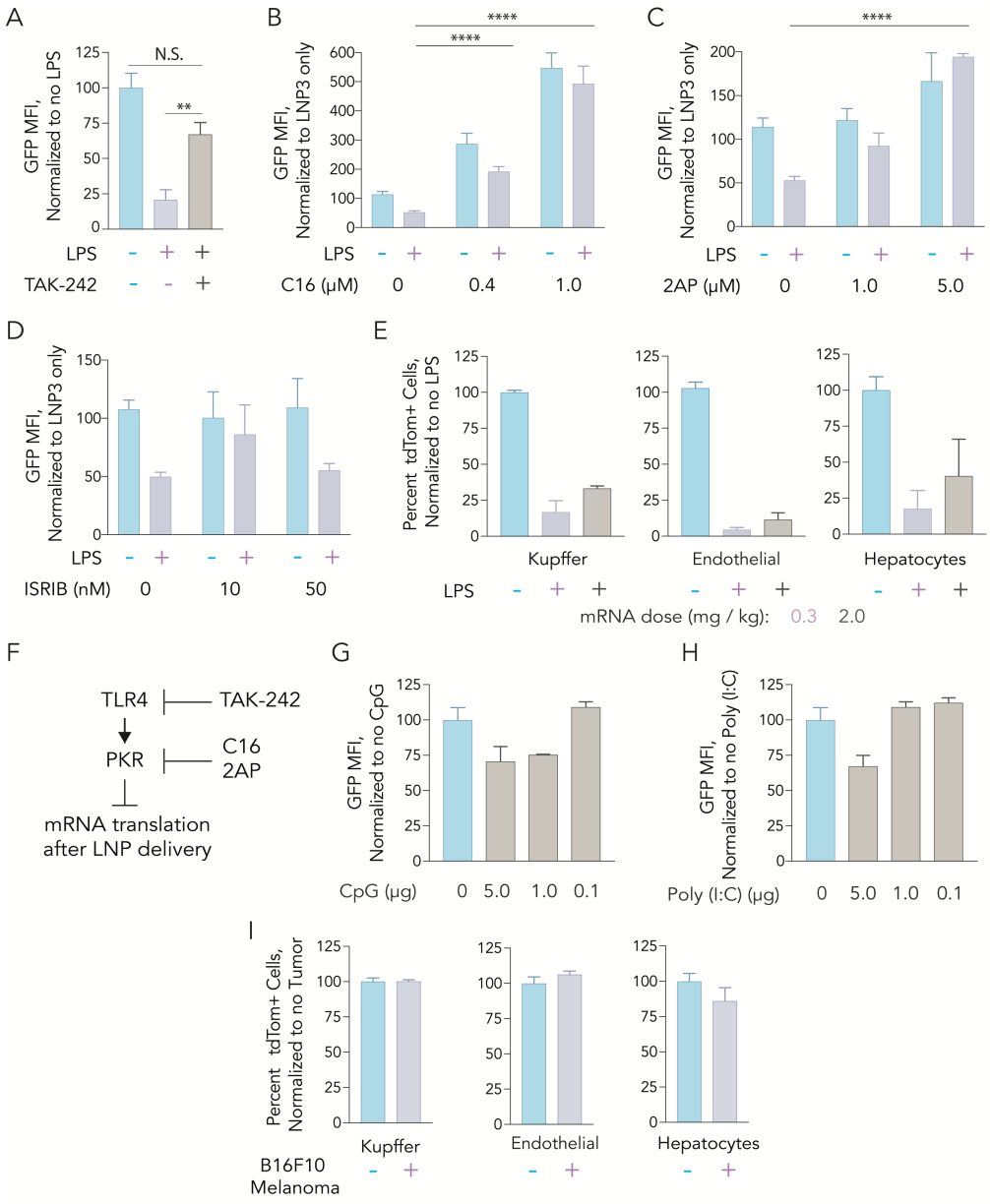

Figure 4.9. (A) When treated with TLR4 inhibitor and LPS, TAK-242, mRNA expression mediated by LNP3 delivery was rescued, when compared to cells treated with 100 ng LPS. GFP expression was non-significant when compared to the control group and the LPS. **P < 0.005, two-tail t test. **(B)** RAWS were treated with C16, **(C)** 2AP, or **(D)** ISRIB 1 hours prior to LPS. Six hours later, cells were treated with LNP3 carrying GFP mRNA and GFP expression was measured. ****P < 0.0001 **(E)** LNP3 carrying Cre mRNA was administered to Ai14 mice at 0.3 or 2 mg / kg. When

comparing 2 mg / kg to 0.3 mg / kg, tdTomato+ cells showed no significant increase. **(F)** TLR4-mediated activation of PKR can lead to inhibition of mRNA translation. Inhibition of TLR4 or PKR can recover translation after LNP delivery. **(G)** RAWS were treated with CpG or **(H)** Poly (I:C) before being treated with LNP3 carrying GFP mRNA, and GFP expression was measured. No significant differences were found between treated and untreated groups. **(I)** LNP3 carrying Cre mRNA was administered to Ai14 mice with and without tumor xenografts. Delivery was evaluated by the percent of tdTomato+ cells in Kupffer cells, Endothelial cells, and hepatocytes. Delivery was not affected by tumors.

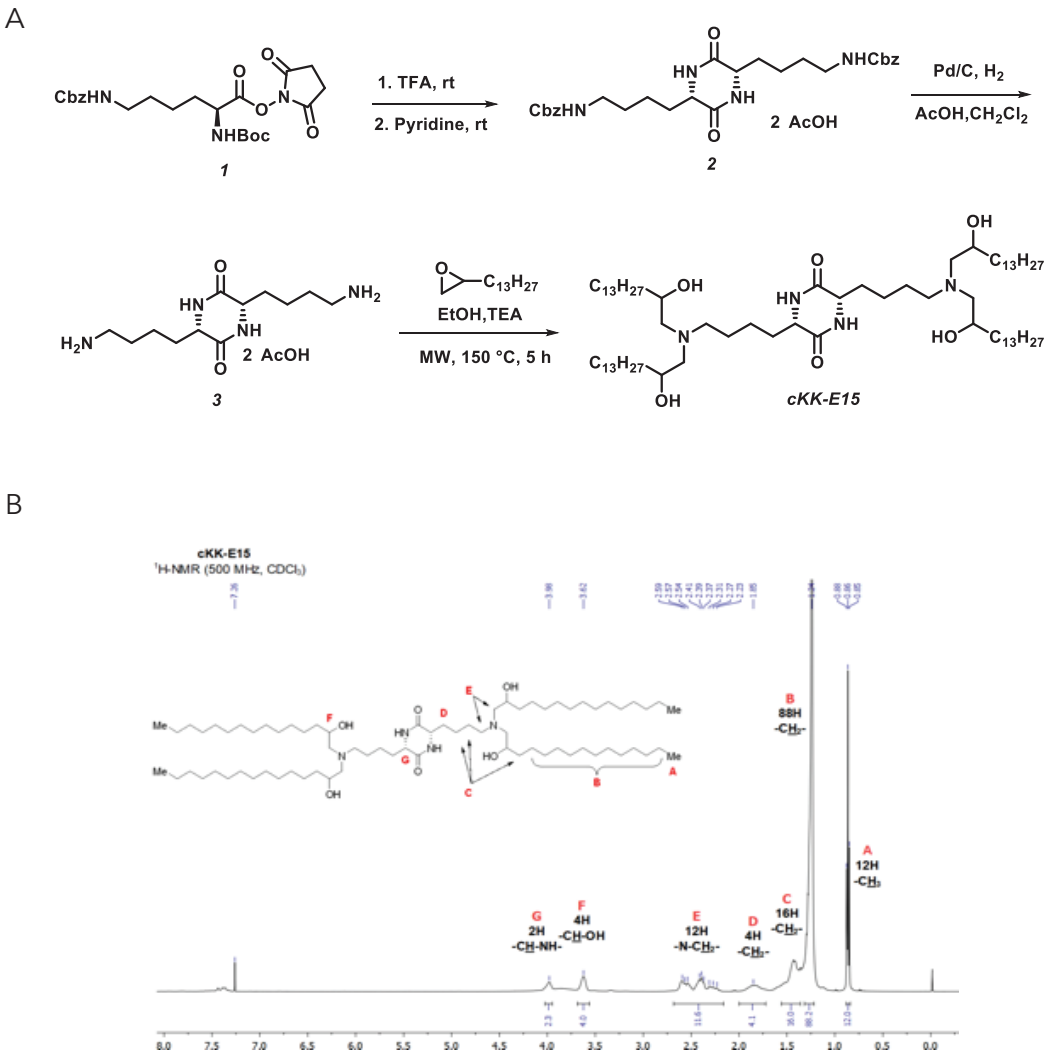

Figure 4.10. (A) Preparation of cKK-E15. Compound 1 was dissolved in DMF. The reaction mixture was stirred at room temperature overnight. The solvents were evaporated under reduced pressure and washed with ethyl acetate to give pure compound 2. Pd/C was added to Compound 2 in acetic acid/CH2Cl2. The oil was solidified by adding ethyl acetate and washed with ethyl acetate to yield compound 3. Triethylamine was added to a solution of compound 3 and tridecyloxirane in EtOH. The reaction mixture was then irradiated in the microwave reactor at 150 ºC for 5 h. Purification of the crude residue via flash column chromatography to become cKK-E15. **(B)** NMR spectra for cKK-E15.

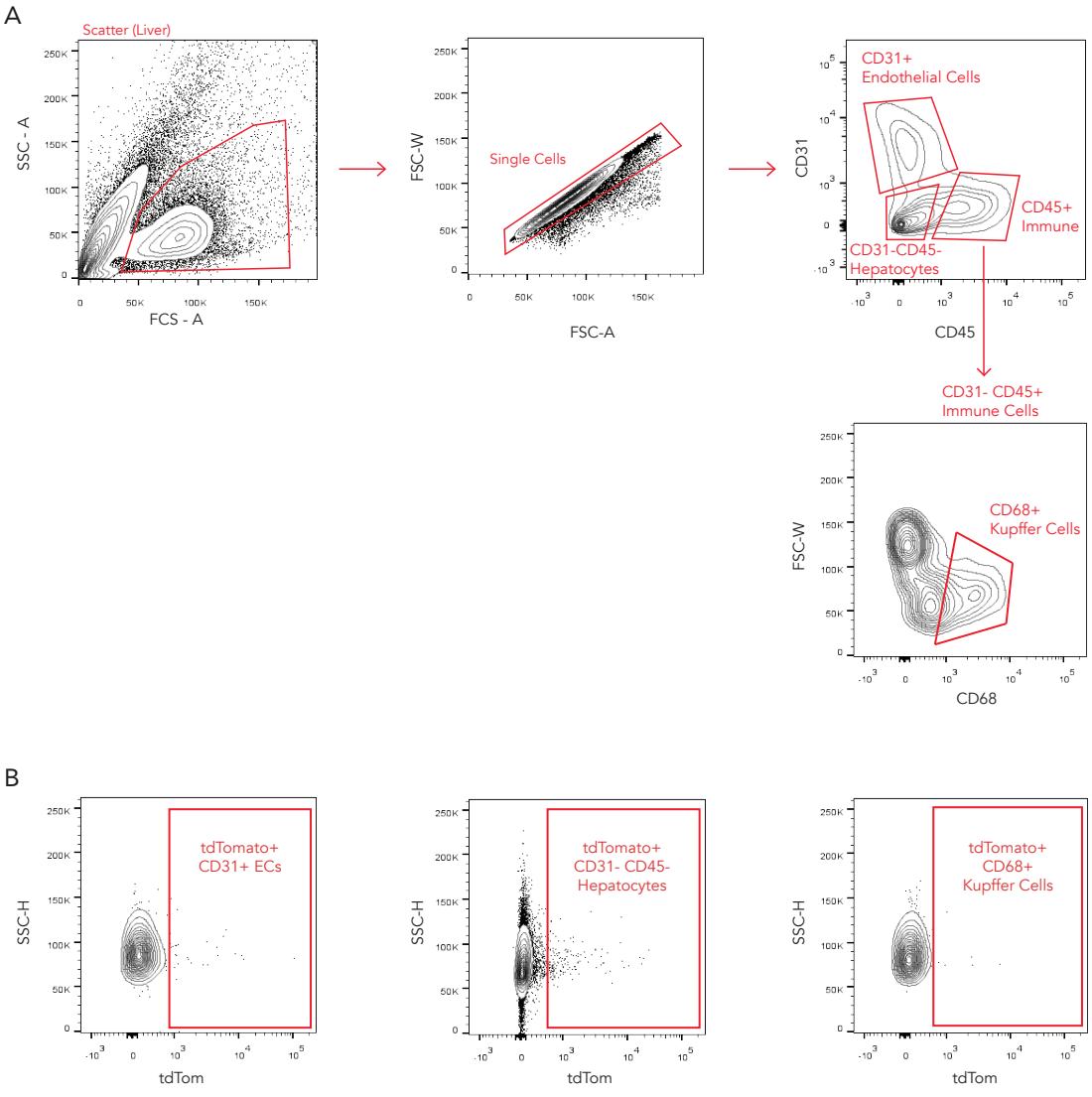

Figure 4.11. (A,B) Representative gating strategies for FACS for cells types in the liver.

CHAPTER 5. CLUSTERED IN VIVO SCREENS REVEAL DESIGN RULES FOR LIPID NANOPARTICLES THAT DELIVER MRNA TO THE LUNG FOLLOWING NEBULIZATION

5.1 Introduction

Once delivered into the cytoplasm, exogenously administered mRNA can express therapeutic nucleases, antigens, antibodies, or other proteins[7]. However, these drugs are limited by the need to deliver mRNA into the cytosol without eliciting an immune response[139]. Laboratories have improved mRNA delivery in mice, rats, pigs, and NHPs using LNPs[2,16,124,142,143,148,159,160,164-169]. Independent of their chemical structure, LNPs are often discovered using a common workflow. First, dozens to hundreds of nanoparticles are made with diverse chemical compositions. Second, drug delivery mediated by these nanoparticles are quantified in vitro one by one. Third, in vitro data are used to select a small number of nanoparticles for in vivo studies. This approach is similar to a precedent set by the siRNA delivery field. In three representative examples[26,66,132], to identify LNPs that deliver siRNA systemically, 4,736 LNPs were tested in vitro, whereas only 14 were tested in vivo.

These and other studies revealed two key lessons we applied to nebulized mRNA delivery vehicles. First, all four components often used to create LNPs - ionizable lipid[26], PEG-lipid[170], cholesterol[76,171], and other lipids (e.g., phospholipids)[165,172] - influence delivery. The resulting four-dimensional chemical space may therefore encompass 1010 or more distinct LNP formulations[124], even without considering active targeting ligands. Second, in vitro nanoparticle delivery can poorly predict in vivo nanoparticle delivery[33,160,173]. These lessons highlight the need for an easily adopted

in vivo alternative to LNP discovery capable of efficiently and iteratively scanning diverse chemical space.

Such an alternative to LNP discovery would be useful if applied to nebulization mediated LNP delivery to the lung. Nebulized nanoparticles have been considered as potential therapies for genetic disease[174] as well as infectious disease, since these drugs could encode nucleases, vaccines, or antibodies targeting SARS-CoV-2 or its entry into human cells[175]. Given that LNPs can be manufactured at human scales, have been FDA approved[176], and have demonstrated acceptable safety in early COVID-19 vaccine clinical trials[177,178], they constitute an alternative to large polymeric[179] and polymer-peptide-based[180] nanoparticles that have delivered mRNA to the lung following nebulization. For example, although large (e.g., 25 kDa) polymers were shown to enable nebulized DNA delivery up to twenty years ago[181,182], nebulized gene therapies using these polymers have not been FDA approved. In a recent example, a polymer for nebulized delivery required a polymer: mRNA mass ratio of 50:1[181], a ratio five-fold higher than LNPs that have progressed into clinical trials.

Demonstrating that an LNP can deliver mRNA to the lungs at low doses would open up a new and potentially clinically relevant chemical space for lung delivery. Yet this task remains difficult since LNPs that deliver mRNA after systemic administration may be dissimilar from LNPs that deliver mRNA to the lungs via nebulization. For example, although state-of-the-art nebulizers are designed to gently aerosolize the therapeutic, nanoparticles still experience shearing forces that can disrupt the structure of the vehicle-drug formulation. A second reason nebulized mRNA differs from systemic delivery is the biology of the airway. When nanoparticles are administered via nebulization, the cells, proteins, biomolecules, and physical barriers with which they interact[183,184]

are distinct from those with which they interact in the bloodstream[38]. Cells in the airways are also heterogenous[185], which may alter delivery.

Driven by the need for lung mRNA delivery vehicles, the lack of established LNP design principles, and the absence of a workflow to identify design principles, we report an in vivo cluster-based iterative screening approach to identify LNP chemical traits that promote lung delivery. We found that (i) PEG is required for LNP formulation and (ii) that the combination of PEG molarity and helper lipid structure and charge influence delivery; this second fact underscores the need to understand multivariate LNP design space. Here, we identify a nanoparticle named Nebulized Lung Delivery 1 (NLD1). The structure of NLD1 is distinct from previously reported nanoparticles for nebulized delivery. Specifically, NLD1 is designed with a high amount of PEG-lipid and cationic helper lipid. While LNP-mediated nucleic acid delivery is often studied with low PEG-lipid molar ratios, we found a greater amount of PEG within an LNP can improve mRNA delivery to the lungs via nebulization. We also found that NLD1 is more effective than clinically relevant LNPs previously optimized for systemic delivery. Finally, we demonstrate that NLD1 can successfully be used to deliver mRNA encoding a broadly neutralizing antibody protecting mice from a lethal dose of H1N1 influenza.

5.2 Results

5.2.1 An in vivo workflow to evaluate how chemically diverse LNPs deliver mRNA to the lung after nebulization

Based on the large LNP chemical space and the poor relationship between in vitro and in vivo delivery, we designed a cluster-based workflow to meet three key criteria. We reasoned the workflow must (i) be easily set up with equipment commonly used in nanoparticle labs, (ii) quantify functional mRNA delivery (i.e., mRNA translated into functional protein) in vivo, and (iii) be

capable of scanning a diverse LNP chemical space iteratively. We previously reported functional in vivo LNP screening systems utilizing DNA barcodes[135,159,160,186,187]; our cluster-based approach is distinct in two ways. First, it does not require next-generation sequencing; this may aid nanoparticle laboratories that do not regularly sequence DNA. Second, it uses a multi-step LNP design process to select LNP formulations detailed below. Inspired by Statistical Design of Experiment (DOE) methodologies[188,189], our cluster-based approach allows us to manipulate several inputs (LNP traits) to determine their effect on in vivo RNA delivery.

In this cluster-based approach (**Fig. 5.1**), we first identify several (in this schematic, three) hypotheses relating a specific LNP chemical trait to in vivo delivery. Second, we treat each hypothesis as an axis in a N-dimensional chemical space. Third, we formulate eight to 12 LNPs at a given extreme of each axis; we term these 'extreme groups'. Fourth, we apply a three-tiered selection to each extreme group: do LNPs within the extreme group form small (<200 nm hydrodynamic diameter), stable (low dispersity, single peak on DLS nanoparticles?; if yes, does the extreme group remain stable after the LNPs are pooled together?; if yes, does the pooled LNPs from the extreme group functionally deliver mRNA into the lungs following nebulization (**Fig. 5.1A**)? Fifth, we 'expand and combine' promising extreme groups by formulating LNPs near the intersection of these groups. Sixth, we individually test all these newly formulated LNPs, assaying whether they form small, stable LNPs, and whether they deliver mRNA in the lung following nebulization (**Fig. 5.1B**). Seventh, we use all these data, including data from groups that failed, to design subsequent nanoparticles. By generating distinct hypotheses, using extreme groups to test these hypotheses, then focusing on promising chemical spaces, we scan a diverse multi-dimensional chemical space in vivo, offering an alternative to traditional in vitro-based screens.

5.2.2 Surveying how four LNP chemical traits influence nebulized lung mRNA delivery in vivo

In this case, data[60,165,171,172,190,191] led us to hypothesize that four variables influenced nebulized LNP delivery: (i) the amount of PEG added to the LNP; (ii) the structure of the lipid-

PEG; (iii) the charge of the phospholipid; and (iv) the presence or absence of cholesterol. We designed six extreme groups, varying molar ratios, components, and charge (**Fig. 5.2A,D**). In all six, we formulated eight to 12 LNPs with the compound 7C1, an oligomer-lipid conjugate18, thereby generating 56 distinct LNPs (**Fig. 5.2B, Fig. 5.3A,B**). 7C1-based LNPs have delivered siRNA in non-human primates[192] and therefore may be viable for potential clinical development.

Using microfluidics[30], we formulated LNPs with mRNA encoding an GPI-anchored nano-luciferase (AncNanoLuc) mRNA at an LNP component: mRNA mass ratio equal to 10:1. AncNanoLuc encoding mRNA was used in place of traditional luciferase since its GPI-anchor allows for the expressed protein to accumulate on the cell surface, acting as a depot for accumulating protein, which increases the sensitivity of the assay. We then analyzed all the LNPs with DLS. Extreme groups A, B, and C failed our control criteria (**Fig. 5.2C**), whereas extreme groups D, E, and F met the criteria (**Fig. 5.2D**). Specifically, many LNPs from extreme group A, B, and C were unstable and had hydrodynamic diameters greater than 200 nm (**Fig. 5.2E, Fig. 5.3A,B**). Group A had very low percentages of PEG-lipid and groups B and C did not have PEG-lipid. We therefore identified our first design rule: PEG-lipid is critical to form stable 7C1-based LNPs. As an additional control for LNP stability, we pooled the LNPs in extreme group D together, measured the hydrodynamic diameter of the pool, and found it to be within the range of diameters making up the pool; the same control was analyzed for extreme groups E and F (**Fig. 5.2E**). Once pooled, the clusters were nebulized and administered at 43 μg of mRNA / mouse (i.e., 6 μg / mouse / particle on average, for N = 7 particles / mouse). Forty-eight hours later, we extracted the lungs, submerged the organs in furimazine, quantified luminescence using an IVIS in vivo imaging system, and calculated the fold change in lung luminescence flux, relative to background. Luminescence was significantly higher in lungs transfected with extreme group E, followed by D and then F (**Fig. 5.2F,G**). These results indicate that cholesterol and helper lipids are not crucial for initial LNP formulation, but they may improve functional LNP delivery.

5.2.3 A screen of LNPs containing cationic lipids from an expanded chemical space

We then expanded a combination of extreme groups D and E. Clusters D contained cationic helper lipids, whereas cluster E contained a neutral lipid and a higher percentage of PEG-lipid. We therefore created 27 LNPs using three charged helper lipids (DOTAP, DOTMA, and 18:0 DDAB), C14PEG2000, cholesterol, 7C1, and 9 different molar ratios of PEG (**Fig. 5.4A, Fig. 5.5A,B**). Molar ratios of PEG varied from low (2.5, 6.5, and 15%) to high (25, 30, 35, 45, 55, 60%). LNPs were once again formulated with microfluidics to carry mRNA encoding AncNanoLuc at an LNP component: mRNA mass ratio equal to 10:1. Sixteen of the 27 LNPs formed stable, monodisperse LNPs with hydrodynamic diameters less than 200nm (**Fig. 5.4B**). We then analyzed whether the average hydrodynamic diameter and PDI of LNPs varied with the cationic lipid (**Fig. 5.4C, Fig. 5.5C**) or the lipid-PEG molar ratio (**Fig. 5.4D, Fig. 5.5D**). LNPs formulated with less PEG-lipid were larger, which may be a useful way to roughly tune LNP size. We then nebulized and administered the 16 stable LNPs at the low dose of 15 μg mRNA / mouse. Forty-eight hours later, we isolated lungs and quantified luciferase luminescence. We observed a non-significant increase in luminescence when LNPs were formulated with 18:0 DDAB, when compared to DOTAP or DOTMA (**Fig. 5.4E**). Interestingly, when we plotted luminescence as a function of the PEG-lipid mole percentage, we observed LNPs formulated with higher amounts of PEG tended to increase luminescence (**Fig. 5.4F,G**). Additionally, we examine the PEG-lipid mole percentage in the top and bottom five performing LNPs. We found that the top five LNPs contained high molar percentages of PEG, whereas the bottom five LNPs typically were comprised of low molar percentages of PEG (**Fig. 5.4H,I**). The data suggests that the amount of PEG is important for formulations and that it affects delivery efficiency. Taken together, these data led us to a second design rule: a combination of cationic helper lipids and high molar percentages of PEG can lead to increased mRNA delivery after nebulization (**Fig. 5.4H,J**).

5.2.4 A screen of LNPs containing neutral lipids from an expanded chemical space

We surmised LNP interactions in the lungs can be driven by several forces including PEG-based hydrophilic interactions as well as charge[193]. We therefore formulated 26 additional LNPs using two phospholipids (DOPE and DSPC), two PEG-lipids with varied tail lengths, (C14PEG2000 and C18PEG2000), cholesterol, and 7C1 (**Fig. 5.6A, Fig. 5.7A**). Since LNPs with high PEG molar ratios were smaller than LNPs with lower PEG molar ratio, this experimental setup also allowed us to evaluate whether LNP size, as opposed to LNP chemistry, caused differences in LNP delivery. Once again, LNPs were formulated with AncNanoLuc mRNA at a mass ratio of 10:1 and LNPs were only nebulized if they were monodispersed with a hydrodynamic diameter less than 200nm (**Fig. 5.6B**). We plotted the average hydrodynamic diameter and PDI as a function of neutral lipid (**Fig. 5.6C, Fig. 5.7B**), PEG amount (**Fig. 5.6D, Fig. 5.7C**), and PEG tail length (**Fig. 5.6E, Fig. 5.7D**); notably, we observed a similar trend with LNP size; LNPs formulated with low PEG-lipid molar ratios tended to be larger than LNPs with high PEG-lipid molar ratios (**Fig. 5.6D**). We also observed a trend with PDI and DSPC or low amounts of PEG-lipid (**Fig. 5.7B,C**).

LNPs that passed the quality control assay were nebulized at a dose of 13.5μg of mRNA / mouse. We used 13.5 μg instead of 15 μg to identify LNPs that deliver at progressively lower doses. Forty-eight hours later, we isolated lungs and quantified luminescence. Consistent with our previous results (**Fig. 5.6E**), we did not observe substantial differences when delivery was plotted as a function of these helper lipids (**Fig. 5.6F**). In addition, we once again observed that delivery changed with PEG; specifically, LNPs formulated with a C18 tail had greater mRNA expression than LNPs formulated with a C14 tail (**Fig. 5.6G**). Moreover, LNPs formulated with lower molar percentages of amounts of PEG, specifically LNPs containing a 15% PEG molar amount, exhibited the higher luciferase expression (**Fig. 5.6H,I**). We then analyzed the top and bottom five performing LNPs, ranked by luminescence. We found that the top five LNPs contained lower amounts of PEG, while the bottom five LNPs contained higher amounts of PEG (**Fig. 5.6J,K**). Additionally, more of the top five LNPs contained PEG with a C18 tail while all five bottom LNP contained PEG with a C14 tail (**Fig. 5.7E**). We again found that molar percent of the components

influences the efficiency of an LNP (**Fig. 5.6L**). These data led us to the preliminary conclusion that LNP chemistry played a more important role in nebulized delivery than LNP size within the ranges we tested. Future work will be needed to understand if LNP size influences delivery across larger ranges. Together, these data suggested a strong correlation between PEG-lipid ratio and helper lipid choice, and therefore, led us to a third design rule: LNPs formulated with a neutral phospholipid lipid require less PEG than LNPs formulated with a cationic helper lipid.

5.2.5 Design rules and optimized LNPs for therapeutic nebulized mRNA delivery

Using our three design rules (**Fig. 5.8A**), we selected an LNP named NLD1 for further analysis (**Fig. 5.8B**). NLD1 formed small LNPs that were stable for four days when stored at 4˚C in 1X PBS (**Fig. 5.8C**). We formulated NLD1 to carry AncNanoLuc mRNA, nebulized it, and administered it to mice at a dose of 20 µg / mouse. We compared mRNA delivery to three controls: (i) 7C3, a previously reported LNP that also uses the 7C1 lipid, (ii) cKK-E12, which delivers RNA to the liver in

s extremely low doses[28], and (iii) MC3, which has been used in a FDA-approved drug[194] (**Fig. 5.9A**). These LNPs have all been licensed for clinical development after optimization for systemic RNA delivery. They therefore provide an opportunity to evaluate whether design rules for systemic mRNA delivery can be applied to nebulized delivery. Forty-eight hours after administering the LNPs, we quantified luminescence and found it to be significantly higher in lungs treated with NLD1 than all three controls (**Fig. 5.8D, Fig. 5.9B,C**). As an additional control, we evaluated whether MC3- and cKK-E12-based LNPs outperformed NLD1 when formulated with the NLD1 molar ratio. The control LNPs did not form stable nanoparticles, demonstrating that NLD1 delivers mRNA to the lungs more efficiently. We evaluated delivery to off-target organs, and observed no luminescence in other tissues after NLD1 treatment (**Fig. 5.9D,E**).

We then evaluated the importance of LNP biophysical stability during the nebulization process. Specifically, we hypothesized that LNPs that survive nebulization ‘least damaged’ may

deliver mRNA more effectively. We therefore measured the stability of NLD1, 7C3, cKK-E12, and MC3 before and after nebulization. By comparing the relative size of different DLS peaks, we found NLD1 was more stable after nebulization than 7C3, cKK-E12, and MC3 (**Fig. 5.10A-D**). We compared LNP morphology before and after nebulization using TEM and found results consistent with our DLS analysis (**Fig. 5.10E**). These data suggest that systemic delivery LNP design rules may not select LNPs that are sufficiently stable for nebulization. Taken together, the fact that NLD1 outperformed clinically relevant LNPs optimized for systemic delivery and the fact that NLD1 stability through nebulization may be important for delivery underscore the value of designing a system to quickly uncover design rules specific for nebulization.

To understand the biodistribution profile of NLD1 in the lungs, we performed fluorescence in situ hybridization (FISH) to visualize the delivered mRNA. We nebulized mice with 100 μg of NLD1 carrying AncNanoLuc mRNA. After four hours, animals were sacrificed, lungs were isolated, and tissues were prepared for imaging. We observed broad delivery of mRNA throughout lung sections with a uniform punctate pattern (**Fig. 5.11A**). The probes displayed high specificity for AncNanoLuc mRNA with minimal background staining (**Fig. 5.11B**). Treated lungs displayed increased mRNA density at the periphery of the lung sections in the more terminal alveolar spaces. In contrast, we observed decreased mRNA density toward the center of the sections nearer to larger air spaces.

Next, analyzed mRNA uptake in four of the major epithelial cell types in the lung4. We included probes against AncNanoLuc and two markers for bronchial epithelial cells (**Fig. 5.11C**). We used probes against Foxj1and Scgb1a1 mRNA to mark ciliated and club bronchial epithelial cells, respectively2. We observed mRNA delivery to these cell types. In separate staining panels, we included probes against Pdpn and Sftpc mRNA to mark alveolar type I and II cells, respectively (**Fig. 5.11D,E**). We detected uptake of AncNanoLuc mRNA in these cell types throughout the lung as well. While we only included probes against epithelial cells, there is likely delivery to other cell types, such as alveolar macrophages. Future studies will be required to fully characterize the mRNA

uptake across more diverse cell types. However, taken with the biodistribution data, we believe these images demonstrate that NLD1 delivers mRNA broadly throughout the lung and results in uptake by the four major epithelial cell subtypes. Both of these properties are critical to achieving a strong therapeutic effect in the lung and represent opportunities for further optimization.

We performed a comprehensive analysis of NLD1 in vivo tolerability by measuring how the expression of 547 inflammatory genes changed after exposure to NLD1. Mice were treated with 50 µg mRNA via nebulization; four hours later, lungs were isolated and gene expression was measured. We chose this timepoint because RNA therapies elicit strong early immune responses that typically resolve by later timepoints such as 24 hours. Thus, we were more likely to observe an immune response at an early timepoint. Relative to untreated mice, only six of 547 genes significantly ($p<0.05$) increased by more than two-fold (**Fig. 5.8E**), demonstrating the NLD1 was well tolerated, even at early timepoints. As control, we separately administered mild dose LPS, and found that 86 genes significantly increased by two-fold (**Fig. 5.8F**). Additionally, no significant weight loss was observed in mice 24 hours after exposure to NLD1 (**Fig. 5.12A**).

We then evaluated whether NLD1 efficiently delivered mRNA encoding for a therapeutic antibody. We chose mRNA encoding membrane anchored FI6 (aFI6), an antibody that binds hemagglutinin, neutralizing 16 subtypes of influenza A viruses[195]. To optimize our dosing regimen, we evaluated the kinetics of membrane anchored protein expression following NLD1 nebulization. After formulating AncNanoLuc into NLD1, we measured luminescence at timepoints between six hours and ten days. We observed high luminescence two days after nebulization as well as lower luminescence up to seven days after nebulization (**Fig. 5.8G,H**). We then investigated whether NLD1 could be re-administered and found that luminescence increased with the number of administrations (**Fig. 5.12B**). Based on these data, we designed a treatment regimen for influenza A virus subtype H1N1 (**Fig. 5.8I**). Specifically, we nebulized mRNA encoding aFI6, and administered it three days and two days before inoculating mice with influenza A/Puerto Rico/8/1934 at 1.5x LD50. We then monitored disease progression over time by measuring mouse

weights over time. Significant weight loss post treatment with influenza is considered a marker to predict eventual death and trigger euthanasia[196]. As expected with the administered viral dose, five of the six control mice died after progressively losing weight (**Fig. 5.8J,K**). By contrast, all six animals treated with NLD1 survived. These results demonstrate the rapid, therapeutic translation of this cluster-based screening system to treat a dangerous infectious disease.

5.3 Discussion

Nebulized mRNA delivery is well positioned to treat diverse lung diseases[197]. However, nebulized RNA therapies will require clinically relevant delivery. The need for delivery is supported by a recent nebulized gene therapy clinical trial, that unfortunately, did not result in sufficient efficacy[174]; notably, the authors highlighted the need for improved delivery.

Concurrent with these advances in lung biology have been improvements in LNP design for systemic RNA delivery, which led to an FDA approved RNA drug[176]. Unlike early LNPs, which had poor therapeutic windows and required high doses for effective delivery, LNPs reported as early as 2010[22] are scalable to human doses and have clinically relevant therapeutic windows[60]. Yet most LNPs have been optimized for systemic delivery. This led to two key questions: First, can LNPs be redesigned for nebulized lung mRNA delivery? Second, how similar or dissimilar will design rules for systemic LNPs be to design rules for nebulized LNPs? By testing our NLD1 against LNPs previously optimized for systemic delivery, our initial data suggest LNP design rules for nebulized delivery can be distinct from design rules for systemic delivery. It is too early to understand whether this conclusion is consistent across all LNP chemistries, however these data support a more important general concept: answering these two key questions requires new LNP discovery workflows. Specifically, based on data demonstrating that many LNP chemical traits influence delivery and that in vitro delivery assays do not predict in vivo delivery, we reasoned an ideal way to discovery new LNPs for nebulized delivery must be easy to set up, enable chemically diverse LNPs to be tested quickly, and be performed directly in vivo. This new screening approach

is important, as it will help scientists test their own nanoparticles of choice. This in vivo screening approach identified of a novel nebulized LNP that produced therapeutically efficacious level of protein. However, future studies should be completed to understand whether NLD-1 based therapies can treat viral challenges that occur on different timescales relative to the NLD-1 treatment. Although we did not test other nanoparticle classes (e.g., peptides, or inorganics), we believe this workflow may be used to study them as well.

By testing a series of chemically distinct structures at low doses in vivo, we identified several design rules for nebulized LNPs. Thousands of additional LNPs will need to be tested before we understand whether these specific rules are applicable to all LNPs. Yet the data do provide compelling evidence that PEG molarity and structure is a critical when designing LNPs. For example, using the same 7C1 lipid, we found a 28-fold difference in delivery between the best- and worst-performing LNPs simply by changing the formulation ratio. Additionally, PEG density can alter PEG configuration[198,199]. Thus, PEG-lipid conformation may affect the efficiency of mRNA delivery to the lungs; future studies should explore the relationship between PEG conformation and nebulized delivery. We also found that the inclusion of a cationic lipids might be important for lung delivery. This hypothesis is consistent with recent work by Cheng et. al. Using their method known as selective organ targeting (SORT), they demonstrate that the inclusion of charged phospholipids could shift LNP delivery away from hepatocytes and facilitate lung delivery[165].

One additional unanswered question we hope to address is the mechanism by which changing the PEG alters nebulized lung delivery. The relationship between PEG density and systemic delivery of nanoparticles has been studied. Many clinically relevant LNP formulations contain PEG-lipids[22,28,176,200] to shield them from opsonization or increase circulation time[137,190,198,201,202]. In addition, nanoparticles developed for lung delivery have been formulated with PEG-lipids to stabilize the particles and reduce clearance[190,203]. However, there remains an important opportunity to understand how PEG density influences nebulized lung delivery. Our first

hypothesis is that the harsh conditions of nebulization predominate; specifically, all LNP formulations are damaged during nebulization, and thus the LNPs that survive this process least damaged deliver mRNA effectively. This hypothesis was consistent with our results that NLD1 was more stable than several control LNPs, which it outperformed in nebulization experiments. This hypothesis also aligned with our results demonstrating that LNPs with high PEG molarity and cationic lipids delivered mRNA in vivo more than LNPs with low PEG molarity; we reasoned that LNPs damaged during nebulization could aggregate, and therefore the combination of steric (PEG) and electrostatic (cationic) interactions, which promote self-assembly, decreased this aggregation. However, our data demonstrating that neutral LNPs deliver more mRNA with low PEG molar amounts do not support this hypothesis. A second hypothesis is that lung biology predominates; more specifically, stable LNP formulations survive nebulization, but are differentially affected by mucus and other physiological barriers within the lung. The most likely hypothesis is that both nebulization and lung biology alter delivery, and the extent to which one predominates over the other varies with the LNP. This is difficult to deconvolute in vivo; we are currently attempting to design experiments to test these hypotheses.

Finally, it is important to acknowledge several additional limitations of this study. First, our results focused on 7C1-containing LNPs, two PEG-lipids, and several helper lipids. In future iterations, we will include more diverse ionizable lipids, PEG-lipids, and helper lipids, at additional molar ratios. Further work should be done to understand other relationships between LNP composition and nebulized delivery. Second, it is possible that the protein expression kinetics we observed may vary with the mRNA payload. Additionally, one unexplored question in the field is whether protein expression kinetics can be altered by immune response. More extensive studies will need to be done to understand the relationship between payload and delivery. Third, these studies were limited to mice. The anatomy of a mouse lung may not be an optimal model for nanoparticle delivery in a human lung. It is possible these results are not replicated in larger animals such as NHPs. Fourth, our data do not exclude the possibility that LNP size may play a critical role

in delivery for larger nanoparticles. Similarly, it may be possible that zeta potential influences LNP delivery. Fifth, several other factors are involved in the pulmonary RNA delivery in diseased states. Specifically, cystic fibrosis (CF) causes severe mucus barriers within the lungs[204]. The mucus penetration of an LNP formulation will be important for the treatment of CF[205]. Finally, while we demonstrated that nebulized NLD-1 could efficiently deliver therapies prior to an infection, future studies will assess whether this vehicle and construct can be used after an infection. Even given these limitations, we believe these data provide evidence that LNP design parameters depend on the route of administration, that a cluster-based approach can efficiently identify nanoparticles that deliver drugs in vivo, and that a mRNA encoding an antibody can protect against an otherwise lethal H1N1 flu challenge.

5.4 Materials and Methods

Anchored Nano-Luciferase encoding mRNA Synthesis. mRNA was synthesized as described previously64. Briefly, the anchored nano-luciferase sequence was ordered as a DNA gBlock from IDT containing a 5' UTR with Kozak sequence, a 3' UTR derived from the mouse alpha globin sequence, and extensions to allow for Gibson assembly. The sequence was human codon optimized using the IDT website. The sequences of the GPI anchor and nano-luciferase has been previously stated[206]. The gBlock was then cloned into a PCR amplified pMA7 vector through Gibson assembly using NEB Builder with 3 molar excess of insert. All reaction transcripts were 0.8% agarose gel purified prior to assembly reaction. Subsequent plasmids from each colony were Sanger sequenced to ensure desired sequence fidelity. Plasmids were linearized with NotI-HF (New England BioLabs) overnight at 37 °C. Linearized templates were purified by ammonium acetate (Thermo Fisher Scientific) precipitation before being rehydrated with nuclease free water. IVT was performed overnight at 37 °C using the HiScribe T7 kit (NEB) following the manufacturer's instructions (N1-methyl-pseudouridine modified). RNA product was treated with DNase I (Aldevron) for 30 min to remove template and purified using lithium chloride precipitation

(Thermo Fisher Scientific). RNA was heat denatured at 65 °C for 10 min before being capped with a Cap1 structure using guanylyl transferase (Aldevron) and 2'-O-methyltransferase (Aldevron). Transcripts were then polyadenylated enzymatically (Aldevron). mRNA was then purified by lithium chloride precipitation, treated with alkaline phosphatase (NEB), and purified again. Concentrations were measured using a Nanodrop. mRNA stock concentrations were 3–5 mg/mL. Purified RNA products were analyzed by gel electrophoresis to ensure purity.

Nanoparticle synthesis. 7C1 and cKK-E12 were synthesized as previously described18,49. Detailed synthesis procedures are in the **Fig. 5.13**. D-Lin-MC3-DMA (MC3) was purchased from MedKoo Biosciences.

Nanoparticle Formulation. Nanoparticles were formulated using a microfluidic device as previously described18. Luciferase mRNA were diluted in 10mM citrate buffer (Teknova). 7C1, PEG-lipids (1,2-dimyristoyl-sn-glycero-3-phosphoethanolamine-N-[methoxy(polyethyleneglycol)-2000] and 1,2-distearoyl-sn-glycero-3-phosphoethanolamine-N-[methoxy(polyethyleneglycol)-2000]), cholesterols, and helper lipids (1,2-dioleoyl-sn-glycero-3-phosphoethanolamine, 1,2-distearoyl-sn-glycero-3-phosphocholine, 1,2-dioleoyl-3-trimethylammonium-propane, 1,2-di-O-octadecenyl-3-trimethylammonium propane, and Dimethyldioctadecylammonium) were diluted in 100% ethanol. All PEGs, cholesterols, and helper lipids were purchased from Avanti Lipids. Citrate and ethanol phases were combined in a microfluidic device by syringes (Hamilton Company) at a flow rate of 3:1.

Nanoparticle Characterization. The diameter and dispersity of the LNPs were measured using DLS (DynaPro Plate Reader II, Wyatt). LNPs were diluted in sterile 1X PBS and analyzed. To avoid using unstable LNPs, and to enable sterile purification using a 0.22 μm filter, LNPs were included only if they met 3 criteria: diameter >20 nm, diameter <200 nm, and correlation function with 1

inflection point. For screens, particles that met these criteria were pooled into respective groups. Particles were dialyzed in a 20 kD dialysis cassettes (Thermo Scientific). The nanoparticle concentration was determined using NanoDrop (Thermo Scientific).

Animal Experiments. All animal experiments were performed in accordance with the Georgia Institute of Technology's IACUC. All animals were housed in the Georgia Institute of Technology Animal Facility. BALBc (BALB/cJ, 000651) were used in all experiments. They were purchased from Jackson Laboratories. In all experiments, we used N = 2-6 mice / group.

Nebulization. Mice were loaded into a custom-built nose-only exposure system constructed of a clear PVC tee and animal restraints (CODA Small Mouse Holder, Kent Scientific). These were connected using a custom 3D-printed nosecone (3D Printing Tech) made of a flexible TPU material. The nebulizer (Aeroneb, Kent Scientific) was then placed on the upward facing port of the tee. Doses were added dropwise to the nebulizer at a rate of 50 μL / mouse / droplet. After each individual droplet was nebulized, the clear tee was inspected until the vaporized dose had cleared (approximately 15-45 seconds per drop). Droplets were added until the desired dose per animal was achieved. After the vapor had cleared following the last droplet, the mice were removed from the restraints.

Whole Organ Imaging. Tissues were isolated 48 hours after administration of LNPs, unless otherwise noted. To measure luminescence, mice were sacrificed, and organs were collected; organs were submerged in Nano-Glo Luciferase Assay Substrate (Promega) for 5 minutes before being placed on solid black paper for imaging. Luminescence was measured using an IVIS imaging system (PerkinElmer, Waltham, MA) and quantified using LivingImage software (PerkinElmer).

Transmission Electron Microscope (TEM). The nanoparticles were loaded onto the formvar coated nickel grids (Electron Microscopy Sciences, Hatfield, PA), followed by negative staining using a 2% phosphotungstic acid solution (Sigma). The morphology of the nanoparticles was imaged using HT7700 TEM (Hitachi, Tokyo, Japan) at 120 kV coupled with the Digital Micrograph camera and software suite (Gatan Inc., Pleasanton, CA).

Toxicity Study. Mice were treated with 50 µg of mRNA encapsulated in NLD1 or 5 µg of LPS. Four hours later, tissues were isolated, and flash frozen on dry ice. RNA was extracted and gene expression was examined using the nanoString nCounter FLEX. Gene expression profiles were analyzed with nanoString nSolver software. Tissues were handled and analyzed through the Emory Integrated Genomics Core (EIGC) at Emory University.

Tissue Immunostaining. Mice were treated with 100 µg of AnNanoLuc encapsulated in NLD1 or 1X PBS via nose cone nebulization. Four hours later, tissues were isolated and fixed in 1mL of 4% PFA for 24 hours. Tissues were paraffin embedded and sectioned through the Emory Winship Cancer Institute Cancer Tissue and Pathology Facility.

mRNA FISH Analysis. Delivered AncNanoLuc mRNA and endogenous mRNA were visualized in tissues using RNAscope Multiplex Fluorescent Reagent Kit v2 (Advanced Cell Diagnostics 323136) according to manufacturer's instructions. A custom probe set was designed against the AncNanoLuc mRNA sequence (ACD 879571). Foxj1 was used as a marker for ciliated bronchial epithelial cells (ACD 317091-C2). Scgb1a1 was used as a marker for club cells (ACD 420351-C3). Pdpn was used as a marker for alveolar type I cells (ACD 437771-C2). Sftpc was used as a marker for alveolar type II cells (ACD 314101-C2). Images for cell type staining were acquired using a Zeiss Plan-Apo 40x 1.3 NA oil objective on an UltraVIEW Spinning Disk Confocal Microscope equipped with a Hamamatsu Flash 4.0v2 CMOS camera. Images for biodistribution analysis were

acquired using a Zeiss Plan-Apo 20x 0.8 NA air objective. Images were captured and processed using Volocity software (PerkinElmer).

H1N1 Flu Study. mRNA encoding for aFI6 was encapsulated in NLD1. Mice were dosed with 50 μg of nebulized aFI6 mRNA per dose at 3 and 2 days prior to infection. Control mice were mock dosed with an equal volume of PBS. Mice were anesthetized with isoflurane and infected with 1.5x LD50 of influenza H1N1 A/Puerto Rico/8/1934, diluted in DMEM. For survival curves, mice weights were monitored until 14 days post infection.

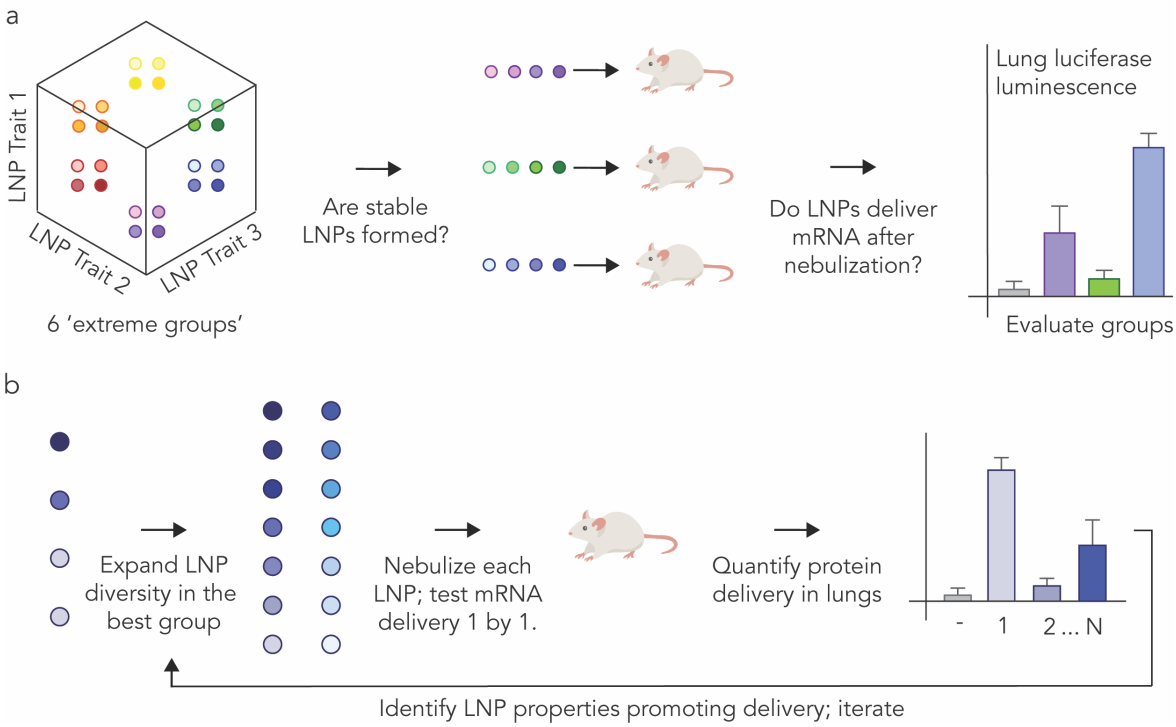

Figure 5.1. (A) An individual chemical trait is treated as an axis. Multiple chemical traits, three in this example, are evaluated simultaneously. Small groups of LNPs at the 'extremes' of this multi-dimensional chemical space are characterized by DLS and luciferase mRNA delivery following nebulization. **(B)** Any promising extreme group is then locally expanded; all the LNPs within this expanded space are characterized individually. The data from this process are used to inform subsequent LNP designs.

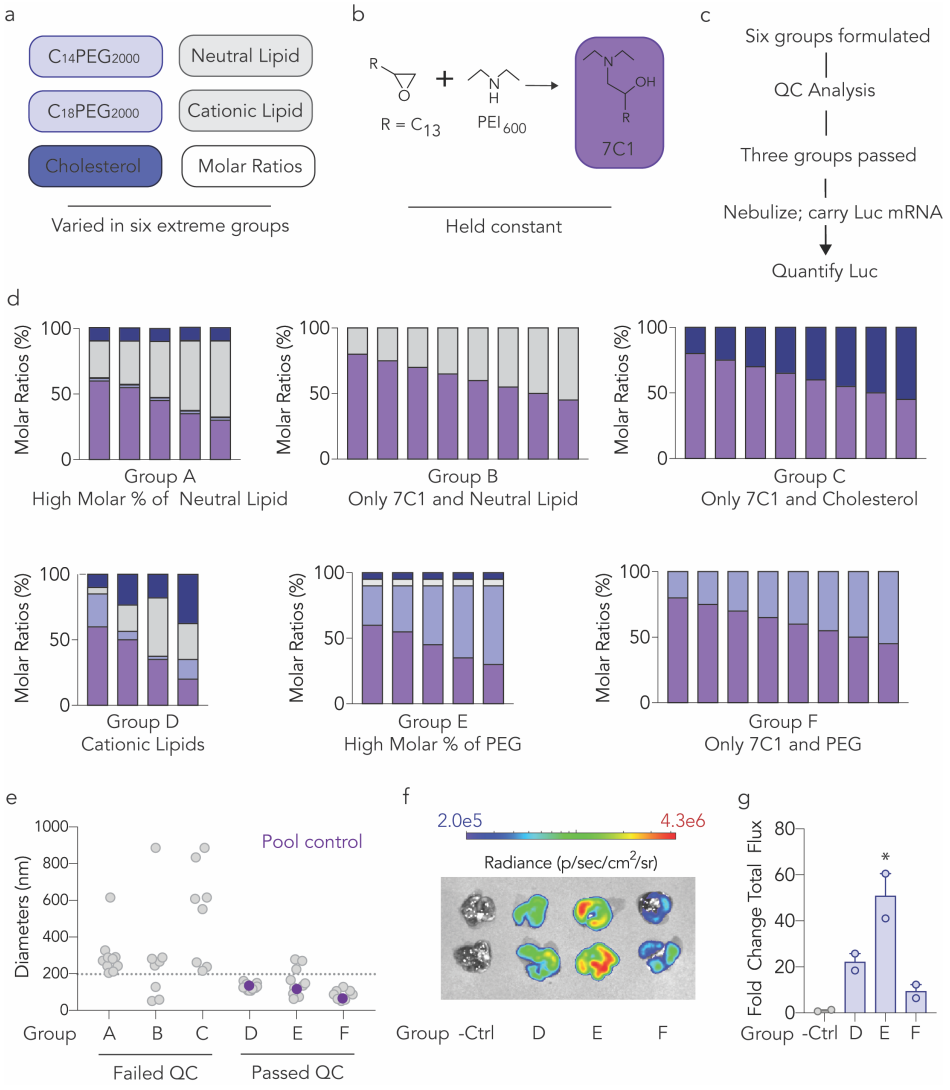

Figure 5.2. (A) We varied the structure and amount of PEG-lipid, the phospholipid charge, and cholesterol within the LNP, while **(B)** the 7C1 compound was kept constant. In this way, we created **(C,D)** six extreme groups, of which three consistently led to stable LNPs **(E)** as measured by hydrodynamic diameter of all LNPs for all six groups. In groups D-F, we found the diameter of the pooled LNPs was within the range of the individual LNPs making up the groups, further suggesting their stability. **(F,G)** Luciferase luminescence in lungs 48 hours after the three groups were nebulized and administered to mice. Unless specified otherwise, *P < 0.01, One-way ANOVA, average +/- SEM, n=2 mice/group.

a

Group A

Components				Molar Ratio				Lipid:RNA Ratio	N:P Ratio	Included in Study	Diameters	PDI
Lipomer	Cholesterol	PEG	Helper	Lipomer	Cholesterol	PEG	Helper					
7C1	Cholesterol	C14PEG2K	DOPE	60	10	2	28	10	6.8	No	243.1	Multimodal
7C1	Cholesterol	C14PEG2K	DOPE	55	10	2	33	10	6.6	No	271.4	0.552
7C1	Cholesterol	C14PEG2K	DOPE	45	10	2	43	10	6.1	No	242.6	Multimodal
7C1	Cholesterol	C14PEG2K	DOPE	35	10	2	53	10	5.6	No	204.89	0.237
7C1	Cholesterol	C14PEG2K	DOPE	30	10	2	58	10	5.2	No	211.62	0.418
7C1	Cholesterol	C14PEG2K	DOPE	60	10	2	28	10	6.8	No	290.4	0.314
7C1	Cholesterol	C14PEG2K	DOPE	55	10	2	33	10	6.6	No	327.7	Multimodal
7C1	Cholesterol	C14PEG2K	DOPE	45	10	2	43	10	6.1	No	288.98	Multimodal
7C1	Cholesterol	C14PEG2K	DOPE	35	10	2	53	10	5.6	No	281.32	0.469
7C1	Cholesterol	C14PEG2K	DOPE	30	10	2	58	10	5.2	No	615.22	Multimodal

Group B

Components				Molar Ratio				Lipid:RNA Ratio	N:P Ratio	Included in Study	Diameters	PDI
Lipomer	Cholesterol	PEG	Helper	Lipomer	Cholesterol	PEG	Helper					
7C1	Cholesterol	C14PEG2K	DOPE	80	20	0	0	10	7.5	No	885.68	Multimodal
7C1	Cholesterol	C14PEG2K	DOPE	75	25	0	0	10	7.5	No	244.8	Multimodal
7C1	Cholesterol	C14PEG2K	DOPE	70	30	0	0	10	7.4	No	265.8	0.469
7C1	Cholesterol	C14PEG2K	DOPE	65	35	0	0	10	7.3	No	52	Multimodal
7C1	Cholesterol	C14PEG2K	DOPE	60	40	0	0	10	7.2	No	59.1	Multimodal
7C1	Cholesterol	C14PEG2K	DOPE	55	45	0	0	10	7.1	No	128.1	Multimodal
7C1	Cholesterol	C14PEG2K	DOPE	50	50	0	0	10	7.0	No	288.98	Multimodal
7C1	Cholesterol	C14PEG2K	DOPE	45	55	0	0	10	6.8	No	281.32	0.469

Group C

Components				Molar Ratio				Lipid:RNA Ratio	N:P Ratio	Included in Study	Diameters	PDI
Lipomer	Cholesterol	PEG	Helper	Lipomer	Cholesterol	PEG	Helper					
7C1	Cholesterol	C14PEG2K	DOPE	80	0	0	20	10	7.3	No	615.22	Multimodal
7C1	Cholesterol	C14PEG2K	DOPE	75	0	0	25	10	7.2	No	552.4	Multimodal
7C1	Cholesterol	C14PEG2K	DOPE	70	0	0	30	10	7.1	No	885.68	Multimodal
7C1	Cholesterol	C14PEG2K	DOPE	65	0	0	35	10	6.9	No	237.07	Multimodal
7C1	Cholesterol	C14PEG2K	DOPE	60	0	0	40	10	6.8	No	215.74	Multimodal
7C1	Cholesterol	C14PEG2K	DOPE	55	0	0	45	10	6.6	No	262.11	0.537
7C1	Cholesterol	C14PEG2K	DOPE	50	0	0	50	10	6.4	No	608.6	Multimodal
7C1	Cholesterol	C14PEG2K	DOPE	45	0	0	55	10	6.2	No	834.5	Multimodal

b

Group D

Components				Molar Ratio				Lipid:RNA Ratio	N:P Ratio	Included in Study	Diameters	PDI
Lipomer	Cholesterol	PEG	Helper	Lipomer	Cholesterol	PEG	Helper					
7C1	Cholesterol	C14PEG2K	DOTAP	60	10	25	5	10	5.7	No	123.3	Multimodal
7C1	Cholesterol	C14PEG2K	DOTAP	50	23.5	6.5	20	10	6.3	No	133.1	Multimodal
7C1	Cholesterol	C14PEG2K	DOTAP	35	18	2.5	44.5	10	5.7	Yes	161.2	0.408
7C1	Cholesterol	C14PEG2K	DOTAP	20	37.5	15	27.5	10	3.8	Yes	117.3	0.323
7C1	Cholesterol	C14PEG2K	DOTMA	60	10	25	5	10	5.7	Yes	149.4	0.453
7C1	Cholesterol	C14PEG2K	DOTMA	50	23.5	6.5	20	10	6.3	Yes	143.7	0.311
7C1	Cholesterol	C14PEG2K	DOTMA	35	18	2.5	44.5	10	5.7	No	107.3	0.526
7C1	Cholesterol	C14PEG2K	DOTMA	20	37.5	15	27.5	10	3.8	No	130.7	Multimodal
7C1	Cholesterol	C14PEG2K	DDAB	60	10	25	5	10	5.7	Yes	108.6	0.459
7C1	Cholesterol	C14PEG2K	DDAB	50	23.5	6.5	20	10	6.3	Yes	107.4	0.186
7C1	Cholesterol	C14PEG2K	DDAB	35	18	2.5	44.5	10	5.8	No	118.2	Multimodal
7C1	Cholesterol	C14PEG2K	DDAB	20	37.5	15	27.5	10	3.9	Yes	124.8	0.362

Group E

Components				Molar Ratio				Lipid:RNA Ratio	N:P Ratio	Included in Study	Diameters	PDI
Lipomer	Cholesterol	PEG	Helper	Lipomer	Cholesterol	PEG	Helper					
7C1	Cholesterol	C14PEG2K	DOPE	60	5	30	5	10	5.5	Yes	73.6	0.203
7C1	Cholesterol	C14PEG2K	DOPE	55	5	35	5	10	5.1	Yes	123	0.42
7C1	Cholesterol	C14PEG2K	DOPE	45	5	45	5	10	4.3	Yes	166	0.189
7C1	Cholesterol	C14PEG2K	DOPE	35	5	55	5	10	3.5	Yes	91.5	0.428
7C1	Cholesterol	C14PEG2K	DOPE	30	5	60	5	10	3.0	Yes	135.1	0.162
7C1	Cholesterol	C18PEG2K	DOPE	60	5	30	5	10	5.4	Yes	148.1	0.146
7C1	Cholesterol	C18PEG2K	DOPE	55	5	35	5	10	5.1	Yes	62.4	0.226
7C1	Cholesterol	C18PEG2K	DOPE	45	5	45	5	10	4.3	No	278.7	0.457
7C1	Cholesterol	C18PEG2K	DOPE	35	5	55	5	10	3.4	No	224.6	Multimodal
7C1	Cholesterol	C18PEG2K	DOPE	30	5	60	5	10	3.0	No	270.2	Multimodal

Group F

Components				Molar Ratio				Lipid:RNA Ratio	N:P Ratio	Included in Study	Diameters	PDI
Lipomer	Cholesterol	PEG	Helper	Lipomer	Cholesterol	PEG	Helper					
7C1	Cholesterol	C14PEG2K	DOPE	80	0	20	0	10	6.5	Yes	86.9	0.299
7C1	Cholesterol	C14PEG2K	DOPE	75	0	25	0	10	6.2	Yes	107.1	0.411
7C1	Cholesterol	C14PEG2K	DOPE	70	0	30	0	10	5.8	Yes	52	0.319
7C1	Cholesterol	C14PEG2K	DOPE	65	0	35	0	10	5.5	Yes	64.6	0.35
7C1	Cholesterol	C14PEG2K	DOPE	60	0	40	0	10	5.1	Yes	128.7	0.382
7C1	Cholesterol	C14PEG2K	DOPE	55	0	45	0	10	4.8	Yes	105.8	0.448
7C1	Cholesterol	C14PEG2K	DOPE	50	0	50	0	10	4.4	Yes	87.1	0.323
7C1	Cholesterol	C14PEG2K	DOPE	45	0	55	0	10	4.0	No	62.4	0.226

Figure 5.3. (A) Detailed outline of nanoparticles included from groups that failed the quality control analysis (A, B, and C). **(B)** Detailed outline of nanoparticles included from groups that passed the quality control analysis (D, E, and F).

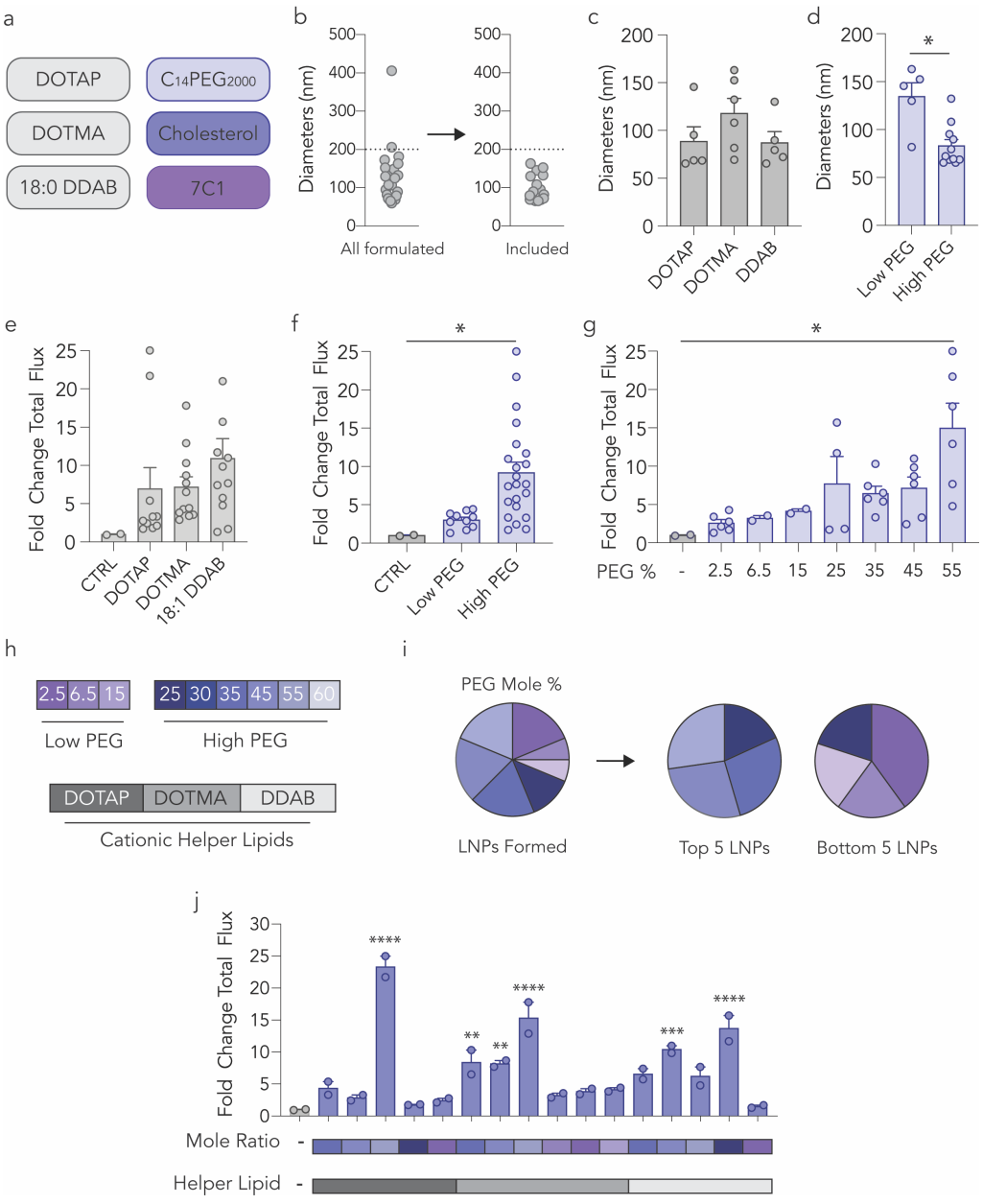

Figure 5.4. (A) LNPs were formulated with one of three cationic lipids, a PEG-lipid, cholesterol, and the compound 7C1. **(B)** LNPs with hydrodynamic diameter less than 200 nm as measured by DLS were tested individually in mice. **(C,D)** LNP diameter as a function of helper lipid and PEG molarity, respectively. *P < 0.005, two-tailed, t-test. **(E-G)** Luminescence of lungs isolated from mice, relative to an untreated control, 48 hours after administration plotted as a function of **(E)** charged lipid and **(F,G)** PEG molarity, respectively. LNPs with cationic lipids, coupled with high

PEG molarity, delivered mRNA to lungs more than LNPs with low PEG molarity. **(H-J)** PEG molarity used in this study as well as found in the best and worst performing LNPs ranked by lung luminescence. Unless specified otherwise, ****P < 0.0001, ***P < 0.0005, **P < 0.004, *P < 0.05, One-way ANOVA, average +/- SEM, n=2 mice/group.

a

Mole Ratio	1	2	3	4	5	6	7	8	9
7C1	60	60	55	45	35	30	35	50	20
PEG	25	30	35	45	55	60	2.5	6.5	15
Cholesterol	10	5	5	5	5	5	18	23.5	37.5
Helper Lipid	5	5	5	5	5	5	44.5	20	27.5

b

Components				Molar Ratio				Lipid:RNA Ratio	N:P Ratio	Included in Study	Diameters	PDI
Lipomer	Cholesterol	PEG	Helper	Lipomer	Cholesterol	PEG	Helper					
7C1	Cholesterol	C14PEG2K	DOTAP	60	5	30	5	10	5.5	No	179.6	0.341
7C1	Cholesterol	C14PEG2K	DOTAP	55	5	35	5	10	5.1	Yes	68.5	0.292
7C1	Cholesterol	C14PEG2K	DOTAP	45	5	45	5	10	4.3	Yes	95.2	0.561
7C1	Cholesterol	C14PEG2K	DOTAP	35	5	55	5	10	3.5	Yes	65.5	0.305
7C1	Cholesterol	C14PEG2K	DOTAP	30	5	60	5	10	3.0	No	193.8	Multimodal
7C1	Cholesterol	C14PEG2K	DOTAP	60	10	25	5	10	5.7	Yes	68.8	0.162
7C1	Cholesterol	C14PEG2K	DOTAP	50	23.5	6.5	20	10	6.3	No	173.1	0.304
7C1	Cholesterol	C14PEG2K	DOTAP	35	18	2.5	44.5	10	5.7	Yes	145.5	0.269
7C1	Cholesterol	C14PEG2K	DOTAP	20	37.5	15	27.5	10	3.8	No	149.1	0.529
7C1	Cholesterol	C14PEG2K	DOTMA	60	5	30	5	10	5.5	No	106.9	Multimodal
7C1	Cholesterol	C14PEG2K	DOTMA	55	5	35	5	10	5.1	Yes	141.1	0.568
7C1	Cholesterol	C14PEG2K	DOTMA	45	5	45	5	10	4.3	Yes	103.4	0.389
7C1	Cholesterol	C14PEG2K	DOTMA	35	5	55	5	10	3.5	Yes	69.4	0.268
7C1	Cholesterol	C14PEG2K	DOTMA	30	5	60	5	10	3.0	No	96.2	Multimodal
7C1	Cholesterol	C14PEG2K	DOTMA	60	10	25	5	10	5.7	No	355.7	Multimodal
7C1	Cholesterol	C14PEG2K	DOTMA	50	23.5	6.5	20	10	6.3	Yes	163.2	0.353
7C1	Cholesterol	C14PEG2K	DOTMA	35	18	2.5	44.5	10	5.7	Yes	152.6	0.202
7C1	Cholesterol	C14PEG2K	DOTMA	20	37.5	15	27.5	10	3.8	Yes	81.9	0.377
7C1	Cholesterol	C14PEG2K	DDAB	60	5	30	5	10	5.5	No	60.2	0.412
7C1	Cholesterol	C14PEG2K	DDAB	55	5	35	5	10	5.1	Yes	89.8	0.455
7C1	Cholesterol	C14PEG2K	DDAB	45	5	45	5	10	4.3	Yes	79.5	0.376
7C1	Cholesterol	C14PEG2K	DDAB	35	5	55	5	10	3.5	Yes	72.2	0.45
7C1	Cholesterol	C14PEG2K	DDAB	30	5	60	5	10	3.0	No	81.5	Multimodal
7C1	Cholesterol	C14PEG2K	DDAB	60	10	25	5	10	5.7	Yes	65.4	0.345
7C1	Cholesterol	C14PEG2K	DDAB	50	23.5	6.5	20	10	6.3	No	206	Multimodal
7C1	Cholesterol	C14PEG2K	DDAB	35	18	2.5	44.5	10	5.8	Yes	130	0.209
7C1	Cholesterol	C14PEG2K	DDAB	20	37.5	15	27.5	10	3.9	No	125.5	Multimodal

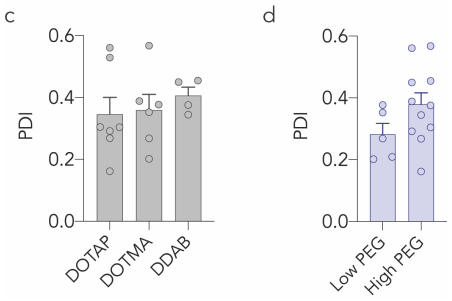

Figure 5.5. (A) Molar ratios of individual LNPs nebulized. **(B)** The first iterations of individually tested LNPs were made of 7C1, cholesterol, $C_{14}PEG_{2000}$, and positive helper lipids at 9 different molar ratios. **(C,D)**) LNP PDI as a function of helper lipid and PEG amount, respectively.

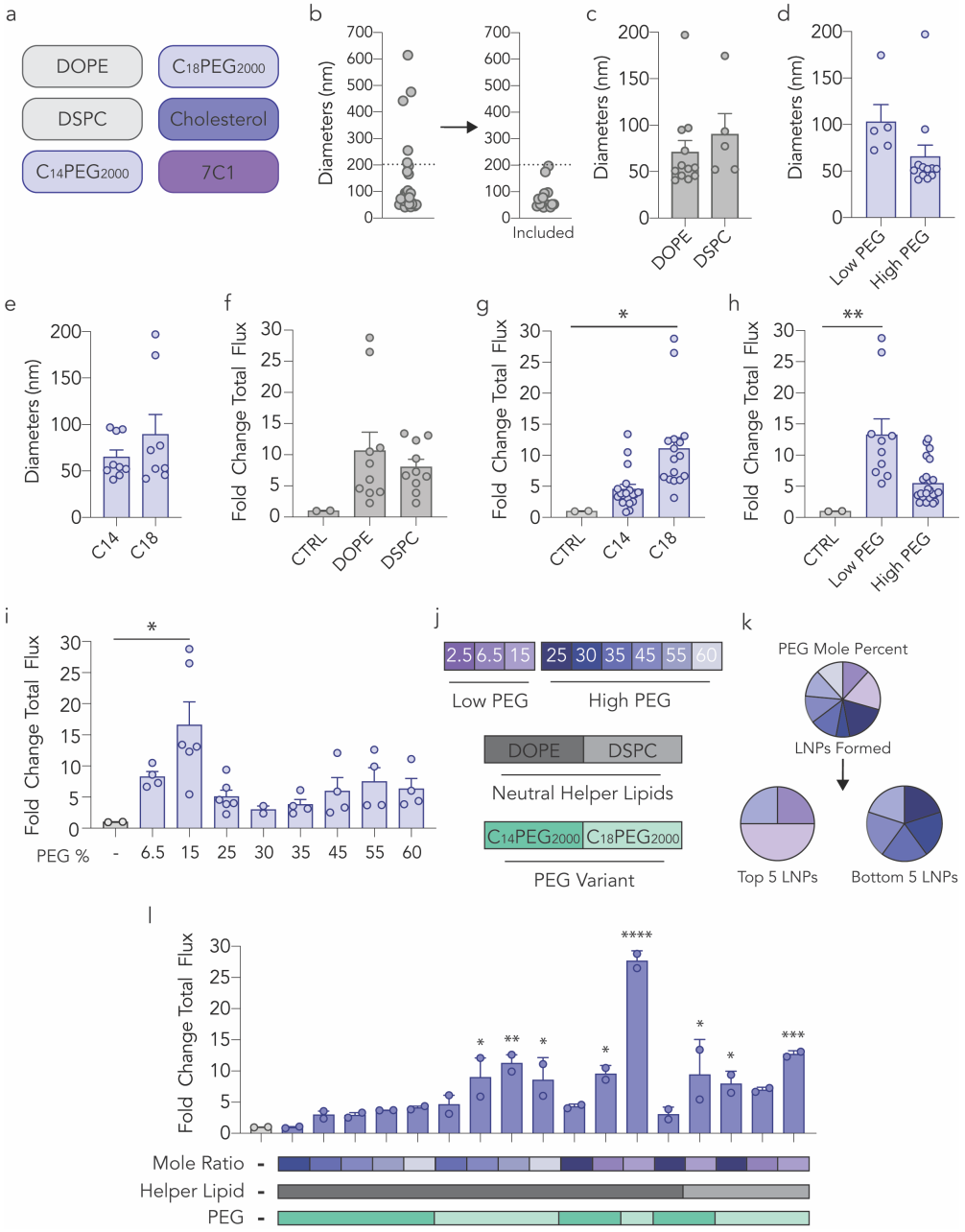

Figure 5.6. (A) LNPs were formulated with one of two neutral lipids lipids, one of two distinct PEG-lipids, cholesterol, and the compound 7C1. **(B)** LNPs with hydrodynamic diameter less than 200 nm as measured by DLS were tested individually in mice. **(C-E)** LNP diameter as a function of helper lipid, PEG molarity,and PEG-lipid tail length respectively. **(F-I)** Luminescence of lungs isolated from mice, relative to an untreated control, 48 hours after administration plotted as a

function of **(F)** neutral helper lipid, **(G)** PEG-lipid tail length, and **(H,I)** PEG molarity, respectively. LNPs with neutral lipids, coupled with low PEG molarity, delivered mRNA to lungs more than LNPs with high PEG molarity. **(J-L)** PEG molarity used in this study as well as found in the best and worst performing LNPs ranked by lung luminescence. Unless specified otherwise, ****P < 0.0001, ***P < 0.0006, **P < 0.009, *P < 0.05, One-way ANOVA, average +/- SEM, n=2 mice/group.

a

Components				Molar Ratio				Lipid:RNA Ratio	N:P Ratio	Included in Study	Diameters	PDI
Lipomer	Cholesterol	PEG	Helper	Lipomer	Cholesterol	PEG	Helper					
7C1	Cholesterol	C14PEG2K	DOPE	60	5	30	5	10	5.5	Yes	45.4	0.199
7C1	Cholesterol	C14PEG2K	DOPE	55	5	35	5	10	5.1	Yes	56.6	0.201
7C1	Cholesterol	C14PEG2K	DOPE	45	5	45	5	10	4.3	Yes	54.2	0.187
7C1	Cholesterol	C14PEG2K	DOPE	35	5	55	5	10	3.5	Yes	50.7	0.308
7C1	Cholesterol	C14PEG2K	DOPE	30	5	60	5	10	3.0	Yes	40.8	0.143
7C1	Cholesterol	C18PEG2K	DOPE	60	5	30	5	10	5.4	No	165.5	Multimodal
7C1	Cholesterol	C18PEG2K	DOPE	55	5	35	5	10	5.1	Yes	45.6	0.201
7C1	Cholesterol	C18PEG2K	DOPE	45	5	45	5	10	4.3	Yes	197.1	0.201
7C1	Cholesterol	C18PEG2K	DOPE	35	5	55	5	10	3.4	Yes	41.7	0.24
7C1	Cholesterol	C18PEG2K	DOPE	30	5	60	5	10	3.0	Yes	53.1	0.259
7C1	Cholesterol	C14PEG2K	DOPE	60	10	25	5	10	5.7	Yes	94.9	0.329
7C1	Cholesterol	C14PEG2K	DOPE	50	23.5	6.5	20	10	6.3	Yes	96.9	0.362
7C1	Cholesterol	C14PEG2K	DOPE	35	18	2.5	44.5	10	5.6	No	209.4	0.527
7C1	Cholesterol	C14PEG2K	DOPE	20	37.5	15	27.5	10	3.8	No	50.6	0.18
7C1	Cholesterol	C18PEG2K	DOPE	60	10	25	5	10	5.7	No	64.9	0.218
7C1	Cholesterol	C18PEG2K	DOPE	50	23.5	6.5	20	10	6.2	No	475.9	0.241
7C1	Cholesterol	C18PEG2K	DOPE	35	18	2.5	44.5	10	5.6	No	103.2	Multimodal
7C1	Cholesterol	C18PEG2K	DOPE	20	37.5	15	27.5	10	3.7	Yes	72.5	0.339
7C1	Cholesterol	C14PEG2K	DSPC	60	10	25	5	10	5.7	Yes	52.2	0.397
7C1	Cholesterol	C14PEG2K	DSPC	50	23.5	6.5	20	10	6.2	No	254.8	0.466
7C1	Cholesterol	C14PEG2K	DSPC	35	18	2.5	44.5	10	5.6	No	442.2	Multimodal
7C1	Cholesterol	C14PEG2K	DSPC	20	37.5	15	27.5	10	3.7	Yes	93.3	0.414
7C1	Cholesterol	C18PEG2K	DSPC	60	10	25	5	10	5.7	Yes	52.4	0.238
7C1	Cholesterol	C18PEG2K	DSPC	50	23.5	6.5	20	10	6.2	Yes	110.6	0.532
7C1	Cholesterol	C18PEG2K	DSPC	35	18	2.5	44.5	10	5.5	No	614.6	Multimodal
7C1	Cholesterol	C18PEG2K	DSPC	20	37.5	15	27.5	10	3.7	Yes	77.4	0.238

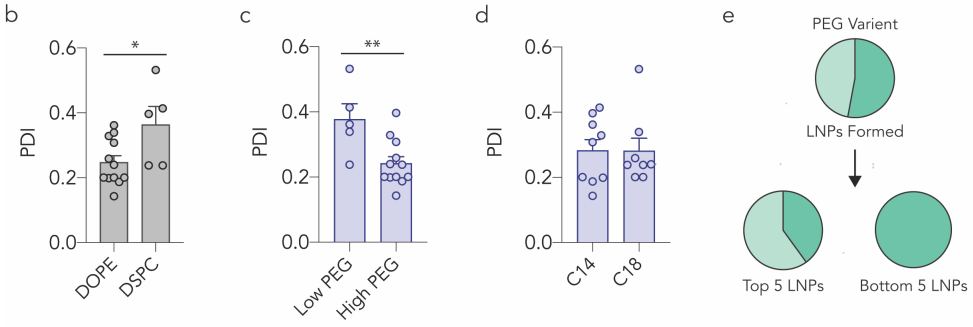

Figure 5.7. (A) The second iterations of individually tested LNPs were comprised of 7C1, cholesterol, $C_{14}PEG_{2000}$, $C_{18}PEG_{2000}$, and neutral helper lipids at 9 different molar ratios. **(B-D)** LNP PDI as a function of helper lipid, PEG amount, and PEG type, respectively. **$P < 0.008$, *$P < 0.03$, two-tailed, t-test. **(E)** PEG tail length found in the best and worst performing LNPs ranked by lung luminescence.

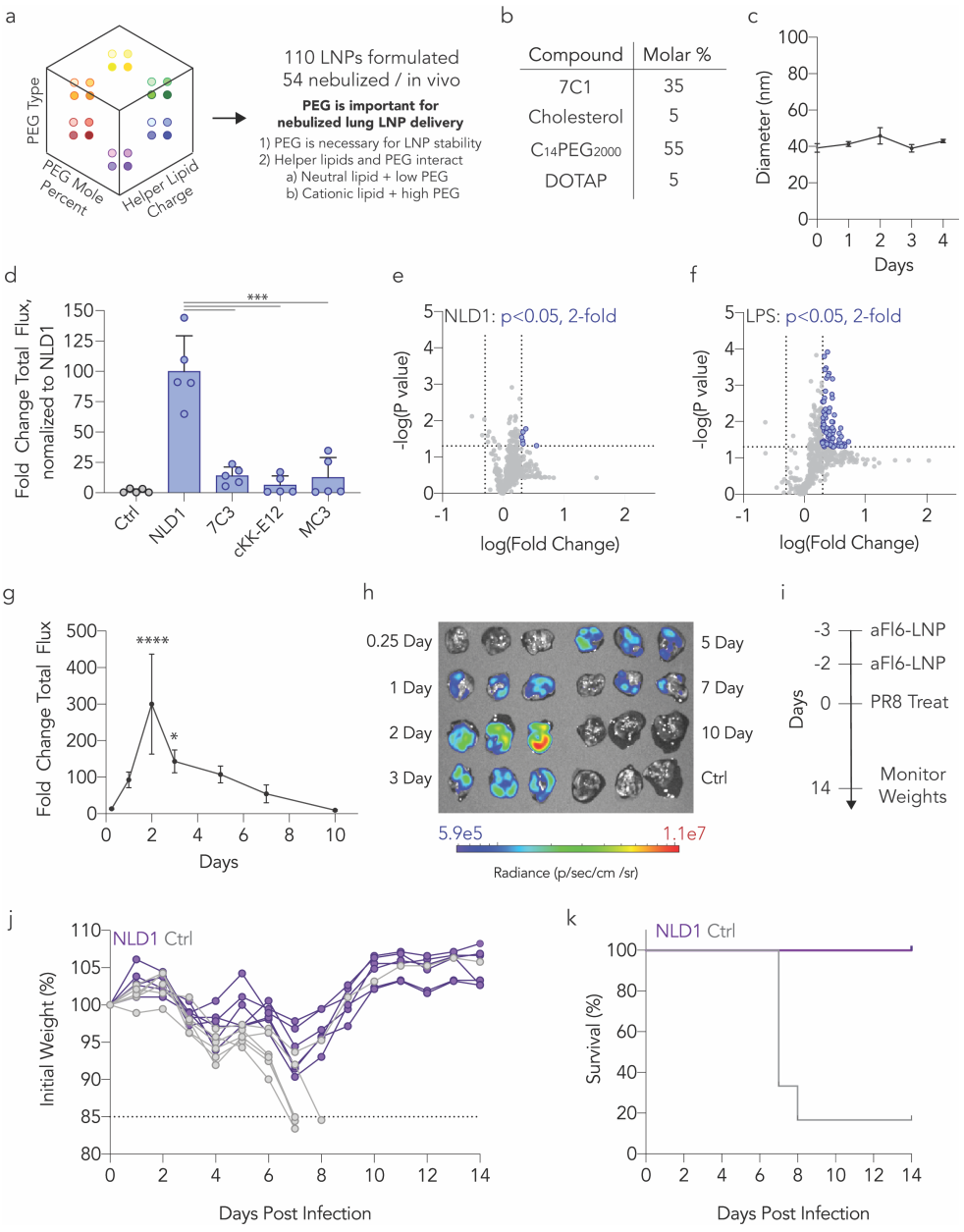

Figure 5.8. (A) LNP delivery to the lung can be improved by carefully selecting the type and molar amount of PEG-lipid. **(C)** NLD1 was designed with a cationic lipid and high amount of PEG-lipid. **(C)** NLD1 forms small, stable LNPs overtime. **(D)** NLD1 delivers mRNA to lungs at low doses in vivo more than leading LNPs previously optimized for systemic mRNA delivery. ***P < 0.0007, One-way ANOVA, average +/- SEM, n=5 mice/group. **(E,F)** 547 inflammatory genes were examine after exposure to NLD1. Compared to an LPS control, NLD1 is well tolerated in vivo.

Dotted vertical lines indicate>2x fold change in gene expression. The dotted horizontal line indicates a p-value of 0.05. **(G,H)** NLD1 carrying AncNanoLuc was administered at a dose of 20 µg / mouse. Protein expression was analyzed over several days. ****P < 0.0001, *P < 0.03, One-way ANOVA, average +/- SEM, n=3 mice/group. **(I)** NLD1 therapeutic treatment regimen for H1N1 study. Mice were treated with two NLD1 treatments (a total dose of 100 µg / mouse) prior to XYZ dose of PR8 virus. **(J,K)** Mouse weights were taken daily for up to 14 days post infection. All mice treated with NLD1 recovered based on weights. Significantly, 5 out of 6 mice treated with H1N1 only lost 85% or more of body weight and were sacrificed. n=6 mice/group.

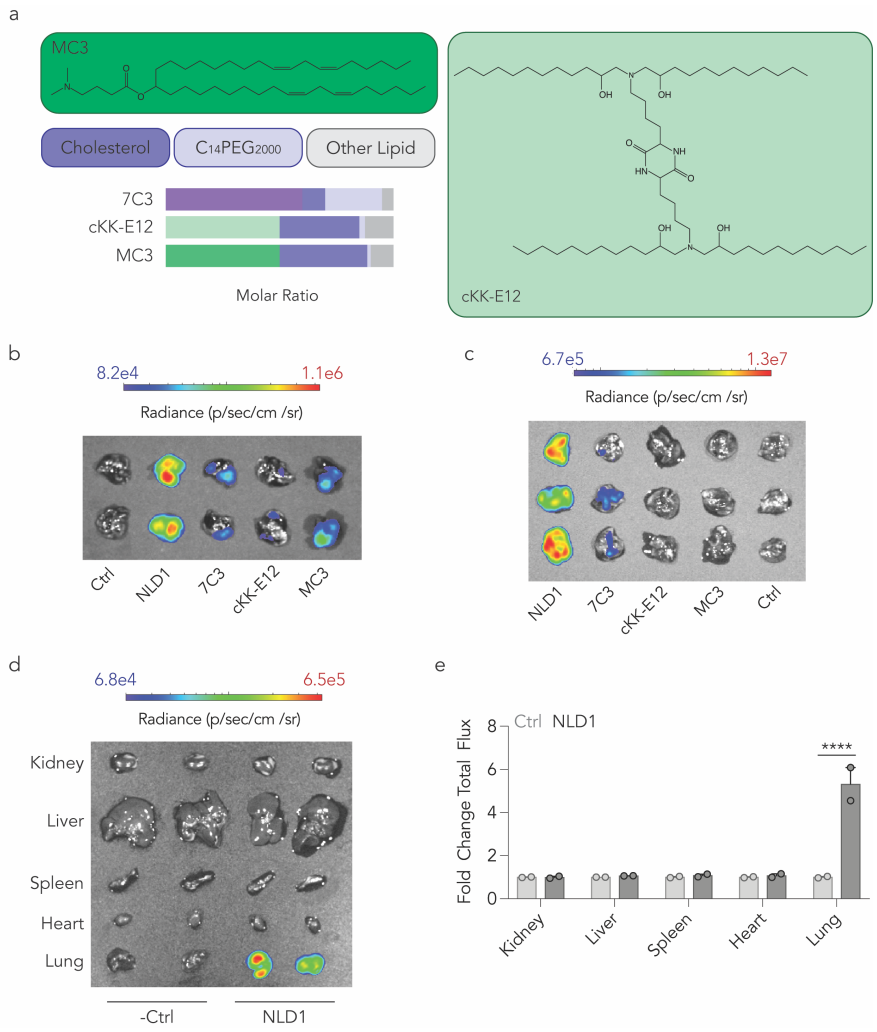

Figure 5.9. (A) 7C3, cKK-E12, and MC3 were formulated by combining the ionizable material 7C3, cKK-E12, or MC3, $C_{14}PEG_{2000}$, cholesterol, and a neutral phospholipid. LNPs were administered via nebulization to lungs and **(B,C)** luciferase luminescence was measured. **(D,E)** 48 hours post nebulization with NLD1, luciferase luminescence was measured in kidney, liver, spleen, heart, and lungs; we only found measurable luminescence in the lungs. ****$P < 0.0001$, One-way ANOVA, average +/- SEM, n=2 mice/group.

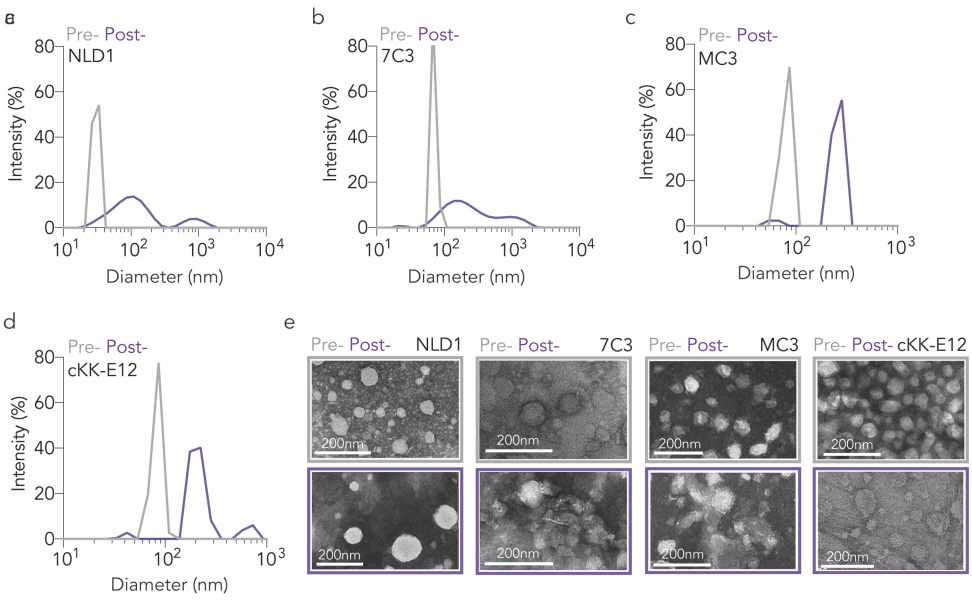

Figure 5.10. (A) LNP diameter pre- and post-nebulization of NLD1, **(B)** 7C3, **(C)** MC3, and **(D)** cKK-E12. **(E)** TEM image of NLD1, 7C3, MC3, and cKK-E12 pre- and post-nebulization.

a

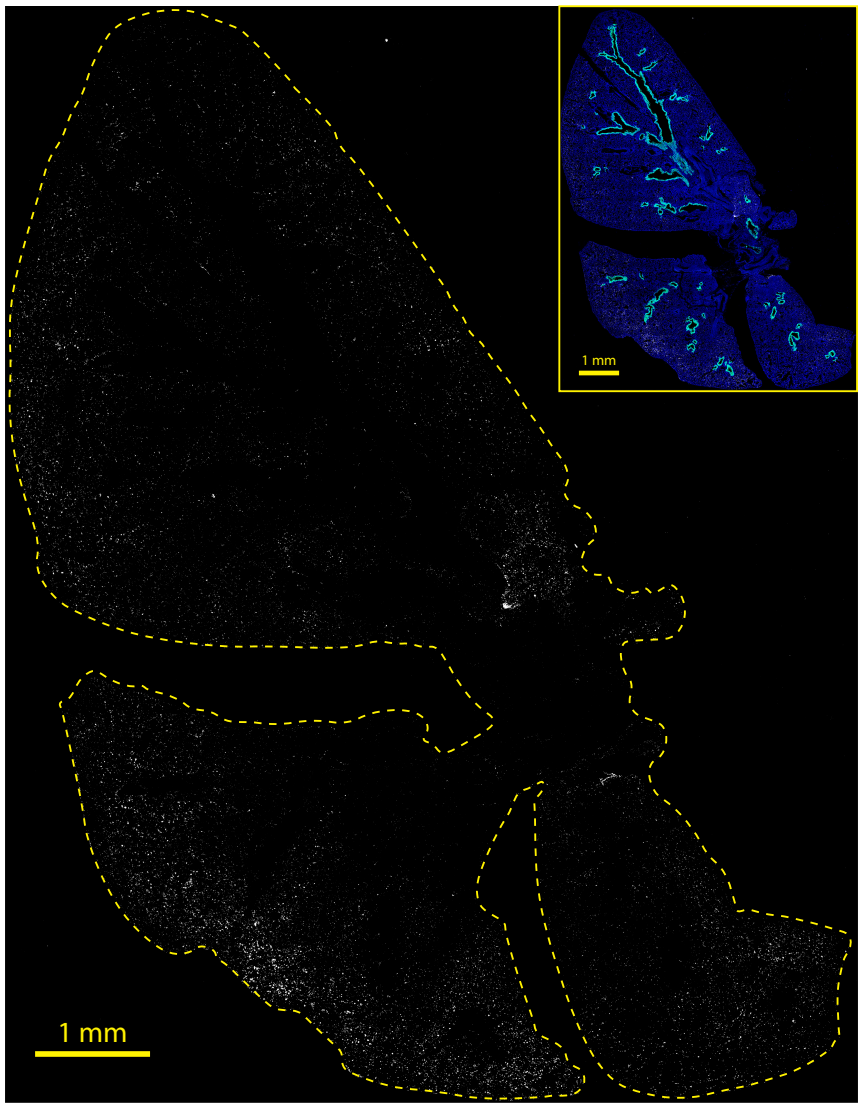

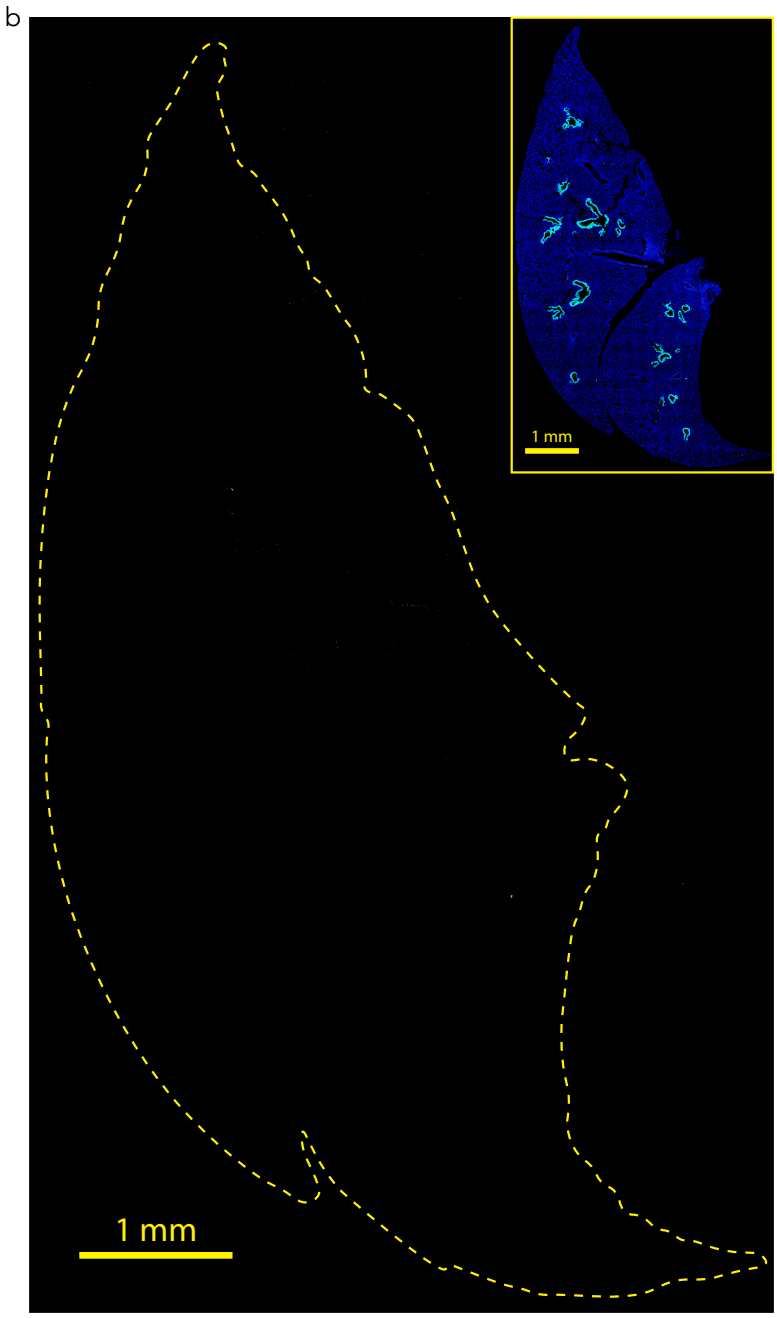
b
1 mm
1 mm

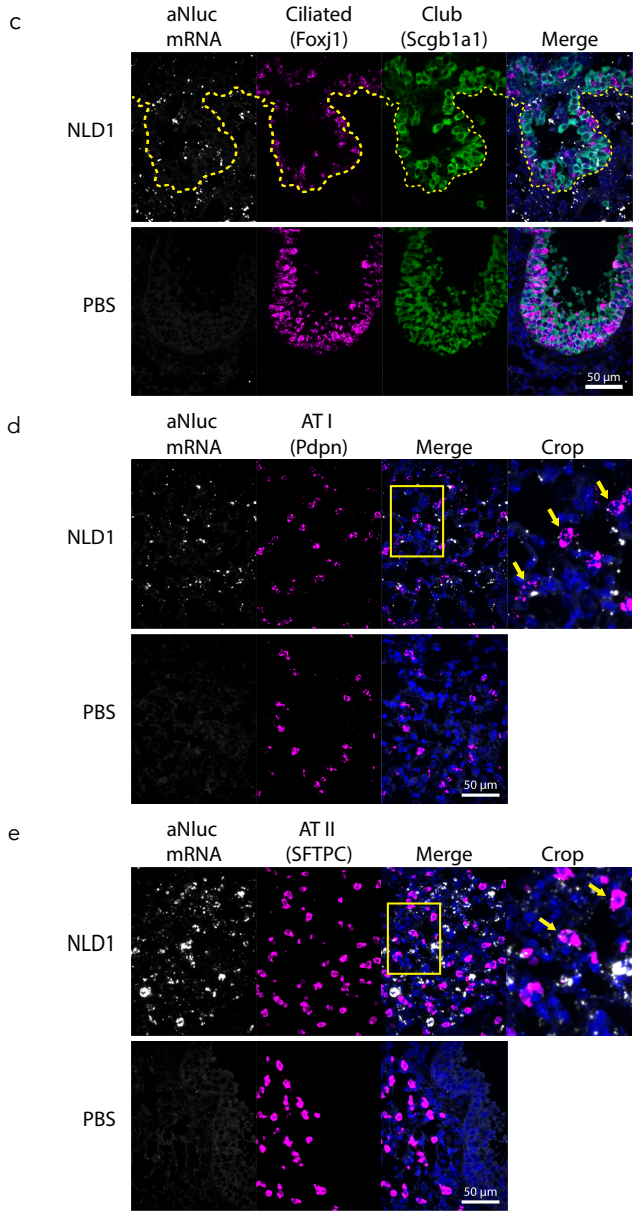

Figure 5.11. (A) Biodistribution of AncNanoLuc mRNA throughout the lung of a mouse 4 hrs post nebulization with 100 µg mRNA. Small inset shows a lung section stained for Scgb1a1 mRNA to mark the bronchial airways (green), AncNanoLuc mRNA (white), and DAPI (blue). The expanded image shows only AncNanoLuc mRNA(white) with an outline of the lung section. The AncNanoLuc mRNA displays a punctatedistribution with higher densi-ties toward the periphery of

the lung. **(B)** Negative control lung section treated with AncNanoLuc probes 4 hours post nebulization with 1x PBS. Small inset shows a lung section stained for Scgb1a1 mRNA to mark the bronchial airways (green), AncNanoLuc mRNA (white), and DAPI (Blue). The expanded image shows only AncNanoLuc mRNA (white) with an outline of the lung section. No major background of the AncNanoLuc mRNA probes was observed in the PBS section. **(C)** FISH analysis for AncNanoLuc mRNA uptake in epithelial cell subtypes. Tissues were obtained 4 hours post nebulization with either 100 μg of AncNanoLuc mRNA in NLD-1or 1x PBS and processed for FISH analysis. Probes against AncNanoLuc mRNA (white)show strong staining in treated tissues. Probes against Foxj1 mRNA marking ciliated bronchial epithelial cells (magenta) and Scgb1a1 mRNA marking bronchial club cells (green) were used to visualize the bronchiolar space. Uptake of AncNanoLuc mRNA was observed in these bronchial epithelial cells**. (D,E)** Probes against Pdpn mRNA and Sftpc mRNA were used to mark alveolar type I and II epithelial cells, respectively (magenta). Uptake of AncNanoLuc mRNA can be seen in both of these cell types as indicated by the yellow arrows.

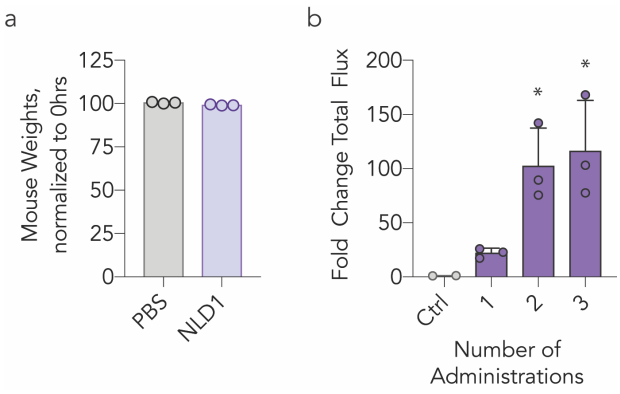

Figure 5.12. (A) Mice showed no significant weight loss after exposure to 50 µg of NLD1 to carry AncNanoLuc mRNA via nebulization. **(B)** NLD1 was readministered at a dose of 20 µg / mouse. *P < 0.04, One-way ANOVA, average +/- SEM, n=3 mice/group

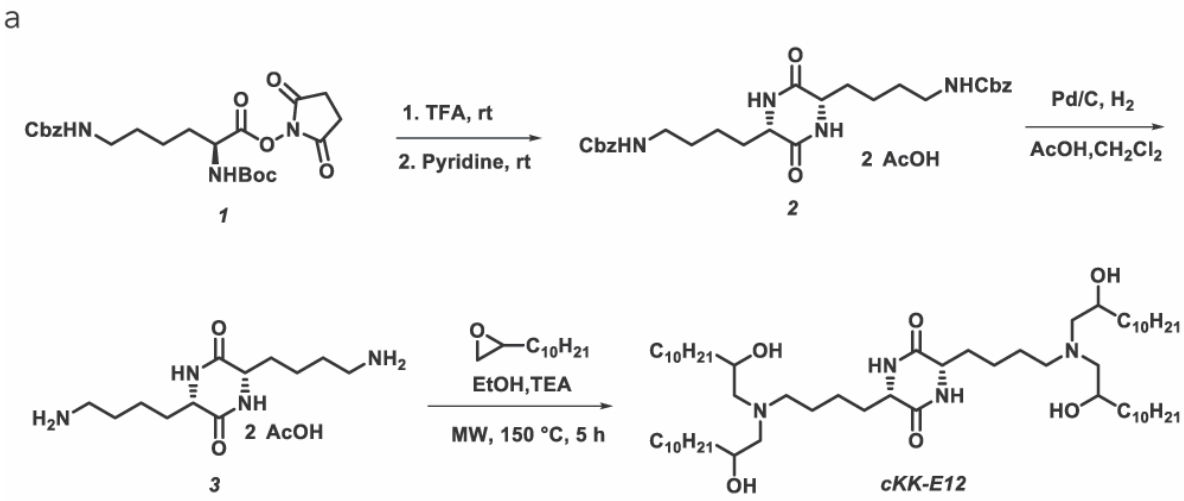

Figure 5.13. (A) Chemical synthesis of cKK-E12.

CHAPTER 6. HIGH THROUGHPUT IN VIVO LNP HELPER LIPID OPTIMIZATION ENABLES SYSTEMIC LUNG GENE EDITING

6.1 Introduction

mRNA-based drugs can treat disease by transiently expressing therapeutic proteins[7]. To achieve a therapeutic effect, mRNA must be internalized into target cells and translated into protein without undergoing RNase-mediated degradation or eliciting an undesirable immune response[139]. One class of delivery vehicles is LNPs, which have delivered mRNA to target cells in several clinical trials. Specifically, LNPs have delivered mRNA-based COVID vaccines into muscle after local administration[178,207], delivered mRNA encoding Cas9 nucleases into the liver after systemic administration, and delivered siRNA to the liver following systemic administration[60]. These data support efforts to design LNPs that deliver mRNA to additional tissues after systemic administration.

Scientists have taken two approaches to promote mRNA delivery to non-liver tissues. In the first, targeting ligands including antibodies or aptamers are added to LNPs. In one example, mRNA loaded LNPs were targeted to Ly6c+ leukocytes utilizing anchored secondary scFv enabling targeting (ASSET), which integrates monoclonal antibodies into the LNPs membrane in order to achieve targeting[141]. In another example, plasmalemma vesicle- associated protein targeting LNPs covalently conjugated with targeting antibodies increased lung protein expression 40-fold compared to the control LNP without the ligands[208]. The second approach scientists use is to alter cellular tropism by changing the chemical composition of the lipids making up the LNP. LNPs without targeting ligands are typically composed of four components: an ionizable or cationic lipid; a PEG-lipid; a cholesterol; and a “helper” lipid. In one example, an LNP was made to selectively deliver mRNA to lung endothelial cells by changing the LNP composition[158]. In another example, RNA-lipoplexes comprised of DOTMA, DOTAP, DOPE, and cholesterol were targeted

to lymphoid-resident dendritic cells by titrating negative charge[167]. In another, the composition of the ionizable lipid in the LNP increased protein expression within spleen B lymphocytes following intravenous administration[209]. Finally, by adding a fifth molecule to the LNP, authors designed LNPs with improved tropism to the spleen and lung following intravenous injection[165].

These studies led us to hypothesize that the LNP helper lipid could be optimized to reduce delivery to the liver and increase delivery to non-liver cell types. To test this hypothesis, we used a DNA-barcoding based functional in vivo mRNA screening system[159,160,186] to evaluate how 18 helper lipids affected LNP diameter, polydispersity, cell type-specific targeting to 19 cell types, using 129 LNPs, all in vivo. These DNA barcoding data identified how helper lipid structure affects LNP delivery in vivo; they also revealed three new LNP compositions that deliver mRNA to distinct cell types at clinically relevant doses.

6.2 Results

6.2.1 Characterizing of helper lipid composition on LNP formation

To test the hypothesis that helper lipid structure could shift mRNA delivery to non-liver cell types, we formulated 144 chemically distinct LNPs with microfluidic mixing16. Specifically, we mixed the canonical nanoparticle components with nucleic acids at a nanoparticle component: nucleic acid mass ratio of 10: 1 (**Fig. 6.1A**). To isolate the effect of the helper lipid, the other three LNP components were previously validated. As a control to ensure changes in delivery were not driven by a specific molar ratio of the four components, we formulated LNPs with four molar ratios (**Fig. 6.1B**, **Fig. 6.2**). Thus, each of the 18 helper lipids was formulated eight times (**Fig. 6.3**). In our helper lipid array, we varied two traits. First, we varied charge: eight carried a neutral charge, seven carried an anionic charge, and three carried a cationic charge. Second, based on the hypothesis that helper lipid traits other than charge could affect LNP delivery via distinct biophysical mechanisms[210,211], we also varied helper lipid tail structure and linker (**Fig. 6.2**). After formulating the 144 LNPs, we investigated whether helper lipid composition influenced LNP

hydrodynamic diameter and polydispersity, as measured by dynamic light scattering (DLS). We observed a relationship between helper lipid charge and the resulting LNP diameter; LNPs with anionic helper lipids formed smaller particles than LNPs formed with cationic helper lipids (**Fig. 6.1C**). We then quantified LNP hydrodynamic diameter as a function of the 18 helper lipids (**Fig. 6.1D**, **Fig. 6.3**) and found no statistical relationship between individual helper lipids and diameter (**Fig. 6.1E**). Finally, we found that LNP hydrodynamic diameter does not change with the molar ratio of helper lipid added to the LNP (**Fig. 6.1F**).

6.2.2 LNP containing cationic helper lipids preferentially deliver to lung cell types compared to neutral and anionic libraries

We then investigated whether helper lipid structure influenced LNP-mediated mRNA delivery in vivo. Given the impracticality of injecting, sacrificing, and performing fluorescent activated cell sorting (FACS) analysis to quantify cell-level delivery in several hundred mice, we utilized a DNA barcoding system that quantifies functional mRNA delivery (i.e., mRNA translated into functional protein) mediated by many LNPs in a single animal at the cellular level13-15 (**Fig. 6.4A**). In this system, LNP-1, with chemical structure 1, is formulated to carry Cre mRNA and DNA barcode 1; LNP-N, with chemical structure N, is formulated to carry Cre mRNA and DNA barcode N. LNPs with a hydrodynamic diameter less than 200 nm and a single peak on the DLS spectrum are pooled and administered to Ai14 mice19. Ai14 cells contain a Lox-Stop-Lox-tdTomato reporter driven by a CAG promoter; cells in which Cre mRNA has been translated into functional protein that excises the Lox-Stop construct from the genome become tdTomato+. tdTomato+ cells are sorted with FACS, and then sequenced to identify barcodes in functionally transfected cells. Thus, functional mRNA delivery is quantified as the percentage of tdTomato+ cells and the relative rank of each individual LNP is calculated as “normalized delivery”, which is analogous to counts per million in RNA-sequencing experiments.

To avoid LNPs with opposite charges mixing after pooling, we performed three separate experiments, creating one library for each lipid charge. Of the 24 cationic LNPs we formulated, 23 met our 200 nm and single DLS peak selection criteria. These LNPs were pooled and injected into four mice at a total dose of 1.0 mg / kg nucleic acid (i.e., 0.043 mg / kg / LNP, on average). We similarly formulated 64 LNPs with a neutral helper lipid; 59 met pooling criteria and were administered to four separate mice at a total dose of 1.0 mg / kg nucleic acid. Finally, we formulated 56 LNPs with an anionic helper lipid, of which 55 met pooling criteria, and were administered to four separate mice at a total dose of 1.0 mg / kg nucleic acid. Three days later, we sacrificed mice and quantified the percentage of tdTomato+ cells for 20 cell types (**Fig. 6.5**). We evaluated the following two controls. Firstly, we included a DNA barcode that was not encapsulated in an LNP as a negative control. Since DNA does not readily enter cells, this barcode should be delivered less efficiently into cells than DNA barcodes carried in LNPs, and thus should have a low normalized delivery, which was consistent with our observations (**Fig. 6.4B**, **Fig. 6.6**). Second, we quantified mouse weights post-LNP administration. Relative to PBS-treated mice, those treated with barcodes did not lose weight (**Fig. 6.7**).

We then quantified mRNA delivery as a function of helper lipid charge in five lung cell types, six liver cell types, four splenic cell types, two heart cell types, and two kidney cell types (Fig. 2D-H). In all five cell types, LNPs formulated with a cationic helper lipid delivered mRNA to the lung, whereas LNPs formulated with neutral or anionic LNPs did not (**Fig. 6.4C**). When cationic helper lipid LNPs were administered, the highest tdTomato+ percentage, over 50%, was measured in endothelial cells, which may be explained by the physical accessibility of these cells when LNPs are administered intravenously. Between 10% and 25% of lung dendritic cells, T cells, B cells, and monocytes were also transfected. These data suggest that immune cells which are less accessible than endothelial cells, may still be transfected by systemically administered LNPs. Interestingly, we observed a distinct trend in the liver. Neutral and anionic helper lipid LNPs led to significantly higher mRNA delivery than cationic helper lipid LNPs (**Fig. 6.4D**). Notably, the

percentage of tdTomato+ lung cells was higher than the percentage of tdTomato+ liver cells when the cationic LNP helper lipids were injected. We observed that spleen delivery did not significantly vary as a function of LNP helper lipid (**Fig. 6.4E**). When we examined delivery in the kidney and heart, we identified low but statistically significantly increases in mRNA delivery were measured with cationic and neutral helper lipid LNPs, compared with anionic helper lipid LNPs (**Fig. 6.4F-G**).

We then used NGS to determine how all 138 LNPs delivered nucleic acids in vivo. First, we investigated whether normalized delivery changed as a function of LNP hydrodynamic diameter and found no relationship between LNP size and delivery within the tested range (**Fig. 6.4H**), which is consistent with our previous results13. Next, we used the normalized delivery to calculate the fold change enrichment of each helper lipid in the lung, liver, and spleen. Enrichment analysis determines how often a specific property appears in particles that performed in the top 10% and bottom 10%. Fold enrichment change is calculated by subtracting enrichment in the bottom 10% from enrichment in the top 10% (**Fig. 6.8A**). In the cationic library, we found that 18:0 DDAB was the most enriched helper lipid in all cell types (**Fig. 6.8B-D**). Next, we studied the enrichment profile of the neutral helper lipids. We did not observe a single helper lipid enrich in all liver or spleen cell types (**Fig. 6.9A-C**). Using the neutral library enrichment data, we investigated the effect of tail structure on delivery by comparing the enrichment of three neutral lipids with the same head group and linker, but different tail structure. We found that the sterate was the most enriched tail structure in both the liver and spleen (**Fig. 6.9D-F**). We then investigated the effect of head group on delivery within the neutral library by comparing the enrichment of four neutral lipids with the same tail group and linker, but different head group. We found that ammonium and methylamine enriched positively while dimethylamine and trimethylamine negatively enriched (**Fig. 6.9G-I**). Finally, we examine the enrichment profile in the anionic library; we found that 18:1 PA enrich the most in all liver and spleen cell types (**Fig. 6.10A-C**). Interestingly, similar to the neutral library, we found that smaller, less complex head groups enriched more than larger, more

complex head groups in the liver and spleen (**Fig. 6.10D-E**). These enrichment analyses lead us to believe there i(s a relationship between tail and head structures and nanoparticle delivery.

6.2.3 Top LNPs from each screen mimicked the screening results

Based on the screening data, we selected the top LNP from each library and quantified whether it delivered mRNA as predicted by the screen. Each LNP was formulated to carry cre mRNA and injected into Ai14 mice at 1.3 mg / kg. Three days later, we quantified the percentage of tdTomato+ cells in the lungs, liver, spleen, kidney, and heart by whole tissues imaging and flow cytometry. Specifically, we formulated a stable, small cationic LNP with cationic helper lipid 18:0 DABB which is referred to as 'Cationic LNP' (**Fig. 6.11A**). We found that the cationic LNP preferentially targeted lung cell types more than liver cell types (**Fig. 6.11B**). Specifically, the Cationic LNP delivered to lung endothelial cells, as predicted by the screen. Additionally, less significant delivery was observed in kidney immune cells and heart endothelial cells (**Fig. 6.11C, Fig. 6.12A**). Next, a small, stable neutral LNP was formulated with neutral helper lipid DSPC (referred to as 'Neutral LNP') (**Fig. 6.11D**). Similar to the screen, the neutral LNP preferentially delivered to liver cell types (**Fig. 6.11E**), most significantly, endothelial and Kupffer cells (**Fig. 6.11F**). Significant delivery was also observed in spleen DCs (**Fig. 6.12B**). Finally, an anionic LNP formed small, stable particles with anionic helper lipid 18:1 PA which is referred to as 'Anionic LNP' (**Fig. 6.11G**). Once again, we observed preferential delivery to liver cells types (**Fig. 6.11H, Fig. 6.12C**) with the highest delivery to endothelial cells (**Fig. 6.11I**). In all cases, we observed no significant weight loss in the mice (**Fig. 6.13**).

6.2.4 Cationic LNPs can be used to efficiently in genome editing

Based on these findings, we decided to focus on the relationship between cationic lipids and lung endothelial delivery. We first evaluated the ability of the cationic LNP to deliver therapeutically relevant payloads intravenously. Gene editing technologies, such as CRISPR–Cas

systems, can be a valuable therapeutic to treat diseases. Gene editing facilitated by LNPs outside the liver would be valuable to the field. Moreover, certain diseases may benefit from intravenous administration of gene modulators. We formulated the Cationic LNP to carry spCas9 mRNA and sgRNA. We intravenously injected WT mice with two doses of sgControl or sgRNA targeting ICAM-2. Five days later, lung and liver cells were isolated; ICAM-2 protein expression and indels were quantified (**Fig. 6.14A, Fig. 6.15**). Compared to the sgControl, we observed a 50% reduction of ICAM-2 expression in lung endothelial cells and no significant reduction in liver endothelial cells (**Fig. 6.14B**). As a confirmation, we observed significant indels in lung endothelial cells when compared to mice treated with the control (**Fig. 6.14C**) using Tracking of Indels by Decomposition [212]; no off-target effects were observed in the liver (**Fig. 6.14D**). These data suggest that cationic LNPs can be used to delivery gene editing tools in vivo.

6.3 Discussion

Systemically administered RNA drugs have been safely delivered to the liver in patients, underscoring the potential value of LNPs with tropism to other tissues. To test the hypothesis that a single LNP trait can increase the ratio of non-liver delivery to liver delivery, we quantified how 137 chemically distinct LNPs delivered mRNA to 19 cell types across the liver, spleen, kidney, heart, and lung in vivo using functional DNA barcoding. These studies revealed that helper lipid composition alters tissue- and cell-level tropism and identified three novel LNPs with tunable in vivo tropism, without the use of targeting ligands. One of these LNPs, named LNP-Lung1, co-delivered Cas9 mRNA and sgRNA, leading to pulmonary gene editing in adult mice. These data support the hypothesis that one LNP component can increase non-liver tropism and suggest that DNA barcoding can be used to understand how LNP chemistry alters delivery *in vivo.*

6.4 Materials and Methods

Cre mRNA Synthesis. mRNA was synthesized as described previously21. Briefly, the anchored nano-luciferase sequence was ordered as a DNA gBlock from IDT containing a 5' UTR with Kozak sequence, a 3' UTR derived from the mouse alpha globin sequence, and extensions to allow for Gibson assembly. The sequence was human codon optimized using the IDT website. The sequences of the GPI anchor and nano-luciferase has been previously stated21. The gBlock was then cloned into a PCR amplified pMA7 vector through Gibson assembly using NEB Builder with 3 molar excess of insert. All reaction transcripts were 0.8% agarose gel purified prior to assembly reaction. Subsequent plasmids from each colony were Sanger sequenced to ensure desired sequence fidelity. Plasmids were linearized with NotI-HF (New England BioLabs) overnight at 37 °C. Linearized templates were purified by ammonium acetate (Thermo Fisher Scientific) precipitation before being rehydrated with nuclease free water. IVT was performed overnight at 37 °C using the HiScribe T7 kit (NEB) following the manufacturer's instructions (N1-methyl-pseudouridine modified). RNA product was treated with DNase I (Aldevron) for 30 min to remove template and purified using lithium chloride precipitation (Thermo Fisher Scientific). RNA was heat denatured at 65 °C for 10 min before being capped with a Cap1 structure using guanylyl transferase (Aldevron) and 2'-O-methyltransferase (Aldevron). Transcripts were then polyadenylated enzymatically (Aldevron). mRNA was then purified by lithium chloride precipitation, treated with alkaline phosphatase (NEB), and purified again. Concentrations were measured using a Nanodrop. mRNA stock concentrations were 3–5 mg/mL. Purified RNA products were analyzed by gel electrophoresis to ensure purity.

Nanoparticle Formulation. Nanoparticles were formulated using a microfluidic device as previously described. cKK-E12 was purchased from Organix. Cre mRNA and DNA barcodes were diluted in 10mM citrate buffer (Teknova). DNA Barcodes were purchases from IDT. All PEGs, cholesterols, and helper lipids were diluted in 100% ethanol and purchased from Avanti Lipids.

Citrate and ethanol phases were combined in a microfluidic device by syringes (Hamilton Company) at a flow rate of 3:1.

Nanoparticle Characterization. The diameter and polydispersity of the LNPs were measured using DLS (DynaPro Plate Reader II, Wyatt). LNPs were diluted in sterile 1X PBS and analyzed. To avoid using unstable LNPs, and to enable sterile purification using a 0.22 μm filter, LNPs were included only if they met 3 criteria: diameter >20 nm, diameter <200 nm, and correlation function with 1 inflection point. For screens, particles that met these criteria were pooled into respective groups. Particles were dialyzed in a 20 kD dialysis cassettes (Thermo Scientific). The nanoparticle concentration was determined using NanoDrop (Thermo Scientific).

Animal Experiments. All animal experiments were performed in accordance with the Georgia Institute of Technology's IACUC. All animals were housed in the Georgia Institute of Technology Animal Facility. Ai14s were breed at the Georgia Institute of Technology Animal. C57BL/6J (B6/000664) were purchased from Jackson Laboratories. In all experiments, we used N = 3-4 mice / group.

Cell Isolation & Staining. Cells were isolated 24 or 72 hours after injection with LNPs unless otherwise noted. Mice were perfused with 20 mL of 1X PBS through the right atrium. Tissues were finely cut, andt hen placed in a digestive enzyme solution with Collagenase Type I (Sigma Aldrich), Collagenase XI(Sigma Aldrich) and Hyaluronidase (Sigma Aldrich) at 37 ºC at 550 rpm for 45 minutes. The digestive enzyme for heart and spleen included Collagenase IV. Cell suspension was filtered through 70μmmesh and red blood cells were lysed. Cells were stained to identify specific cell populations and sorted using the BD FacsFusion cell sorters in the Georgia Institute of TechnologyCellular Analysis Core. The antibody clones used were: anti-CD31 (390, BioLegend), anti-CD45.2 (104,5BioLegend), anti-CD68 (FA11, Biolengend), anti-CD11b (M1/70, Biolegend),

anti-CD11c (FC, BioLegend), CD3 (17A2, BioLegend), CD19 (6D5, BioLegend), LIVE/DEAD™ Fixable Far-Red Dead Cell Stain (Invitrogen), PE anti-mCD47 (miap301, BioLegend). Representative flow gates are located in Supplementary **Fig. 6.16**. PBS-injected Ai14 mice were used to gate tdTomato populations for intravenous administration.

PCR Amplification. All samples were amplified and prepared for sequencing using a one-step PCR protocol as previously described.. More specifically, 1 μL of primers (5 uM for Final Reverse / Forward, 0.5 uM for Base Forward) were added to 5 μL of Kapa HiFi 2X master mix, and 4 μL template DNA/water. When the PCR reaction did not produce clear bands, the primer concentrations, DNA template input, PCR temperature, and number of cycles were optimized for individual samples.

Deep Sequencing. Illumina deep sequencing were performed on an Illumina MiniseqTM. Primers were designed based on Nextera XT adapter sequences.

Data Normalization. Counts for each particle, per tissue, were normalized to the barcoded LNP mixture we injected into the mouse. This 'input' DNA provided the DNA counts and was used to normalize DNA counts from the cells and tissues.

Tissue Immunostaining. Mice were treated with 1 mg / kg of cre mRNA encapsulated in LNPs. Cells were treated with 200 μg of cre mRNA encapsulated in LNPs. Four hours later, tissues or cells were fixed in 1mL of 4% PFA for 24 hours. Cells were washed with 1X PBS. Tissues were cryoprotected in 30% sucrose for 48 hours at 4C. In tissue base molds, tissues were embedded in optimal cutting temperature compound (Tissue-Tek) and frozen. Blocks were stored at -80C. Tissues were sectioned through the Emory Winship Cancer Institute Cancer Tissue and Pathology Facility.

Microscopy. Images for cell type staining were acquired using a Zeiss Plan-Apo 20x 1.3 NA oil objective on an UltraVIEW Spinning Disk Confocal Microscope equipped with a Hamamatsu Flash 4.0v2 CMOS camera. Images for biodistribution analysis were acquired using a Zeiss Plan-Apo 20x 0.8 NA air objective. Images were captured and processed using Volocity software (PerkinElmer).

Data Analysis & Statistics. Sequencing results were processed using a custom python-based tool to extract raw barcode counts for each tissue. These raw counts were then normalized with an R script prior for further analysis. Statistical analysis was done using GraphPad Prism 8. Data is plotted as mean ± standard error mean unless otherwise stated.

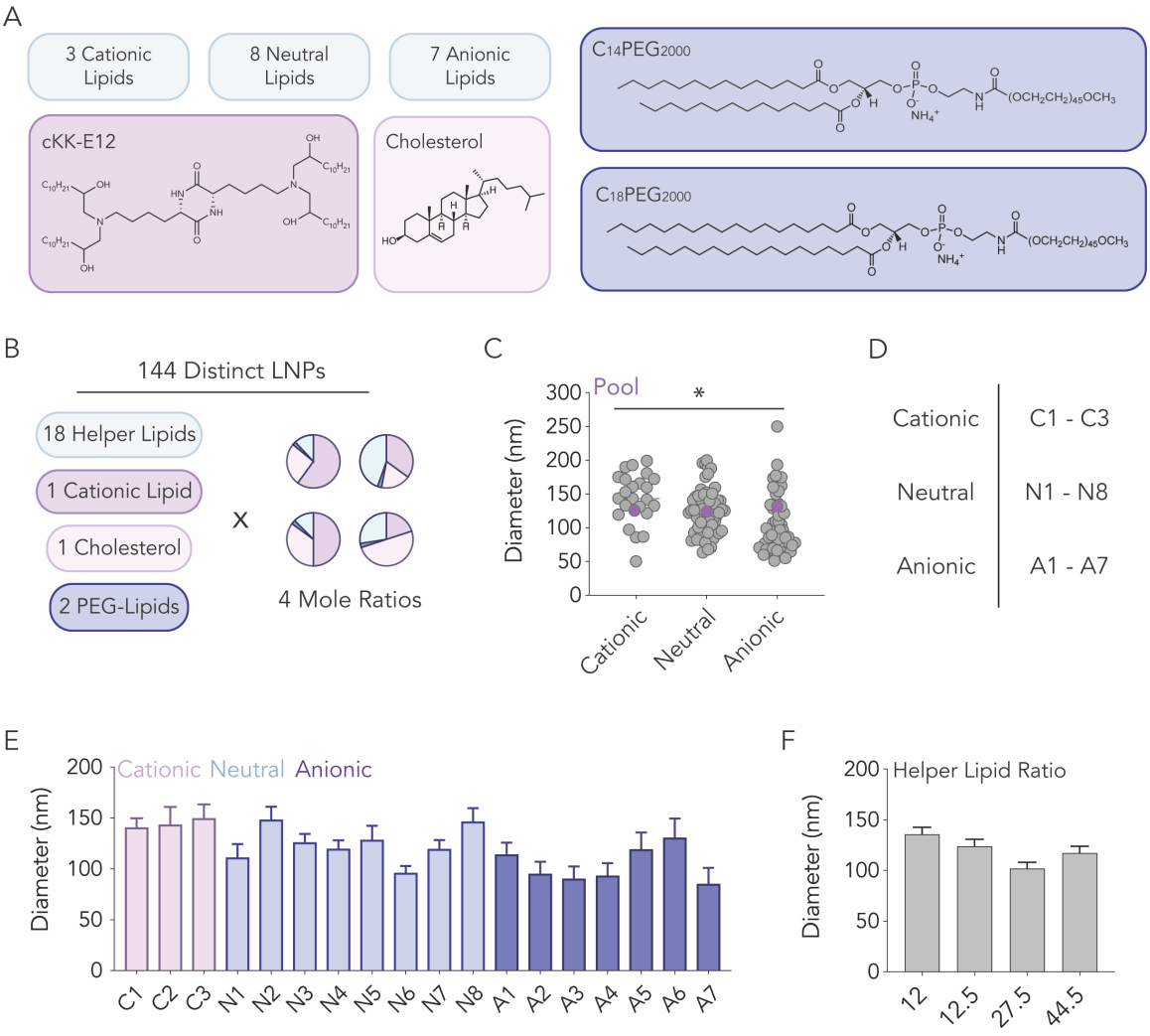

Figure 6.1 (A,B) 144 chemically distinct LNPs were created by varying the helper lipid content as well as the molar ratios of the four components added to the LNP. **(C)** Hydrodynamic diameter of all individual LNPs (gray) as well as the pool of LNPs that were mixed together (purple). The diameter of the pool was within the range of the LNPs comprising that pool. **(D,E)** Helper lipid as a function of diameter. **(F)** The diameter of LNPs in relation to the amount of charged helper lipid.

A

Molar Ratio				
Helper Lipid	12	12.5	27.5	44.5
Cationic Lipid	60	50	20	35
Cholesterol	26	35	50	18
PEG-Lipid	2	2.5	2.5	2.5

Figure 6.2 (A) Molar ratios used in the LNP screens.

A

Name	Charge	ID	Structure
18:0 DDAB	Cationic	C1	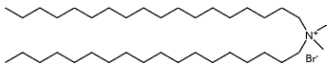
DOTAP	Cationic	C2	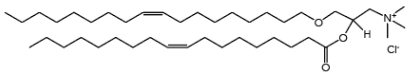
DOTMA	Cationic	C3	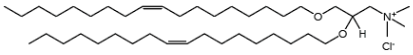

B

Name	Charge	ID	Structure
18:1 Lyso PE	Neutral	N1	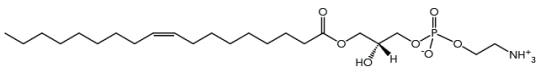
18:1 Lyso PC	Neutral	N2	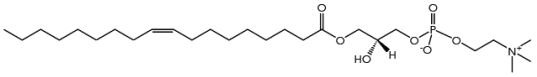
DOPC	Neutral	N3	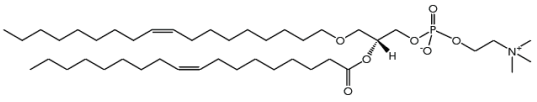
DOPE	Neutral	N4	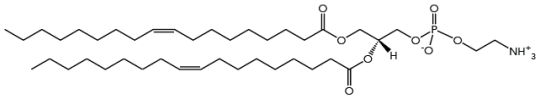
18:1 Monomethyl PE	Neutral	N5	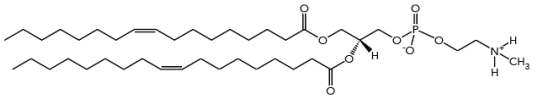
18:1 Dimethyl PE	Neutral	N6	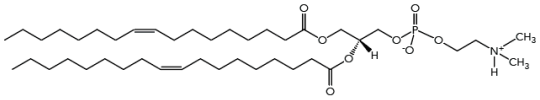
18:0 PC	Neutral	N7	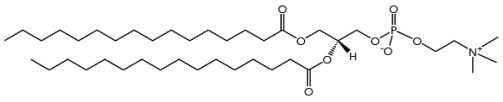
18:1 Caproylamine PE	Neutral	N8	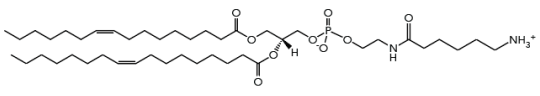

C

Name	Charge	ID	Structure
18:1 PA	Anionic	A1	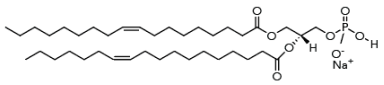
18:1 Phosphatidylmethanol	Anionic	A2	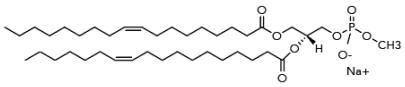
18:1 Phosphatidylethanol	Anionic	A3	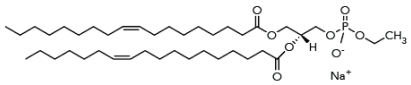
18:1 Phosphatidylpropanol	Anionic	A4	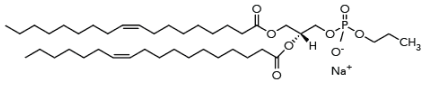
DOPG	Anionic	A5	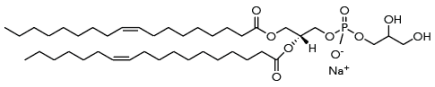
DOPS	Anionic	A6	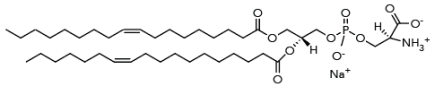
18:1 Biotinyl PE	Anionic	A7	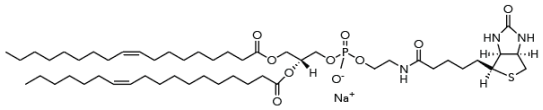

Figure 6.3 Helper lipids used in the **(A)** cationic, **(B)** neutral, and **(C)** anionic libraries.

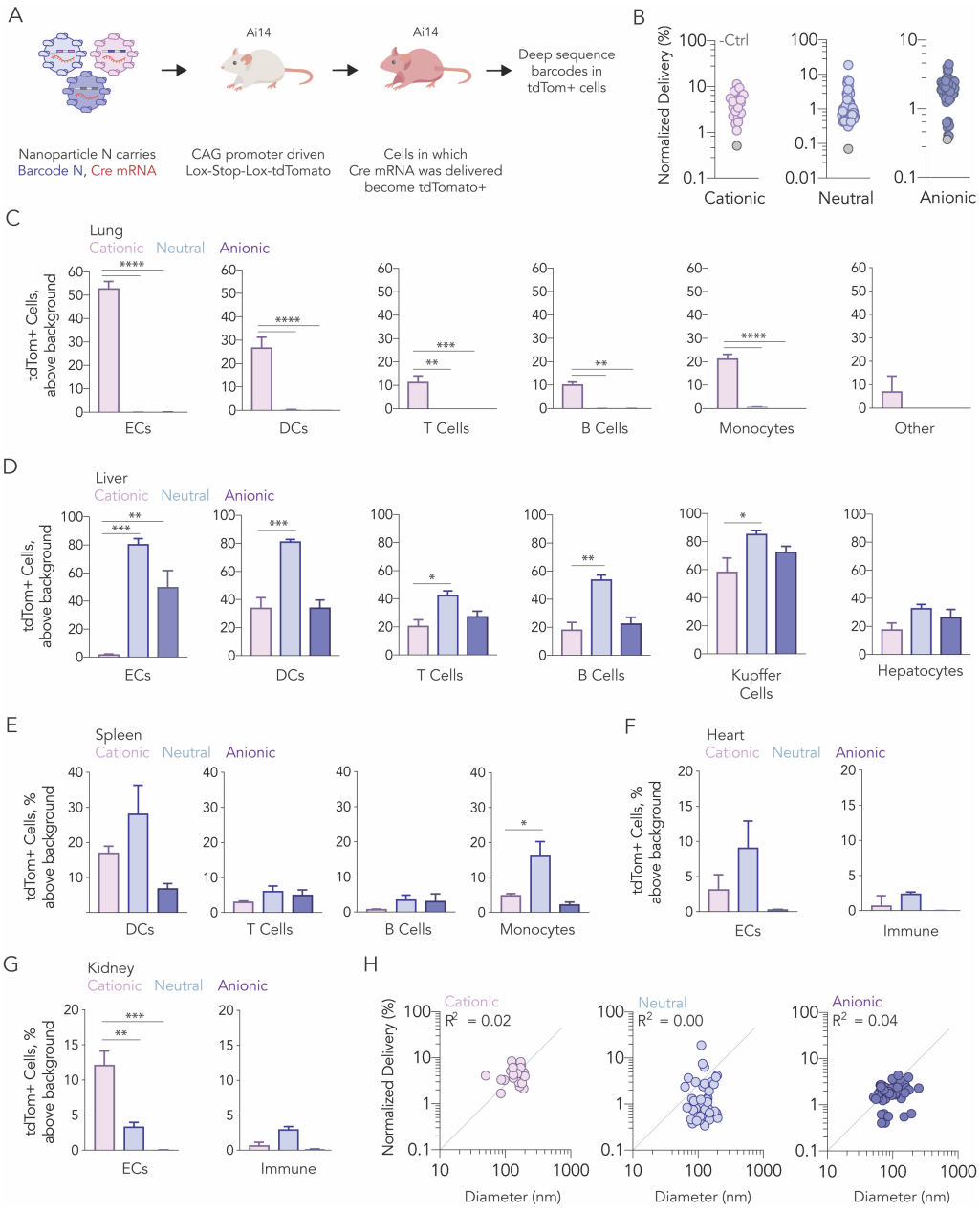

Figure 6.4 (A) LNPs were formulated to carry a DNA barcode and Cre mRNA. 137 LNPs were pooled into their respective library and were then administered to Ai14 mice. After 3 days, tdTomato signal was quantified and tdTomato+ cells were isolated. NGS identified LNPs that functionally transfect cells in vivo. **(B)** Normalized delivery of all LNPs across all cell types in each library. The control, unencapsulated barcoded delivered less efficiently than barcodes

delivered by LNPs. **(C)** tdTomato+ signal in multiple lung, **(D)** liver, **(E)** spleen, **(F)** heart, and **(G)** kidney. These data show a preferential delivery to lung cell types by the cationic LNPs; in contrast, no delivery was observed by the neutral and anionic LNP pools to lung cell types. **(H)** We found no relationship between diameter and delivery in all three experiments.

A

Cell Types	Flow Markers
Liver Hepatocytes	CD31- CD45-
Liver Endothelial Cells	CD31+ CD45-
Liver Dendritic Cells	CD31- CD45+ CD11c+
Liver T Cells	CD31- CD45+ CD3+
Liver B Cells	CD31+ CD45+ CD19+
Liver Kupffer Cells	CD31- CD45+ CD68+
Lung Endothelial Cells	CD31+ CD45-
Lung Dendritic Cells	CD31- CD45+ CD11c+
Lung T Cells	CD31- CD45+ CD3+
Lung B Cells	CD31+ CD45+ CD19+
Lung Monocytes	CD31+ CD45+ CD11b+
Lung Other	CD31- CD45-
Spleen Dendritic Cells	CD31- CD45+ CD11c+
Spleen T Cells	CD31- CD45+ CD3+
Spleen B Cells	CD31+ CD45+ CD19+
Spleen Monocytes	CD31+ CD45+ CD11b+
Heart Endothelial Cells	CD31+ CD45-
Heart Immune Cells	CD31- CD45+
Kidney Endothelial Cells	CD31+ CD45-
Kidney Immune Cells	CD31- CD45+

Figure 6.5 (A) Cell type specific markers for cells isolated.

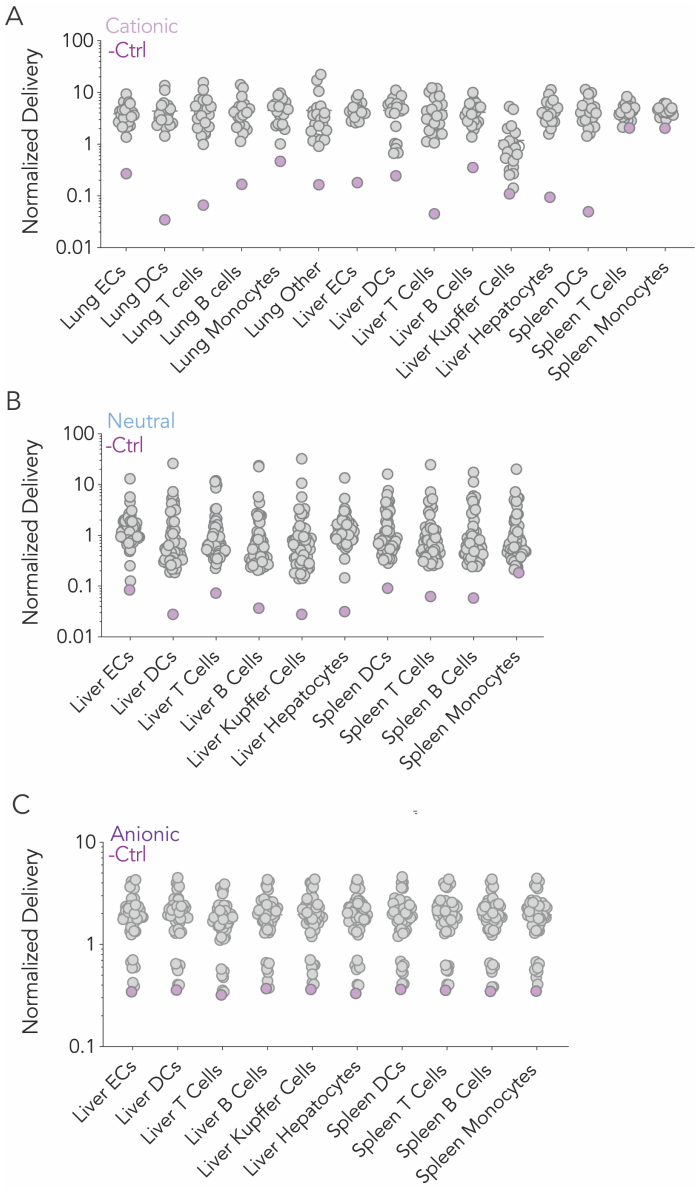

Figure 6.6 Normalized delivery of all LNPs for various cell types. The negative control, free DNA barcode, delivery was lower than barcodes delivered by LNPs in the **(A)** cationic, **(B)** neutral, and **(C)** anionic screens.

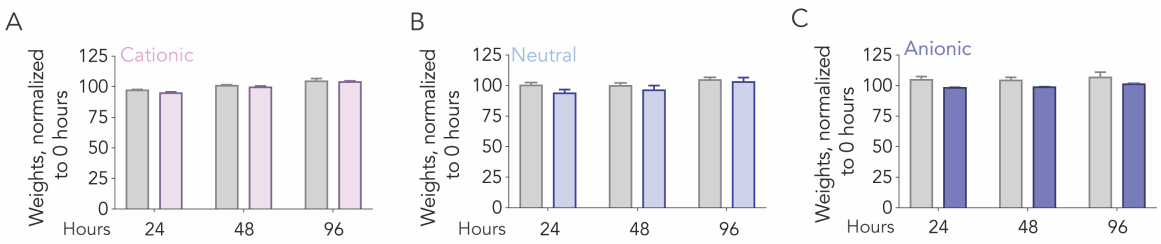

Figure 6.7 (A) Mouse weights measured 24, 48, and 96 hours after administration of PBS or cationic, **(B)** neutral, and **(C)** anionic LNPs carrying cre mRNA and DNA barcodes.

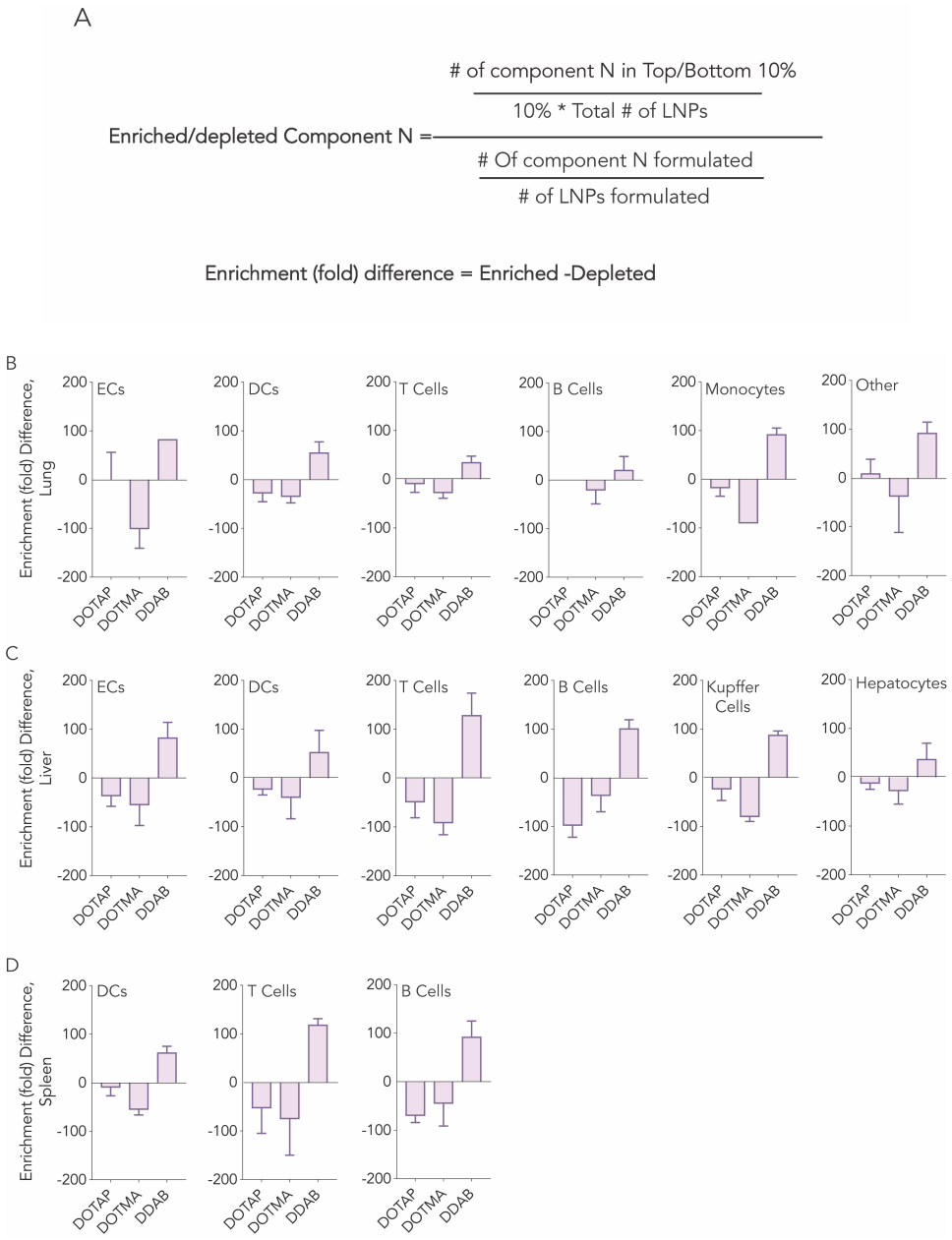

Figure 6.8 (A) Enrichment (fold) difference is calculated through the shown formula. Fold enrichment was calculated for cationic LNPs delivered to **(B)** lung cells, **(C)** liver cells, and **(D)** spleen cells.

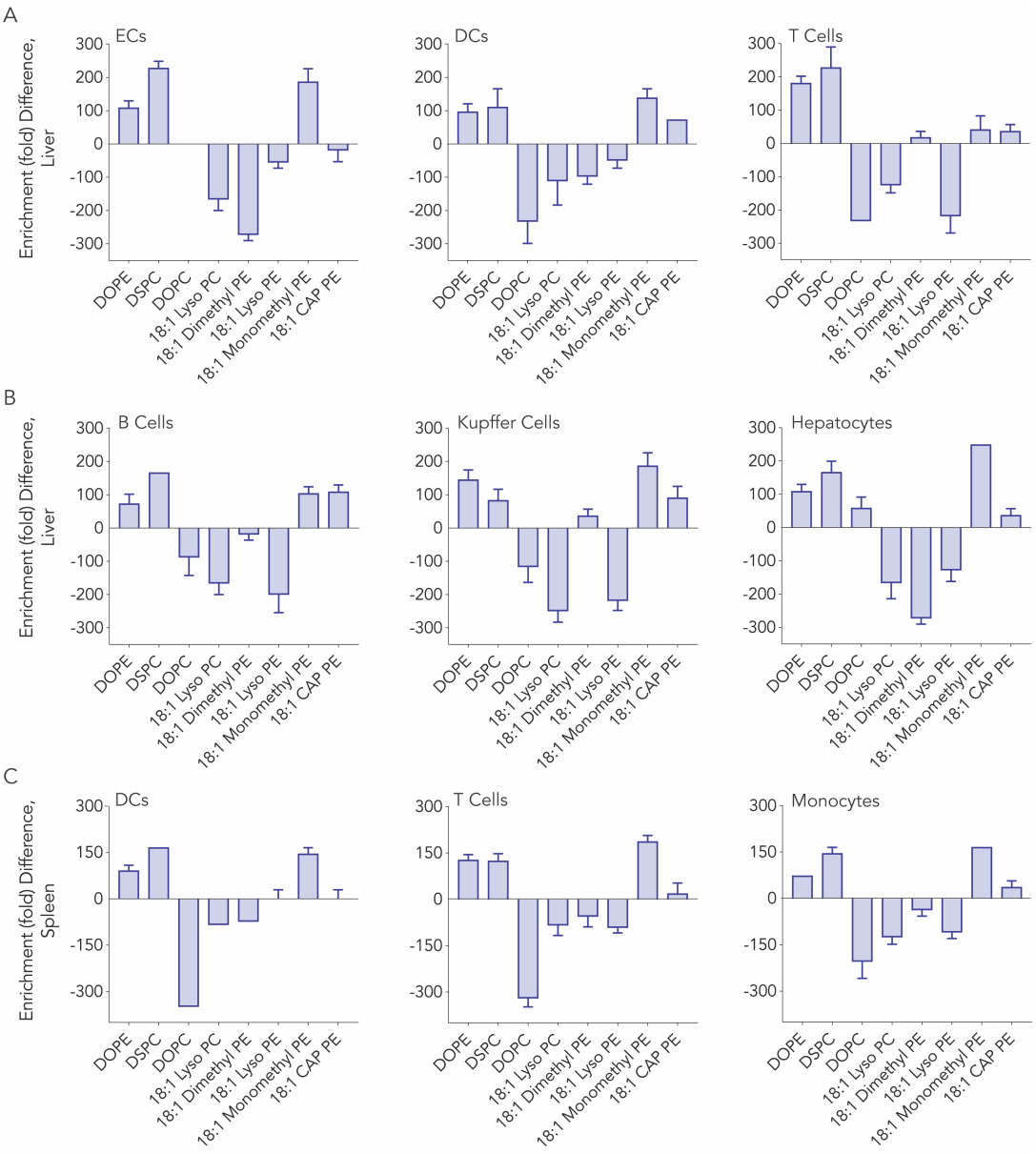
A
Enrichment (fold) Difference, Liver
ECs
DCs
T Cells
B
B Cells
Kupffer Cells
Hepatocytes
C
Enrichment (fold) Difference, Spleen
DCs
T Cells
Monocytes
300
200
150
100
0
-100
-150
-200
-300
DOPE
DSPC
DOPC
18:1 Lyso PC
18:1 Dimethyl PE
18:1 Lyso PE
18:1 Monomethyl PE
18:1 CAP PE

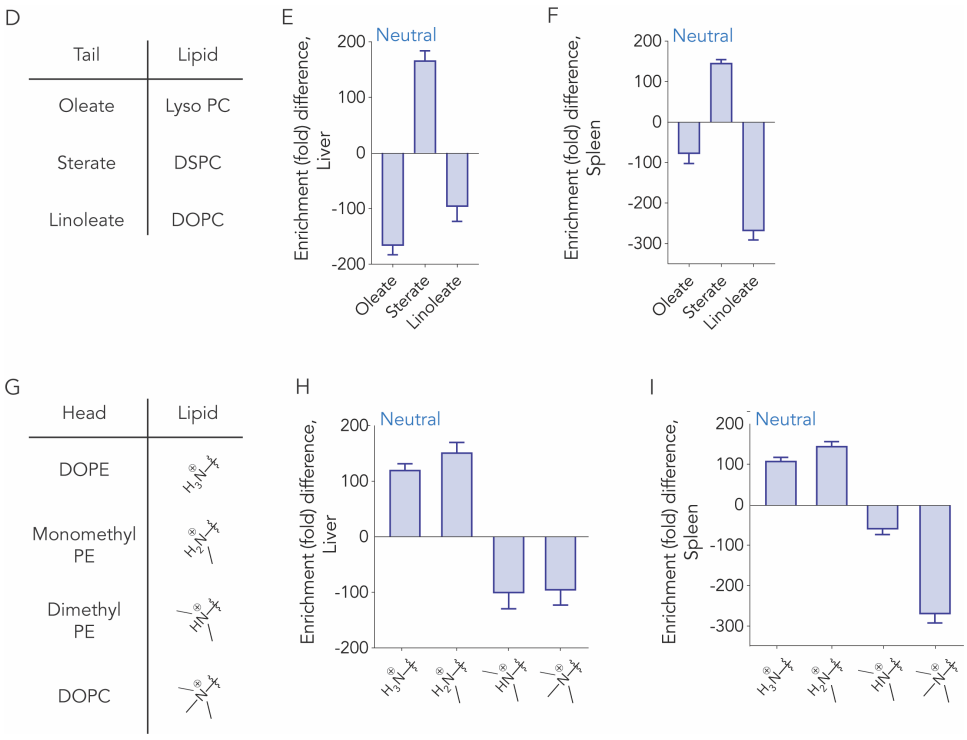

Figure 6.9 (A,B) Fold enrichment was calculated for neutral LNPs delivered to liver cells, and **(C)** spleen cells. **(D,E)** Fold enrichment was calculated for all three tail structures in the liver and **(F)** spleen. **(G,H)** Fold enrichment was calculated for four different head groups in the liver and **(I)** spleen.

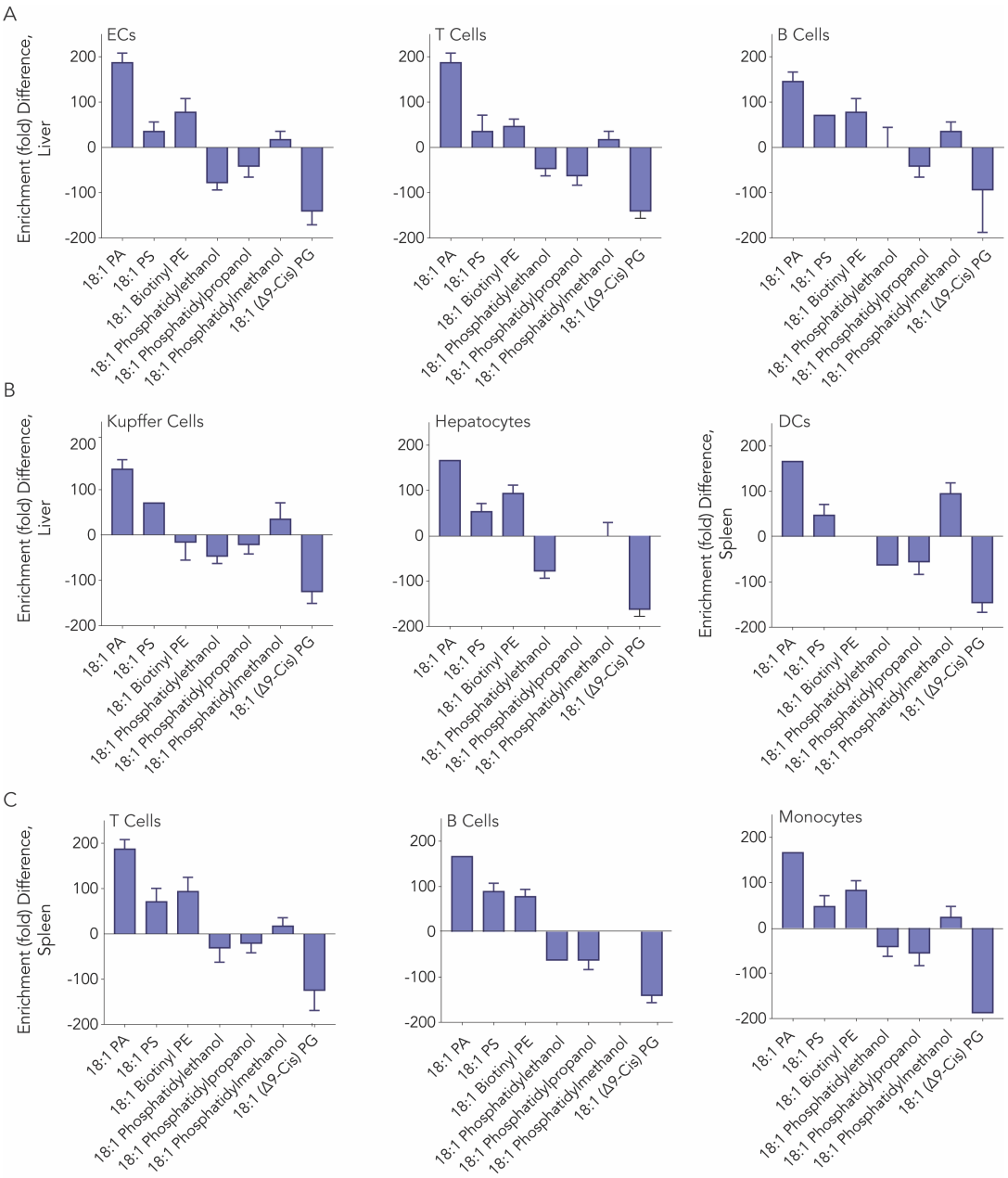
A
ECs
T Cells
B Cells
B
Kupffer Cells
Hepatocytes
DCs
C
T Cells
B Cells
Monocytes
Enrichment (fold) Difference, Liver
Enrichment (fold) Difference, Spleen
200
100
0
-100
-200
18:1 PA
18:1 PS
18:1 Biotinyl PE
18:1 Phosphatidylethanol
18:1 Phosphatidylpropanol
18:1 Phosphatidylmethanol
18:1 (Δ9-Cis) PG

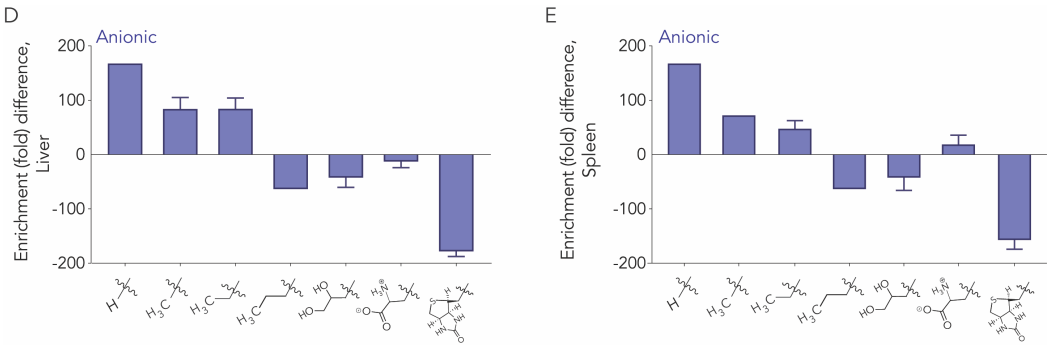

Figure 6.10 (A,B) Fold enrichment was calculated for anionic LNPs delivered to liver cells, and **(C)** spleen cells. **(D)** Fold enrichment was calculated for sevem different head groups in the liver and **(E)** spleen.

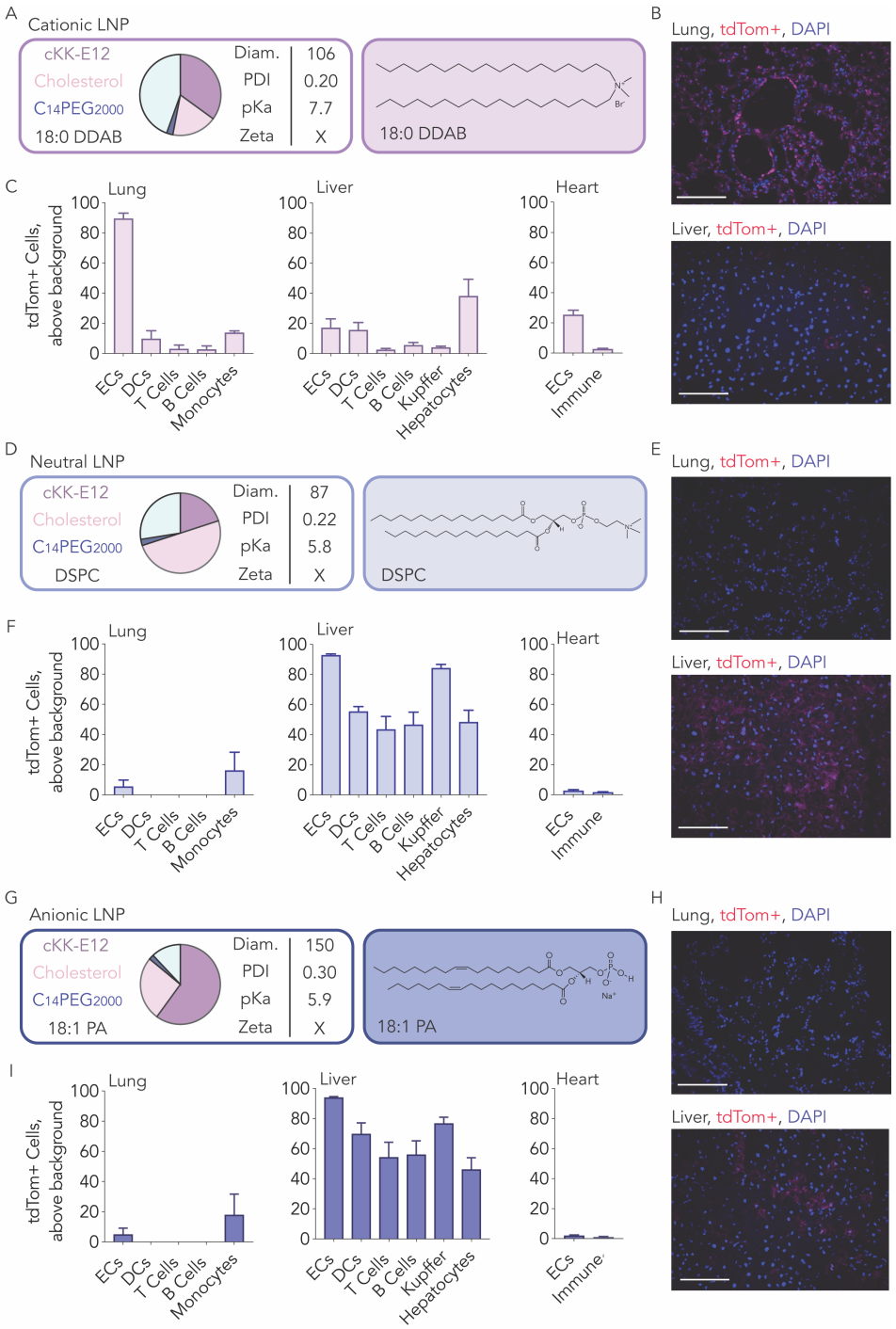

Figure 6.11 (A) The top LNP from the cationic screen (labeled Cationic LNP) was formulated with cre mRNA and administered to Ai14 mice at a dose of 1.3 mg / kg. We observed delivery to **(B,C)** lungs cells types more than liver cell types. **(D)** The top LNP from the neutral screen (labeled

Neutral LNP) was formulated with cre mRNA and administered to Ai14 mice at a dose of 1.3 mg / kg. We observed delivery to **(E,F)** liver cells types more than lung cell types. **(G)** The top LNP from the anionic screen (labeled Anionic LNP) was formulated with cre mRNA and administered to Ai14 mice at a dose of 1.3 mg / kg. We observed delivery to **(H,I)** liver cells types more than lung cell types.

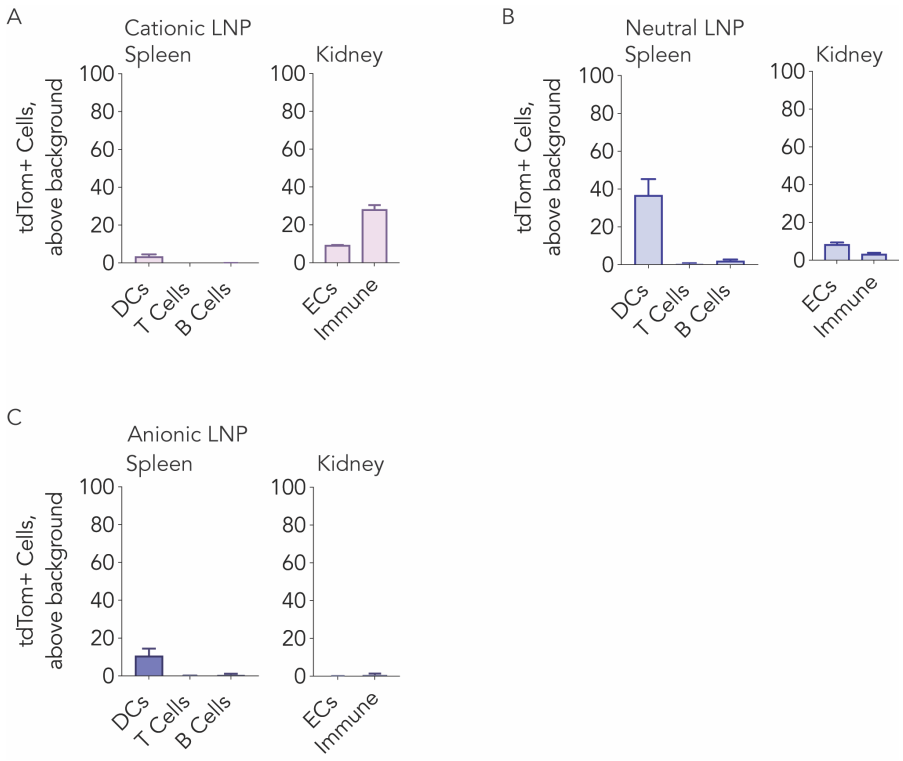

Figure 6.12 (A) Delivery to the spleen and kidney by the Cationic LNP, **(B)** Neutral LNP, and **(C)** Cationic LNP.

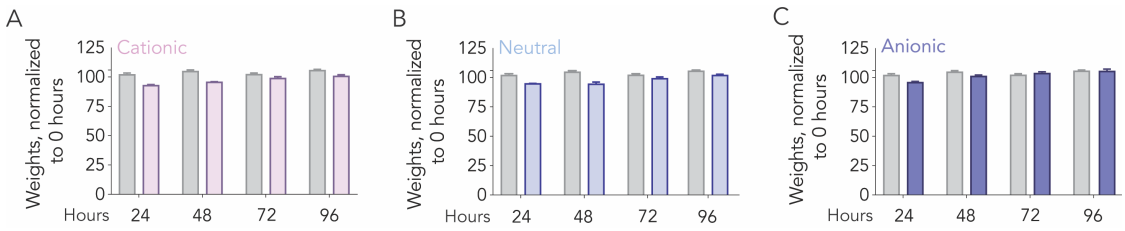

Figure 6.13 (A) Mouse weights measured 24, 48, 72, and 96 hours after administration of PBS or top cationic, **(B)** neutral, and **(C)** anionic LNPs carrying cre mRNA.

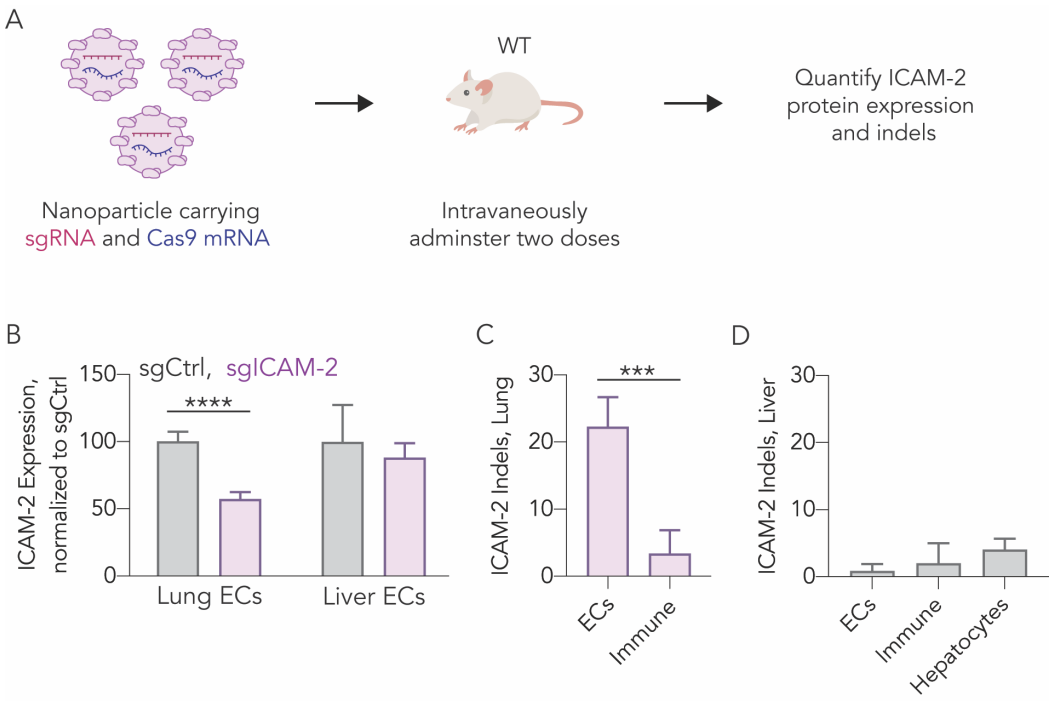

Figure 6.14 (A) The Cationic LNP was formulated carrying Cas9 mRNA and sgRNA targeting ICAM-2 (sgICAM-2) or a control (sgRNA targeting GFP, sgCtrl). Two doses of 1 mg / kg were administered two days apart. Five days later, ICAM-2 protein expression and indels were quantified. **(B)** Normalized ICAM-2 expression in lung and liver endothelial cells after exposure to the Cationic LNP with sgControl or sgICAM-2. **(C)** Indel analysis at ICAM-2 in lung endothelial cells and immune cells, and **(D)** liver endothelial cells, immune cells, and hepatocytes.

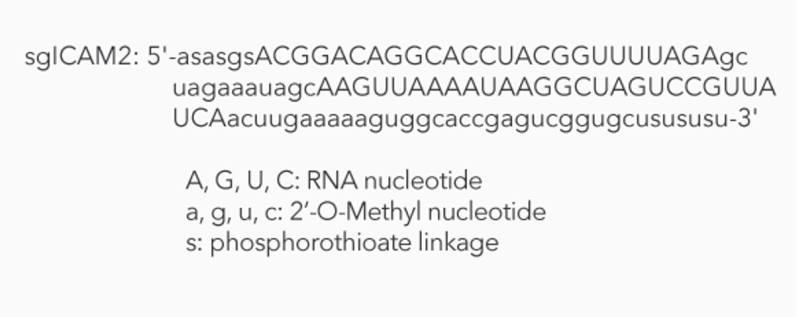

Figure 6.15 (A) Sequence and chemical modifications for sgICAM-2.

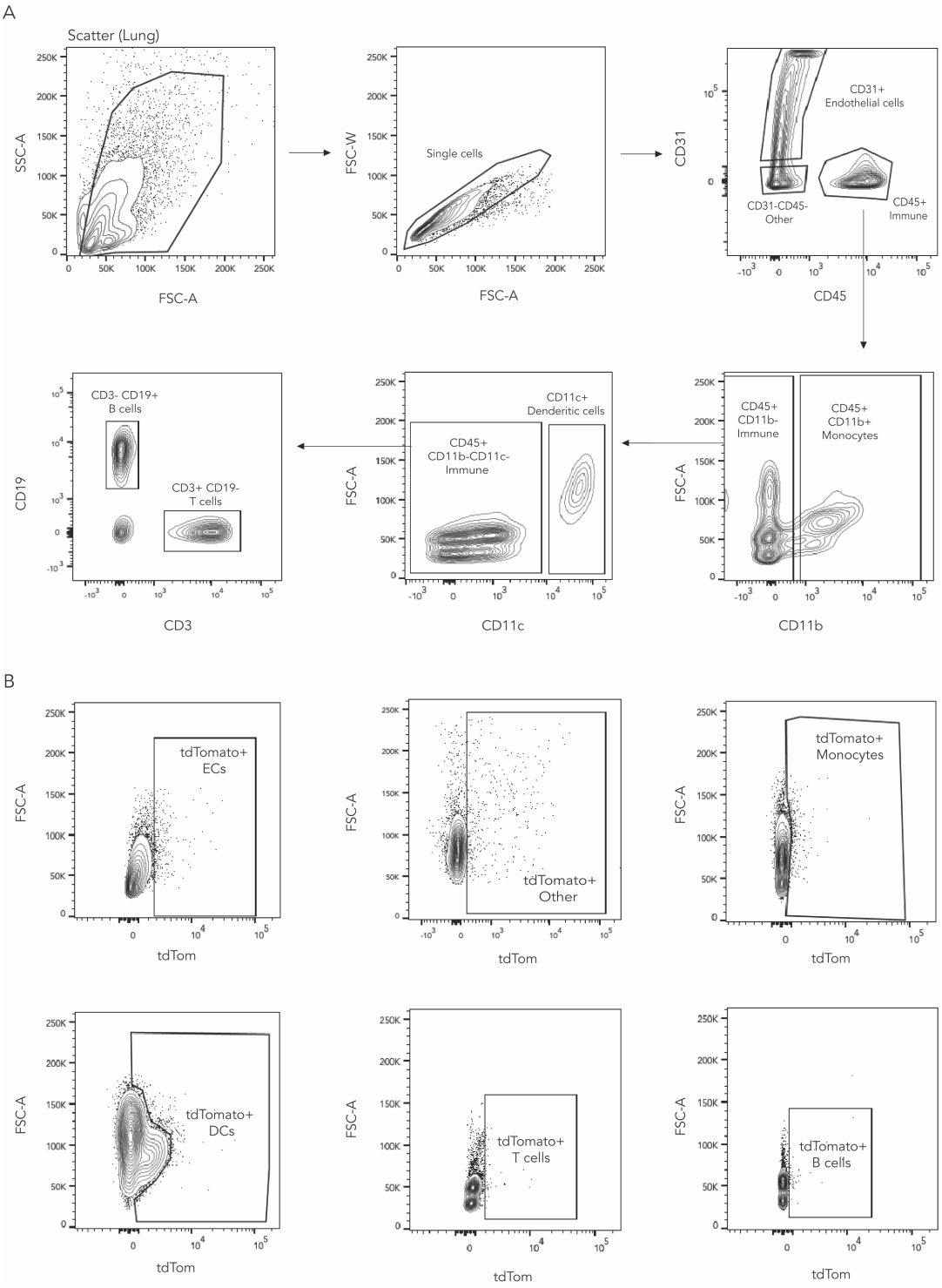
A
Scatter (Lung)
SSC-A
FSC-A
Single cells
FSC-W
FSC-A
CD31
CD31+
Endothelial cells
CD31-CD45-
Other
CD45+
Immune
CD45
CD19
CD3- CD19+
B cells
CD3+ CD19-
T cells
CD3
FSC-A
CD11c+
Denderitic cells
CD45+
CD11b-CD11c-
Immune
CD11c
FSC-A
CD45+
CD11b-
Immune
CD45+
CD11b+
Monocytes
CD11b
B
FSC-A
tdTomato+
ECs
tdTom
FSC-A
tdTomato+
Other
tdTom
FSC-A
tdTomato+
Monocytes
tdTom
FSC-A
tdTomato+
DCs
tdTom
FSC-A
tdTomato+
T cells
tdTom
FSC-A
tdTomato+
B cells
tdTom

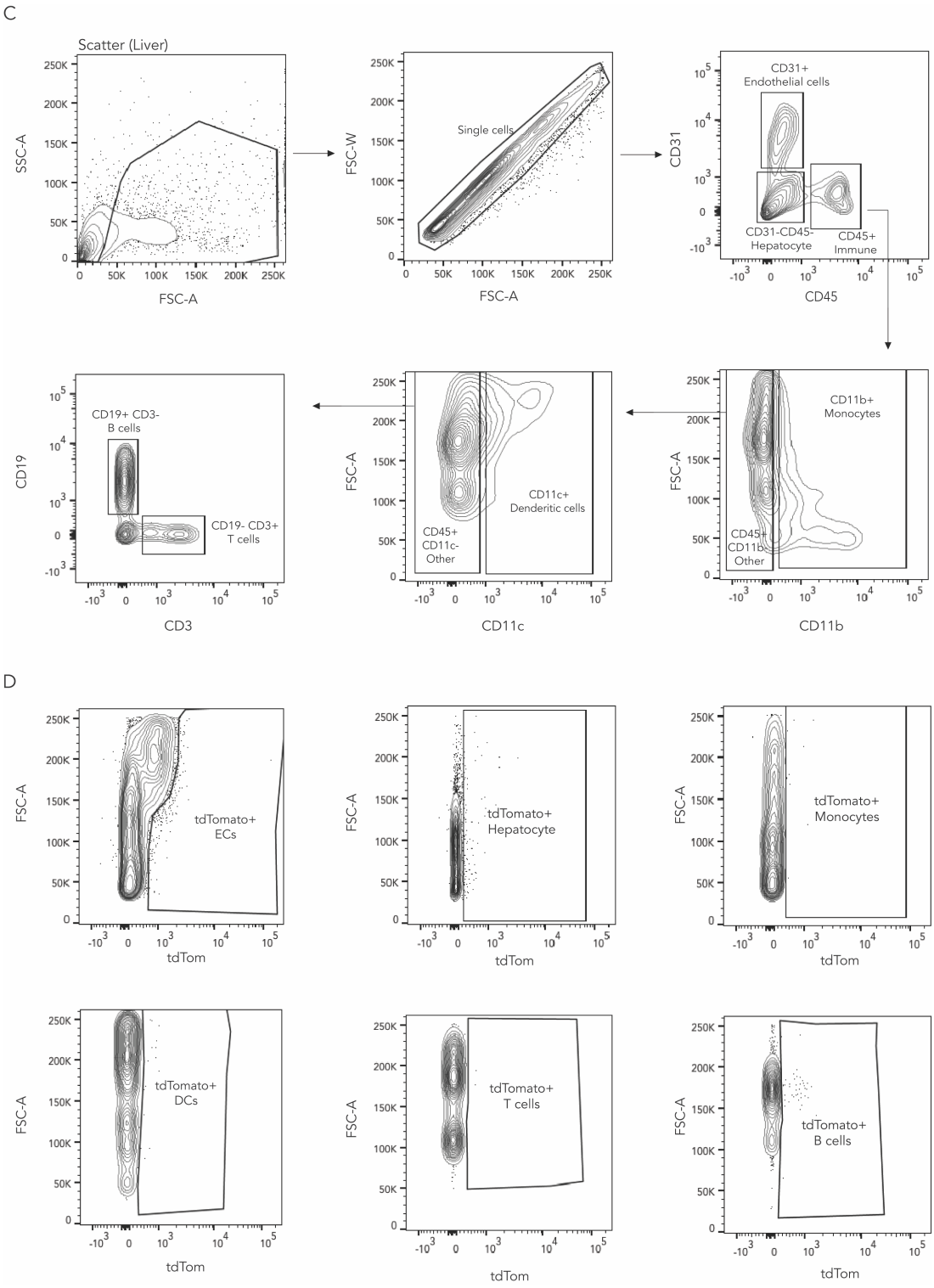
C
Scatter (Liver)
SSC-A
FSC-A
FSC-W
Single cells
CD31
CD31+
Endothelial cells
CD31-CD45-
Hepatocyte
CD45+
Immune
CD45
CD19
CD19+ CD3-
B cells
CD19- CD3+
T cells
CD3
FSC-A
CD11c+
Denderitic cells
CD45+
CD11c-
Other
CD11c
CD11b+
Monocytes
CD45+
CD11b-
Other
CD11b
D
tdTom
tdTomato+
ECs
tdTomato+
Hepatocyte
tdTomato+
Monocytes
tdTomato+
DCs
tdTomato+
T cells
tdTomato+
B cells

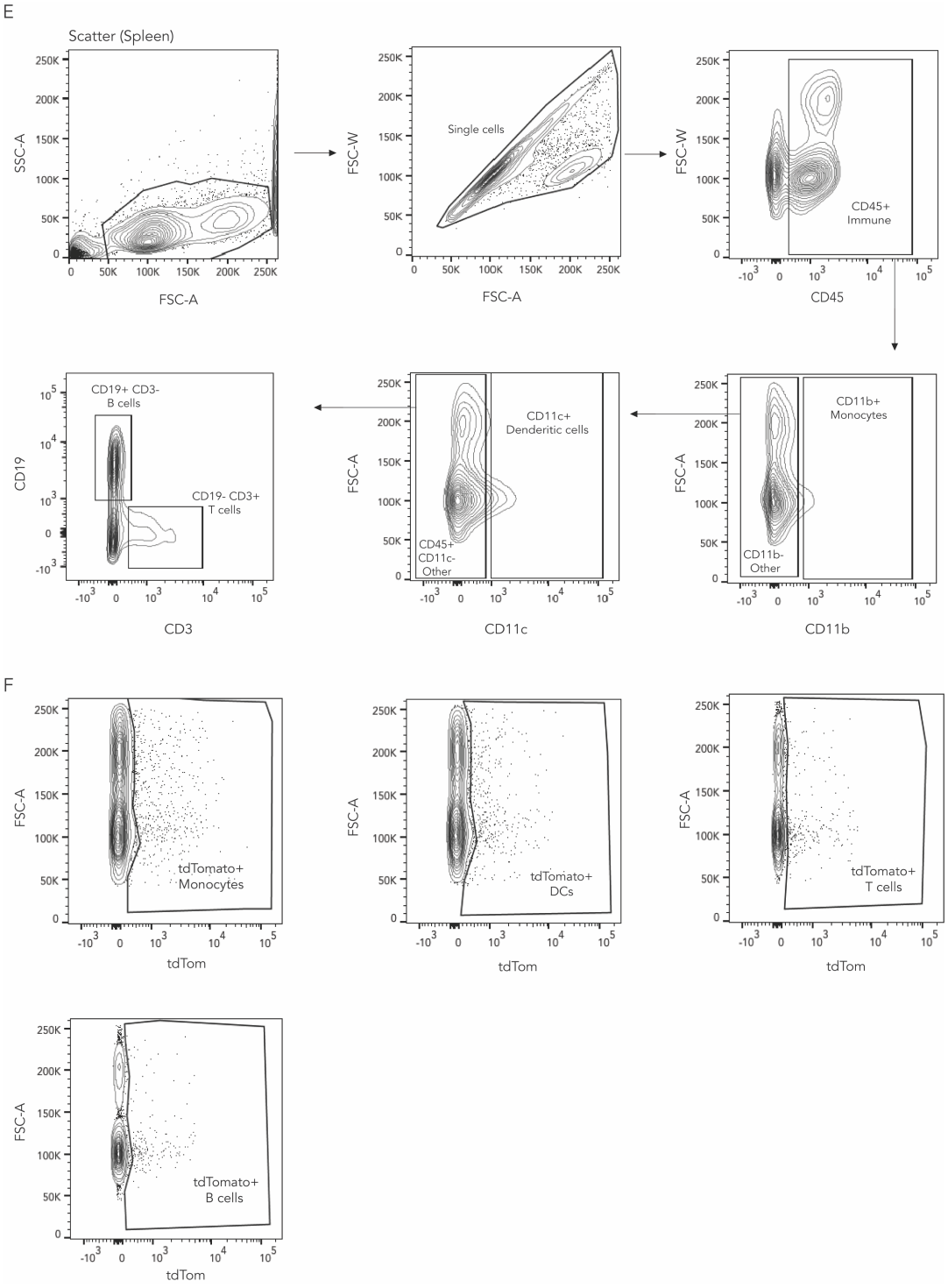
E
Scatter (Spleen)
SSC-A
FSC-A
FSC-W
Single cells
CD45+
Immune
CD45
CD11b+
Monocytes
CD11b
CD11c+
Denderitic cells
CD11c
CD45+
CD11c-
Other
CD11b-
Other
CD19+ CD3-
B cells
CD19- CD3+
T cells
CD19
CD3
F
tdTomato+
Monocytes
tdTomato+
DCs
tdTomato+
T cells
tdTomato+
B cells
tdTom

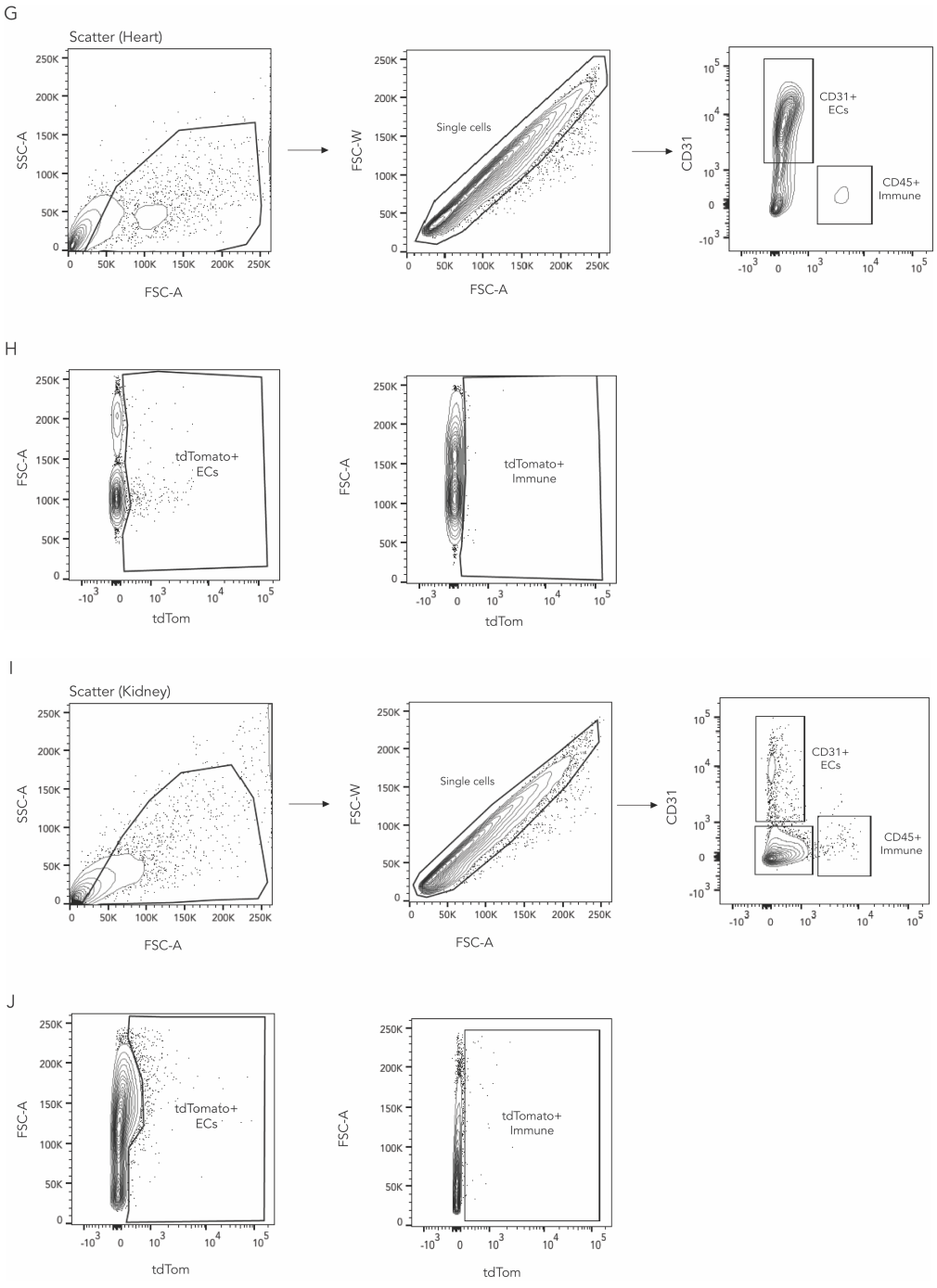

Figure 16.16 (A,B) Representative gating strategies for FACS for cells types in the lung, **(C,D)** liver, **(E,F)** spleen, **(G,H)** heart, and **(I,J)** kidney.

CHAPTER 7. PERSPECTIVES AND FUTURE WORK

Oligonucleotides, and in particular RNA-based therapies, can be used to modulate the expression of any gene, making them a promising way to treat or manage disease. Currently, there are ten oligonucleotides that have been approved by the FDA[213]. One of the advantages of RNA-based therapies are their ability to target or produce any protein. RNAi therapies such as siRNAs can modulate RNA translation and suppress the translation of any gene transcript. mRNA therapies can transiently produce any protein and do not require genome integration. As discussed in this work, LNPs have become an attractive way to deliver nucleic acid therapies to target cell types. The first LNP-based RNAi drug was approved by the FDA in 2018. Today, LNPs carrying mRNA have been approved as vaccines for SARS-CoV-2. These advances demonstrate that LNPs and nucleic acid drugs can be an integral part of world health and disease treatment.

While RNA therapies continue to enter the clinic, there is still a need for safe and efficient drugs. Systemic delivery to non-liver cell types will require further examination, innovation, and improvement. Additionally, one challenge with mRNA therapeutics is their capability to be effectively delivered to target cell types. While new chemical methods allow for the rapid development of novel lipid-based components, it can be laborious and expensive to test hundreds to thousands of novels LNPs. One solution is the use of high-throughput screening systems, which have proven to be valuable in the field of drug delivery and nanomedicine. DNA barcoding–based screening systems in particular have been used to identify new particles that efficiently deliver mRNA[76,159,160,214] and siRNA[45,135,159,187] *in vivo*. In the last four years, DNA barcoding has allowed for over 5,000 lipid nanoparticles to be screened *in vivo*, in published and unpublished work, by the lab of Dr. James Dahlman. But while screening platforms can increase the likelihood that RNA therapies will be clinically approved, we can make significant efforts to improve the field of drug delivery.

First, we can improve the way drug delivery vehicles are discovered. Traditionally, nanoparticles are tested and characterized *in vitro*. While successful nucleic acid drugs must overcome complex *in vivo* barriers, nanoparticles are often screened in cell culture conditions. Even though *in vitro* and *in vivo* delivery involves different physiological obstacles, nanoparticle performance is first evaluated *in vitro* and only then are some LNPs tested *in vivo*. We have shown that *in vivo* LNP delivery is not predicted by *in vitro* delivery using cell culture conditions[33]. However, it is impractical, expensive, and time consuming to individually test each nanoparticle *in vivo*. Thus, high-throughput screening systems are among the most practical ways to measure the delivery of multiple particles *in vivo*. The data generated by these screens will only continue to grow, and the incorporation of artificial intelligence and computer modeling will be one way to process and innovate with these large data sets.

The current screening systems described in this work allow us to test thousands of particles, simultaneously, in a single mouse. However, the systems described are dependent on i) specialized rodent models (i.e. Ai14 mice or GFP-expressing mice) or ii) the knockdown of genes expressed only in specific cell types. These factors can greatly restrict the hypotheses posed by researchers. Thus, a more accessible screening platform is needed that is free from these constraints. An ideal platform would be compatible with i) various species, ii) genetic knockout models, and iii) disease models. The payload would need to either target a universally expressed gene (e.g., siRNA or sgRNA payload) or deliver an exogenous reporter (mRNA payload). Novel screening platforms would allow for a better understanding of the biology involved in delivery.

Second, we need to better understand the genes that influence potent drug delivery *in vivo*. For example, scientists have found that some LNP-mediated delivery is dependent on the presence of serum ApoE; the interactions between ApoE and the LDLR cell surface receptor are critical for nanoparticle uptake. Additionally, disease states can create atypical cell states or tissue structures. These abnormal states can dramatically affect the potency of a drug uptake and function. In this work, we discuss the role of inflammation on drug delivery. We found that TLR4 activation can

inhibit mRNA delivery by LNPs; TLR4 activation has been shown in various disease states. Drug delivery systems may improve as we better understand the cells involved in uptake and the genes required for functional delivery. One way to explore the regulatory genes of drug delivery is the use of transcriptomics and RNA-sequencing technologies. Transcriptomic profiles post-delivery can provide insight regarding the genes involved in uptake and translation of nucleic acid drugs. Transcriptomics-based studies have been used to understand the effects of biomaterials and gene expression; scientist anticipate that omics-like dataset applied to nanomedicines will answer important questions about the biology of drug delivery[215].

Third, we need to explore the tolerability and potency of drug delivery vehicles across various animal models. Studies show that delivery vehicles behave differently in different animal models. For example, scientists found AAVs that delivered payloads across the blood–brain barrier[56] in one species of mouse but not another[216,217]. These studies demonstrate the necessity of understanding how nanomedicines behave in various animal models. Importantly, as drugs are scaled into larger animal models such as NHPs, therapeutic efficiency decreases. This is in part due to a more severe immune response in larger animals compared to smaller rodents such as mice[218,219]. Thus, delivery vehicles studied in mice might behave differently in NHPs or humans. It is therefore important to study how drugs deliver in larger animal models to identify drugs that work efficiently in these models. This will allow for a greater number of drugs to translate into the clinic.

Nevertheless, the development of nucleic acid drugs provides a bright future for patients. siRNA-based therapies interact with their target molecules through complementary Watson–Crick base pairing. mRNA-based therapies will produce any protein encoded in the mRNA sequence. Because of this, RNA therapies are relatively straightforward to design, are generated to be highly specific, and can be designed to knock down or replace any protein. Furthermore, delivery systems such as LNPs that deliver one RNA therapy can be exploited to deliver other RNAs of similar size. By contrast, small-molecule drugs require laborious screening efforts, and they can only treat a small portion of the protein coding genome[1].

In 2020, the COVID-19 pandemic caused by SARS-CoV-2 affected 220 countries and resulted in more than 1.4 million deaths[220]. In late 2020, two vaccines were approved for clinical use against COVID-19; they will be the first messenger RNA-based vaccines approved for clinical use. Additionally, these mRNA vaccines would be delivered in LNP vehicles to target cells. The rapid development and efficient translation of these vaccines highlight an important achievement for RNA-based drugs and LNP delivery systems. RNA therapies can be rapidly produced, customized for specific disease, and safely administered to patients, demonstrating their significance in medicine.

REFERENCES

1. Dixon SJ, Stockwell BR: Identifying druggable disease-modifying gene products. Curr Opin Chem Biol 13:549-55, 2009

2. Kaczmarek JC, Kowalski PS, Anderson DG: Advances in the delivery of RNA therapeutics: from concept to clinical reality. Genome medicine 9:60-60, 2017

3. Urnov FD, Rebar Ej Fau - Holmes MC, Holmes Mc Fau - Zhang HS, et al: Genome editing with engineered zinc finger nucleases.

4. Joung JK, Sander JD: TALENs: a widely applicable technology for targeted genome editing. Nat Rev Mol Cell Biol 14:49-55, 2013

5. Doudna JA, Charpentier E: The new frontier of genome engineering with CRISPR-Cas9. Science 346:1258096, 2014

6. Hsu PD, Lander ES, Zhang F: Development and applications of CRISPR-Cas9 for genome engineering. Cell 157:1262-78, 2014

7. Sahin U, Kariko K, Tureci O: mRNA-based therapeutics--developing a new class of drugs. Nat Rev Drug Discov 13:759-80, 2014

8. Coelho T, Adams D, Silva A, et al: Safety and Efficacy of RNAi Therapy for Transthyretin Amyloidosis. New England Journal of Medicine 369:819-829, 2013

9. Rizk M, Tuzmen S: Update on the clinical utility of an RNA interference-based treatment: focus on Patisiran. Pharmgenomics Pers Med 10:267-278, 2017

10. Crooke ST, Baker BF, Kwoh TJ, et al: Integrated Safety Assessment of 2'-O-Methoxyethyl Chimeric Antisense Oligonucleotides in NonHuman Primates and Healthy Human Volunteers. Mol Ther 24:1771-1782, 2016

11. Foster DJ, Brown CR, Shaikh S, et al: Advanced siRNA Designs Further Improve In Vivo Performance of GalNAc-siRNA Conjugates. Mol Ther 26:708-717, 2018

12. Sehgal A, Barros S, Ivanciu L, et al: An RNAi therapeutic targeting antithrombin to rebalance the coagulation system and promote hemostasis in hemophilia. Nat Med 21:492-7, 2015

13. Jiang C, Mei M, Li B, et al: A non-viral CRISPR/Cas9 delivery system for therapeutically targeting HBV DNA and pcsk9 in vivo. Cell Res 27:440-443, 2017

14. Miller JB, Zhang S, Kos P, et al: Non-Viral CRISPR/Cas Gene Editing In Vitro and In Vivo Enabled by Synthetic Nanoparticle Co-Delivery of Cas9 mRNA and sgRNA. Angew Chem Int Ed Engl 56:1059-1063, 2017

15. Thess A, Grund S, Mui BL, et al: Sequence-engineered mRNA Without Chemical Nucleoside Modifications Enables an Effective Protein Therapy in Large Animals. Mol Ther 23:1456-64, 2015

16. Bahl K, Senn JJ, Yuzhakov O, et al: Preclinical and Clinical Demonstration of Immunogenicity by mRNA Vaccines against H10N8 and H7N9 Influenza Viruses. Mol Ther 25:1316-1327, 2017

17. Sahin U, Derhovanessian E, Miller M, et al: Personalized RNA mutanome vaccines mobilize poly-specific therapeutic immunity against cancer. Nature 547:222-226, 2017

18. Tebas P, Stein D, Tang WW, et al: Gene editing of CCR5 in autologous CD4 T cells of persons infected with HIV. N Engl J Med 370:901-10, 2014

19. Lorenzer C, Dirin M, Winkler A-M, et al: Going beyond the liver: Progress and challenges of targeted delivery of siRNA therapeutics. 203:1-15, 2015

20. Meade BR, Gogoi K, Hamil AS, et al: Efficient delivery of RNAi prodrugs containing reversible charge-neutralizing phosphotriester backbone modifications. 32:1256-1261, 2014

21. Jiang W, Kim BY, Rutka JT, et al: Nanoparticle-mediated cellular response is size-dependent. Nat Nanotechnol 3:145-50, 2008

22. Semple SC, Akinc A, Chen J, et al: Rational design of cationic lipids for siRNA delivery. Nat Biotechnol 28:172-6, 2010

23. Stefanick JF, Ashley JD, Bilgicer B: Enhanced Cellular Uptake of Peptide-Targeted Nanoparticles through Increased Peptide Hydrophilicity and Optimized Ethylene Glycol Peptide-Linker Length. ACS Nano 7:8115-8127, 2013

24. Champion JA, Katare YK, Mitragotri S: Making polymeric micro- and nanoparticles of complex shapes. Proceedings of the National Academy of Sciences 104:11901-11904, 2007

25. Kedmi R, Veiga N, Ramishetti S, et al: A modular platform for targeted RNAi therapeutics. Nat Nanotechnol 13:214-219, 2018

26. Akinc A, Zumbuehl A, Goldberg M, et al: A combinatorial library of lipid-like materials for delivery of RNAi therapeutics. Nature Biotechnology 26:561-569, 2008

27. Love KT, Mahon KP, Levins CG, et al: Lipid-like materials for low-dose, in vivo gene silencing. Proc Natl Acad Sci U S A 107:1864-9, 2010

28. Dong Y, Love KT, Dorkin JR, et al: Lipopeptide nanoparticles for potent and selective siRNA delivery in rodents and nonhuman primates. Proc Natl Acad Sci U S A 111:3955-60, 2014

29. Zhou K, Nguyen LH, Miller JB, et al: Modular degradable dendrimers enable small RNAs to extend survival in an aggressive liver cancer model. Proceedings of the National Academy of Sciences 113:520-525, 2016

30. Chen D, Love KT, Chen Y, et al: Rapid Discovery of Potent siRNA-Containing Lipid Nanoparticles Enabled by Controlled Microfluidic Formulation. Journal of the American Chemical Society 134:6948-6951, 2012

31. Leung AK, Tam YY, Chen S, et al: Microfluidic Mixing: A General Method for Encapsulating Macromolecules in Lipid Nanoparticle Systems. J Phys Chem B, 2015

32. Whitehead KA, Dorkin JR, Vegas AJ, et al: Degradable lipid nanoparticles with predictable in vivo siRNA delivery activity. Nat Commun 5:4277, 2014

33. Paunovska K, Sago CD, Monaco CM, et al: A Direct Comparison of in Vitro and in Vivo Nucleic Acid Delivery Mediated by Hundreds of Nanoparticles Reveals a Weak Correlation. Nano Letters 18:2148-2157, 2018

34. Zuckerman JE, Choi CHJ, Han H, et al: Polycation-siRNA nanoparticles can disassemble at the kidney glomerular basement membrane. Proceedings of the National Academy of Sciences of the United States of America 109:3137-3142, 2012

35. Tsoi KM, Macparland SA, Ma X-Z, et al: Mechanism of hard-nanomaterial clearance by the liver. Nature Materials 15:1212-1221, 2016

36. Akinc A, Querbes W, De S, et al: Targeted Delivery of RNAi Therapeutics With Endogenous and Exogenous Ligand-Based Mechanisms. Molecular Therapy 18:1357-1364, 2010

37. Bertrand N, Grenier P, Mahmoudi M, et al: Mechanistic understanding of in vivo protein corona formation on polymeric nanoparticles and impact on pharmacokinetics. Nature Communications 8, 2017

38. Monopoli MP, Aberg C, Salvati A, et al: Biomolecular coronas provide the biological identity of nanosized materials. Nat Nanotechnol 7:779-86, 2012

39. Rohner NA, Thomas SN: Melanoma growth effects on molecular clearance from tumors and biodistribution into systemic tissues versus draining lymph nodes. J Control Release 223:99-108, 2016

40. Gilleron J, Querbes W, Zeigerer A, et al: Image-based analysis of lipid nanoparticle–mediated siRNA delivery, intracellular trafficking and endosomal escape. Nature Biotechnology 31:638-646, 2013

41. Sigismund S, Confalonieri S, Ciliberto A, et al: Endocytosis and signaling: cell logistics shape the eukaryotic cell plan. Physiol Rev 92:273-366, 2012

42. Zhang Y, Sloan SA, Clarke LE, et al: Purification and Characterization of Progenitor and Mature Human Astrocytes Reveals Transcriptional and Functional Differences with Mouse. Neuron 89:37-53, 2016

43. Willmore A-MA, Simón-Gracia L, Toome K, et al: Targeted silver nanoparticles for ratiometric cell phenotyping. 2016

44. Medina DX, Householder KT, Ceton R, et al: Optical barcoding of PLGA for multispectral analysis of nanoparticle fate in vivo. 2017

45. Dahlman JE, Kauffman KJ, Xing Y, et al: Barcoded nanoparticles for high throughput in vivo discovery of targeted therapeutics. Proceedings of the National Academy of Sciences 114:2060-2065, 2017

46. Yaari Z, Da Silva D, Zinger A, et al: Theranostic barcoded nanoparticles for personalized cancer medicine. Nature Communications 7:13325, 2016

47. Metzker ML: Sequencing technologies - the next generation. Nat Rev Genet 11:31-46, 2010

48. Joung J, Engreitz JM, Konermann S, et al: Genome-scale activation screen identifies a lncRNA locus regulating a gene neighbourhood. Nature 548:343-346, 2017

49. Patel SJ, Sanjana NE, Kishton RJ, et al: Identification of essential genes for cancer immunotherapy. Nature 548:537-542, 2017

50. Shalem O, Sanjana NE, Hartenian E, et al: Genome-scale CRISPR-Cas9 knockout screening in human cells. Science 343:84-7, 2014

51. Kheirolomoom A, Kim CW, Seo JW, et al: Multifunctional Nanoparticles Facilitate Molecular Targeting and miRNA Delivery to Inhibit Atherosclerosis in ApoE(-/-) Mice. ACS Nano 9:8885-97, 2015

52. Chen S, Sanjana NE, Zheng K, et al: Genome-wide CRISPR screen in a mouse model of tumor growth and metastasis. Cell 160:1246-60, 2015

53. Chow RD, Guzman CD, Wang G, et al: AAV-mediated direct in vivo CRISPR screen identifies functional suppressors in glioblastoma. Nat Neurosci 20:1329-1341, 2017

54. Wang G, Chow RD, Ye L, et al: Mapping a functional cancer genome atlas of tumor suppressors in mouse liver using AAV-CRISPR-mediated direct in vivo screening. Sci Adv 4:eaao5508, 2018

55. Pei W, Feyerabend TB, Rossler J, et al: Polylox barcoding reveals haematopoietic stem cell fates realized in vivo. Nature 548:456-460, 2017

56. Deverman BE, Pravdo PL, Simpson BP, et al: Cre-dependent selection yields AAV variants for widespread gene transfer to the adult brain. Nat Biotechnol 34:204-9, 2016

57. Lisowski L, Dane AP, Chu K, et al: Selection and evaluation of clinically relevant AAV variants in a xenograft liver model. Nature 506:382-6, 2014

58. Mingozzi F, High KA: Therapeutic in vivo gene transfer for genetic disease using AAV: progress and challenges. Nat Rev Genet 12:341-55, 2011

59. Pasi KJ, Rangarajan S, Georgiev P, et al: Targeting of Antithrombin in Hemophilia A or B with RNAi Therapy. N Engl J Med 377:819-828, 2017

60. Adams D, Gonzalez-Duarte A, O'Riordan WD, et al: Patisiran, an RNAi Therapeutic, for Hereditary Transthyretin Amyloidosis. N Engl J Med 379:11-21, 2018

61. Lorenzer C, Dirin M, Winkler AM, et al: Going beyond the liver: progress and challenges of targeted delivery of siRNA therapeutics. J Control Release 203:1-15, 2015

62. Tsoi KM, MacParland SA, Ma XZ, et al: Mechanism of hard-nanomaterial clearance by the liver. Nat Mater 15:1212-1221, 2016

63. Zhang YN, Poon W, Tavares AJ, et al: Nanoparticle-liver interactions: Cellular uptake and hepatobiliary elimination. J Control Release 240:332-348, 2016

64. Dahlman JE, Barnes C, Khan OF, et al: In vivo endothelial siRNA delivery using polymeric nanoparticles with low molecular weight. Nat Nano 9:648-655, 2014

65. Hao J, Kos P, Zhou K, et al: Rapid Synthesis of a Lipocationic Polyester Library via Ring-Opening Polymerization of Functional Valerolactones for Efficacious siRNA Delivery. J Am Chem Soc 29:9206-9209, 2015

66. Siegwart DJ, Whitehead KA, Nuhn L, et al: Combinatorial synthesis of chemically diverse core-shell nanoparticles for intracellular delivery. Proc Natl Acad Sci U S A 108:12996-3001, 2011

67. Akinc A, Zumbuehl A, Goldberg M, et al: A combinatorial library of lipid-like materials for delivery of RNAi therapeutics. Nat Biotechnol 26:561-9, 2008

68. Paunovska K, Sago CD, Monaco CM, et al: A Direct Comparison of in Vitro and in Vivo Nucleic Acid Delivery Mediated by Hundreds of Nanoparticles Reveals a Weak Correlation. Nano Lett 18:2148-2157, 2018

69. Patel S, Ashwanikumar N, Robinson E, et al: Boosting Intracellular Delivery of Lipid Nanoparticle-Encapsulated mRNA. Nano Lett 17:5711-5718, 2017

70. Sahay G, Querbes W, Alabi C, et al: Efficiency of siRNA delivery by lipid nanoparticles is limited by endocytic recycling. Nat Biotechnol 31:653-8, 2013

71. Gilleron J, Querbes W, Zeigerer A, et al: Image-based analysis of lipid nanoparticle-mediated siRNA delivery, intracellular trafficking and endosomal escape. Nat Biotechnol 31:638-46, 2013

72. Wittrup A, Ai A, Liu X, et al: Visualizing lipid-formulated siRNA release from endosomes and target gene knockdown. Nat Biotechnol 33:870-6, 2015

73. Bertrand N, Grenier P, Mahmoudi M, et al: Mechanistic understanding of in vivo protein corona formation on polymeric nanoparticles and impact on pharmacokinetics. Nat Commun 8:777, 2017

74. Akinc A, Querbes W, De S, et al: Targeted delivery of RNAi therapeutics with endogenous and exogenous ligand-based mechanisms. Mol Ther 18:1357-64, 2010

75. Willoughby JLS, Chan A, Sehgal A, et al: Evaluation of GalNAc-siRNA Conjugate Activity in Pre-clinical Animal Models with Reduced Asialoglycoprotein Receptor Expression. Mol Ther 26:105-114, 2018

76. Paunovska K, Gil CJ, Lokugamage MP, et al: Analyzing 2000 in Vivo Drug Delivery Data Points Reveals Cholesterol Structure Impacts Nanoparticle Delivery. ACS Nano 12:8341-8349, 2018

77. Wang M, Thanou M: Targeting nanoparticles to cancer. Pharmacol Res 62:90-9, 2010

78. Ostergaard ME, Yu J, Kinberger GA, et al: Efficient Synthesis and Biological Evaluation of 5'-GalNAc Conjugated Antisense Oligonucleotides. Bioconjug Chem 26:1451-5, 2015

79. El-Sayed IH, Huang X, El-Sayed MA: Selective laser photo-thermal therapy of epithelial carcinoma using anti-EGFR antibody conjugated gold nanoparticles. Cancer Lett 239:129-35, 2006

80. Stevens PJ, Sekido M, Lee RJ: A folate receptor-targeted lipid nanoparticle formulation for a lipophilic paclitaxel prodrug. Pharm Res 21:2153-7, 2004

81. Davis ME, Zuckerman JE, Choi CH, et al: Evidence of RNAi in humans from systemically administered siRNA via targeted nanoparticles. Nature 464:1067-70, 2010

82. Muro S, Garnacho C, Champion JA, et al: Control of endothelial targeting and intracellular delivery of therapeutic enzymes by modulating the size and shape of ICAM-1-targeted carriers. Mol Ther 16:1450-8, 2008

83. Conesa A, Madrigal P, Tarazona S, et al: A survey of best practices for RNA-seq data analysis. Genome Biol 17:13, 2016

84. Lee MN, Ye C, Villani AC, et al: Common genetic variants modulate pathogen-sensing responses in human dendritic cells. Science 343:1246980, 2014

85. Vanlandewijck M, He L, Mae MA, et al: A molecular atlas of cell types and zonation in the brain vasculature. Nature 554:475-480, 2018

86. Zeisel A, Munoz-Manchado AB, Codeluppi S, et al: Brain structure. Cell types in the mouse cortex and hippocampus revealed by single-cell RNA-seq. Science 347:1138-42, 2015

87. Rozenblatt-Rosen O, Stubbington MJT, Regev A, et al: The Human Cell Atlas: from vision to reality. Nature 550:451-453, 2017

88. Collinet C, Stoter M, Bradshaw CR, et al: Systems survey of endocytosis by multiparametric image analysis. Nature 464:243-9, 2010

89. Palm W, Thompson CB: Nutrient acquisition strategies of mammalian cells. Nature 546:234-242, 2017

90. Doherty GJ, McMahon HT: Mechanisms of endocytosis. Annu Rev Biochem 78:857-902, 2009

91. Voigt J, Christensen J, Shastri VP: Differential uptake of nanoparticles by endothelial cells through polyelectrolytes with affinity for caveolae. Proc Natl Acad Sci U S A 111:2942-7, 2014

92. Shamay Y, Shah J, Isik M, et al: Quantitative self-assembly prediction yields targeted nanomedicines. Nat Mater 17:361-368, 2018

93. Cheng Z, Liu L, Wang Z, et al: Hypoxia Activates Src and Promotes Endocytosis Which Decreases MMP-2 Activity and Aggravates Renal Interstitial Fibrosis. Int J Mol Sci 19, 2018

94. Shihata WA, Putra MRA, Chin-Dusting JPF: Is There a Potential Therapeutic Role for Caveolin-1 in Fibrosis? Front Pharmacol 8:567, 2017

95. Gvaramia D, Blaauboer ME, Hanemaaijer R, et al: Role of caveolin-1 in fibrotic diseases. Matrix Biol 32:307-15, 2013

96. Yokomori H, Ando W, Yoshimura K, et al: Increases in endothelial caveolin-1 and cavins correlate with cirrhosis progression. Micron 76:52-61, 2015

97. Maniatis NA, Chernaya O, Shinin V, et al: Caveolins and lung function. Adv Exp Med Biol 729:157-79, 2012

98. Sotgia F, Martinez-Outschoorn UE, Pavlides S, et al: Understanding the Warburg effect and the prognostic value of stromal caveolin-1 as a marker of a lethal tumor microenvironment. Breast Cancer Res 13:213, 2011

99. Witkiewicz AK, Dasgupta A, Sotgia F, et al: An absence of stromal caveolin-1 expression predicts early tumor recurrence and poor clinical outcome in human breast cancers. Am J Pathol 174:2023-34, 2009

100. Yang G, Truong LD, Wheeler TM, et al: Caveolin-1 expression in clinically confined human prostate cancer: a novel prognostic marker. Cancer Res 59:5719-23, 1999

101. Wiechen K, Sers C, Agoulnik A, et al: Down-regulation of caveolin-1, a candidate tumor suppressor gene, in sarcomas. Am J Pathol 158:833-9, 2001

102. Gaudreault SB, Dea D, Poirier J: Increased caveolin-1 expression in Alzheimer's disease brain. Neurobiol Aging 25:753-9, 2004

103. Kassan A, Egawa J, Zhang Z, et al: Caveolin-1 regulation of disrupted-in-schizophrenia-1 as a potential therapeutic target for schizophrenia. J Neurophysiol 117:436-444, 2017

104. Chand S, Edwards NC, Chue CD, et al: Caveolin-1 single-nucleotide polymorphism and arterial stiffness in non-dialysis chronic kidney disease. Nephrol Dial Transplant 31:1140-4, 2016

105. Tourkina E, Bonner M, Oates J, et al: Altered monocyte and fibrocyte phenotype and function in scleroderma interstitial lung disease: reversal by caveolin-1 scaffolding domain peptide. Fibrogenesis Tissue Repair 4:15, 2011

106. Del Galdo F, Lisanti MP, Jimenez SA: Caveolin-1, transforming growth factor-beta receptor internalization, and the pathogenesis of systemic sclerosis. Curr Opin Rheumatol 20:713-9, 2008

107. Chen D, Love KT, Chen Y, et al: Rapid discovery of potent siRNA-containing lipid nanoparticles enabled by controlled microfluidic formulation. J Am Chem Soc 134:6948-51, 2012

108. Sager HB, Dutta P, Dahlman JE, et al: RNAi targeting multiple cell adhesion molecules reduces immune cell recruitment and vascular inflammation after myocardial infarction. Science Translational Medicine 8:342ra80-342ra80, 2016

109. Yun S, Budatha M, Dahlman JE, et al: Interaction between integrin alpha5 and PDE4D regulates endothelial inflammatory signalling. Nat Cell Biol, 2016

110. Sager HB, Hulsmans M, Lavine KJ, et al: Proliferation and Recruitment Contribute to Myocardial Macrophage Expansion in Chronic Heart Failure. Circ Res 119:853-64, 2016

111. White K, Lu Y, Annis S, et al: Genetic and hypoxic alterations of the microRNA-210-ISCU1/2 axis promote iron-sulfur deficiency and pulmonary hypertension. EMBO Mol Med 7:695-713, 2015

112. Platt RJ, Chen S, Zhou Y, et al: CRISPR-Cas9 knockin mice for genome editing and cancer modeling. Cell 159:440-55, 2014

113. Coelho T, Adams D, Silva A, et al: Safety and efficacy of RNAi therapy for transthyretin amyloidosis. N Engl J Med 369:819-29, 2013

114. Sahay G, Alakhova DY, Kabanov AV: Endocytosis of nanomedicines. J Control Release 145:182-95, 2010

115. Meng F, Wang J, Ping Q, et al: Quantitative Assessment of Nanoparticle Biodistribution by Fluorescence Imaging, Revisited. ACS Nano 12:6458-6468, 2018

116. Yang W: Nucleases: diversity of structure, function and mechanism. Q Rev Biophys 44:1-93, 2011

117. Hindson CM, Chevillet JR, Briggs HA, et al: Absolute quantification by droplet digital PCR versus analog real-time PCR. Nat Methods 10:1003-5, 2013

118. Dahlman JE, Kauffman KJ, Xing Y, et al: Barcoded nanoparticles for high throughput in vivo discovery of targeted therapeutics. Proc Natl Acad Sci U S A 114:2060-2065, 2017

119. Ni CW, Kumar S, Ankeny CJ, et al: Development of immortalized mouse aortic endothelial cell lines. Vasc Cell 6:7, 2014

120. Yaari Z, da Silva D, Zinger A, et al: Theranostic barcoded nanoparticles for personalized cancer medicine. Nat Commun 7:13325, 2016

121. Podrez EA, Poliakov E, Shen Z, et al: Identification of a novel family of oxidized phospholipids that serve as ligands for the macrophage scavenger receptor CD36. J Biol Chem 277:38503-16, 2002

122. Mattern HM, Raikar LS, Hardin CD: The effect of caveolin-1 (Cav-1) on fatty acid uptake and CD36 localization and lipotoxicity in vascular smooth muscle (VSM) cells. Int J Physiol Pathophysiol Pharmacol 1:1-14, 2009

123. Kuai R, Li D, Chen YE, et al: High-Density Lipoproteins (HDL) – Nature's Multi-Functional Nanoparticles. ACS nano 10:3015-3041, 2016

124. Lokugamage MP, Sago CD, Dahlman JE: Testing thousands of nanoparticles in vivo using DNA barcodes. Current Opinion in Biomedical Engineering 7:1-8, 2018

125. Khalil DN, Smith EL, Brentjens RJ, et al: The future of cancer treatment: immunomodulation, CARs and combination immunotherapy. Nat Rev Clin Oncol 13:273-90, 2016

126. Shifrut E, Carnevale J, Tobin V, et al: Genome-wide CRISPR Screens in Primary Human T Cells Reveal Key Regulators of Immune Function. Cell 175:1958-1971.e15, 2018

127. Kumar P, Ban HS, Kim SS, et al: T cell-specific siRNA delivery suppresses HIV-1 infection in humanized mice. Cell 134:577-86, 2008

128. Ramishetti S, Kedmi R, Goldsmith M, et al: Systemic Gene Silencing in Primary T Lymphocytes Using Targeted Lipid Nanoparticles. ACS Nano 9:6706-16, 2015

129. Smith TT, Stephan SB, Moffett HF, et al: In situ programming of leukaemia-specific T cells using synthetic DNA nanocarriers. Nat Nanotechnol 12:813-820, 2017

130. Cheng Z, Al Zaki A, Hui JZ, et al: Multifunctional nanoparticles: cost versus benefit of adding targeting and imaging capabilities. Science 338:903-10, 2012

131. Majorovits E, Nejmeddine M, Tanaka Y, et al: Human T-lymphotropic virus-1 visualized at the virological synapse by electron tomography. PLoS One 3:e2251, 2008

132. Dahlman JE, Barnes C, Khan OF, et al: In vivo endothelial siRNA delivery using polymeric nanoparticles with low molecular weight. Nature Nanotechnology 9:648-655, 2014

133. Sago CD, Lokugamage MP, Lando GN, et al: Modifying a Commonly Expressed Endocytic Receptor Retargets Nanoparticles in Vivo. Nano Lett, 2018

134. Villani AC, Satija R, Reynolds G, et al: Single-cell RNA-seq reveals new types of human blood dendritic cells, monocytes, and progenitors. Science 356, 2017

135. Sago CD, Lokugamage MP, Islam FZ, et al: Nanoparticles that deliver RNA to bone marrow identified by in vivo directed evolution. Journal of the American Chemical Society, 2018

136. Wang C, Ye Y, Hu Q, et al: Tailoring Biomaterials for Cancer Immunotherapy: Emerging Trends and Future Outlook. Adv Mater 29, 2017

137. Blanco E, Shen H, Ferrari M: Principles of nanoparticle design for overcoming biological barriers to drug delivery. Nature Biotechnology 33:941-951, 2015

138. Zhang S, Gao H, Bao G: Physical Principles of Nanoparticle Cellular Endocytosis. ACS Nano 9:8655-71, 2015

139. Hajj KA, Whitehead KA: Tools for translation: non-viral materials for therapeutic mRNA delivery. Nature Reviews Materials 2:17056, 2017

140. Carlsson L, Clarke JC, Yen C, et al: Biocompatible, Purified VEGF-A mRNA Improves Cardiac Function after Intracardiac Injection 1 Week Post-myocardial Infarction in Swine. Mol Ther Methods Clin Dev 9:330-346, 2018

141. Veiga N, Goldsmith M, Granot Y, et al: Cell specific delivery of modified mRNA expressing therapeutic proteins to leukocytes. Nature Communications 9:4493, 2018

142. Zhu X, Yin L, Theisen M, et al: Systemic mRNA Therapy for the Treatment of Fabry Disease: Preclinical Studies in Wild-Type Mice, Fabry Mouse Model, and Wild-Type Non-human Primates. Am J Hum Genet 104:625-637, 2019

143. Richner JM, Himansu S, Dowd KA, et al: Modified mRNA Vaccines Protect against Zika Virus Infection. Cell 168:1114-1125.e10, 2017

144. Kose N, Fox JM, Sapparapu G, et al: A lipid-encapsulated mRNA encoding a potently neutralizing human monoclonal antibody protects against chikungunya infection. Science immunology 4:eaaw6647, 2019

145. Yang Y, Lv J, Jiang S, et al: The emerging role of Toll-like receptor 4 in myocardial inflammation. Cell Death Dis 7:e2234, 2016

146. Pardi N, Hogan MJ, Porter FW, et al: mRNA vaccines - a new era in vaccinology. Nat Rev Drug Discov 17:261-279, 2018

147. Van Hoeven N, Fox CB, Granger B, et al: A Formulated TLR7/8 Agonist is a Flexible, Highly Potent and Effective Adjuvant for Pandemic Influenza Vaccines. Sci Rep 7:46426, 2017

148. Liang F, Lindgren G, Lin A, et al: Efficient Targeting and Activation of Antigen-Presenting Cells In Vivo after Modified mRNA Vaccine Administration in Rhesus Macaques. Mol Ther 25:2635-2647, 2017

149. Gay NJ, Symmons MF, Gangloff M, et al: Assembly and localization of Toll-like receptor signalling complexes. Nature Reviews Immunology 14:546, 2014

150. Kagan JC, Su T, Horng T, et al: TRAM couples endocytosis of Toll-like receptor 4 to the induction of interferon-beta. Nat Immunol 9:361-8, 2008

151. Tan Y, Zanoni I, Cullen TW, et al: Mechanisms of Toll-like Receptor 4 Endocytosis Reveal a Common Immune-Evasion Strategy Used by Pathogenic and Commensal Bacteria. Immunity 43:909-22, 2015

152. De Creus A, Abe M, Lau AH, et al: Low TLR4 expression by liver dendritic cells correlates with reduced capacity to activate allogeneic T cells in response to endotoxin. J Immunol 174:2037-45, 2005

153. Das A, Yang CS, Arifuzzaman S, et al: High-Resolution Mapping and Dynamics of the Transcriptome, Transcription Factors, and Transcription Co-Factor Networks in Classically and Alternatively Activated Macrophages. Front Immunol 9:22, 2018

154. Cabanski M, Steinmuller M, Marsh LM, et al: PKR regulates TLR2/TLR4-dependent signaling in murine alveolar macrophages. Am J Respir Cell Mol Biol 38:26-31, 2008

155. Garcia MA, Gil J, Ventoso I, et al: Impact of protein kinase PKR in cell biology: from antiviral to antiproliferative action. Microbiol Mol Biol Rev 70:1032-60, 2006

156. Tavares AJ, Poon W, Zhang YN, et al: Effect of removing Kupffer cells on nanoparticle tumor delivery. Proc Natl Acad Sci U S A 114:E10871-e10880, 2017

157. Yin H, Song C-Q, Suresh S, et al: Structure-guided chemical modification of guide RNA enables potent non-viral in vivo genome editing. Nature Biotechnology, 2017

158. Kauffman KJ, Oberli MA, Dorkin JR, et al: Rapid, Single-Cell Analysis and Discovery of Vectored mRNA Transfection In Vivo with a loxP-Flanked tdTomato Reporter Mouse. Mol Ther Nucleic Acids 10:55-63, 2018

159. Paunovska K, Da Silva Sanchez AJ, Sago CD, et al: Nanoparticles Containing Oxidized Cholesterol Deliver mRNA to the Liver Microenvironment at Clinically Relevant Doses. Adv Mater:e1807748, 2019

160. Sago CD, Lokugamage MP, Paunovska K, et al: High-throughput in vivo screen of functional mRNA delivery identifies nanoparticles for endothelial cell gene editing. Proceedings of the National Academy of Sciences, 2018

161. Couch Y, Trofimov A, Markova N, et al: Low-dose lipopolysaccharide (LPS) inhibits aggressive and augments depressive behaviours in a chronic mild stress model in mice. J Neuroinflammation 13:108, 2016

162. Kirschman JL, Bhosle S, Vanover D, et al: Characterizing exogenous mRNA delivery, trafficking, cytoplasmic release and RNA-protein correlations at the level of single cells. Nucleic Acids Res 45:e113, 2017

163. Kleffel S, Posch C, Barthel SR, et al: Melanoma Cell-Intrinsic PD-1 Receptor Functions Promote Tumor Growth. Cell 162:1242-56, 2015

164. Sabnis S, Kumarasinghe ES, Salerno T, et al: A Novel Amino Lipid Series for mRNA Delivery: Improved Endosomal Escape and Sustained Pharmacology and Safety in Non-human Primates. Mol Ther 26:1509-1519, 2018

165. Cheng Q, Wei T, Farbiak L, et al: Selective organ targeting (SORT) nanoparticles for tissue-specific mRNA delivery and CRISPR-Cas gene editing. Nat Nanotechnol, 2020

166. Fenton OS, Kauffman KJ, McClellan RL, et al: Customizable Lipid Nanoparticle Materials for the Delivery of siRNAs and mRNAs. Angew Chem Int Ed Engl 57:13582-13586, 2018

167. Kranz LM, Diken M, Haas H, et al: Systemic RNA delivery to dendritic cells exploits antiviral defence for cancer immunotherapy. Nature 534:396-401, 2016

168. Miao L, Li L, Huang Y, et al: Delivery of mRNA vaccines with heterocyclic lipids increases anti-tumor efficacy by STING-mediated immune cell activation. Nat Biotechnol 37:1174-1185, 2019

169. Zhang X, Li B, Luo X, et al: Biodegradable Amino-Ester Nanomaterials for Cas9 mRNA Delivery in Vitro and in Vivo. ACS Appl Mater Interfaces 9:25481-25487, 2017

170. Mui BL, Tam YK, Jayaraman M, et al: Influence of Polyethylene Glycol Lipid Desorption Rates on Pharmacokinetics and Pharmacodynamics of siRNA Lipid Nanoparticles. Mol Ther Nucleic Acids 2:e139, 2013

171. Patel S, Ashwanikumar N, Robinson E, et al: Naturally-occurring cholesterol analogues in lipid nanoparticles induce polymorphic shape and enhance intracellular delivery of mRNA. Nat Commun 11:983, 2020

172. Ball RL, Hajj KA, Vizelman J, et al: Lipid Nanoparticle Formulations for Enhanced Co-delivery of siRNA and mRNA. Nano Lett 18:3814-3822, 2018

173. Negron K, Khalasawi N, Lu B, et al: Widespread gene transfer to malignant gliomas with In vitro-to-In vivo correlation. Journal of Controlled Release 303:1-11, 2019

174. Alton E, Armstrong DK, Ashby D, et al: Repeated nebulisation of non-viral CFTR gene therapy in patients with cystic fibrosis: a randomised, double-blind, placebo-controlled, phase 2b trial. Lancet Respir Med 3:684-691, 2015

175. Dhama K, Sharun K, Tiwari R, et al: COVID-19, an emerging coronavirus infection: advances and prospects in designing and developing vaccines, immunotherapeutics, and therapeutics. Hum Vaccin Immunother:1-7, 2020

176. Akinc A, Maier MA, Manoharan M, et al: The Onpattro story and the clinical translation of nanomedicines containing nucleic acid-based drugs. Nat Nanotechnol 14:1084-1087, 2019

177. Mulligan MJ, Lyke KE, Kitchin N, et al: Phase 1/2 study of COVID-19 RNA vaccine BNT162b1 in adults. Nature, 2020

178. Jackson LA, Anderson EJ, Rouphael NG, et al: An mRNA Vaccine against SARS-CoV-2 - Preliminary Report. N Engl J Med, 2020

179. Patel AK, Kaczmarek JC, Bose S, et al: Inhaled Nanoformulated mRNA Polyplexes for Protein Production in Lung Epithelium. Adv Mater 31:e1805116, 2019

180. Guan S, Munder A, Hedtfeld S, et al: Self-assembled peptide-poloxamine nanoparticles enable in vitro and in vivo genome restoration for cystic fibrosis. Nat Nanotechnol 14:287-297, 2019

181. Densmore CL, Orson FM, Xu B, et al: Aerosol delivery of robust polyethyleneimine-DNA complexes for gene therapy and genetic immunization. Mol Ther 1:180-8, 2000

182. Rudolph C, Ortiz A, Schillinger U, et al: Methodological optimization of polyethylenimine (PEI)-based gene delivery to the lungs of mice via aerosol application. J Gene Med 7:59-66, 2005

183. Raesch SS, Tenzer S, Storck W, et al: Proteomic and Lipidomic Analysis of Nanoparticle Corona upon Contact with Lung Surfactant Reveals Differences in Protein, but Not Lipid Composition. ACS Nano 9:11872-85, 2015

184. Yin B, Chan CKW, Liu S, et al: Intrapulmonary Cellular-Level Distribution of Inhaled Nanoparticles with Defined Functional Groups and Its Correlations with Protein Corona and Inflammatory Response. ACS Nano 13:14048-14069, 2019

185. Montoro DT, Haber AL, Biton M, et al: A revised airway epithelial hierarchy includes CFTR-expressing ionocytes. Nature 560:319-324, 2018

186. Lokugamage MP, Gan Z, Zurla C, et al: Mild Innate Immune Activation Overrides Efficient Nanoparticle-Mediated RNA Delivery. Adv Mater:e1904905, 2019

187. Lokugamage MP, Sago CD, Gan Z, et al: Constrained Nanoparticles Deliver siRNA and sgRNA to T Cells In Vivo without Targeting Ligands. Adv Mater 31:e1902251, 2019

188. Jones B, Nachtsheim CJ: A Class of Three-Level Designs for Definitive Screening in the Presence of Second-Order Effects. Journal of Quality Technology 43:1-15, 2011

189. Kauffman KJ, Dorkin JR, Yang JH, et al: Optimization of Lipid Nanoparticle Formulations for mRNA Delivery in Vivo with Fractional Factorial and Definitive Screening Designs. Nano Lett 15:7300-6, 2015

190. Kaczmarek JC, Patel AK, Kauffman KJ, et al: Polymer-Lipid Nanoparticles for Systemic Delivery of mRNA to the Lungs. Angew Chem Int Ed Engl 55:13808-13812, 2016

191. Kumar V, Qin J, Jiang Y, et al: Shielding of Lipid Nanoparticles for siRNA Delivery: Impact on Physicochemical Properties, Cytokine Induction, and Efficacy. Mol Ther Nucleic Acids 3:e210, 2014

192. Khan OF, Kowalski PS, Doloff JC, et al: Endothelial siRNA delivery in nonhuman primates using ionizable low-molecular weight polymeric nanoparticles. Sci Adv 4:eaar8409, 2018

193. Huckaby JT, Lai SK: PEGylation for enhancing nanoparticle diffusion in mucus. Adv Drug Deliv Rev 124:125-139, 2018

194. Semple SC, Akinc A, Chen J, et al: Rational design of cationic lipids for siRNA delivery. Nature Biotechnology 28:172-176, 2010

195. Tiwari PM, Vanover D, Lindsay KE, et al: Engineered mRNA-expressed antibodies prevent respiratory syncytial virus infection. Nat Commun 9:3999, 2018

196. Gonzalez AJ, Ijezie EC, Balemba OB, et al: Attenuation of Influenza A Virus Disease Severity by Viral Coinfection in a Mouse Model. J Virol 92, 2018

197. Sahu I, Haque A, Weidensee B, et al: Recent Developments in mRNA-Based Protein Supplementation Therapy to Target Lung Diseases. Mol Ther 27:803-823, 2019

198. Hak S, Helgesen E, Hektoen HH, et al: The effect of nanoparticle polyethylene glycol surface density on ligand-directed tumor targeting studied in vivo by dual modality imaging. ACS Nano 6:5648-58, 2012

199. Georgiev GA, Sarker DK, Al-Hanbali O, et al: Effects of poly (ethylene glycol) chains conformational transition on the properties of mixed DMPC/DMPE-PEG thin liquid films and monolayers. Colloids Surf B Biointerfaces 59:184-93, 2007

200. Corbett KS, Flynn B, Foulds KE, et al: Evaluation of the mRNA-1273 Vaccine against SARS-CoV-2 in Nonhuman Primates. N Engl J Med 383:1544-1555, 2020

201. Suk JS, Xu Q, Kim N, et al: PEGylation as a strategy for improving nanoparticle-based drug and gene delivery. Adv Drug Deliv Rev 99:28-51, 2016

202. Pelaz B, del Pino P, Maffre P, et al: Surface Functionalization of Nanoparticles with Polyethylene Glycol: Effects on Protein Adsorption and Cellular Uptake. ACS Nano 9:6996-7008, 2015

203. Mangal S, Gao W, Li T, et al: Pulmonary delivery of nanoparticle chemotherapy for the treatment of lung cancers: challenges and opportunities. Acta Pharmacol Sin 38:782-797, 2017

204. Rubin BK: Mucus structure and properties in cystic fibrosis. Paediatr Respir Rev 8:4-7, 2007

205. Da Silva Sanchez A, Paunovska K, Cristian A, et al: Treating Cystic Fibrosis with mRNA and CRISPR. Hum Gene Ther 31:940-955, 2020

206. Lindsay KE, Vanover D, Thoresen M, et al: Aerosol Delivery of Synthetic mRNA to Vaginal Mucosa Leads to Durable Expression of Broadly Neutralizing Antibodies against HIV. Mol Ther 28:805-819, 2020

207. Walsh EE, Frenck RW, Falsey AR, et al: Safety and Immunogenicity of Two RNA-Based Covid-19 Vaccine Candidates. New England Journal of Medicine, 2020

208. Li Q, Chan C, Peterson N, et al: Engineering Caveolae-Targeted Lipid Nanoparticles To Deliver mRNA to the Lungs. ACS Chemical Biology 15:830-836, 2020

209. Fenton OS, Kauffman KJ, Kaczmarek JC, et al: Synthesis and Biological Evaluation of Ionizable Lipid Materials for the In Vivo Delivery of Messenger RNA to B Lymphocytes. Adv Mater 29, 2017

210. Kulkarni JA, Darjuan MM, Mercer JE, et al: On the Formation and Morphology of Lipid Nanoparticles Containing Ionizable Cationic Lipids and siRNA. ACS Nano 12:4787-4795, 2018

211. Kulkarni JA, Witzigmann D, Leung J, et al: On the role of helper lipids in lipid nanoparticle formulations of siRNA. Nanoscale 11:21733-21739, 2019

212. Brinkman EK, Chen T, Amendola M, et al: Easy quantitative assessment of genome editing by sequence trace decomposition. Nucleic Acids Res 42:e168, 2014

213. Roberts TC, Langer R, Wood MJA: Advances in oligonucleotide drug delivery. Nature Reviews Drug Discovery 19:673-694, 2020

214. Gan Z, Lokugamage MP, Hatit MZC, et al: Nanoparticles containing constrained phospholipids deliver mRNA to liver immune cells in vivo without targeting ligands. Bioengineering & Translational Medicine 5:e10161, 2020

215. Paunovska K, Loughrey D, Sago CD, et al: Using Large Datasets to Understand Nanotechnology. Advanced Materials 31:1902798, 2019

216. Hordeaux J, Yuan Y, Clark PM, et al: The GPI-Linked Protein LY6A Drives AAV-PHP.B Transport across the Blood-Brain Barrier. Mol Ther 27:912-921, 2019

217. Huang Q, Chan KY, Tobey IG, et al: Delivering genes across the blood-brain barrier: LY6A, a novel cellular receptor for AAV-PHP.B capsids. bioRxiv:538421, 2019

218. Khera E, Thurber GM: Pharmacokinetic and Immunological Considerations for Expanding the Therapeutic Window of Next-Generation Antibody-Drug Conjugates. BioDrugs 32:465-480, 2018

219. Maier MA, Jayaraman M, Matsuda S, et al: Biodegradable lipids enabling rapidly eliminated lipid nanoparticles for systemic delivery of RNAi therapeutics. Mol Ther 21:1570-8, 2013

220. Dai L, Gao GF: Viral targets for vaccines against COVID-19. Nature Reviews Immunology 21:73-82, 2021